Università degli Studi di Milano

FACOLTA' DI SCIENZE E TECNOLOGIE

Department of Chemistry
Doctorate Course in Industrial Chemistry
XXXIII Cycle, 2017-2020

PhD thesis

Pros and cons of nanomaterials: study of Halloysite-based nanocomposites for biomedical/catalytic purposes and evaluation of environmental aquatic toxicity of CeO_2 nanoparticles.

Hady Hamza

R11988

Supervisor: Prof. Daniela Maggioni

Coordinator: Prof. Dominique Roberto

Table of Contents

Part Two Ceria-based nanocomposites for environment toxicological studies

Acknowledgements

I would like to express my sincere gratitude to my thesis advisor, Prof. Daniela Maggioni, for accepting me as her student, whose expertise; understanding, care, and patience during the past three years played a vital role in my successful completion of PhD work. Without her help, I would not be the person I am today. I will forever be cherishing her beautiful friendship, guidance, and always be in contact with her in future work.

I would like to thank Stefano Cattaneo, Marco Galli and Katarzyna Fidecka for sharing their ideas and expertise in synthetic chemistry, which later helped in improving my research results.

I also thank my lab mates whom I worked with: Delia, Grazia, Emma, Xani, Erika, Daniel, Giovanni, and Ilaria, I appreciate their friendship and help in my research.

Special thanks to Prof. Monica Panigati and Prof. Lucia Carlucci who constantly supported and encouraged me throughout my staying in Italy.

To my parents, my wife and all my family, for their unconditional love and support during good and bad times: thank you.

Lastly, I would like to thank Università degli Studi di Milano, which allowed me to undertake the doctorate studies and supported me in a form of a scholarship.

Table of abbreviations

Term	Definition
AAS	Atomic absorption spectroscopy
A-HNT	Australian halloysite nanotube
ALA	aminolevulinic acid
ATSDR	Agency for Toxic Substances and Disease Registry
Au NPs	gold nanoparticles
CAL	Cinnamaldehyde
CAT	catalase
CNT	carbon nanotubes
COH	cinnamyl alcohol
CTAB	cetyltrimethylammonium bromide
DHN	1,5-dihydroxynaphtalene
DMSA	dimercaptosuccinic acid
ETS	electron transport system
FC	Field Cooled
GA	gallic acid
GNS	gold nanostars
GR	glutathione reductase
GSH	reduced glutathione
GSTs	glutathione-s-transferases
HCAL	hydrocinnamaldehyde
HCOH	hydrocinnamyl alcohol
HEPES	4-(2-hydroxyethyl)-1-piperazineethanesulfonic acid
h-HNT	hydroxilated Halloysite nanotubes
HNT	Halloysite nanotubes
HPD	hematoporphyrin derivatives
IL	intraligand
ILCT	intraligand transfer
IMNT	imogolite nanotube
LLCT	ligand-to-ligand charge transfer
LMCT	ligand-to-metal charge transfer
MC	metal-centred
MFH	magnetic fluid hyperthermia
MLCT	metal-to-ligand charge transfer
MMCT	metal-to-metal charge transfer
MNPs	metal nanoparticles
MRI	magnetic resonance
NIR	near-infrared
Nms	nanomaterials
NOM	natural organic matter
NPs	nanoparticles
OA	oleic acid

PA	protocatechuic acid
PDA	16-phosphonohexadecanoic acid
PDT	photodynamic therapy
PPR	phenyl propane
PS	photosensitizer
PVP	poly(N-vinylpyrolidone)
ROS	reactive oxygen species
S-HNT	Sigma-Aldrich halloysite
SOD	superoxy-dismutase
SPION	Superparamagnetic iron oxide nanoparticles
SPR	Surface Plasmon Resonance
TDP	tetradecylphosphonic acid
TEA	triethylamine
TEM	Transmission Electron Microscopy
TGA	Thermogravimetric analysis
TMAOH	tetramethylammonium hydroxide
XRD	x-ray powder diffraction
ZFC	Zero Field Cooled

Aims and objectives.

My Ph.D. dealt mainly with the study of halloysite nanotubes (HNT), and their interaction with molecules and nanoparticles as potential for potential applications either in biomedicine or in catalysis. A minor part of my Ph.D work was dedicated to the preparation and characterization of Ceria nanoparticles stabilized with polymers of different charge, to investigate, in collaboration with the group of prof Della Torre and Binelli, their effect on various animal and bacterial models relative to their possible toxic effects especially in the aquatic environment.

I started the first part of my thesis by introducing the clay material HNT. HNT is a unique natural nanomaterial composed of double-layered aluminosilicate with a hollow tubular structure in the micro range. A preliminary literature survey revealed that HNT, due to their physical and chemical features, could be suitable for many application fields like medicine and catalysis (**Chapter 1**). We started our aim by synthesizing some HNT adducts possibly suitable for hyperthermia applications by selectively load superparamagnetic iron oxides (SPIONs) into the inner lumen of HNT. The magnetic properties of the loaded SPIONs did not change after their trapping inside the HNT lumen. The SPION-in-HNT nanocomposite was synthesized through the pre-modification of the HNT inner lumen such that it becomes suitable to be suitable to load the apolar SPION as synthesized by thermal decomposition method without a further step of ligand exchange (**Chapter 2**). To extend the loading to another kind of NP for hyperthermia applications, we tried to load gold nanoparticles. The gold NPs can be synthesized in various shapes; we synthesized spherical and star shapes of gold for our purpose. Gold can be loaded inside the inner lumen in the studied shapes, but the low concentration of gold suspension hampered a massive loading into the HNT lumen. (**Chapter 3**). The second part of the work with Halloysites was devoted to the preparation and characterization of HNT adducts with luminescent molecules able to act as photosensitizers for photodynamic therapy (PDT). For this purpose, we were interested in loading perfluorinated porphyrin, in their non-coordinated- and Zn-coordinated form, inside the lumen of HNT. The release of the photosensitizer by the inner lumen was slowed down compared to the release of the perfluorinated drugs adsorbed in the outer surface of HNT. (**Chapter 4**). To use HNT as a dual vector for drug delivery, we synthesized HNT-Ru photosensitizer. The photosensitizer was covalently bonded to the silica part of the outer surface of HNT, leaving the inner lumen free for potentially an extra loading with another drug. The photophysical properties of synthesized nanocomposite were then tested (**Chapter 5**). Finally, concerning HNT, we aimed to synthesize a new synthetic Au-Pt nanoparticle supported over HNT with different Au-to-Pt molar ratios via a sol immobilization method for catalytic purposes. The synthesized catalyst showed that the activity toward hydrogenation of C=O of cinnamaldehyde increased with increasing the molar ratio of Au/Pt (**Chapter 6**).

Unfortunately, the product potentially useful for biomedical purposes were not tested at least at cellular level, and this lack to the work was essentially due to the COVID-19 pandemic situation that slowed down a lot of collaboration especially with biologist collaborators.

The last part of my thesis was devoted to synthesizing nanoceria and covering it with natural polymer available in the aquatic system as alginate and chitosan. Ceria NPs surrounded by both Alginate and Chitosan showed no acute toxicity effects at the average environmental concentration level of the two tested natural macromolecules (**Chapter 7**).

Part one
Halloysites-based nanocomposites

Chapter 1

Halloysite nanotubes Introduction

1. Clay minerals

The phyllosilicates, or sheet silicates, are an important class of minerals that includes the micas, chlorite, serpentine, talc and clay minerals groups. Phyllosilicate crystals consist of silicon, aluminum or magnesium, oxygen, and hydroxyl groups, with various associated cations. These ions and OH groups are organized into two-dimensional structures called sheets, occurring in two types: tetrahedral sheets (T) and octahedral sheets (O). A continuous (T) sheet formed by $[M_2O_5]^{2-}$ species, where M (Si^{4+}, Al^{3+} or Fe^{3+}) is placed in the centre of the tetrahedron and the four oxygen atoms are located in the edges. Three out of the four oxygens from each tetrahedron are shared with other tetrahedral (**Figure 1**). In the O sheet, the smallest structural unit of the octahedral sheets contains three octahedra. If the cations are 2+ ions like Mg^{2+} or Fe^{2+}, all the three octahedra have cations at their centre and the sheet takes on the structure of trioctahedral (as Brucite) $[M(OH)_3]$, in which each O or OH ion is surrounded by 3 divalent cations. If the cations are 3+ like Al^{3+} or Fe^{3+}, only two octahedra are occupied and one octahedron is vacant and the sheet takes on the structure of dioctahedral (as Gibbsite) $[M(OH)_3]$, in which each O or OH ion is surrounded by 2 trivalent cations (**Figure 1**).[1,2] Depending on the ratio of tetrahedral to octahedral sheets in the crystalline unit cell (1:1 or 2:1), the layer-stacking sequences and the presence of interlayer materials, different phyllosilicates species can be classified (**Figure 2**). For the anions, in the case of TO, there are three planes of anions: one plane consists of the *basal* O^{2-} ions of the tetrahedral sheet, the second consists of *apical* O^{2-} ions (being the fourth tetrahedral corner points in a direction normal to the T sheet) common to both the tetrahedral and octahedral sheets plus OH- belonging to the octahedral sheet, and the third consists only of OH^- belonging to the octahedral sheet.[3] In the case of TOT sequence, there are four planes of anions: the outer two planes consist of the basal oxygen (O's) of the two tetrahedral sheets, while the two inner planes consist of oxygen atoms common to the octahedral sheet and one of the tetrahedral sheets, plus the hydroxyls (OH's) of the octahedral sheet (**Figure 3**). The layer repetition defines the d_{001} (basal spacing or layer stacking), and it is the fundamental parameter, representing the thickness of the unit cell and this spacing is characteristic of the type of the present stacking. It is labelled using the Miller indices (=hkl value), and they are determined by x-ray powder diffraction (XRD).

Since clay minerals like kaolinite, halloysite, bentonite, sepiolite and laponite are available in large amounts at low cost, they have been used as raw materials for hundreds of industrial applications such as in pharmaceuticals, cosmetic, paints, dyes, construction, environmental

remediation, food processing and for centuries artisans have been using halloysite clay to make porcelain, ceramic and other fine china.[4,5]

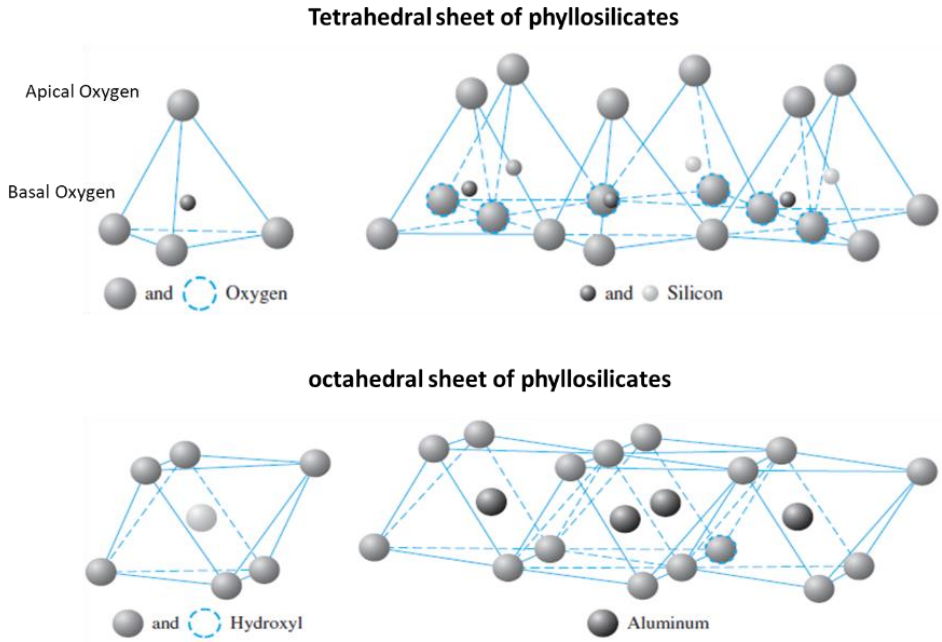

Figure 1 Tetrahedral and octahedral sheets of the phyllosilicates.[6,7]

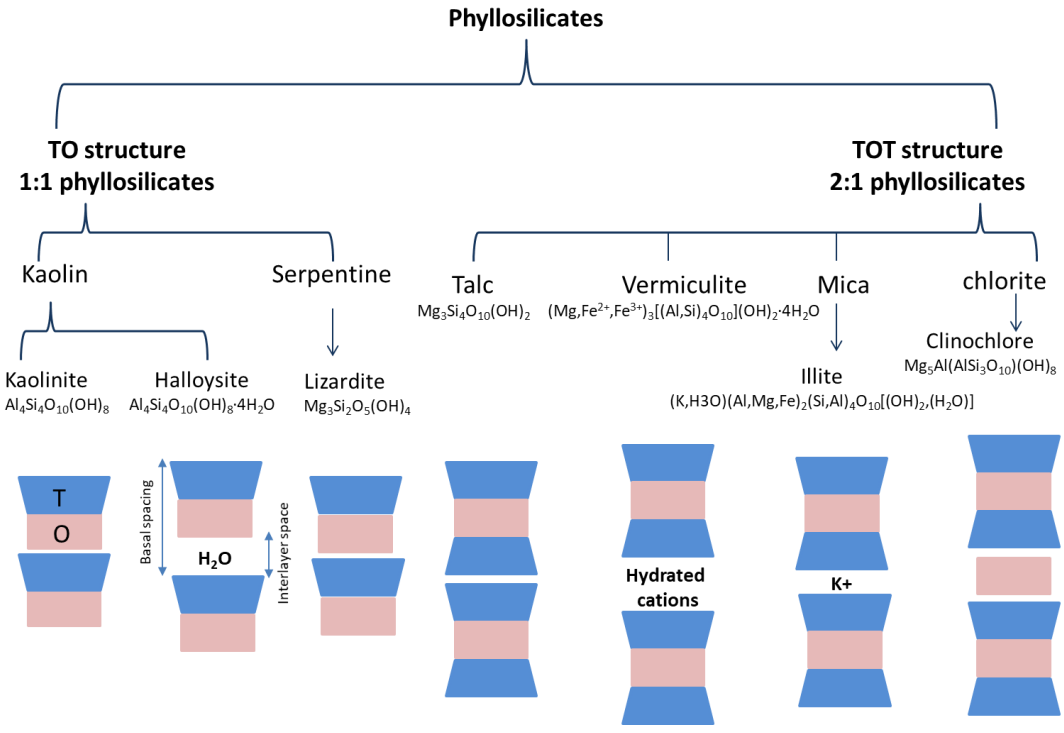

Figure 2 Schematic classification of phyllosilicate clay minerals.[1,2,8]

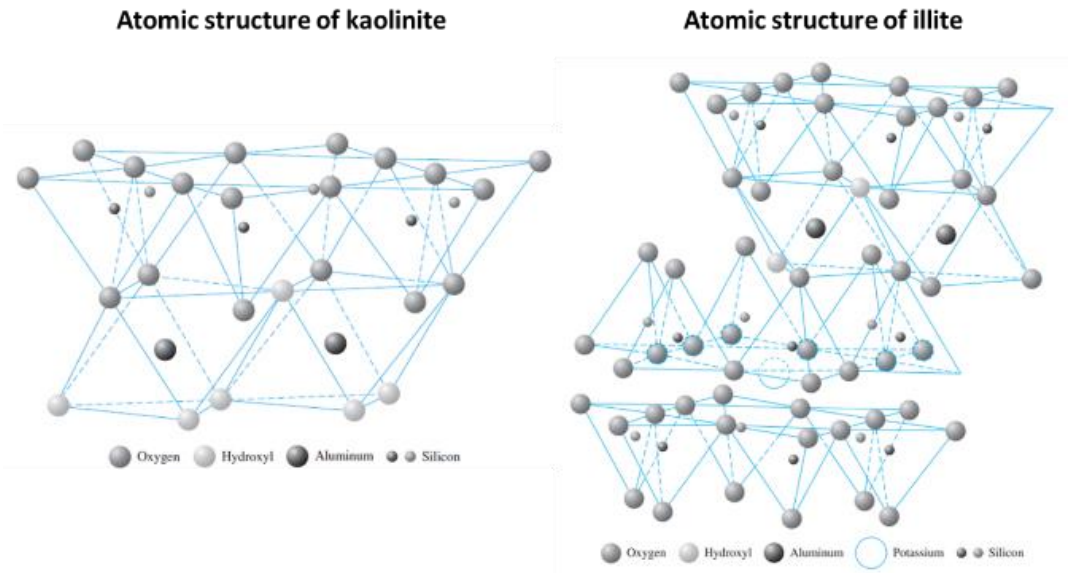

Figure 3 Atomic structure of Kaolinite (1:1) and Illite (2:1) clay minerals [7]

Recently, among the plethora of clay minerals, great attention has been paid to the use of kaolin minerals as excipients in pharmacological preparations for both topical and oral administration (**Figure. 4a**). In this context, halloysite, an aluminosilicate clay of the kaolin group, is becoming attractive for the scientific community as proved by the more and more increasing number of publications. Since 2005, the number of patents has virtually equalled the number of papers on HNT. These observations provide clear evidence that research on halloysite is readily translated into important new technologies, perhaps to a greater extent than the research on any other clay mineral (**Figure 4b**). So, halloysite nanotubes were the main research topic of these conducted PhD studies and will be described in the following part.

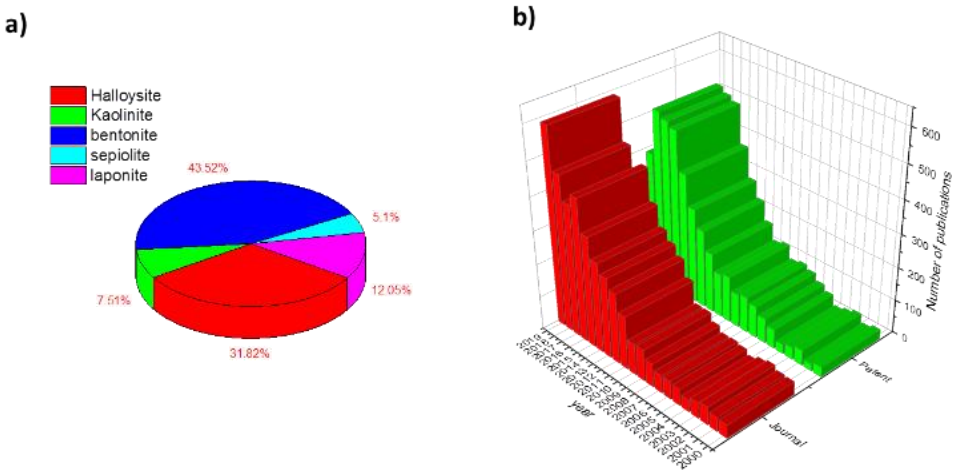

Figure 4 Comparison of a) the number of scientific publication on the Halloysite, Kaolinite, Bentonite, Sepiolite, Laponite terms with the term drug. (b) the annual number of scientific papers and patent related to halloysite. Data analysis was done on February 2021 using the SciFinder database. The data reflects the past 20 years**.**

2. Halloysite clay mineral

Halloysite is a naturally occurring kaolin mineral with the same chemical composition as kaolinite, except for higher water content, and have usually a tubular morphology **(Figure 5**). Thousands of tons of HNT are available from natural deposits in countries such as China, the United States of America, Mexico, Brazil, France, Spain, New Zealand, Australia and others.[9–11] The layer of halloysite consists of one sheet SiO_4 tetrahedra combined with one sheet of AlO_6 octahedra. The ideal unit formula for halloysite-7A and halloysite-10A is $Al_2Si_2O_5(OH)_4.nH_2O$ where n = 0 and 2, respectively. [12]

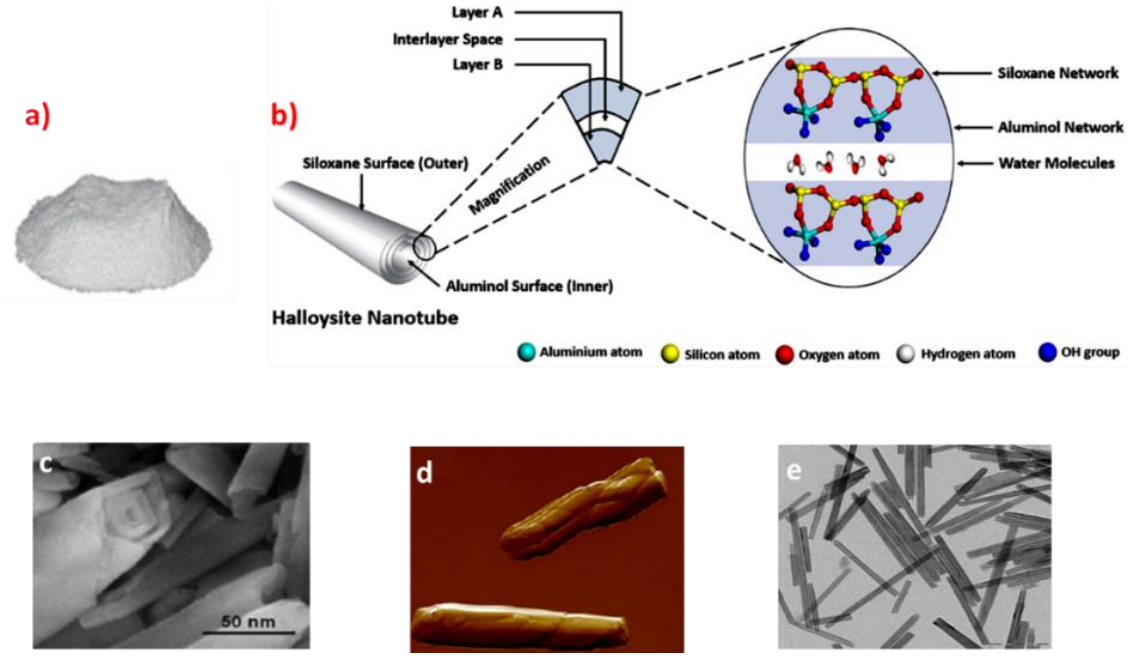

Figure 5 (a) HNT powder. (b) Schematic illustration of the crystal structure[13], (c&d) SEM and AFM image of Applied Minerals Inc., NY [14], (e) TEM of Australian HNT used in our research.

2.1. History

Jean Baptiste Julien d'Omalius d'Halloy discovered halloysite mineral in Angleur, Belgium and it was named after him in 1826[15], and they are found widely deposited in soils worldwide. In the 19th century, this material was originally distinguished from kaolinite based on its higher proportion of water. HNTis one of the most promising natural green nanomaterials due to the countless properties they possess and research on HNT and their applications have been extensively going.[16] Up until about 2005, the main uses of HNT had been as an alternative raw substance to kaolinite for ceramics. Since then, however, there has been tremendous increase in studies aimed at the uses of HNT. The readily available and relatively cheap nanotubular forms of halloysite have potential uses in nanocomposites with polymers, as vectors for active agents,

e.g. in medicine, agriculture, cosmetics, and environmental remediation, as well as in nano-templating, as supports for catalysts.[17]

2.2. Origin

HNT product like other clay minerals is resulting from weathering or mainly due to hydrothermal alteration of alumino-silicate minerals. Over geological time, which is counted in millions of years, clay deposits as kaolinite in ocean deep, where temperatures and pressures are significant, undergo recrystallization to other forms like halloysite. HNT either in a few deposits presented in almost pure form and contains 90–95 wt% of tubes or, is accompanied by different types of associated minerals. For instance, the Matauri Bay HNT deposit (in Northland, New Zealand), formed by the low-temperature hydrothermal alteration of rhyolite and dacite volcanic rocks, is mainly associated with quartz, cristobalite, and feldspar. The Dragon Mine HNT deposit (in Utah, USA), formed by the hydrothermal alteration of dolomite, is associated with Kaolinite, gibbsite, alunite, and quartz.[18]

HNT main constituents are aluminium (20.90 %), silicon (21.76 %) and hydrogen (1.56 %). The conditions of formation are much similar to that for kaolinite and the two polytypes often occur together.[19] Rarity of halloysite compared to kaolinite is owing to stability ($\Delta H_{f\ kaolinite}$ = -4115.30 kJ/mol, $\Delta H_{f\ halloysite}$ = -4092.93 kJ/mol)[20], so with enough time ≈ 120 Ka (120 thousand annual), the halloysite may be replaced by the more stable kaolinite during the dehydration of halloysite (**Figure 6**).[21,22]

Interestingly, the reverse has also been observed, apparently, as a result of the hydration of kaolinite which causes rolling of 1:1 layers (**Figure 7**),[23] so HNT is often referred to as rolled kaolin (typically 10 to 20 aluminosilicate layers roll into a cylinder with packing periodicity of 0.72 nm).[14,24,25]

Few sharp edges at the external layer of the tubes are evident from the previous SEM image (**Figure 5c**) These edges in the upper layers were predicted as specific lines of the sheet defects rolled to HNT.[26] Bates et al. proposed that the 1:1 layer of Kaolin rolls to form HNT, with the tetrahedral sheet on the outside of the curve, to minimize the misfit of the larger tetrahedral and smaller octahedral sheets.[27] Also this direction of rotation is favoured because of the least resistance offered by Si-Si repulsion.[28] The existence of a water layer may facilitate layer rolling because it reduces the interlayer bonding. So synthesis of halloysite from kaoline could be done practically using solvothermal and exfoliation methods.[29–31]

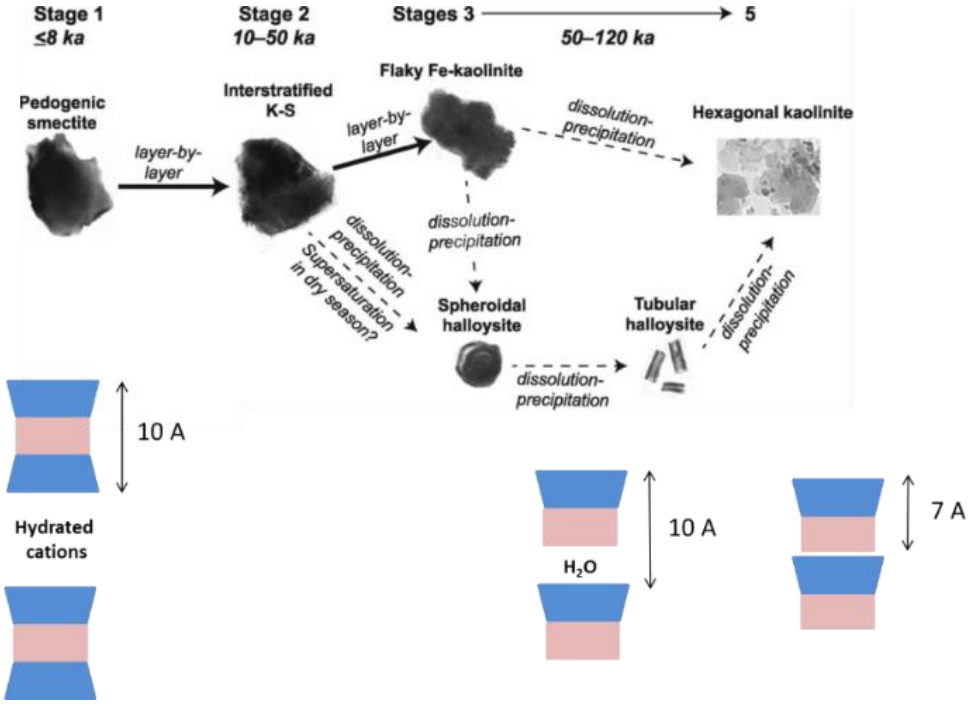

Figure 6 Schematic diagram of the evolution of the clay-mineral assemblage over time.[22]

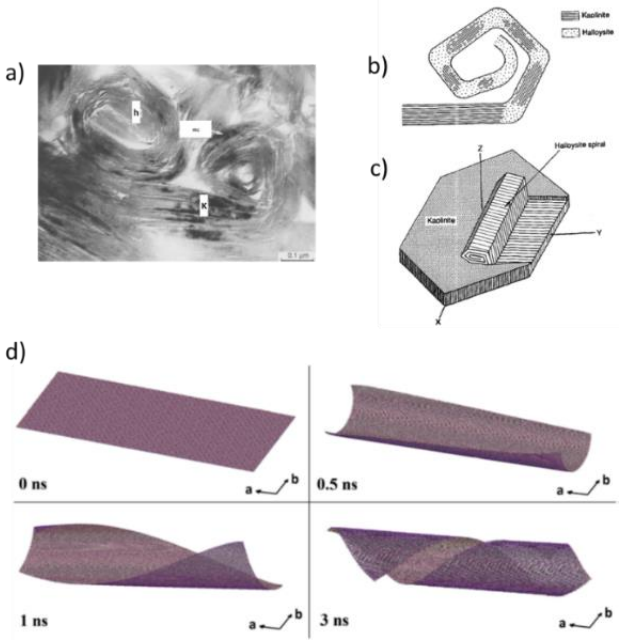

Figure 7. (a)Captured kaolinite transformation into rolled halloysite tubes. k stands for kaolinite, h for rolling halloysite, while mc (mottled diffraction contrast) signifies straight sections of halloysite, similar to kaolinite; (b) Schematic explanation of halloysite development from kaolinite; (c) Part of kaolinite spiralling into the form of halloysite on kaolinite plate; (d) Computer simulations. Twisting kaolinite layer in time into halloysite structure with a diameter of 27 nm.[23,32]

2.3. Physico-chemical features of halloysite

Colour. Pure HNT is a white mineral, even though in some cases the mineral is coloured from yellowish to brown. Impurities like Fe^{3+}, Cr^{3+}, Ti^{4+} ions may substitute Al^{3+} or Si^{4+} and are the reason for halloysite colouring.[14]

Morphology. Naturally occurring HNT appears in varied morphologies, such as platy, spheroidal, and tubular. However, the tubular structure is the dominant morphology of HNT in nature.[33] The crystallization conditions and geological occurrence of HNT are closely related to its morphology. For example, the HNT exhibits spheroidal morphology when recrystallized from supersaturated solutions of volcanic glass and pumice.[12] However, the HNT exhibits a tubular morphology when formed by the hydrothermal alteration of biotite,[34] by the weathering of feldspar in granitic rocks in southern Italy, [35] and by the topological alteration of platy Kaolinite.[25]

Features. Due to their different chemical composition, the HNT undergo ionization in aqueous media in an opposite way, generating tubes with oppositely charged inner and outer surfaces. This charge separation occurs in water within a wide pH range from 2.5 to 8.5.[36] The tubes have a length in the range of 0.2-30 µm,[12], while the inner and outer diameters of the tubes are in the ranges of 10–100 nm and 30–190 nm, respectively. The common characterization of HNT are summarized in **Table 1**.

Table 1 Common physical and chemical characteristics of HNT.

HNT characteristic	Value	ref
Length	0.2–30 µm	12,16,37
Inner diameter	10-100 nm	38,39
Outer diameter	30-190 nm	37,38
Elastic modulus	130-340 GPa	16,40
Particle size range in aqueous solution	50-450 nm	16,41,42
BET surface area	22.1–81.6 $m^2.g^{-1}$	16,18
Pore space	14–46.8%	16,42
Lumen space	11–39%	16
Density	2.14-2.59 $g.cm^{-3}$	16
Cation exchange capacity	Dehydrated HNT: 5-10 meq/100 g	42,43
	Hydrated HNT: 40-50 meq/100 g	
Surface charge	Negative outer - siloxanes	36,44
	Positive inner - aluminols	

2.4. The relation between Halloysite and other nanotubes (imogolite & CNT)

HNT exhibit several advantages over synthetic nanotubes, such as carbon nanotubes (CNT). According to Lvov et al., the price of HNT is as low as $4 per kg, which is much lower than that of CNT ($500 per kg). HNT is available at the scale of thousands of tons, comparing with the gram scale for CNT. Thus, HNT can easily meet mass-scale applications in the industry. As a naturally occurring nanomaterial, the exploitation of HNT requires less energy consumption and causes negligible environmental pollution. HNT has been proven to be biocompatible with low

cytotoxicity, but CNT is toxic. Therefore, HNT is regarded as a green nanomaterial. Compared with imogolite nanotube (IMNT), which is naturally occurring,[45] the pore size of HNT is much larger. This enables HNT to be capable of hosting large-sized molecules, such as, for example, various enzymes.[46] The characteristics of HNT, IMNT, and CNT are summarized in **Table 2**.

Table 2 Typical properties of HNT, IMNT and CNT.[14,47]

	Halloysite (HNT)	Imogolite (IMNT)	Carbon Nanotube (CNT)
Chemical formula	$Al_2Si_2O_5(OH)_4$	$Al_4Si_2O_6(OH)_8$	C
Surface chemistry	SiO_2 (external) $Al(OH)_3$ (internal)	$Al(OH)_3$ (external) SiO_2 (internal)	graphene (both side)
Surface charge at pH 2–9	Negative	Positive	Not charged
Common Length	0.5–2 µm	1–5 µm	1–5 µm
Common external diameter	50–100 nm	2–10 nm	2–10 nm
Common Inner diameter	10–20 nm	1–5 nm	1–3 nm
Specific surface area, m2/g	100–150	300–400	15–250
Obtaining method	from nature	from nature or synthesis	from synthesis
Quantity available	tons	milligrams	grams
Price	$4 per kg	not commercialized	$500 per kg
Biocompatibility	Biocompatible	Biocompatible	Health hazard
Water wettability	Hydrophilic	Hydrophilic	Hydrophobic

Nevertheless, some challenges hinder the direct use of HNT directly in industry: 1) the different HNT morphology, which depends on the chemical composition of a deposit area and on the effects of dehydration;[48] 2) the contamination of some HNT deposits with trace amounts of metal ions as iron lead to the color change of HNT mineral into yellowish.[49,50] The contaminants must be removed for some applications 3) pristine HNT have a variable length, which has an effect on the HNT dispersibility.[16] For that reasons, pretreatment steps are required, consisitnig in purification and uniformation of the HNT length as much as possible.

2.5. HNT Modification

The HNT modification refers to the introduction of functional groups onto the host material, which can be achieved by either physical modifications (wrapping the modifier onto the host by van der Waals forces, hydrogen bonding, and electrostatic attraction), chemical modifications (by covalently attaching the modifier to the host) or etching (by annealing, or treatment with acidic and/or alkali medium). The physical properties (solubility, dispersion, hydrophilicity/hydrophobicity, etc.) and the chemical properties (reactivity, biotoxicity, etc.) of the host can be carefully tailored for a specific modification, and will consequently promote the performance of the host when used in some applications.

In the case of HNT, multiple surfaces (the external surface, the interlayer surface, and the internal lumen surface) could potentially be modified. The external surface is composed of siloxane (Si–O–Si) groups and of a small number of aluminol (Al–OH) and silanol (Si–OH) groups exposed on the edges and surface defects of the HNT. The internal lumen surface consists of a gibbsite-like array of aluminol (Al–OH) groups.[38] That allows for selective chemical modification

of HNT surface either through electrostatic interaction or through successive reactions with phosphonic acid (interior) and silylating (exterior) agents, and that produces a new type of adsorbent with tunable properties.[51] Also in general to modify the inner lumen an evacuation pretreatment is required as well as a pH adjustment. As an example, silylation could occur also in the inner lumen if there is an evacuation pretreatment,[38] or under controlled pH.[52]

So, to optimize the properties of the HNT for a specific application, the functionalization HNT is extremely important for processing and enhancing the properties of HNT.[16,24,53–58] **Table 3** summarizes several mechanisms for HNT modifications and functionalization, including main applications and applied substances.

Table 3 Examples of purification, modification and functionalization process of HNT

Modification		Application	Method and substances applied	Reference
HNT purification		Dispersion-centrifugation-drying technique	10 wt% water suspension with heating to 60 °C	18,59
		H_2O_2 to remove organic impurities	H_2O_2 aqueous solution (30%)	60
Covalent functionalization	**Outer surface**	• Reduction of the polarity • shielding of the hydroxyl groups • changing the chemical composition of the surface to hydrocarbons • creation of functional groups on the surface • Increase the interfacial adhesion of the HNT	Grafting silanes via condensation between the hydrolyzed silanes and the surface hydroxyl groups of the HNT 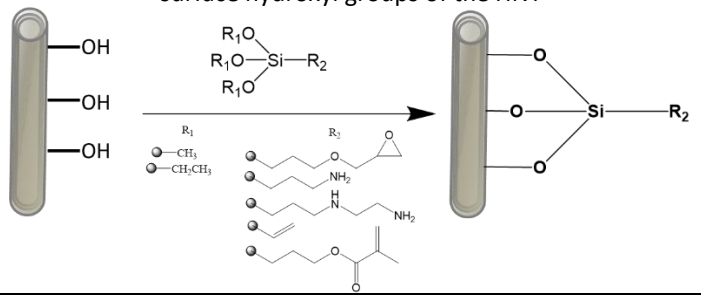	16,61–63
		• Enhance biocompatibility of several nanomaterials • Increase release time of dye loaded inside lumen	3-Aminopropyltriethoxysilane **(APTES)** (interacts with outer and inner OH)	52,64,65
		• Introducing a +ve charge to outer surface • drug encapsulation • anti-cancer therapies	3-azidopropyl trimethoxysilane	66,67
		• Surface modifier (introduce double bonds onto the surface of HNT to form sites for polymerization) • Improve dispersion in polymers solution (prevent agglomeration)	3-methacryloxypropyltrimethoxysilane 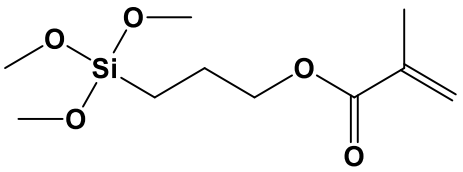	68,69

		• Outer surface Functionalization with ionic liquids to be as support for Palladium particles in catalytic application • Enhance synthesis of new designs of biocompatible multicavity nanomaterials which can load and release two or more drugs in a synergistic and complementary manner	3-mercaptopropyl trimethoxysilane 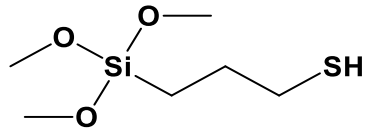	70–73
		• improve the interfacial adhesion between HNT and the polyvinylchloride	poly(butylenes adipate)	74
	Inner Lumen (evacuation pretreatment required)	• Change morphology of nanotubes to nanoplatelets • increase the basal spacing from 7.2 to 15.1 Å	Phenyl phosphonic acid	75
		• selective loading of hydrophobic molecules and nanoparticle	Octadecyl phosphonic acid; tetradecyl phosphonic acid bond to the alumina sites at the tube lumen but not the outer siloxane surface	51,76
		• selective modification of inner lumen • Green chemistry synthesis reduce the utilization and generation of hazardous substances	a catechol derivative 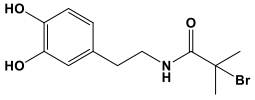	77
		• Synthesis of fluorescence probe for the detection of low concentration of hydrogen peroxide	Arylboronic acid 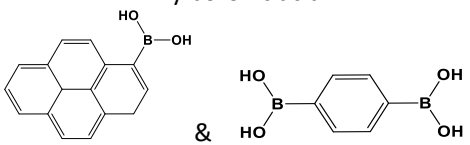	78,79

		• Enhance loading of pentoxifylline drug which prevent inflammation		
		• selectively deposited palladium nanoparticles inside halloysite lumen for catalytic applications	imidazolium ionic liquid 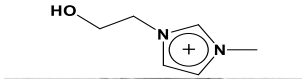 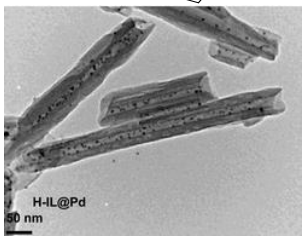	80
Non-covalent functionalization	**Inner lumen (evacuation pretreatment required)**	• Improvement of thermal stability	• emulsion polymerization of polystyrene over HNT in presence of sodium dodecyl sulfate	81
		• Enhance the negative charge to control the capture of tumor cells and blood cells • Increase water stabilization • biocompatible materials for gas delivery applications. • Enhance lumen affinity towards apolar molecules	Anionic surfactants as sodium dodecanoate or Perfluorinated carboxylic acids	55,82,83
		• Improvement of tensile properties • increase of the thermal stability of the polymer • enhance stability for cosmetics and medical applications	Negative biopolymer Alginate & pectin	84,85

		• Enhance removal ability towards aromatic hydrocarbons, such as pyrene and toluene • encapsulate aromatic oils in aqueous phase	Cucurbituril	86,87
		• low toxic Carbon dots delivery vehicles for sustained radical scavenging • advanced antiaging polymeric composites. • biological labeling and bioimaging	Carbon dot	88
	Outer surface	• Enhance tensile and flexural properties • Utilized to design clay incorporated polymer composites with better interfacial properties	2,5-bis(2-benzoxazolyl) thiophene (BBT) 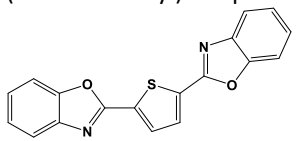 HNT tend to absorb (BBT) via electron transferring interactions	89
		• increase tensile stress, Young's modulus and thermal stability • scaffold synthesis for tissue engineering application	Positive biopolymer Chitosan the amine groups and hydroxyl groups on the chitosan interact with the Si-O bonds of HNT via hydrogen bonding interactions	84,85,90–92
		• Become neutral HNT surface to control the capture of tumor cells and blood cells • Enhance precipitation in aqueous medium	Cationic surfactant as decyltrimethylammonium bromide	55,82
		• Introducing a +ve charge to outer surface	High branched polyethyleneimine	93–95

		• Loading and Control the release of Clove bud oil, an insect repellent, for food packaging applications • Synthesis a non-viral vector was developed for loading and intracellular delivery of DNA	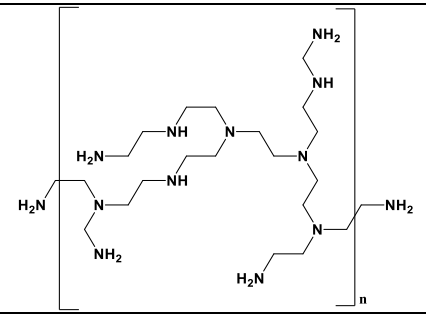	
		• Enhance HNT dispersion in water for 6 weeks • improve the biocompatibility for biomedical applications	DNA & amylose 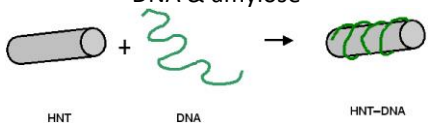 	96,97
Modification	**Alkali treatment**	• Maximize the density of hydroxyl groups on silica • Increase the dispersibility of HNT in polar solvents • Increase the pore volume • Increase the inner lumen diameter from 15 to 30 nm	Sodium Hydroxide react with the tetrahedral silicate to create silanol (Si-OH) groups (desilication)	60,98,99
	Acid activation	• Disaggregation of HNT • dissolution of inner layers to increase the inner diameter (dealumination) • replacement of interlayer cations by protons enhance Pb removal from lead contaminated water	Sulphuric acid, acetic acid, acrylic acid 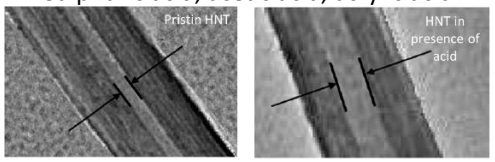 Lumen diameter 10 nm Outer diameter 60 nm Lumen diameter 20 nm Outer diameter 60 nm	99–102
	Acid and heat activation	• Dehydroxylation of the structural aluminol groups (HNT becomes amorphous)	Sulphuric acid and calcination changes in the pore structure and remove the physically bounded water	103,104

		• decrease of the adsorption capacity for cationic drug Increase the Percentage of Drug released		
	Ultrasonic activation and uniform viscosity centrifugation	• preparing homogeneous and length controllable HNT • cutting HNT length to (140 -240 nm)	combination of ultrasonic treatment and two-step uniform viscosity centrifugation 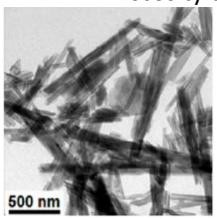 Prestin HNT 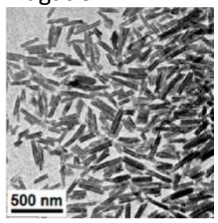 Short HNT	105

2.6. Applications

Due to the versatile features of the large surface area, high porosity, and tunable surface chemistry, as well as the rapid development of nano technique, tubular HNT clay has garnered worldwide research interest in the past decade and found abundant applications in many fields. For example, the use of HNT as a nano-container for the encapsulation and controlled releases of chemically or biologically active molecules, such as corrosion inhibitors and drugs, has been extensively and intensively studied.[47] The applications of inexpensive HNT for water purification[106] as Yu et al. introduced the HNT-derived nanocomposites for water treatment from pollutant removal to water filtration.[107] Also, HNT were employed as support for catalytic nanoparticles,[17,108] as nanoreactors,[46] or nano-template for material synthesis.[109,110]

Hereafter we will summarize the application of HNT in medicine.

Medicine. The demonstration of the toxicity of HNT toward living organisms is crucially important. HNT has a good biocompatibility, which means that tissue contact with halloysite is not harmful, because it was assessed for invertebrate model [111] and cell cultures. [112,113] Tthe viability of the human cells in presence of HNT was preserved at low concentrations. However, there are no biological mechanisms to degrade HNT in the body, i.e. not biodegradable [37], but due to their small size the HNT will be naturally removed from the body.[114,115] These very low cytotoxicity character makes HNT the future nanomaterial to the development of new products. For cell membrane penetration, HNT requires further step of scission and that through ball milling [96]or dip sonication[105].

Drug loading. Due to the high loading capacity and biocompatibility, halloysite nanotubes are good candidates for the fabrication of intracellular drug-delivery vehicles. Halloysites have been suggested as versatile nanosized hollow carriers, which combine effective drug loading from solution through vacuum [116]or straightforward approaches through surface chemistry modification.[24]

A general procedure for the halloysite loading is as follows **(Figure 8)**:

- Halloysite is mixed as a dry powder with a saturated (highly concentrated) solution of the drug.
- The suspension is stirred and evacuated with a vacuum pump. Suspension should be kept under vacuum for 10–30 min then allowed to atmospheric pressure. Slight fizzling of the solution under vacuum indicates that air is removed from the tubes. Once the vacuum is broken, the solution enters into the lumen and the loaded compound condensates within the tube. This has to be repeated 3–4 times to increase the loading efficiency. The maximum loading percentage ~ 10-30 wt % depends on the estimated diameter of halloysite lumens.[46]
- After loading, tubes are washed to remove the loosely attached substance from the external walls, dried and embedded into polymers.

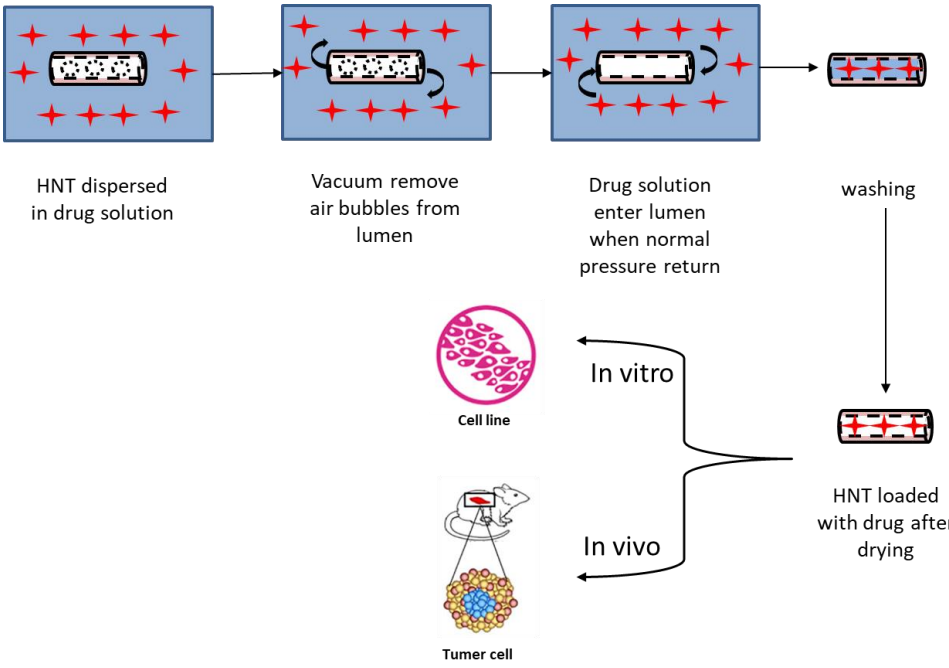

Figure 8 Loading halloysite nanotubes with Drug by vacuum cycles.

The drug released from the HNT can last 30–100 times longer than the drug alone or in other carriers. Adding a polymer coating to the drug-loaded HNT surface further slows the drug release rate. If the reactants are loaded into the tubes and reactions are induced, the tubes can act as nano-scale reactors.[46]

Numerous drugs, loaded into the HNT tubes, or adsorbed on HNT surface are summarized in **Table 4**.

Table 4 HNT in drug loading and delivery.

Site of Drug	Drug	HNT and Modifier	Loading wt %	Cell Line	Application and target	references
Inner Lumen	Dexamethasone	Pristine HNT followed by multilayer coating with polymer different in charge after loading by vacuum	7.0 vol%	MCF-7 3T3	Controlled release of drug and cytotoxicity test	117
	Gamma-aminobutyric acid (GABA)	Pristine HNT	1.7 %	cerebellar granule cells of rats	Controlled release of drug, cytotoxicity, and seizure inhibition test	41
	curcumin	HNT- functionalized with triazolium salts	12.5 %	BCPAP, SW1736, 8505 C and C643	Controlled release of drug and evaluate cytotoxic effects (hepatic cancer)	66
	brilliant green	HNT capped with dextrin	40.0 %	A549 and Hep3b	Controlled release of drug and cytotoxicity test	118
	Rabeprazole	Pristine HNT	8.3 %		Controlled release of drug with preventing the acidic degradation of RAB in stomach	119
	pentoxifylline	HNT inner lumen modified with 1,4 phenylenebisdiboronic acid	7.0 %		Controlled drug release for the inflammation inhibition	79
	paclitaxel	Pristine HNT coated with polymer after loading	7.5 %	A549 and HeLa	Controlled release of drug for anticancer therapy	120
Outer Surface	Ofloxacin	Alkali treatment and composite chitosan- magnetic halloysite modification	7.3 %		Controlled release of drug	121
	curcumin	Halloysite functionalized with cysteamine	2.9 %	HA22T/VGH and Hep3B	Controlled release of drug for anticancer therapy	122
	cardanol	triazole-HNT system	10 %	HA22T/VGH, Hep3B and HepG2	Controlled release of drug and evaluate cytotoxic effects	67
	Doxorubicin	HNT modified with chitosan or Folic acid	2.0-2.6 %	HeLa and MCF-7	Controlled release of drug for anticancer therapy	115,123

2.7. Characterization

Generally any clay minerals can be characterized through many instruments. Average interplanar distances and the average composition of the atomic planes can be derived from XRD study. The morphology of aggregates is determined by SEM. DTA and TGA studies are concerned with the water molecules in clays. TEM investigates the shapes of individual crystals and the compositions of these individual crystals. IR methods investigate the relations of individual molecules in the crystals, OH, H_2O, Si-O etc. HRTEM analysis, here the atomic layers of the atoms themselves are visible to the investigator's eye via the electron beam. [124]
I will try to summarize the main instrument used mainly in my thesis**.**

Transmission electron microscopes (TEM) [125,126]

The TEM microscope was firstly built by Knoll and Ruska in 1932. This type of microscope provides information about internal composition of the material. On the contrary to Scanning Electron Microscope, TEM produces images using electrons transmitted through the sample. The emission source can be a cathode, tungsten filament or needle as well as a lanthanum hexaboride (LaB6) single crystal. When the gun is connected to such high voltage light source and given sufficient current, it begins to emit electrons either by thermionic or field of electron emission into the vacuum. The emitted electron beam is condensed by condensing lenses on the sample holder on which the sample to be analyzed is deposited and then passed completely through the sample. For this reason, the latter must have a very small thickness. Next the signal from transmitted electrons is converted to the bright image. Instead, electrons that were stopped on the sample correspond to the black areas.TEM (**Figure 9**).works in high vacuum to prevent the electron beam from being deflected by contamination in the air .

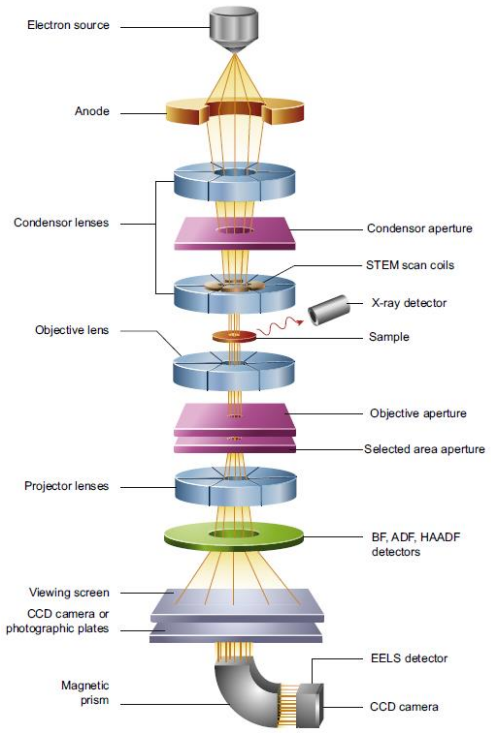

Figure 9. Illustration of Transmission Electron Microscope set up.[122]

Prior to TEM studies of halloysite-based samples, the analyzed material was dispersed in aqueous solution (1.0 mg/mL) and deposited on the 300-mesh cooper grid coated with carbon and Formvar. Such prepared samples were dried in air overnight and analyzed with CM TEM (80 kW) (Philips) equipped with CCD camera (Morada), at the University of Milan, Italy.

Dynamic Light Scattering (DLS)

Monochromatic and coherent light is scattered when a solution containing particles smaller than its wavelength is irradiated. This scattering phenomenon undergoes fluctuations in intensity due to the Brownian motion of the particles which can then be correlated to the dimension of the nanoparticles in solution.[127]

Figure 10 shows a simplified scheme of the instrument. A monochromatic light beam, usually produced by a laser, passes first through a polariser lens and then through the sample cell. Part of this beam is scattered in all the directions by the particles suspended in the sample solution. The detector, generally positioned at a fixed angle, monitor fluctuations of intensity generated by the Brownian motion of the particles: the smaller the particles, the stronger are these fluctuations (**Figure 11**).

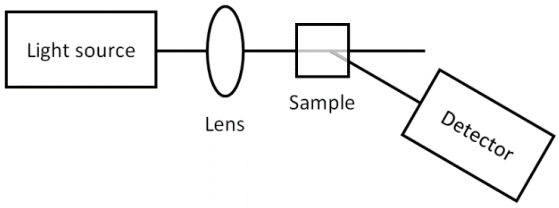

Figure 10. Schematic representation of a DLS instrument with the main components.[128]

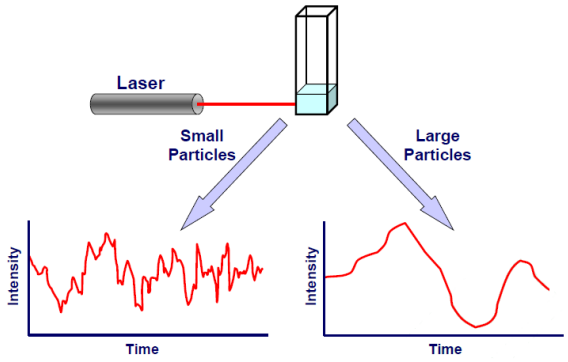

Figure 11. Intensity fluctuations for small and large particles. [129]

These changes in intensity are mathematically expressed by the decay rate (Γ), which can be defined as (**Eq.1.1**):

$$\Gamma = q^2 D \qquad \text{(Eq. 1.1)}$$

Where q is the wave vector (that is function of the refractive index of the sample, the angle at which the detector is located and the incident laser wavelength) and D is the diffusion coefficient. The diffusion coefficient, in particular, can be correlated to the hydrodynamic radius (R) of the nanoparticles by means of the Stokes-Einstein equation (**Eq.1.2**):

$$d_H = \frac{kT}{3\pi\eta D} \qquad \text{(Eq. 1.2)}$$

where d_H is the hydrodynamic diameter, k the Boltzmann's constant, T the absolute temperature, η the medium viscosity and D the diffusion coefficient. By the combination of previous two equations, it is therefore possible to calculate the average hydrodynamic radius from intensity fluctuations at a specific detection angle.

The primary result obtained by a DLS measurement is an intensity size distribution, *i.e.* a plot of scattered light intensity vs particles size. Due to the dependence of the scattered light intensity on the particle radius ($I \alpha d^6$) this distribution is highly sensitive to the presence of large particles that can easily shadow smaller populations, even if present only as a minority. From this distribution both volume (equivalent to the mass or weight distribution) and number distributions can be obtained, provided the particles absorbtion and refractive index (usually assumed to be the same as the bulk material) are known. It is generally advised to use the volume and/or number distribution only for estimating the relative amount of material in different peaks and not as a size measurement (**Figure. 12**).

DLS analysis presented in this thesis were performed with a Malvern Zetasizer Nano ZS. The light source was a He-Ne laser operating at a fixed wavelength of 633 nm, and the analysis were conducted in DLS disposable cuvettes at a constant temperature of 25 °C. Refractive indexes of nanoparticles were obtained from an online database (refractiveindex.info). At least three sets of analysis were conducted on every sample, and the coherent results averaged out. No pre-treatment of the sample was necessary, and the analysis was simply conducted placing 1 mL of colloid solution into a DLS disposable cuvette. The final data were elaborated by Malvern software and used as is.

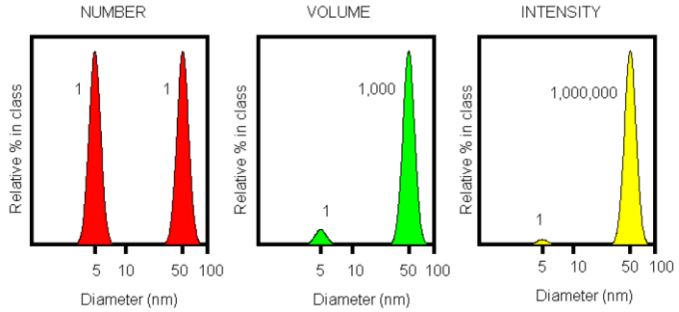

Figure 12 Number, volume and intensity distributions of a bimodal mixture of 5 and 50nm lattices present in equal numbers.[130]

ζ–potential analysis

A second useful information that can be obtained via DLS analysis is the NP ζ–potential. When an object is exposed to a fluid its surface will be coated by an electrical double layer of ions (**Figure 13**). The ideal plane between the two layers is called Stern layer. The external plane that surrounds the second layer is called slipping plane, and it ideally separates the solvent fraction that moves jointly with the NPs from the other mobile solvent. The ζ–potential is the electric potential at this plane, and is widely used as an indicator of the stability of a NP dispersion: particles with high ζ–potential will repel each other, avoiding flocculation and precipitation. Usually a ζ–potential > ±30 mV is required to achieve stable dispersion over time.

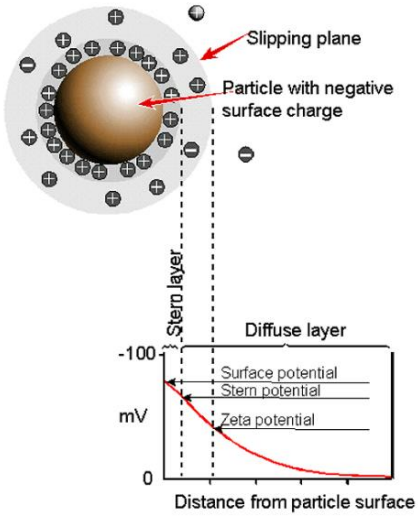

Figure 13 Schematic representation of zeta potential.[131]

ζ–potential measurements are based on the principle of electrophoresis: the NP suspension is first subjected to an external magnetic field. The particles will then start moving toward one of the electrodes (depending on their charge sign) with a speed that is dependent on their ζ–potential. The Henry equation (**Eq.1.3**) correlates the ζ–potential with the electrophoretic mobility (the ratio between particle velocity and electric field strength):

$$U_E = \frac{2\varepsilon\zeta f(ka)}{3\eta} \qquad \text{(Eq. 1.3)}$$

where *UE* is the electrophoretic mobility, ε the dielectric constant of the medium, η the viscosity, ζ the ζ–potential and *f(ka)* is Henry's function, a function of the ratio of particle radius to double layer thickness (*ka*). Henry's function is usually approximated to 1.5 in polar media. The electrophoretic mobility is measured using the Doppler effect: the DLS laser is passed through the sample undergoing electrophoresis and the shift in the frequency of its scattered light, caused by the moving particles, is measured. This frequency shift is directly proportional to the particle velocity and allows the determination of the electrophoretic mobility.

pH-dependent ζ–potential measurements were done at the University of Milan, Milan, Italy. Prior to analysis, samples were dispersed in milliq water medium (C= 0.5 mg/mL) for halloysitebased powders were prepared and disaggregated (5min) using sonication bath (5510 Branson, Italy). The analyzed material was titrated using NaOH (0.1M) and HCl (0.1M) solutions in order to obtain adequate pH. The pH was measured by pH-meter (Amel Instruments, 338 pH-meter, Italy). Such prepared samples were then placed in cuvettes, to then immerse in them zeta dip cell (Zen 1002). The zeta potential analysis was performed using zetasizer (Malvern Zetasizer Nano series 2S) at the University of Milan, Italy. Each measurement was performed three times and consisted of 10–100 runs with equilibration time of 60 s. The zeta potential results are shown as mean ± SD. Other detailed measurement specifications are listed below: Material: SiO2 (for halloysite-based samples), Refractive Index (RI): 1.485; Absorption: 0.01; Dispersant: water; Temperature: 25 ℃; Model: Smuchowski.

3. Bibliography

(1) Cecilia, J. A.; García-Sancho, C.; Vilarrasa-García, E.; Jiménez-Jiménez, J.; Rodriguez-Castellón, E. Synthesis, Characterization, Uses and Applications of Porous Clays Heterostructures: A Review. *Chem. Rec.* **2018**, *18* (7–8), 1085–1104. https://doi.org/doi:10.1002/tcr.201700107.

(2) Goldman, L. J.; Greenfield, L. I.; Damle, A. S.; Kingsbury, G. L.; Northeim, C.; Truesdale, R. *Clay Liners for Waste Management Facilities*; 1990.

(3) Schulze, D. G. An Introduction to Soil Mineralogy. In 'Minerals in Soil Environments'. 2nd Edn.(Eds JB Dixon and SB Weed.) Pp. 32–3. *Soil Sci. Soc. Am. Madison, WI* **1989**.

(4) Murray, H. H. Chapter 1 Introduction. In *Applied Clay Mineralogy*; Murray, H. H. B. T.-D. in C. S., Ed.; Elsevier, 2006; Vol. 2, pp 1–6. https://doi.org/10.1016/S1572-4352(06)02001-0.

(5) Rapp, G. Ceramic Raw Materials BT - Archaeomineralogy; Rapp, G., Ed.; Springer Berlin Heidelberg: Berlin, Heidelberg, 2009; pp 183–200. https://doi.org/10.1007/978-3-540-78594-1_8.

(6) Genedy, M.; Stormont, J.; Matteo, E.; Taha, M. R. Examining Epoxy-Based Nanocomposites in Wellbore Seal Repair for Effective CO2 Sequestration. *Energy Procedia*. 2014, pp 5798–5807. https://doi.org/10.1016/j.egypro.2014.11.612.

(7) Das, B. M.; Sobhan, K. *Principles of Geotechnical Engineering*; Cengage Learning, 2013.

(8) Nanzyo, M.; Kanno, H. Secondary Minerals BT - Inorganic Constituents in Soil: Basics and Visuals; Nanzyo, M., Kanno, H., Eds.; Springer Singapore: Singapore, 2018; pp 37–58. https://doi.org/10.1007/978-981-13-1214-4_3.

(9) Wilson, I. R. Kaolin and Halloysite Deposits of China. *Clay Miner.* **2004**, *39* (1), 1–15. https://doi.org/DOI: 10.1180/000985543910116.

(10) Patterson, S. H.; Murray, H. H. *Kaolin, Refractory Clay, Ball Clay, and Halloysite in North America, Hawaii, and the Caribbean Region*; 1984. https://doi.org/10.3133/pp1306.

(11) Wilson, I. R.; de Souza Santos, H.; de Souza Santos, P. Kaolin and Halloysite Deposits of Brazil. *Clay Miner.* **2006**, *41* (3), 697–716. https://doi.org/DOI: 10.1180/0009855064130213.

(12) Joussein, E.; Petit, S.; Churchman, J.; Theng, B.; Righi, D.; Delvaux, B. Halloysite Clay Minerals – a Review. *Clay Minerals*. 2005, p 383. https://doi.org/10.1180/0009855054040180.

(13) Satish, S.; Tharmavaram, M.; Rawtani, D. Halloysite Nanotubes as a Nature's Boon for Biomedical Applications. *Nanobiomedicine* **2019**, *6*, 1849543519863625–1849543519863625. https://doi.org/10.1177/1849543519863625.

(14) Lvov, Y.; Abdullayev, E. Functional Polymer–Clay Nanotube Composites with Sustained Release of Chemical Agents. *Prog. Polym. Sci.* **2013**, *38* (10), 1690–1719. https://doi.org/https://doi.org/10.1016/j.progpolymsci.2013.05.009.

(15) Khobragade, P. S.; Hansora, D. P.; Naik, J. B.; Chatterjee, A. Flame Retarding Performance of Elastomeric Nanocomposites: A Review. *Polym. Degrad. Stab.* **2016**, *130*, 194–244. https://doi.org/https://doi.org/10.1016/j.polymdegradstab.2016.06.001.

(16) Liu, M.; Jia, Z.; Jia, D.; Zhou, C. Recent Advance in Research on Halloysite Nanotubes-Polymer Nanocomposite. *Prog. Polym. Sci.* **2014**, *39* (8), 1498–1525. https://doi.org/https://doi.org/10.1016/j.progpolymsci.2014.04.004.

(17) Massaro, M.; Colletti, C. G.; Lazzara, G.; Milioto, S.; Noto, R.; Riela, S. Halloysite Nanotubes as Support for Metal-Based Catalysts. *J. Mater. Chem. A* **2017**, *5* (26), 13276–13293. https://doi.org/10.1039/C7TA02996A.

(18) Pasbakhsh, P.; Churchman, G. J.; Keeling, J. L. Characterisation of Properties of Various Halloysites Relevant to Their Use as Nanotubes and Microfibre Fillers. *Appl. Clay Sci.* **2013**, *74*, 47–57. https://doi.org/https://doi.org/10.1016/j.clay.2012.06.014.

(19) El Amrani El Hassani, I.; Sadik, C. Geology and Mineralogy of Clays for Nanocomposites: State of Knowledge and Methodology. In *Nanoclay Reinforced Polymer Composites: Nanocomposites and Bionanocomposites*; Mohammad, J., Qaiss, A. el K., Bouhfid, R., Eds.; Springer Singapore: Singapore, 2016; pp 85–113. https://doi.org/10.1007/978-981-10-1953-1_4.

(20) Blanc, P.; Piantone, P.; Lassin, A.; Burnol, A. Thermochimie: Sélection de Constantes Thermodynamiques Pour Les Éléments Majeurs, Le Plomb et Le Cadmium. *Rapp. Final BRGM RP-54902-FR* **2006**.

(21) Lázaro, B. B. Halloysite and Kaolinite: Two Clay Minerals with Geological and Technological Importance. *Rev. la Acad. Ciencias Exactas, Físicas, Químicas y Nat. Zaragoza* **2015**, No. 70, 7–

38.
(22) Ryan, P. C.; Huertas, F. J.; Hobbs, F. W. C.; Pincus, L. N. KAOLINITE AND HALLOYSITE DERIVED FROM SEQUENTIAL TRANSFORMATION OF PEDOGENIC SMECTITE AND KAOLINITE-SMECTITE IN A 120 Ka TROPICAL SOIL CHRONOSEQUENCE. *Clays Clay Miner.* **2016**, *64* (5), 639–667. https://doi.org/10.1346/CCMN.2016.064030.
(23) Robertson, I. D. M.; Eggleton, R. A. Weathering of Granitic Muscovite to Kaolinite and Halloysite and of Plagioclase-Derived Kaolinite to Halloysite. *Clays Clay Miner.* **1991**, *39* (2), 113–126. https://doi.org/10.1346/CCMN.1991.0390201.
(24) Lvov, Y.; Aerov, A.; Fakhrullin, R. Clay Nanotube Encapsulation for Functional Biocomposites. *Adv. Colloid Interface Sci.* **2014**, *207*, 189–198. https://doi.org/https://doi.org/10.1016/j.cis.2013.10.006.
(25) Singh, B.; Gilkes, R. J. An Electron Optical Investigation of the Alteration of Kaolinite to Halloysite. *Clays Clay Miner.* **1992**, *40* (2), 212–229. https://doi.org/10.1346/CCMN.1992.0400211.
(26) Kirkman, J. H. Morphology and Structure of Halloysite in New Zealand Tephras. *Clays Clay Miner.* **1981**, *29* (1), 1–9. https://doi.org/10.1346/CCMN.1981.0290101.
(27) Bates, T. F.; Hildebrand, F. A.; Swineford, A. Morphology and Structure of Endellite and Halloysite. *Am. Mineral.* **1950**, *35* (7–8), 463–484.
(28) Singh, B. Why Does Halloysite Roll?—A New Model. *Clays Clay Miner.* **1996**, *44* (2), 191–196. https://doi.org/10.1346/CCMN.1996.0440204.
(29) Xu, H.; Jin, X.; Chen, P.; Shao, G.; Wang, H.; Chen, D.; Lu, H.; Zhang, R. Preparation of Kaolinite Nanotubes by a Solvothermal Method. *Ceram. Int.* **2015**, *41* (5, Part A), 6463–6469. https://doi.org/https://doi.org/10.1016/j.ceramint.2015.01.085.
(30) Kuroda, Y.; Ito, K.; Itabashi, K.; Kuroda, K. One-Step Exfoliation of Kaolinites and Their Transformation into Nanoscrolls. *Langmuir* **2011**, *27* (5), 2028–2035. https://doi.org/10.1021/la1047134.
(31) Chen, J.; Cui, Y.; Liu, M.; Huang, H.; Deng, F.; Mao, L.; Wen, Y.; Tian, J.; Zhang, X.; Wei, Y. Surface Grafting of Fluorescent Polymers on Halloysite Nanotubes through Metal-Free Light-Induced Controlled Polymerization: Preparation, Characterization and Biological Imaging. *Mater. Sci. Eng. C* **2020**, *111*, 110804. https://doi.org/https://doi.org/10.1016/j.msec.2020.110804.
(32) Prishchenko, D. A.; Zenkov, E. V; Mazurenko, V. V; Fakhrullin, R. F.; Lvov, Y. M.; Mazurenko, V. G. Molecular Dynamics of the Halloysite Nanotubes. *Phys. Chem. Chem. Phys.* **2018**, *20* (8), 5841–5849. https://doi.org/10.1039/C7CP06575B.
(33) Ma, W.; Wu, H.; Higaki, Y.; Takahara, A. Halloysite Nanotubes: Green Nanomaterial for Functional Organic-Inorganic Nanohybrids. *Chem. Rec.* **2018**, *18* (7–8), 986–999. https://doi.org/10.1002/tcr.201700093.
(34) Papoulis, D.; Tsolis-Katagas, P.; Kalampounias, A. G.; Tsikouras, B. Progressive Formation of Halloysite from the Hydrothermal Alteration of Biotite and the Formation Mechanisms of Anatase in Altered Volcanic Rocks from Limnos Island, Northeast Aegean Sea, Greece. *Clays Clay Miner.* **2009**, *57* (5), 566–577. https://doi.org/10.1346/CCMN.2009.0570505.
(35) Adamo, P.; Violante, P.; Wilson, M. J. Tubular and Spheroidal Halloysite in Pyroclastic Deposits in the Area of the Roccamonfina Volcano (Southern Italy). *Geoderma* **2001**, *99* (3), 295–316. https://doi.org/https://doi.org/10.1016/S0016-7061(00)00076-8.
(36) VEERABADRAN, N. G.; PRICE, R. R.; LVOV, Y. M. CLAY NANOTUBES FOR ENCAPSULATION AND SUSTAINED RELEASE OF DRUGS. *Nano* **2007**, *02* (02), 115–120. https://doi.org/10.1142/S1793292007000441.
(37) Lvov, Y.; Wang, W.; Zhang, L.; Fakhrullin, R. Halloysite Clay Nanotubes for Loading and Sustained Release of Functional Compounds. *Adv. Mater.* **2016**, *28* (6), 1227–1250. https://doi.org/https://doi.org/10.1002/adma.201502341.
(38) Yuan, P.; Southon, P. D.; Liu, Z.; Green, M. E. R.; Hook, J. M.; Antill, S. J.; Kepert, C. J. Functionalization of Halloysite Clay Nanotubes by Grafting with γ-Aminopropyltriethoxysilane. *J. Phys. Chem. C* **2008**, *112* (40), 15742–15751. https://doi.org/10.1021/jp805657t.
(39) Joo, Y.; Sim, J. H.; Jeon, Y.; Lee, S. U.; Sohn, D. Opening and Blocking the Inner-Pores of Halloysite. *Chem. Commun.* **2013**, *49* (40), 4519–4521. https://doi.org/10.1039/C3CC40465J.
(40) Massaro, M.; Noto, R.; Riela, S. Past, Present and Future Perspectives on Halloysite Clay Minerals. *Molecules* **2020**, *25* (20), 4863. https://doi.org/10.3390/molecules25204863.

(41) Yurtdaş Kırımlıoğlu, G.; Yazan, Y.; Erol, K.; Cengelli, C. Gamma-Aminobutyric Acid Loaded Halloysite Nanotubes and In Vitro-In Vivo Evaluation for Brain Delivery. *Int. J. Pharm.* **2015**, *495*. https://doi.org/10.1016/j.ijpharm.2015.08.087.
(42) Ferrari, P. C.; Araujo, F. F.; Pianaro, S. A. Halloysite Nanotubes-Polymeric Nanocomposites: Characteristics, Modifications and Controlled Drug Delivery Approaches . *Cerâmica* . scielo 2017, pp 423–431.
(43) Grim, R. E. *Clay Mineralogy*; International series in the earth sciences; McGraw-Hill, 1953.
(44) Taroni, T.; Meroni, D.; Fidecka, K.; Maggioni, D.; Longhi, M.; Ardizzone, S. Halloysite Nanotubes Functionalization with Phosphonic Acids: Role of Surface Charge on Molecule Localization and Reversibility. *Appl. Surf. Sci.* **2019**, *486*, 466–473. https://doi.org/https://doi.org/10.1016/j.apsusc.2019.04.264.
(45) Ma, W.; Yah, W. O.; Otsuka, H.; Takahara, A. Application of Imogolite Clay Nanotubes in Organic–Inorganic Nanohybrid Materials. *J. Mater. Chem.* **2012**, *22* (24), 11887–11892. https://doi.org/10.1039/C2JM31570J.
(46) Shchukin, D. G.; Sukhorukov, G. B.; Price, R. R.; Lvov, Y. M. Halloysite Nanotubes as Biomimetic Nanoreactors. *Small* **2005**, *1* (5), 510–513. https://doi.org/10.1002/smll.200400120.
(47) Lvov, Y. M.; Shchukin, D. G.; Möhwald, H.; Price, R. R. Halloysite Clay Nanotubes for Controlled Release of Protective Agents. *ACS Nano* **2008**, *2* (5), 814–820. https://doi.org/10.1021/nn800259q.
(48) Ramadass, K.; Singh, G.; Lakhi, K. S.; Benzigar, M. R.; Yang, J.-H.; Kim, S.; Almajid, A. M.; Belperio, T.; Vinu, A. Halloysite Nanotubes: Novel and Eco-Friendly Adsorbents for High-Pressure CO2 Capture. *Microporous Mesoporous Mater.* **2019**, *277*, 229–236. https://doi.org/https://doi.org/10.1016/j.micromeso.2018.10.035.
(49) Liu, R.; Yan, C.; Wang, H.; Xiao, G.; Tu, D. Occurrence and Characterization Microstructure of Iron Impurities in Halloysite. *Journal of Nanoscience and Nanotechnology*. 2015, pp 7385–7390. https://doi.org/10.1166/jnn.2015.10577.
(50) Abdullayev, E.; Abbasov, V.; Lvov, Y. Halloysite Clay Nanotubes: Structural Study and Technological Applications. *Process. Petrochemistry Oil Refin.* **2009**, *3–4*, 260–273.
(51) Yah, W. O.; Takahara, A.; Lvov, Y. M. Selective Modification of Halloysite Lumen with Octadecylphosphonic Acid: New Inorganic Tubular Micelle. *J. Am. Chem. Soc.* **2012**, *134* (3), 1853–1859. https://doi.org/10.1021/ja210258y.
(52) Yuan, P.; Southon, P. D.; Liu, Z.; Kepert, C. J. Organosilane Functionalization of Halloysite Nanotubes for Enhanced Loading and Controlled Release. *Nanotechnology* **2012**, *23* (37), 375705. https://doi.org/10.1088/0957-4484/23/37/375705.
(53) Pasbakhsh, P.; Ismail, H.; Fauzi, M. N. A.; Bakar, A. A. EPDM/Modified Halloysite Nanocomposites. *Appl. Clay Sci.* **2010**, *48* (3), 405–413. https://doi.org/https://doi.org/10.1016/j.clay.2010.01.015.
(54) Daitx, T. S.; Carli, L. N.; Crespo, J. S.; Mauler, R. S. Effects of the Organic Modification of Different Clay Minerals and Their Application in Biodegradable Polymer Nanocomposites of PHBV. *Appl. Clay Sci.* **2015**, *115*, 157–164. https://doi.org/https://doi.org/10.1016/j.clay.2015.07.038.
(55) Mitchell, M. J.; Castellanos, C. A.; King, M. R. Surfactant Functionalization Induces Robust, Differential Adhesion of Tumor Cells and Blood Cells to Charged Nanotube-Coated Biomaterials under Flow. *Biomaterials* **2015**, *56*, 179–186. https://doi.org/https://doi.org/10.1016/j.biomaterials.2015.03.045.
(56) Joo, Y.; Jeon, Y.; Lee, S. U.; Sim, J. H.; Ryu, J.; Lee, S.; Lee, H.; Sohn, D. Aggregation and Stabilization of Carboxylic Acid Functionalized Halloysite Nanotubes (HNT-COOH). *J. Phys. Chem. C* **2012**, *116* (34), 18230–18235. https://doi.org/10.1021/jp3038945.
(57) Abdullayev, E.; Lvov, Y. Halloysite Clay Nanotubes as a Ceramic "Skeleton" for Functional Biopolymer Composites with Sustained Drug Release. *J. Mater. Chem. B* **2013**, *1* (23), 2894–2903. https://doi.org/10.1039/C3TB20059K.
(58) Du, M.; Guo, B.; Jia, D. Newly Emerging Applications of Halloysite Nanotubes: A Review. *Polym. Int.* **2010**, *59* (5), 574–582. https://doi.org/10.1002/pi.2754.
(59) Jackson, M. L. R. *Soil Chemical Analysis*; Prentice-Hall, 1958.
(60) Zeng, S.; Reyes, C.; Liu, J.; Rodgers, P. A.; Wentworth, S. H.; Sun, L. Facile Hydroxylation of Halloysite Nanotubes for Epoxy Nanocomposite Applications. *Polymer (Guildf).* **2014**, *55* (25), 6519–6528. https://doi.org/https://doi.org/10.1016/j.polymer.2014.10.044.

(61) Poikelispää, M.; Das, A.; Dierkes, W.; Vuorinen, J. Synergistic Effect of Plasma-Modified Halloysite Nanotubes and Carbon Black in Natural Rubber—Butadiene Rubber Blend. *J. Appl. Polym. Sci.* **2013**, *127* (6), 4688–4696. https://doi.org/10.1002/app.38080.

(62) Zhong, S.; Zhou, C.; Zhang, X.; Zhou, H.; Li, H.; Zhu, X.; Wang, Y. A Novel Molecularly Imprinted Material Based on Magnetic Halloysite Nanotubes for Rapid Enrichment of 2,4-Dichlorophenoxyacetic Acid in Water. *J. Hazard. Mater.* **2014**, *276*, 58–65. https://doi.org/https://doi.org/10.1016/j.jhazmat.2014.05.013.

(63) Liu, M.; Guo, B.; Du, M.; Lei, Y.; Jia, D. Natural Inorganic Nanotubes Reinforced Epoxy Resin Nanocomposites. *J. Polym. Res.* **2008**, *15* (3), 205–212. https://doi.org/10.1007/s10965-007-9160-4.

(64) Del Buffa, S.; Bonini, M.; Ridi, F.; Severi, M.; Losi, P.; Volpi, S.; Al Kayal, T.; Soldani, G.; Baglioni, P. Design and Characterization of a Composite Material Based on Sr(II)-Loaded Clay Nanotubes Included within a Biopolymer Matrix. *J. Colloid Interface Sci.* **2015**, *448*, 501–507. https://doi.org/https://doi.org/10.1016/j.jcis.2015.02.043.

(65) Barot, T.; Rawtani, D.; Kulkarni, P. Physicochemical and Biological Assessment of Silver Nanoparticles Immobilized Halloysite Nanotubes-Based Resin Composite for Dental Applications. *Heliyon* **2020**, *6* (3), e03601–e03601. https://doi.org/10.1016/j.heliyon.2020.e03601.

(66) Riela, S.; Massaro, M.; Colletti, C. G.; Bommarito, A.; Giordano, C.; Milioto, S.; Noto, R.; Poma, P.; Lazzara, G. Development and Characterization of Co-Loaded Curcumin/Triazole-Halloysite Systems and Evaluation of Their Potential Anticancer Activity. *Int. J. Pharm.* **2014**, *475* (1), 613–623. https://doi.org/https://doi.org/10.1016/j.ijpharm.2014.09.019.

(67) Massaro, M.; Colletti, C. G.; Noto, R.; Riela, S.; Poma, P.; Guernelli, S.; Parisi, F.; Milioto, S.; Lazzara, G. Pharmaceutical Properties of Supramolecular Assembly of Co-Loaded Cardanol/Triazole-Halloysite Systems. *Int. J. Pharm.* **2015**, *478* (2), 476–485. https://doi.org/https://doi.org/10.1016/j.ijpharm.2014.12.004.

(68) Zhou, C.; Li, H.; Zhou, H.; Wang, H.; Yang, P.; Zhong, S. Water-Compatible Halloysite-Imprinted Polymer by Pickering Emulsion Polymerization for the Selective Recognition of Herbicides. *J. Sep. Sci.* **2015**, *38* (8), 1365–1371. https://doi.org/10.1002/jssc.201401469.

(69) Zhang, J.; Zhang, D.; Zhang, A.; Jia, Z.; Jia, D. Poly (Methyl Methacrylate) Grafted Halloysite Nanotubes and Its Epoxy Acrylate Composites by Ultraviolet Curing Method. *J. Reinf. Plast. Compos.* **2013**, *32* (10), 713–725. https://doi.org/10.1177/0731684412472745.

(70) Massaro, M.; Riela, S.; Cavallaro, G.; Gruttadauria, M.; Milioto, S.; Noto, R.; Lazzara, G. Eco-Friendly Functionalization of Natural Halloysite Clay Nanotube with Ionic Liquids by Microwave Irradiation for Suzuki Coupling Reaction. *J. Organomet. Chem.* **2014**, *749*, 410–415. https://doi.org/https://doi.org/10.1016/j.jorganchem.2013.10.044.

(71) Massaro, M.; Riela, S.; Lazzara, G.; Gruttadauria, M.; Milioto, S.; Noto, R. Green Conditions for the Suzuki Reaction Using Microwave Irradiation and a New HNT-Supported Ionic Liquid-like Phase (HNT-SILLP) Catalyst. *Appl. Organomet. Chem.* **2014**, *28* (4), 234–238. https://doi.org/10.1002/aoc.3114.

(72) Massaro, M.; Riela, S.; Lo Meo, P.; Noto, R.; Cavallaro, G.; Milioto, S.; Lazzara, G. Functionalized Halloysite Multivalent Glycocluster as a New Drug Delivery System. *J. Mater. Chem. B* **2014**, *2* (44), 7732–7738. https://doi.org/10.1039/C4TB01272K.

(73) Massaro, M.; Piana, S.; Colletti, C. G.; Noto, R.; Riela, S.; Baiamonte, C.; Giordano, C.; Pizzolanti, G.; Cavallaro, G.; Milioto, S.; Lazzara, G. Multicavity Halloysite–Amphiphilic Cyclodextrin Hybrids for Co-Delivery of Natural Drugs into Thyroid Cancer Cells. *J. Mater. Chem. B* **2015**, *3* (19), 4074–4081. https://doi.org/10.1039/C5TB00564G.

(74) Yin, B.; Hakkarainen, M. Core–Shell Nanoparticle–Plasticizers for Design of High-Performance Polymeric Materials with Improved Stiffness and Toughness. *J. Mater. Chem.* **2011**, *21* (24), 8670–8677. https://doi.org/10.1039/C1JM10624D.

(75) Tang, Y.; Deng, S.; Ye, L.; Yang, C.; Yuan, Q.; Zhang, J.; Zhao, C. Effects of Unfolded and Intercalated Halloysites on Mechanical Properties of Halloysite–Epoxy Nanocomposites. *Compos. Part A Appl. Sci. Manuf.* **2011**, *42* (4), 345–354. https://doi.org/https://doi.org/10.1016/j.compositesa.2010.12.003.

(76) Hamza, H.; Ferretti, A. M.; Innocenti, C.; Fidecka, K.; Licandro, E.; Sangregorio, C.; Maggioni, D. An Approach for Magnetic Halloysite Nanocomposite with Selective Loading of Superparamagnetic Magnetite Nanoparticles in the Lumen. *Inorg. Chem.* **2020**.

https://doi.org/10.1021/acs.inorgchem.0c01039.
(77) Yah, W. O.; Xu, H.; Soejima, H.; Ma, W.; Lvov, Y.; Takahara, A. Biomimetic Dopamine Derivative for Selective Polymer Modification of Halloysite Nanotube Lumen. *J. Am. Chem. Soc.* **2012**, *134* (29), 12134–12137. https://doi.org/10.1021/ja303340f.
(78) Zhang, H.; Ren, T.; Ji, Y.; Han, L.; Wu, Y.; Song, H.; Bai, L.; Ba, X. Selective Modification of Halloysite Nanotubes with 1-Pyrenylboronic Acid: A Novel Fluorescence Probe with Highly Selective and Sensitive Response to Hyperoxide. *ACS Appl. Mater. Interfaces* **2015**, *7* (42), 23805–23811. https://doi.org/10.1021/acsami.5b08600.
(79) Liu, F.; Bai, L.; Zhang, H.; Song, H.; Hu, L.; Wu, Y.; Ba, X. Smart H2O2-Responsive Drug Delivery System Made by Halloysite Nanotubes and Carbohydrate Polymers. *ACS Appl. Mater. Interfaces* **2017**, *9* (37), 31626–31633. https://doi.org/10.1021/acsami.7b10867.
(80) K. Dedzo, G.; Ngnie, G.; Detellier, C. PdNP Decoration of Halloysite Lumen via Selective Grafting of Ionic Liquid onto the Aluminol Surfaces and Catalytic Application. *ACS Appl. Mater. Interfaces* **2016**, *8* (7), 4862–4869. https://doi.org/10.1021/acsami.5b10407.
(81) Lin, Y.; Ng, K. M.; Chan, C.-M.; Sun, G.; Wu, J. High-Impact Polystyrene/Halloysite Nanocomposites Prepared by Emulsion Polymerization Using Sodium Dodecyl Sulfate as Surfactant. *J. Colloid Interface Sci.* **2011**, *358* (2), 423–429. https://doi.org/https://doi.org/10.1016/j.jcis.2011.03.009.
(82) Cavallaro, G.; Lazzara, G.; Milioto, S. Exploiting the Colloidal Stability and Solubilization Ability of Clay Nanotubes/Ionic Surfactant Hybrid Nanomaterials. *J. Phys. Chem. C* **2012**, *116* (41), 21932–21938. https://doi.org/10.1021/jp307961q.
(83) Cavallaro, G.; Lazzara, G.; Milioto, S.; Palmisano, G.; Parisi, F. Halloysite Nanotube with Fluorinated Lumen: Non-Foaming Nanocontainer for Storage and Controlled Release of Oxygen in Aqueous Media. *J. Colloid Interface Sci.* **2014**, *417*, 66–71. https://doi.org/https://doi.org/10.1016/j.jcis.2013.11.026.
(84) Bertolino, V.; Cavallaro, G.; Lazzara, G.; Merli, M.; Milioto, S.; Parisi, F.; Sciascia, L. Effect of the Biopolymer Charge and the Nanoclay Morphology on Nanocomposite Materials. *Ind. Eng. Chem. Res.* **2016**, *55* (27), 7373–7380. https://doi.org/10.1021/acs.iecr.6b01816.
(85) Bertolino, V.; Cavallaro, G.; Lazzara, G.; Milioto, S.; Parisi, F. Biopolymer-Targeted Adsorption onto Halloysite Nanotubes in Aqueous Media. *Langmuir* **2017**, *33* (13), 3317–3323. https://doi.org/10.1021/acs.langmuir.7b00600.
(86) Massaro, M.; Riela, S.; Cavallaro, G.; Colletti, C. G.; Milioto, S.; Noto, R.; Lazzara., G. Ecocompatible Halloysite/Cucurbit[8]Uril Hybrid as Efficient Nanosponge for Pollutants Removal. *ChemistrySelect* **2016**, *1* (8), 1773–1779. https://doi.org/10.1002/slct.201600322.
(87) Biddeci, G.; Cavallaro, G.; Di Blasi, F.; Lazzara, G.; Massaro, M.; Milioto, S.; Parisi, F.; Riela, S.; Spinelli, G. Halloysite Nanotubes Loaded with Peppermint Essential Oil as Filler for Functional Biopolymer Film. *Carbohydr. Polym.* **2016**, *152*, 548–557. https://doi.org/https://doi.org/10.1016/j.carbpol.2016.07.041.
(88) Wu, S.; Qiu, M.; Guo, B.; Zhang, L.; Lvov, Y. Nanodot-Loaded Clay Nanotubes as Green and Sustained Radical Scavengers for Elastomer. *ACS Sustain. Chem. Eng.* **2017**, *5* (2), 1775–1783. https://doi.org/10.1021/acssuschemeng.6b02523.
(89) Liu, M.; Guo, B.; Zou, Q.; Du, M.; Jia, D. Interactions between Halloysite Nanotubes and 2,5-Bis(2-Benzoxazolyl) Thiophene and Their Effects on Reinforcement of Polypropylene/Halloysite Nanocomposites. *Nanotechnology* **2008**, *19* (20), 205709. https://doi.org/10.1088/0957-4484/19/20/205709.
(90) Liu, M.; Zhang, Y.; Wu, C.; Xiong, S.; Zhou, C. Chitosan/Halloysite Nanotubes Bionanocomposites: Structure, Mechanical Properties and Biocompatibility. *Int. J. Biol. Macromol.* **2012**, *51* (4), 566–575. https://doi.org/https://doi.org/10.1016/j.ijbiomac.2012.06.022.
(91) De Silva, R. T.; Pasbakhsh, P.; Goh, K. L.; Chai, S.-P.; Ismail, H. Physico-Chemical Characterisation of Chitosan/Halloysite Composite Membranes. *Polym. Test.* **2013**, *32* (2), 265–271. https://doi.org/https://doi.org/10.1016/j.polymertesting.2012.11.006.
(92) Liu, M.; Wu, C.; Jiao, Y.; Xiong, S.; Zhou, C. Chitosan–Halloysite Nanotubes Nanocomposite Scaffolds for Tissue Engineering. *J. Mater. Chem. B* **2013**, *1* (15), 2078–2089. https://doi.org/10.1039/C3TB20084A.
(93) Lvov, Y.; Price, R.; Gaber, B.; Ichinose, I. Thin Film Nanofabrication via Layer-by-Layer Adsorption of Tubule Halloysite, Spherical Silica, Proteins and Polycations. *Colloids Surfaces A*

Physicochem. Eng. Asp. **2002**, *198–200*, 375–382. https://doi.org/https://doi.org/10.1016/S0927-7757(01)00970-0.
(94) Kim, J.; Park, N.; Na, J. H.; Han, J. Development of Natural Insect-Repellent Loaded Halloysite Nanotubes and Their Application to Food Packaging to Prevent Plodia Interpunctella Infestation. *J. Food Sci.* **2016**, *81* (8), E1956–E1965. https://doi.org/10.1111/1750-3841.13373.
(95) Long, Z.; Zhang, J.; Shen, Y.; Zhou, C.; Liu, M. Polyethyleneimine Grafted Short Halloysite Nanotubes for Gene Delivery. *Mater. Sci. Eng. C* **2017**, *81*, 224–235. https://doi.org/https://doi.org/10.1016/j.msec.2017.07.035.
(96) Shamsi, M. H.; Geckeler, K. E. The First Biopolymer-Wrapped Non-Carbon Nanotubes. *Nanotechnology* **2008**, *19* (7), 75604. https://doi.org/10.1088/0957-4484/19/7/075604.
(97) Chang, P. R.; Xie, Y.; Wu, D.; Ma, X. Amylose Wrapped Halloysite Nanotubes. *Carbohydr. Polym.* **2011**, *84* (4), 1426–1429. https://doi.org/https://doi.org/10.1016/j.carbpol.2011.01.038.
(98) Wang, Q.; Zhang, J.; Wang, A. Alkali Activation of Halloysite for Adsorption and Release of Ofloxacin. *Appl. Surf. Sci.* **2013**, *287*, 54–61. https://doi.org/https://doi.org/10.1016/j.apsusc.2013.09.057.
(99) White, R. D.; Bavykin, D. V; Walsh, F. C. The Stability of Halloysite Nanotubes in Acidic and Alkaline Aqueous Suspensions. *Nanotechnology* **2012**, *23* (6), 65705. https://doi.org/10.1088/0957-4484/23/6/065705.
(100) Abdullayev, E.; Joshi, A.; Wei, W.; Zhao, Y.; Lvov, Y. Enlargement of Halloysite Clay Nanotube Lumen by Selective Etching of Aluminum Oxide. *ACS Nano* **2012**, *6* (8), 7216–7226. https://doi.org/10.1021/nn302328x.
(101) Garcia-Garcia, D.; Ferri, J. M.; Ripoll, L.; Hidalgo, M.; Lopez-Martinez, J.; Balart, R. Characterization of Selectively Etched Halloysite Nanotubes by Acid Treatment. *Appl. Surf. Sci.* **2017**, *422*, 616–625. https://doi.org/https://doi.org/10.1016/j.apsusc.2017.06.104.
(102) Banaś, D.; Kubala-Kukuś, A.; Braziewicz, J.; Majewska, U.; Pajek, M.; Wudarczyk-Moćko, J.; Czech, K.; Garnuszek, M.; Słomkiewicz, P.; Szczepanik, B. Study of Properties of Chemically Modified Samples of Halloysite Mineral with X-Ray Fluorescence and X-Ray Powder Diffraction Methods. *Radiat. Phys. Chem.* **2013**, *93*, 129–134. https://doi.org/https://doi.org/10.1016/j.radphyschem.2013.05.028.
(103) Kadi, S.; Lellou, S.; Marouf-Khelifa, K.; Schott, J.; Gener-Batonneau, I.; Khelifa, A. Preparation, Characterisation and Application of Thermally Treated Algerian Halloysite. *Microporous Mesoporous Mater.* **2012**, *158*, 47–54. https://doi.org/https://doi.org/10.1016/j.micromeso.2012.03.014.
(104) Wang, Q.; Zhang, J.; Zheng, Y.; Wang, A. Adsorption and Release of Ofloxacin from Acid- and Heat-Treated Halloysite. *Colloids Surfaces B Biointerfaces* **2014**, *113*, 51–58. https://doi.org/https://doi.org/10.1016/j.colsurfb.2013.08.036.
(105) Rong, R.; Xu, X.; Zhu, S.; Li, B.; Wang, X.; Tang, K. Facile Preparation of Homogeneous and Length Controllable Halloysite Nanotubes by Ultrasonic Scission and Uniform Viscosity Centrifugation. *Chem. Eng. J.* **2016**, *291*, 20–29. https://doi.org/https://doi.org/10.1016/j.cej.2016.01.082.
(106) Maziarz, P.; Prokop, A.; Matusik, J. A Comparative Study on the Removal of Pb(II), Zn(II), Cd(II) and As(V) by Natural, Acid Activated and Calcined Halloysite. *Geol. Geophys. Environ. Vol 41, No 1 (2015)DO - 10.7494/geol.2015.41.1.108* **2015**.
(107) Yu, L.; Wang, H.; Zhang, Y.; Zhang, B.; Liu, J. Recent Advances in Halloysite Nanotube Derived Composites for Water Treatment. *Environ. Sci. Nano* **2016**, *3* (1), 28–44. https://doi.org/10.1039/C5EN00149H.
(108) Vinokurov, V. A.; Stavitskaya, A. V; Chudakov, Y. A.; Ivanov, E. V; Shrestha, L. K.; Ariga, K.; Darrat, Y. A.; Lvov, Y. M. Formation of Metal Clusters in Halloysite Clay Nanotubes. *Sci. Technol. Adv. Mater.* **2017**, *18* (1), 147–151. https://doi.org/10.1080/14686996.2016.1278352.
(109) Fan, H.; Shen, W. Carbon Nanosheets: Synthesis and Application. *ChemSusChem* **2015**, *8* (12), 2004–2027. https://doi.org/10.1002/cssc.201500141.
(110) Liu, G.; Kang, F.; Li, B.; Huang, Z.; Chuan, X. Characterization of the Porous Carbon Prepared by Using Halloysite as Template and Its Application to EDLC. *J. Phys. Chem. Solids* **2006**, *67* (5), 1186–1189. https://doi.org/https://doi.org/10.1016/j.jpcs.2006.01.044.
(111) Fakhrullina, G. I.; Akhatova, F. S.; Lvov, Y. M.; Fakhrullin, R. F. Toxicity of Halloysite Clay

Nanotubes in Vivo: A Caenorhabditis Elegans Study. *Environ. Sci. Nano* **2015**, *2* (1), 54–59. https://doi.org/10.1039/C4EN00135D.
(112) Ahmed, F. R.; Shoaib, M. H.; Azhar, M.; Um, S. H.; Yousuf, R. I.; Hashmi, S.; Dar, A. In-Vitro Assessment of Cytotoxicity of Halloysite Nanotubes against HepG2, HCT116 and Human Peripheral Blood Lymphocytes. *Colloids Surfaces B Biointerfaces* **2015**, *135*, 50–55. https://doi.org/https://doi.org/10.1016/j.colsurfb.2015.07.021.
(113) Vergaro, V.; Abdullayev, E.; Lvov, Y. M.; Zeitoun, A.; Cingolani, R.; Rinaldi, R.; Leporatti, S. Cytocompatibility and Uptake of Halloysite Clay Nanotubes. *Biomacromolecules* **2010**, *11* (3), 820–826. https://doi.org/10.1021/bm9014446.
(114) Long, Z.; Wu, Y.-P.; Gao, H.-Y.; Zhang, J.; Ou, X.; He, R.-R.; Liu, M. In Vitro and in Vivo Toxicity Evaluation of Halloysite Nanotubes. *J. Mater. Chem. B* **2018**, *6* (44), 7204–7216. https://doi.org/10.1039/C8TB01382A.
(115) Yang, J.; Wu, Y.; Shen, Y.; Zhou, C.; Li, Y.-F.; He, R.-R.; Liu, M. Enhanced Therapeutic Efficacy of Doxorubicin for Breast Cancer Using Chitosan Oligosaccharide-Modified Halloysite Nanotubes. *ACS Appl. Mater. Interfaces* **2016**, *8* (40), 26578–26590. https://doi.org/10.1021/acsami.6b09074.
(116) Lisuzzo, L.; Cavallaro, G.; Pasbakhsh, P.; Milioto, S.; Lazzara, G. Why Does Vacuum Drive to the Loading of Halloysite Nanotubes? The Key Role of Water Confinement. *J. Colloid Interface Sci.* **2019**, *547*, 361–369. https://doi.org/https://doi.org/10.1016/j.jcis.2019.04.012.
(117) Veerabadran, N. G.; Mongayt, D.; Torchilin, V.; Price, R. R.; Lvov, Y. M. Organized Shells on Clay Nanotubes for Controlled Release of Macromolecules. *Macromol. Rapid Commun.* **2009**, *30* (2), 99–103. https://doi.org/10.1002/marc.200800510.
(118) Dzamukova, M. R.; Naumenko, E. A.; Lvov, Y. M.; Fakhrullin, R. F. Enzyme-Activated Intracellular Drug Delivery with Tubule Clay Nanoformulation. *Sci. Rep.* **2015**, *5* (1), 10560. https://doi.org/10.1038/srep10560.
(119) Kırımlıoğlu, G. Y.; Yazan, Y. Development, Characterization and in Vitro Release Characteristics of Rabeprazole Sodium in Halloysite Nanotubes. *Eur Int J Sci Technol* **2016**, *5*, 99–109.
(120) Yendluri, R.; Lvov, Y.; de Villiers, M. M.; Vinokurov, V.; Naumenko, E.; Tarasova, E.; Fakhrullin, R. Paclitaxel Encapsulated in Halloysite Clay Nanotubes for Intestinal and Intracellular Delivery. *J. Pharm. Sci.* **2017**, *106* (10), 3131–3139. https://doi.org/https://doi.org/10.1016/j.xphs.2017.05.034.
(121) Wang, Q.; Zhang, J.; Mu, B.; Fan, L.; Wang, A. Facile Preparation of Magnetic 2-Hydroxypropyltrimethyl Ammonium Chloride Chitosan/Fe3O4/Halloysite Nanotubes Microspheres for the Controlled Release of Ofloxacin. *Carbohydr. Polym.* **2014**, *102*, 877–883. https://doi.org/https://doi.org/10.1016/j.carbpol.2013.10.071.
(122) Massaro, M.; Amorati, R.; Cavallaro, G.; Guernelli, S.; Lazzara, G.; Milioto, S.; Noto, R.; Poma, P.; Riela, S. Direct Chemical Grafted Curcumin on Halloysite Nanotubes as Dual-Responsive Prodrug for Pharmacological Applications. *Colloids Surfaces B Biointerfaces* **2016**, *140*, 505–513. https://doi.org/https://doi.org/10.1016/j.colsurfb.2016.01.025.
(123) Guo, M.; Wang, A.; Muhammad, F.; Qi, W.; Ren, H.; Guo, Y.; Zhu, G. Halloysite Nanotubes, a Multifunctional Nanovehicle for Anticancer Drug Delivery. *Chinese J. Chem.* **2012**, *30* (9), 2115–2120. https://doi.org/10.1002/cjoc.201200657.
(124) Velde, B. *Introduction to Clay Minerals: Chemistry, Origins, Uses and Environmental Significance.*; Chapman and Hall Ltd, 1992.
(125) Kohl, H.; Reimer, L. *Transmission Electron Microscopy: Physics of Image Formation*; Springer, 2008.
(126) Inkson, B. J. 2 - Scanning Electron Microscopy (SEM) and Transmission Electron Microscopy (TEM) for Materials Characterization; Hübschen, G., Altpeter, I., Tschuncky, R., Herrmann, H.-G. B. T.-M. C. U. N. E. (NDE) M., Eds.; Woodhead Publishing, 2016; pp 17–43. https://doi.org/https://doi.org/10.1016/B978-0-08-100040-3.00002-X.
(127) Chu B. Dynamic Light Scattering. In *Soft-Matter Characterization*; Borsali, R., Pecora, R., Eds.; Springer Netherlands, 2008; pp 335–372.
(128) Ramos, A. P. 4 - Dynamic Light Scattering Applied to Nanoparticle Characterization. In *Micro and Nano Technologies*; Da Róz, A. L., Ferreira, M., de Lima Leite, F., Oliveira, O. N. B. T.-N. T., Eds.; William Andrew Publishing, 2017; pp 99–110. https://doi.org/https://doi.org/10.1016/B978-0-323-49778-7.00004-7.
(129) Analyitical Instruments Specialists www.atascientific.com.au.

(130) Instruments, M. Dynamic Light Scattering: An Introduction in 30 Minutes. Technical Note Malvern. *MRK656-01* **2012**, 1–8.
(131) Instruments, M. Tech Note: Zeta Potential - An Introduction in 30 Minutes. **2005**, 1.

Chapter 2

An approach for magnetic halloysite nanocomposite with selective loading of SPION in the lumen

Hady Hamza, Anna Maria Ferretti, Claudia Innocenti, Katarzyna Fidecka, Emanuela Licandro, Claudio Sangregorio, and Daniela Maggioni

Inorg. Chem. 2020, 59, 17, 12086–12096.

1 Introduction

One of the most interesting features of Halloysite (HNT) is its different chemical composition of the outer silica and the inner alumina parts. HNT inner lumen is positively charged due to exposed OH groups' protonation and the possible coordination vacancy at Al^{3+} sites. [1] Instead, the outer part is negatively charged due to the few OH groups only present in the structural defects of the siloxane layer and at the edges of the nanotubes.[2]

Thanks to these features, HNT have been already employed as possible drug delivery vectors[3–5] for proteins and small drugs,[6,7] since negatively charged drugs can be easily retained by the positive lumen, which could act as an inorganic nanocapsule for controlled release.[8,9] Conversely, long oligonucleotide strands, despite the negative charge, cannot be loaded in the HNT inner lumen possibly due to the large size. Nevertheless, they can be delivered by immobilizing them on the outer surface through different strategies[6,10–12]

Superparamagnetic iron oxide nanoparticles (SPION) made of magnetite (Fe_3O_4) have been studied in depth in the last decades, especially for biomedical field applications.[13–18] Indeed, their superparamagnetism is essential for safe use in vivo since their total magnetization is null in the absence of an applied external magnetic field, thus preventing any aggregation event that could cause capillary occlusion. They possess many useful features for both imaging and therapy: first, they are biocompatible and biodegradable,[19,20] and they can be exploited as contrast agents in magnetic resonance (MRI), as drug delivery carriers, for various separating techniques, and as heat mediators for magnetic fluid hyperthermia (MFH) treatments, among others.[21] SPION have also been extensively used for triggering the drug release from several different nanocomposites[22–25] or nanoporous systems.[26]

Due to the biocompatibility of both HNT[1] and SPION, many previous research studies focused on the preparation of HNT−SPION nanocomposites, but in most cases, the SPION was anchored on the outer surface of HNT[27–34] or grown by coprecipitation in the HNT lumen.[35,36] In this last case, the crystallinity, the size of nanoparticles and their magnetic properties were hardly controllable. To the best of our knowledge, preformed magnetic NPs have never been selectively loaded in the inner lumen of HNT so far. In contrast, the loading of preformed SPION with shaped properties would be of interest for many applications, such as MRI or MFH. Moreover, the inner loading could give rise to higher oxidative resistance of NPs compared to

their anchoring on the HNT external surface. HNT could act as a protective barrier slowing down the molecular oxygen action, as recently previewed for carbon nanotubes filled with SPION.[37]

In the literature, there are many examples of *in situ* formed nanoparticles (NPs), selectively loaded inside HNT lumen.[38] But still, in many cases, the growing NPs interacted with the outer surface instead of the inner one only. Selective inner growth has been reported for the ability of Au NPs to selectively form in the HNT lumen;[39] the same was achieved for Ru-based metallic clusters.[40] The last one mentions the possibility of growing iron oxide NPs made by a coprecipitation method.[36]

Only very few examples report the loading of preformed NPs in the HNT lumen. Specifically, either through the charge difference method between negative NPs and positive lumen, as in the case of silver [41] and palladium NPs,[42] or through exploiting the vacuum pouring technique as in carbon nanodots.[43]

The goal of this work was to find a reliable and reproducible method to selectively fill the HNT lumen with pre-formed SPION possessing well-defined and possibly good magnetic properties. The final aim of this study was to obtain HNT-SPION as a "building block" for further developments of suitable nanocomposites. The nanocomposites based on SPION-in-HNT could be useful for different applications, such as i) in the biomedical field, as new theranostic agents for MRI, MFH and controlled release of a drug by an external magnetic stimulus; ii) in catalysis, with the double advantage to recover the system due to the magnetic NPs in the inner lumen leaving the external HNT surface available for further decoration with catalytic organometallic compounds or other types of nanoparticles; iii) in water remediation, by exploiting a capturing agent or a photo-reactive organometallic compound anchored on the external surface while maintaining the ability to magnetically recover the nanocomposite; iv) in tissue engineering for the development of 3D scaffolds able to align cells of an anisotropic growing tissue.

2 Results and discussion

To fill the HNT with magnetic NPs, we investigated three distinct approaches (depicted in **Scheme 1**): the electrostatic interaction, the *in situ* formation of SPION, and the pre-modification approach. All these three strategies are described in the next paragraphs, even though only the third one gave us the desired HNT-SPION adduct.

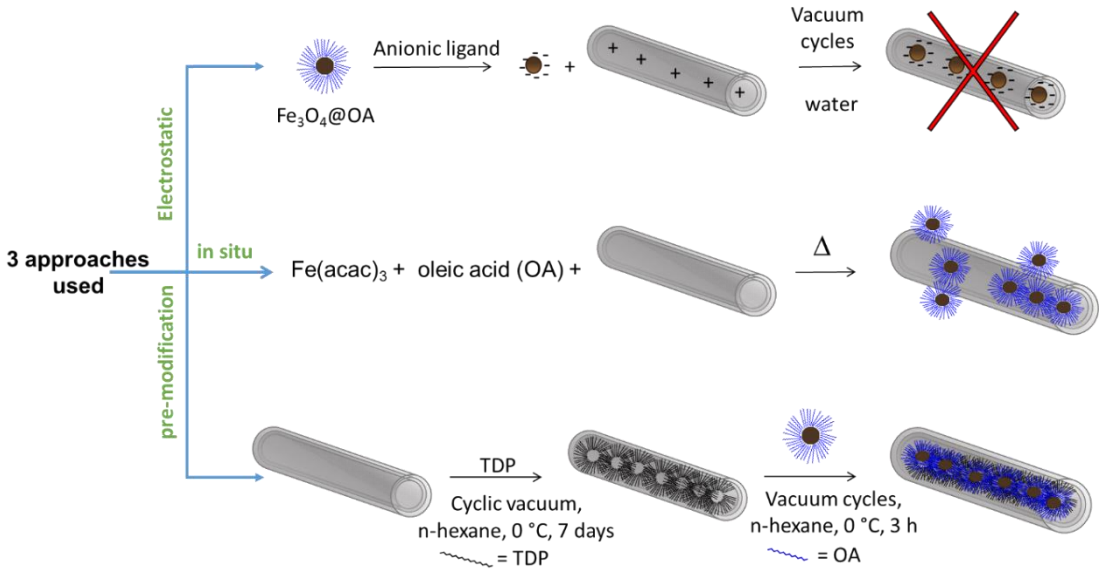

Scheme 1 Schematic depiction of the three distinct approaches followed in this study to obtain HNT-SPION nanocomposite with the selective loading of SPION in the inner part.

2.1 Attempts to prepare SPION-in-HNT using water-dispersible negatively charged SPION: the electrostatic approach.

The first method tried to exploit the charge difference between the inner and the outer part of the HNT. Indeed, the inner layer of alumina remains positively charged up to pH 8.5, whilst the external silica layer is negatively charged for almost all the pH range above 1.5.[44] This charge difference has been extensively exploited for the loading of small negatively charged molecules into HNT inner lumen and their forward sustain release at the intended site.[45] Hence, despite the overall negative charge of HNT at physiological pH, the inner alumina remains positively charged to a certain extent. As already mentioned in the Introduction, just a few examples were reported on the loading of pre-formed NPs in the HNT lumen.[41–43] One of them was carried out using small negative Ag NPs.[41] In that case, the prepared NPs were tiny (ca 2.6 nm), the loading procedure was extremely simple and involved the use of neither sonication nor vacuum cycles to induce the NPs to enter into the HNT lumen, so that it can be concluded the diffusion by Brownian motions was effective enough to fill the HNT lumen with NPs.

We tried to follow the same approach but applying vacuum/N_2 cycles in order to exploit the strong capillary pressures affecting the HNT lumen, and taking into account that the HNT inner diameter measured by TEM was ~ 15.3 ± 0.3 nm (**Figure 1**). Hence, we prepared negatively charged SPION of a suitably small size, ranging from 5.1 to 6.9 nm. This size was judged to be a good compromise between the need of employing NPs small enough to enter the lumen but, at the same time, big enough to maintain good magnetic properties. We adopted different approaches for the SPION synthesis (resumed in **Table 1**), passing from a simple coprecipitation method [46] to thermal decomposition syntheses.[47,48] Indeed, one of the main goals of this work was the development of a strategy to fill HNT with the best NPs in terms of magnetic properties. It is well known that, for SPION, the best magnetic properties are

achievable through thermal decomposition syntheses, able to modulate size and crystallinity.[49]

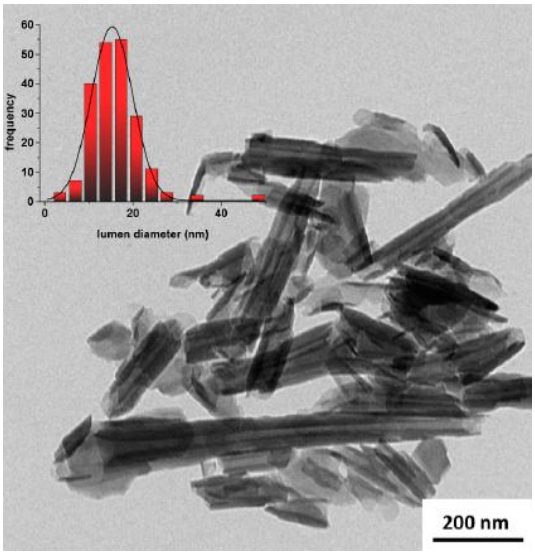

Figure 1 TEM micrograph of a HNT sample (inset: HNT lumen diameter distribution).

In **Table 1** we reported the data of the several essays we made with the electrostatic attraction approach. These implied a slight variation of the SPION dimension, but most of all, the variation of the surface capping ligands that in vain were changed, trying to encourage the entry of negatively charged SPION into the nanotube lumen avoiding early SPION aggregation. Despite all the efforts made, none of the attempted procedures was successful.

Table 1 Mean size (diameter, nm) of synthesized SPION as measured by TEM and DLS on water suspensions. The synthetic method used is indicated together with the relative reference (DMSA = dimercaptosuccinic acid; GA = gallic acid; TMAOH = tetramethylammonium hydroxide; PA = protocatechuic acid; OA = oleic acid).

Sample ID	Ref	NPs Synthesis Method	NP Stabilizer	TEM/nm	DLS/nm (hexane) [b]	DLS/nm (water)
SPION1@DMSA	46	Coprecipitation with NaOH	DMSA [50]	5.3 ± 1.0	13.1 ± 3.0	13.5 ± 2.4
SPION2@DMSA	46	Coprecipitation without NaOH	DMSA [50]	---[a]	10.6 ± 4.0	---
SPION3@DMSA[c]	47	Thermal decomposition using Fe(acac)3	DMSA [50]	5.1 ± 1.6	8.0 ± 1.9	---
SPION4@GA	48	Thermal decomposition using iron oleate	GA [15]			13.0 ± 2.5
SPION4@TMAOH	48	Thermal decomposition using iron oleate	TMAOH [51]	6.9 ± 1.0	10.7 ± 2.3	10.0 ± 3.0
SPION4@PA	48	Thermal decomposition using iron oleate	PA [15]			13.0 ± 4.0
SPION3@OA[c]	47	Thermal decomposition using $Fe(acac)_3$	OA	6.1 ± 1.3	10.9 ± 3.0	----

[a] The TEM images were not acquired on this sample.
[b] The DLS measurement was performed in n-hexane suspension on the as-prepared SPION@OA.
[c] The synthetic procedure for the preparation of SPION@OA was the same, but repeated twice, leading to slightly different. mean size values

We started preparing SPION1@OA[46] where OA stands for oleic acid, with a hydrodynamic diameter of 13.5 ± 4 nm (see DLS measurement reported in **Figure 2**), which was slightly smaller than the average inner HNT diameter.

In order to prepare negatively charged NPs, the oleate molecular layer was removed and substituted with a proper negatively charged stabilizing molecule. Hence, a first ligand exchange process was carried out with the bi-functional molecule dimercaptosuccinic acid (DMSA),[50] which is able on one side to bind to the surface and on the other side to self-deprotonate, giving rise to negatively charged as well as water-compatible SPION. The ligand exchange possibly needs to occur without NP aggregation, hence maintaining the hydrodynamic size observed on the starting SPION stabilized by OA. After the ligand exchange step, the SPION1@DMSA showed a hydrodynamic diameter suitable for the HNT loading (see **Figure 3**).

The loading tests were then carried out bringing the starting pristine-halloysite suspension to acidic pH (~3-4) in order to maximize the charge difference between the inner part of HNT (still enough positive at this pH) and the magnetic nanoparticle (still largely negative). However, both sonication and/or applied vacuum/N_2 cycles - to induce the air bubbles naturally present in the halloysites to come out, as well as the NPs of opposite charge to enter in the lumen - were not effective, and SPION were not found in the HNT inner part by TEM investigation. On the contrary, they always formed aggregates accumulating outside the nanoclay, and in some cases interacting with the HNT edges only (**Figure 4**).

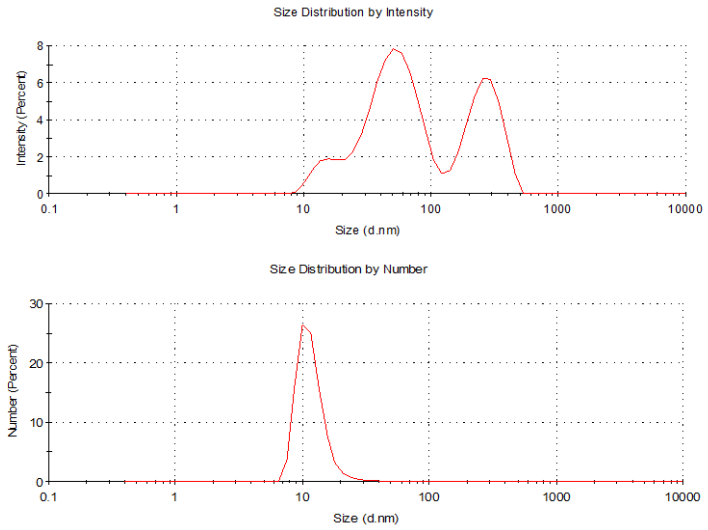

Figure 2 DLS of SPION1@OA suspended in n-hexane, synthesised by a coprecipitation method in a biphasic system and in the presence of NaOH. Top: Intensity-weighted diameter distribution, showing the presence of three distinct populations centred at 13.5 nm, 50 nm and 270 nm. Bottom: Number-weighted diameter distribution, showing that the large majority of the NPs belong to the smaller population, being the other two ascribable to sporadic aggregates.

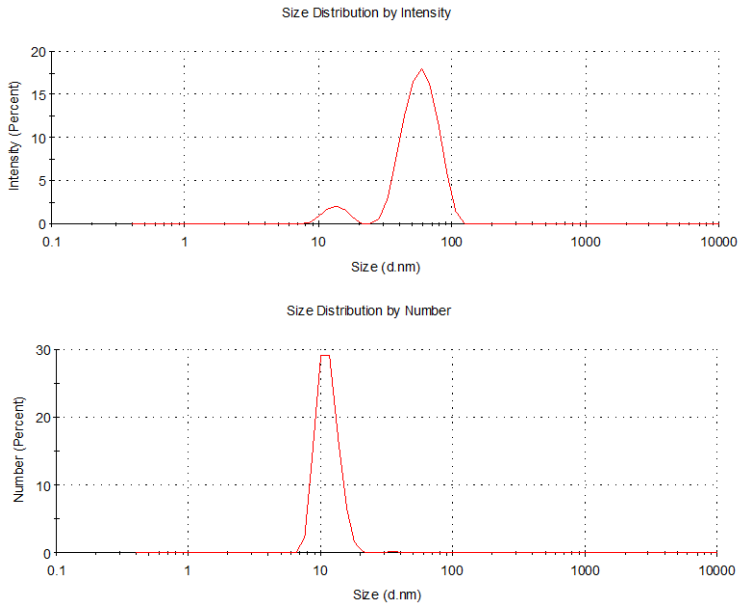

Figure 3 DLS of SPION1@DMSA suspended in milliQ water after ligand exchange from SPION1@OA. Top: Intensity-weighted diameter distribution, showing the presence of two distinct populations centred at 13.5 nm and 60 nm. Bottom: Number-weighted diameter distribution, showing that the large majority of the NPs belong to the smaller population, being the other ascribable to sporadic aggregates of the main single NPs.

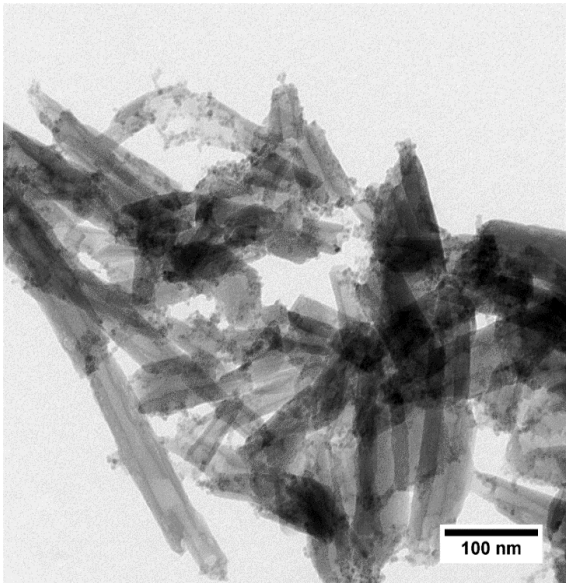

Figure 4 TEM micrograph of pristine HNT treated with SPION1@DMSA in water suspension by vacuum/nitrogen cycles and sonication

We then considered decreasing the size of the SPION by adopting different synthetic approaches for SPION2@OA (with a hydrodynamic diameter of 10.6 ± 4 nm,[46] see DLS size distribution in **Figure 5**) and SPION3@OA (with a hydrodynamic diameter of 8.0 ± 1.9 nm, see DLS size distribution in **Figure 6a**, and a mean diameter by TEM of 5.1 ± 1.6 nm, [47] **Figure 6b**).

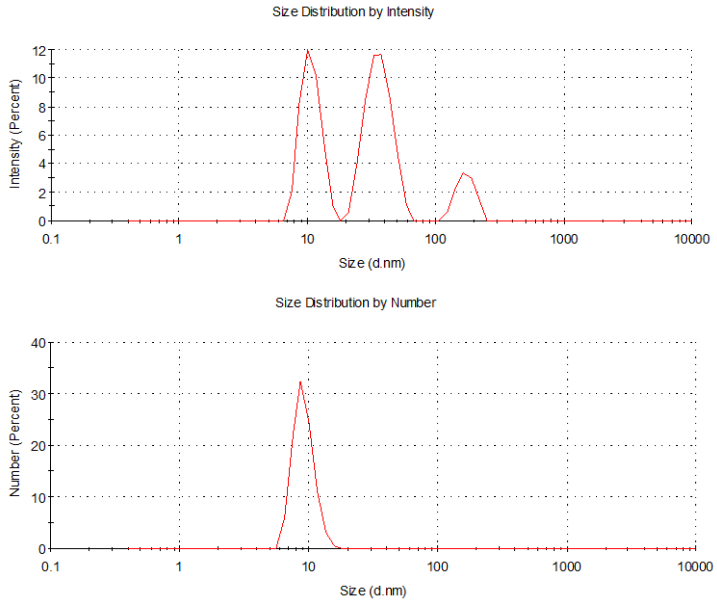

Figure 5 DLS of SPION2@OA suspended in n-hexane, synthesised by a coprecipitation method in a biphasic system without NaOH. Top: Intensity-weighted diameter distribution, showing the presence of three distinct populations centred at 10.6 nm, 35 nm and 150 nm. Bottom: Number-weighted diameter distribution, showing that the large majority of the NPs belong to the smaller population, being the other two due to sporadic aggregates.

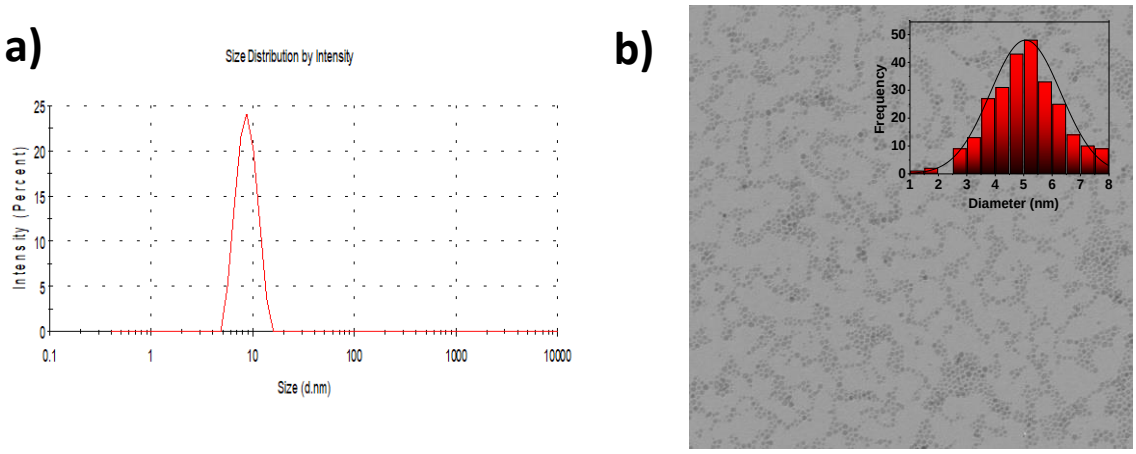

Figure 6. a) Intensity-weighted diameter distribution by DLS measurements on SPION3@OA suspended in n-hexane, synthesised by a thermal decomposition method. b) TEM micrograph of the same sample. In the inset it is reported the size distribution derived by Image-J software.

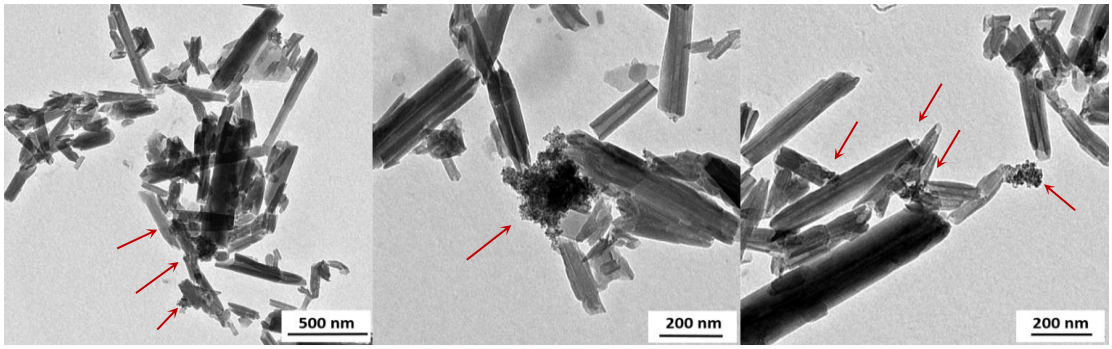

Figure 7. TEM images of pristine HNT treated with SPION3@DMSA in water suspension by vacuum/nitrogen cycles. Red arrows indicate the sites of SPIONs accumulation.

To explain the unsuccessful loading process, the hypothesis is that the DMSA could induce early aggregation of SPION during the reduced pressure/N_2 process, especially at acidic pH values. DMSA could form S-S bridges or hydrogen bonds between DMSA molecules lying onto different SPION, especially when they are pushed to stay in a small volume. Thus, we changed the type of hydrophilic coating, employing other bi-functional molecules, i.e. gallic acid (GA),[15] 16-phosphonohexadecanoic acid (PDA) and protocatechuic acid (PA) or the peptizing agent tetramethylammonium hydroxide (TMAOH)[51] (see **Scheme 2**). Except of PDA that did not give good suspensions after the ligand exchange, all the other molecules tested (see **Scheme 2**) effectively displaced the oleate molecules from the NP surface, giving rise to stable water colloids (see **Figures 8 and 10** for DLS measurements and **Figures 9 and 11** for TEM images of SPION4@GA and SPION4@PA, respectively). Nevertheless, in no case we did get the loading in the HNT inner.

Contrary to what observed for the other samples of SPION covered with DMSA, GA and PA, in the case of SPION4@TMAOH loading test (see DLS size distribution in **Figure 12**), we did not observe any change in color of the recovered powders as well as any magnetic attraction when an external magnet was applied, and no TEM image was acquired.

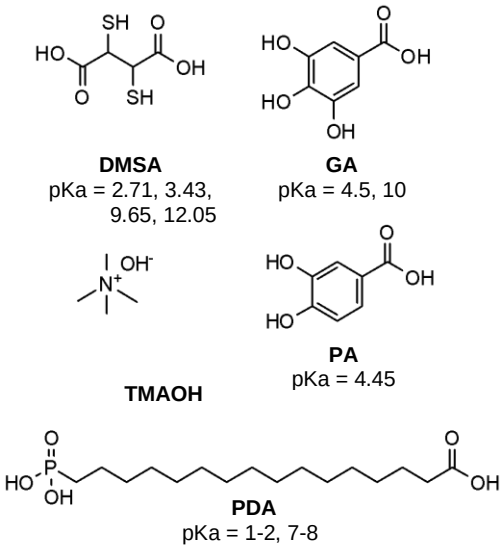

Scheme 2 Scheme of bifunctional ligands used for the OA exchange on SPION with their pKa.

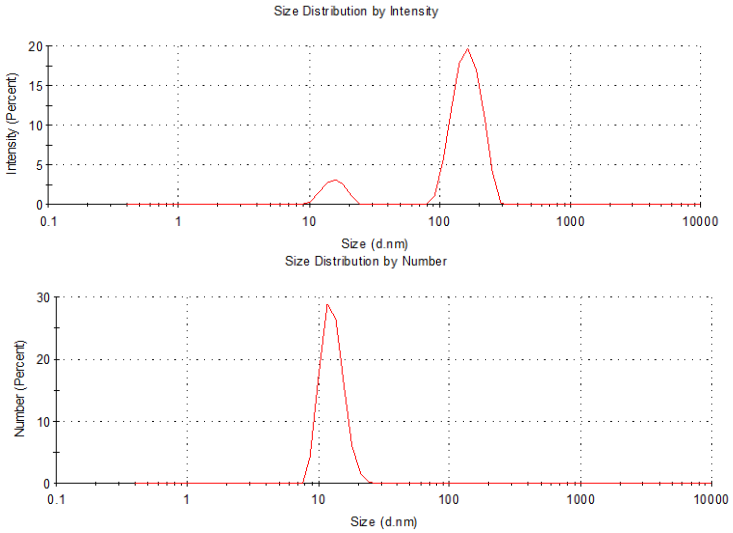

Figure 8. DLS of SPION4@GA SPIONs suspended in MilliQ water after ligand exchange. Top: Intensity-weighted diameter distribution, showing the presence of two distinct populations centred at 13.0 nm and 160 nm. Bottom: Number-weighted diameter distribution, showing that the large majority of the NPs belong to the smaller population, being the other ascribable to sporadic aggregates of the main single NPs.

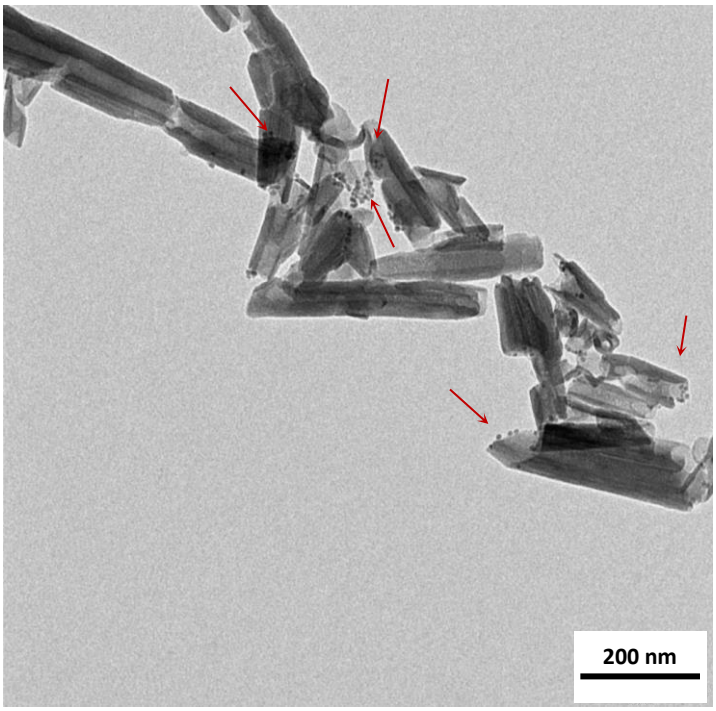

Figure 9 TEM micrograph of pristine HNT treated with SPION4@GA in water suspension by vacuum/nitrogen cycles. Red arrows indicate the sites of SPIONs accumulation.

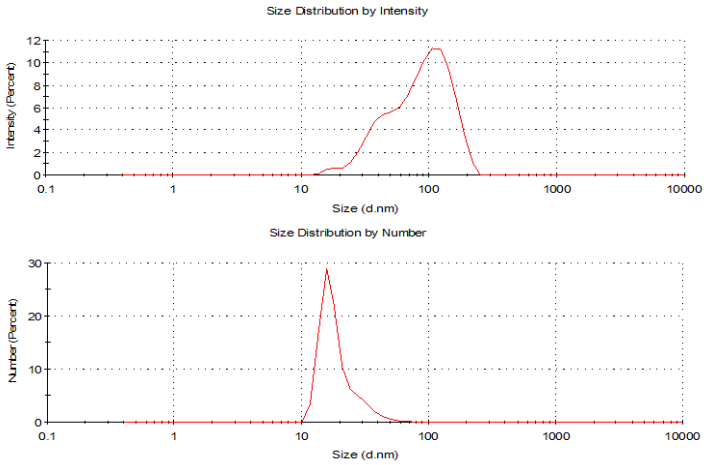

Figure 10 DLS of SPION4@PA suspended in milliQ water. Top: Intensity-weighted diameter distribution, showing the presence of three distinct populations centred at 13.0 nm, 40 nm and 102 nm. Bottom: Number-weighted diameter distribution, showing that the large majority of the NPs belong to the smaller population, being the other two ascribable to sporadic aggregates.

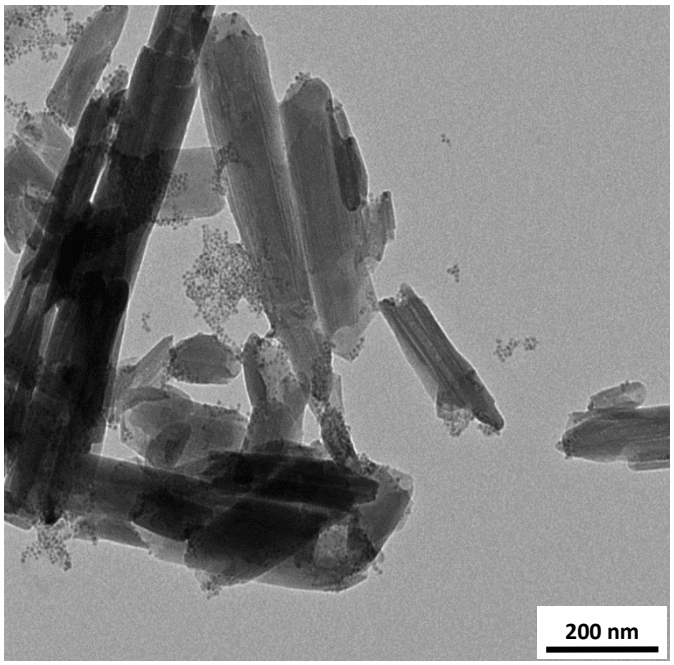

Figure 11 TEM micrograph of pristine HNT treated with SPION@PA in water suspension by vacuum/nitrogen cycles.

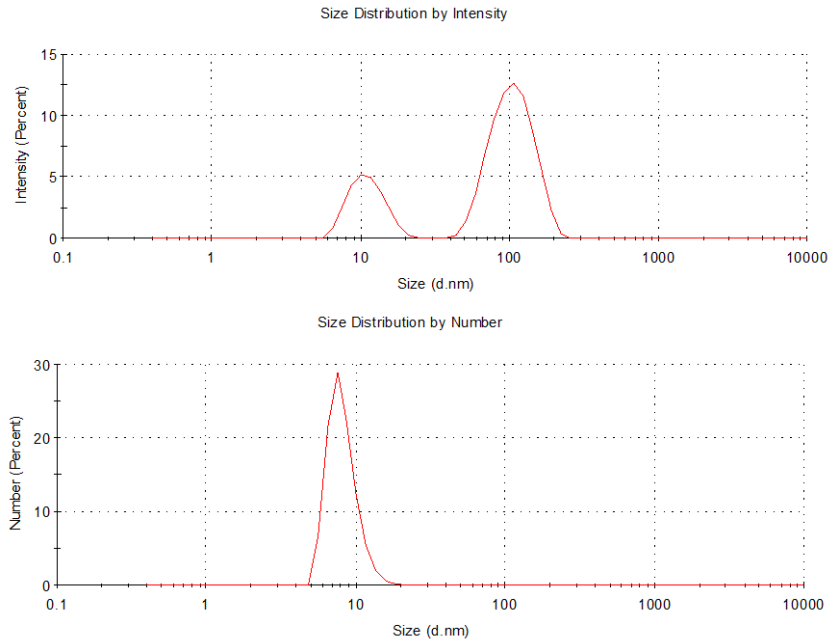

Figure 12 DLS of SPION4@TMAOH suspended in MilliQ water after ligand exchange. Top: Intensity-weighted diameter distribution, showing the presence of two distinct populations centred at 10.0 nm and 100 nm. Bottom: Number-weighted diameter distribution, showing that the large majority of the NPs belong to the smaller population, being the other ascribable to sporadic aggregates of the main single NPs.

We therefore concluded that the electrostatic attraction, useful for small molecules loading in HNT lumen,[7,8,45] as well as for tiny non-magnetic NPs,[41–43] was not effective in the case of these magnetic nanoparticles, regardless of the SPION size or coating. This could be due to the SPION mutual attraction in water, that can be reinforced by additional attractive forces such as hydrogen bonds between different particles, especially when they are in the restricted space volume at the entrance of the halloysite lumen in conditions of reduced pressure.

2.2 Attempts of SPION-in-HNT preparation using thermal decomposition in the presence of pristine HNT.

In this case, we tried to carry out an *in situ* thermal decomposition synthesis of SPIONs in the presence of HNT as reported in the literature[50] (**Scheme 1**). The chosen method for the synthesis of SPIONs was in principle able to lead to highly magnetized and monodispersed SPIONs into HNT. Thus, the iron precursor and the other reactants were made diffusing into the lumen of HNT, reducing the pressure in the vessel for some minutes before starting the reflux, to assure the diffusion into the lumen of the reaction mixture. HNT-SPION adduct was washed thoroughly using ethanol by centrifugation. The light brown powder recovered was magnetic, being attracted by a neodymium-iron-boron magnet and was dispersible in water. Unfortunately, TEM analysis of the obtained product showed that, even if some SPION were localized inside the HNT (highlighted in **Figure 13** by red arrows), they were also found attached to the external surface, showing that the growth of NPs was not selectively confined to the HNT lumen. Moreover, SPION were not highly monodispersed and, owing to the effect of high temperature, the outer surface of HNT was partly etched.

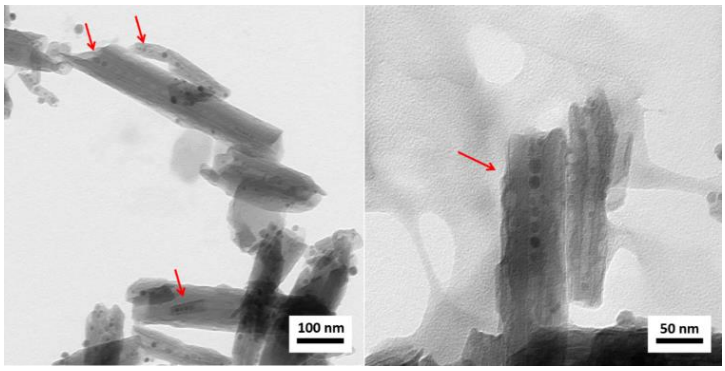

Figure 13. TEM images of HNT-SPION adduct obtained by thermal decomposition of iron precursor in the presence of HNT at high temperature and preceded by a vacuum/nitrogen cycle. Red arrows mark the SPION grown in the inner lumen of HNT.

2.3 SPION-in-HNT by functionalization of the inner lumen of HNT with tetradecylphosphonic acid (TDP).

The failed attempts obtained by pursuing the two previous paths prompted us to verify whether the SPION could be inserted in their native state, that is with the apolar capping agent (oleate) still on the surface, by properly modifying the lumen polarity of HNT. From the literature, it is known that it is possible to selectively functionalize the lumen of HNT using a phosphonic acid, which preferentially reacts with alumina compared to silica.[52,53] The inner surface of HNT was successfully modified with tetradecylphosphonic acid (TDP). [53] To ascertain whether the reaction had taken place, we employed several analytical techniques. As a first qualitative assay, we used Nile Red dye. Indeed, this molecule is very sensitive to the environment in which it is dispersed, in that both the absorption and the emission are heavily perturbed.[54] Nile Red is highly emissive in hydrophobic environments, as the one present in the functionalized lumen with TDP, while it is completely quenched in water. After the loading of Nile Red (see Experimental Part for details) the HNT-TDP turned purple, hence they were thoroughly washed with water to remove all the possible externally interacting dye. The still wet purple HNT-TDP sample, observed under UV light irradiation, exhibited a red luminescence. On the contrary, the pristine HNT treated in the same way with Nile Red and washed with water turned purple as well, but they did not show any emission under the UV light irradiation, as, on the contrary, the HNT-TDP did. This behavior was ascribed to the different microenvironment in which the dye is lying: in the case of HNT-TDP sample, the Nile Red is likely intercalated into the apolar long aliphatic chains, thus preserving Nile Red from the quenching provoked by its direct interaction with water (**Figure 14**).

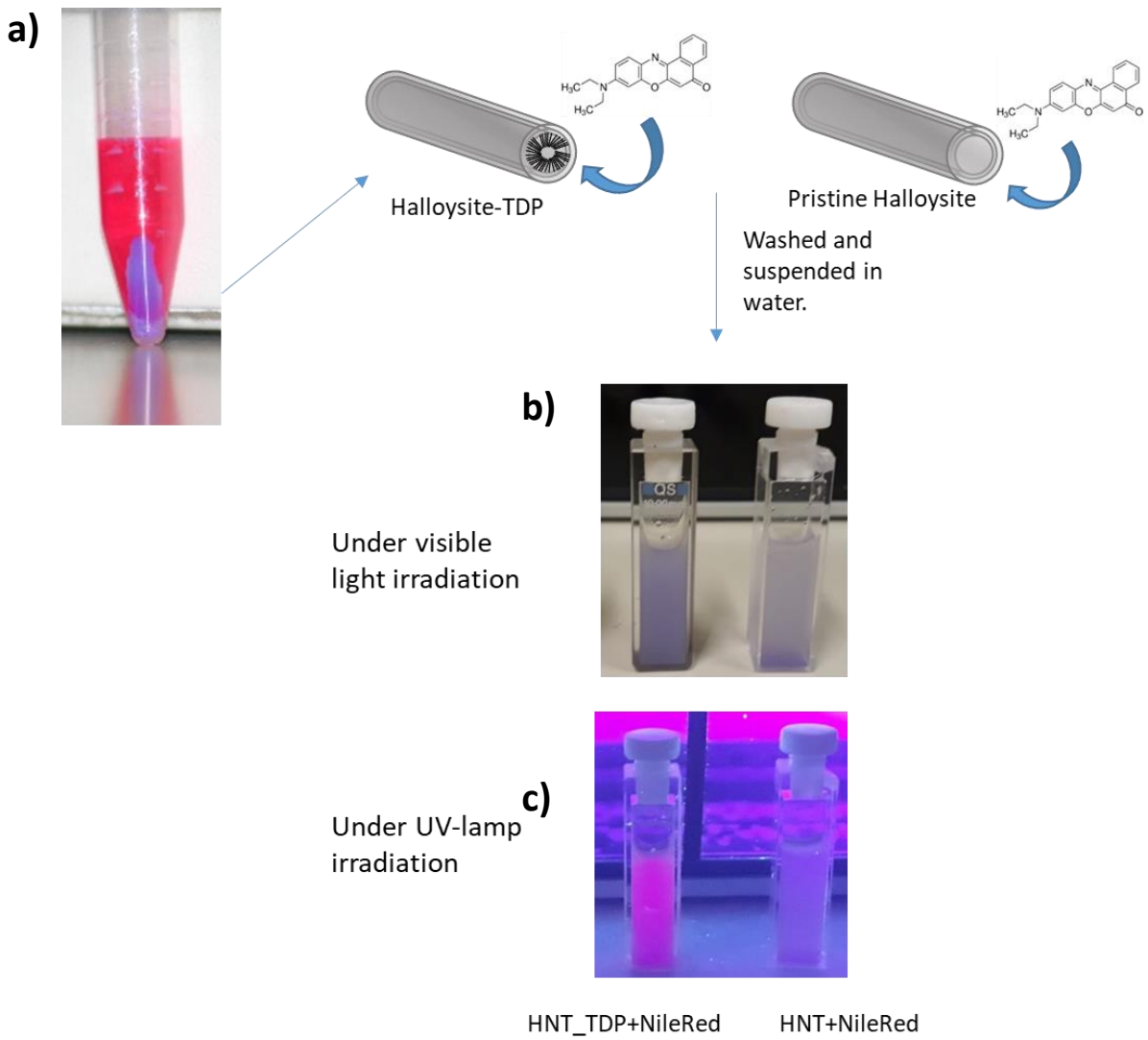

Figure 14. Digital pictures showing (a) the HNT interacted with an ethanol solution of Nile Red dye; (b) HNT-TDP (left) and pristine HNT (right) treated with Nile Red and irradiated by visible light; (c) the same samples of panel (b) irradiated by UV-light.

ATR-FTIR spectroscopy (**Figure 15a**) and thermogravimetric analysis (TGA, **Figure 15b**) confirmed the successful functionalization of halloysites. The ATR-FTIR spectrum of HNT-TDP (**Figure 15a**, top), as well as the one of pristine HNT (**Figure 15a**, middle), showed the characteristic sharp bands related to Al-OH stretching of lumen and interlayer alumina peaking at 3692 and 3624 cm^{-1}, respectively, and of the OH stretching of hydrogen-bonded water present in the interlayers (3551 cm^{-1}).[52] The spectrum of HNT-TDP showed the stretching bands of the aliphatic chain in the region between 3000-2800 cm^{-1} (2959, 2919 and 2851 cm^{-1}), together with the deformation (scissoring) of CH_2 groups (1468 cm^{-1}), while the bands due to the C-P-O stretching in the region 1100 – 800 cm^{-1} overlapped with the very intense bands of HNT, hampering their visualization and attribution. Finally, the broad P-O-H band for the unbound TDP visible in the TDP spectrum (bottom) at ~ 2300 cm^{-1} as well as the complete disappearing of the P=O band vibration at 1211 cm^{-1} suggest that TDP is bonded to the halloysites, and in particular to the alumina lumen layer, in a deprotonated form.[52,53]

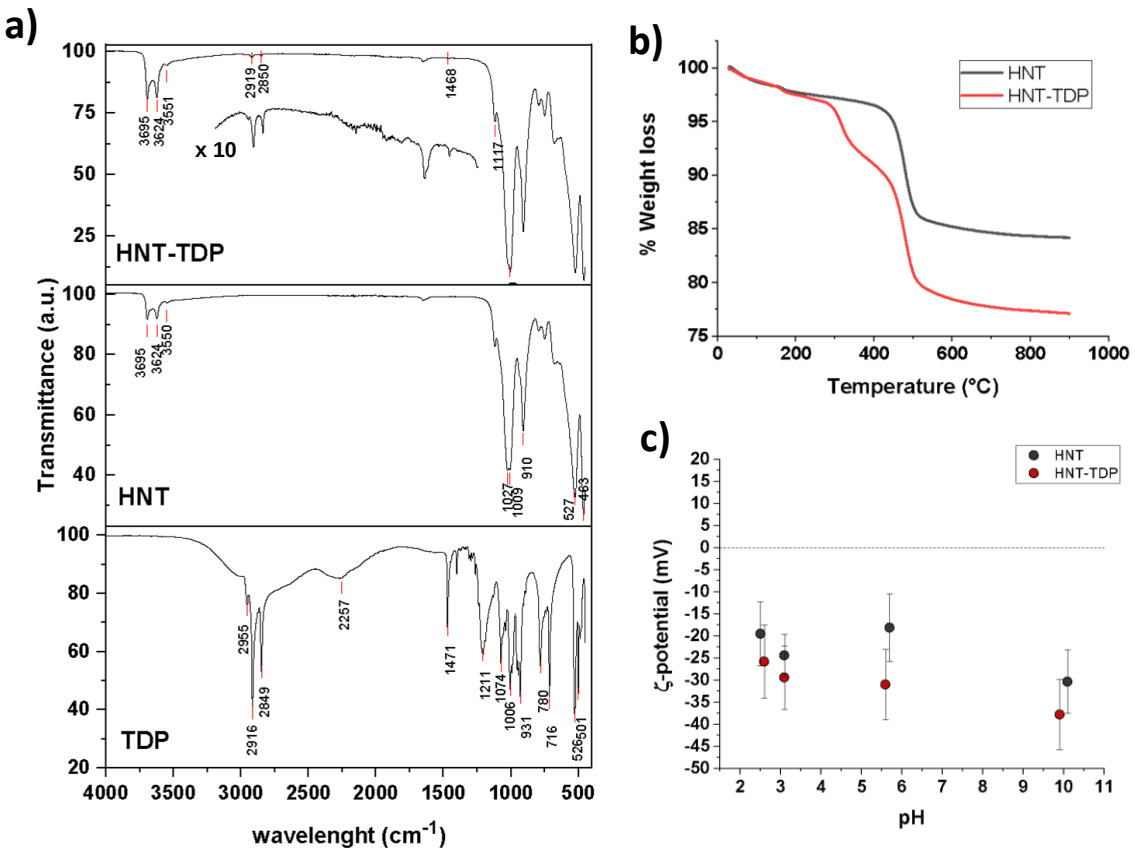

Figure 15 Characterization of the HNT-TDP (a) FTIR spectrum of HNT-TDP (top; the inset shows the magnified region of the spectrum containing signals of TDP) compared with the FTIR spectra of HNT (middle) and TDP (bottom); (b) thermogravimetric analysis (TGA) of pristine HNT and HNT-TDP derivative; (c) ζ-potential analyses of suspensions of HNT and HNT-TDP.

TGA analysis of HNT (black trace of **Figure 15b**) showed a mass loss step (ca. 2.5 %) corresponding to the loss of adsorbed water on surface (onset T = 45 °C) and into interlayer (onset T = 163 °C), and a second mass loss step (ca. 14.6%, onset T = 450 °C, inflection point at 480 °C) assigned to the dehydroxylation of structural AlOH groups of halloysites.[55] Differently, the TGA profile of HNT-TDP (red trace of **Figure 15b**) showed an extra mass loss step (ca. 5.4 %, onset T= 300 °C, inflection point at 320 °C) attributed to the degradation of TDP.

We carried out also the analysis of ζ-potential before and after the treatment with TDP and the obtained values as a function of pH are shown in **Figure 15c**. The observation of a more negative value for HNT-TDP is not only a further confirmation of the interaction of the HNT with the TDP but, indirectly, it also suggests the TDP localization is in the inner part of the nanotube. Indeed, if the phosphonic acid mostly interacts with the positively charged inner part, it neutralizes a portion of these charges, thus making slightly more negative the whole nanotube, as experimentally observed.

The preparation of SPION-in-HNT nanocomposite was achieved using SPION3@OA nanoparticles, obtained by the same thermal decomposition method[47] used previously (see **§ 2.1**), that this time afforded magnetic NPs with 6.1 ± 1.3 nm mean diameter as shown by transmission electron microscope (**Figure 16a**) and a hydrodynamic diameter of 10.9. ± 3.0 nm (**Figure 17**).

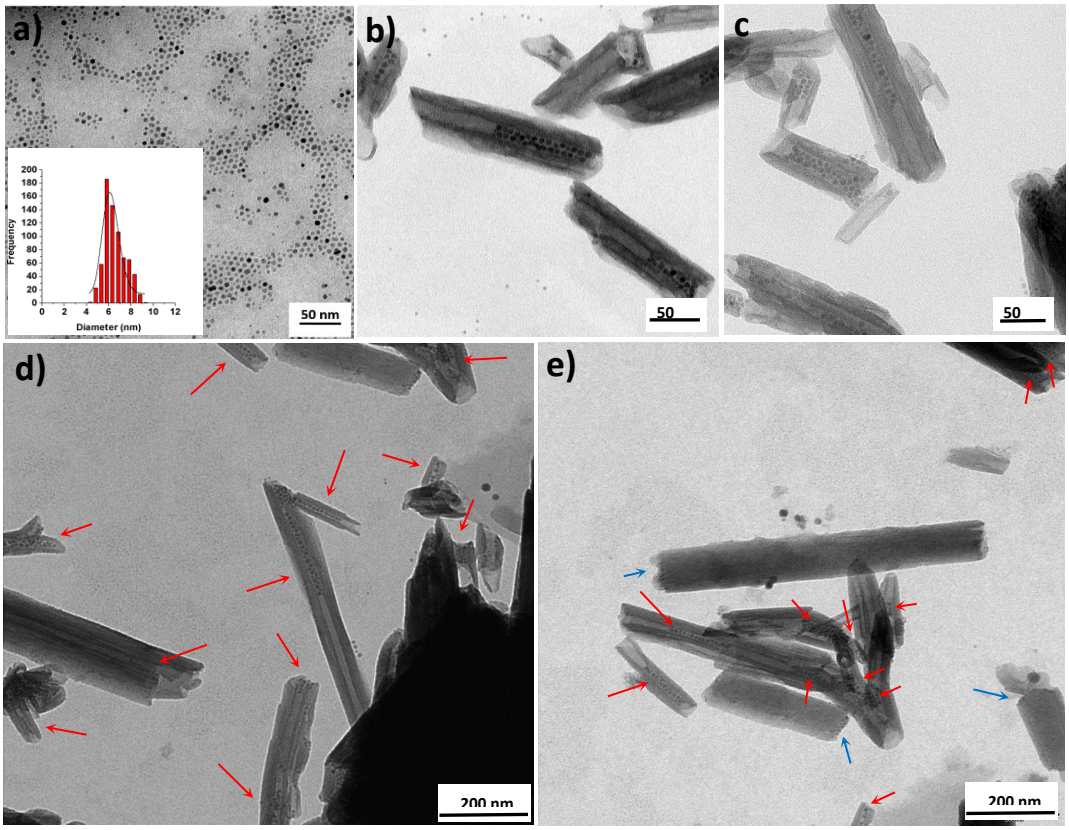

Figure 16 TEM micrographs of (a) as-synthesized SPION@OA (in the inset the SPION diameter distribution); (b-e) SPION-in-HNT prepared by pre-functionalization of HNT with TDP in the lumen. Panels (b) and (c) show images taken at higher magnification compared to (d) and (e). Red arrows mark the HNT containing SPION. Blue arrows indicate SPION at the edge of few HNT.

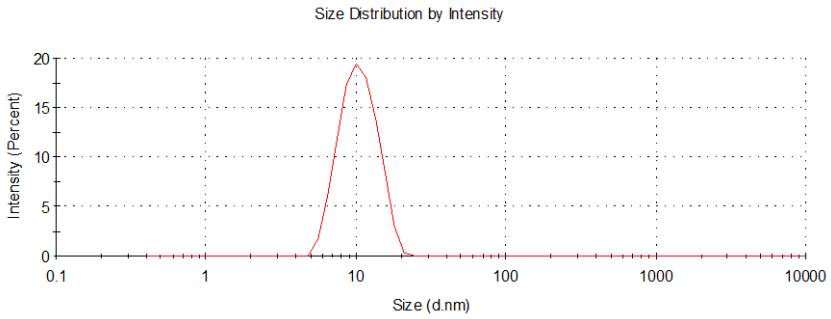

Figure 17. DLS of SPION3@OA suspended in n-hexane, synthesised by thermal decomposition and then used for the loading in the HNT-TDP.

The as-synthesized SPION@OA were effectively loaded into the HNT lumen by using repeated vacuum/N_2 cycles under stirring while keeping the temperature at 0 °C with an ice bath to avoid the heavy evaporation of the volatile solvent. The procedure was repeated until the light brown color of the suspension (due to SPION@OA) turned transparent, and conversely the deposited HNT turned from white to brown. The SPION loading was selectively directed into the inner part of HNT, without any relevant interaction with the HNT outer surface, as clearly shown by TEM analysis (**Figure 16b-e**). This result shows that the size and the nature of coating of SPION have a major role in successful loading into the inner lumen of

HNT. Despite the fact that SPIONs used in the electrostatic approach (**see above § 2.1**) were in the size range 5.1-6.9 nm, which is less than the half of the inner lumen diameter, no loading was observed when they were coated with DMSA or the other polar molecules. On the contrary, SPION@OA were able to reach the inner lumen probably mostly due to the apolar weak interactions between the aliphatic chains on NPs (OA) and in the inner lumen of the nanotubes (TDP). The TDP functionalization is also mandatory to observe the effective loading of SPION. Indeed, treating SPION3@OA with pristine HNT resulted in just sporadic loading into HNT, as clearly showed by TEM images (**Figure 18**).

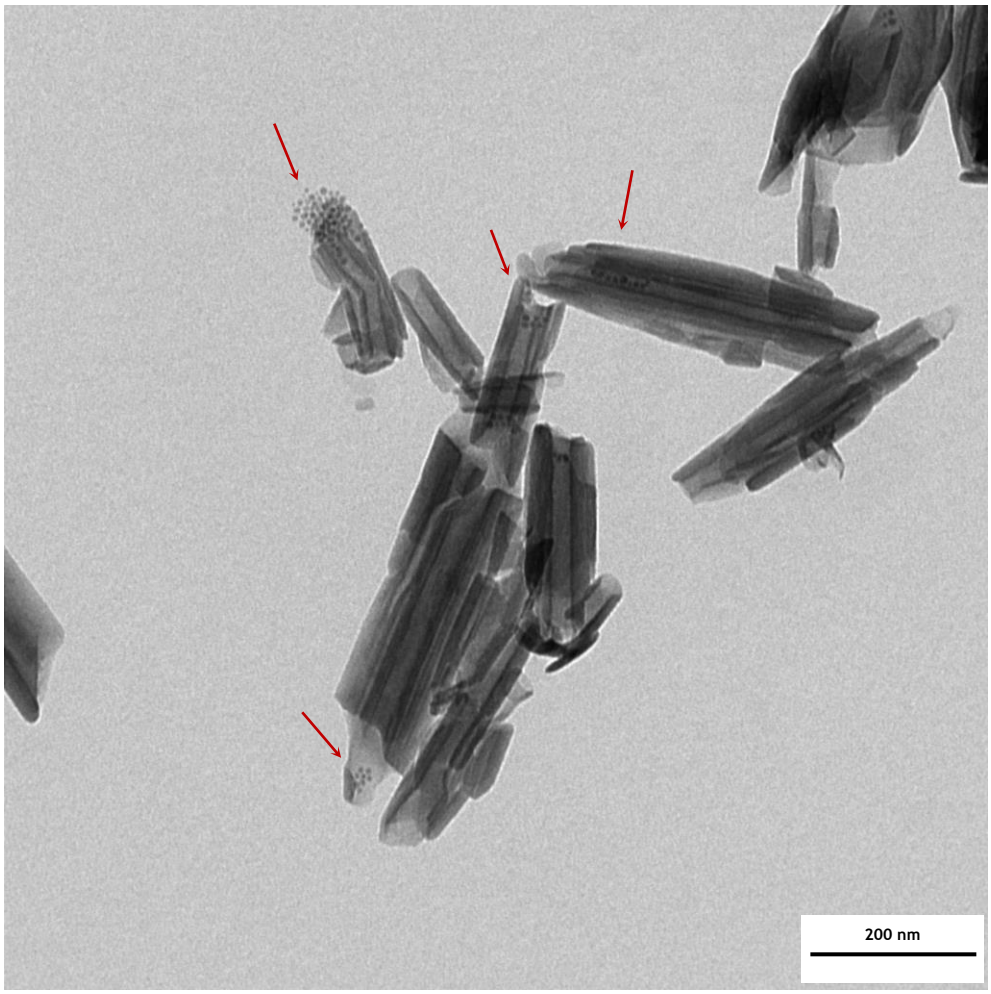

Figure 18. TEM micrograph of pristine HNT treated with SPION3@OA in n-hexane and with several repeated vacuum cycles. Red arrows indicate the sites of SPIONs accumulation.

Unfortunately, the commercial pristine HNT used in this work were of low quality if compared with other HNT deriving from other mines. In some images we evidenced the presence of unrolled HNT or kaolin-like sheets (see **Figure 19**). In **Figure 16e** there is a marked difference between the usual HNT, filled with SPION, that presents a lumen and walls clearly distinguishable (indicated with red arrows), and some peculiar HNT (highlighted with light blue arrows) that have a much larger diameter and do not show clearly the lumen, as if they are not empty, thus hampering the entrance of SPION. In this case some SPION interacted preferentially with the HNT edges rather than with the lumen. Moreover, when we tried to completely fill all the HNT by doubling the SPION amount, we noticed by TEM analysis (**Figure**

20) that only a part concurred to increase the amount of SPION into HNT, the remaining been captured by the kaolin-like sheets.

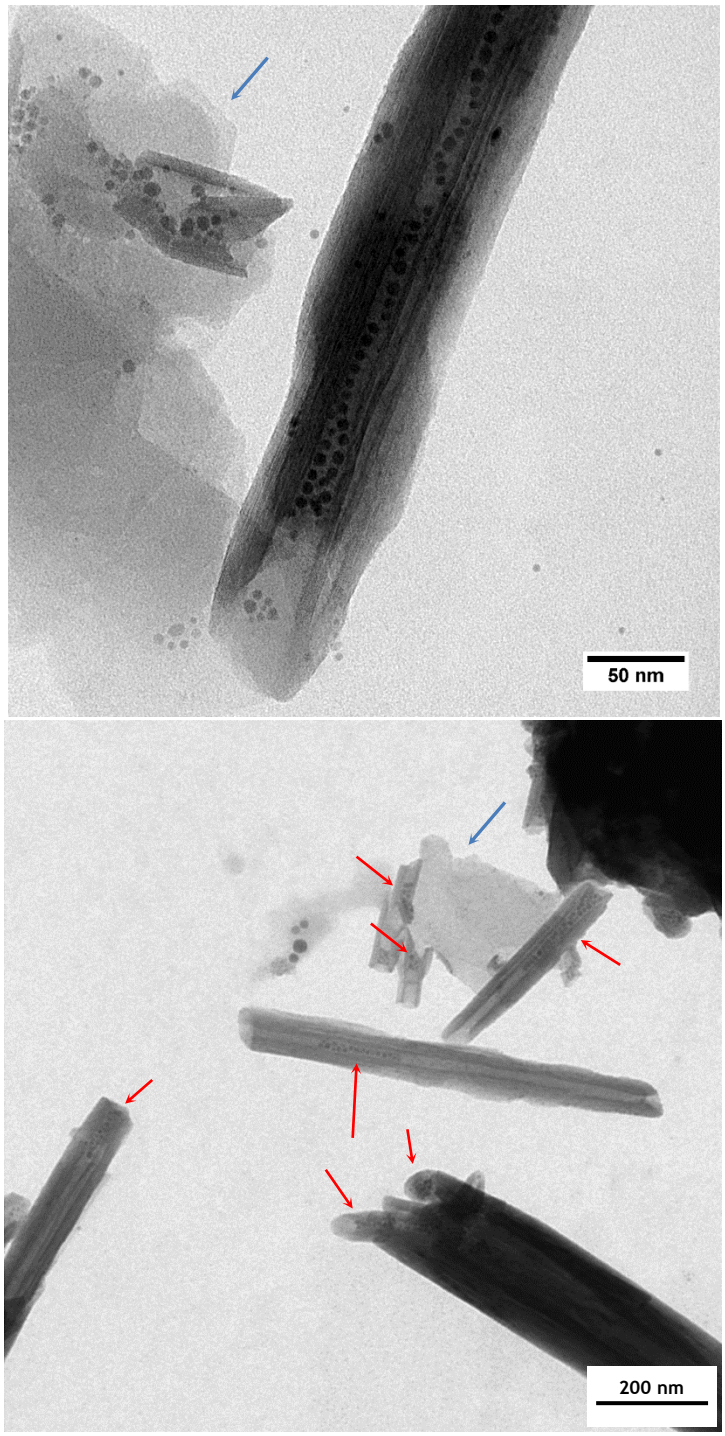

Figure 19. TEM micrographs of HNT-TDP treated with SPION3@OA in n-hexane and with several repeated vacuum cycles. Red arrows indicate the sites of SPIONs accumulation, while the light blue arrows indicate kaolin-like sheets.

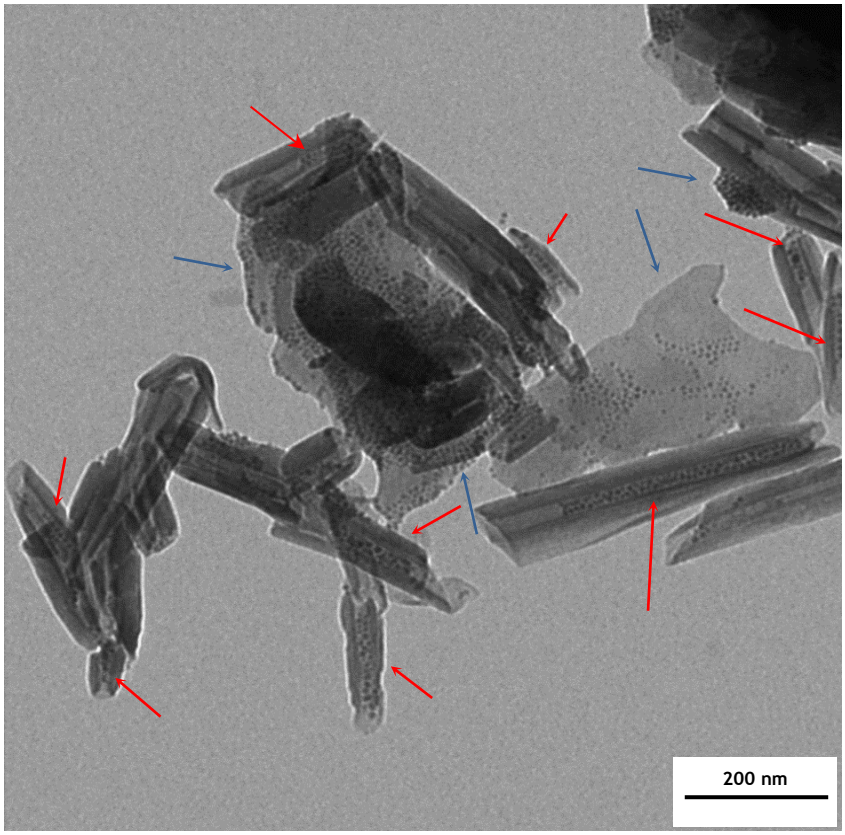

Figure 20. TEM micrographs of HNT-TDP treated with a double amount of SPION3@OA in n-hexane and with several repeated vacuum cycles. Red arrows indicate the sites of SPIONs accumulation, while the light blue arrows indicate kaolin-like sheets.

2.4 Australian HNT with a larger lumen filled with apolar SPION@OA.

Although very promising, the results obtained so far are not totally satisfying in terms of the amount of SPION embedded in the HNT. We ascribed this behaviour to the poor quality of the commercial HNT batch, containing some large and apparently filled HNT. To verify this hypothesis, we considered a new sample of HNT derived from the Camel Lake mine (Australia). These HNT are characterized by a higher regularity than Aldrich HNT (**Figure 21**), with a larger lumen (23.8 ± 6.0 nm), even though they are on average longer (770 ± 300 nm). As in the case of the commercial HNT, we made apolar the inner lumen of Australian HNT (A-HNT from now on) by a selective functionalization with TDP. Also in this case the SPION@OA were loaded selectively within the A-HNT@TDP, but only when a maximum amount of 0.4 mg SPION per 10 mg of HNT was used (**Figure 22**). As for the commercial HNT, the SPION did not fill completely the lumen. Nevertheless, when we tried to increase the SPION / HNT mass ratio, we found that SPION were massively localized also outside the lumen (**Figure 23**). At the same time, some semi-full or apparently empty HNT were visible, although the lumen of the A-HNT was on average wider, such as not to prevent the entrance of NPs of 5-6 nm diameter. We think that the ability of air to escape from the HNT is essential to fully fill a nanotube. Indeed, in some TEM images, air bubbles seem to be present within the inner lumen where SPION

were not localized (see **Figure 22**, blue arrows). Moreover, to be more effective in the removal of air contained in the HNT lumen, we applied a pre-vacuum cycle to the HNT before adding the SPION. In that case, we did not find a significant number of particles in the lumen, but all external to the HNT (**Figure 24**). This evidence made us conclude that the entry of SPION in the lumen takes place immediately after the break of the vacuum and the restoration of the ambient pressure in the reaction vessel.[43] Obviously, the proper concentration of NPs must be present to make the loading as effective as possible.

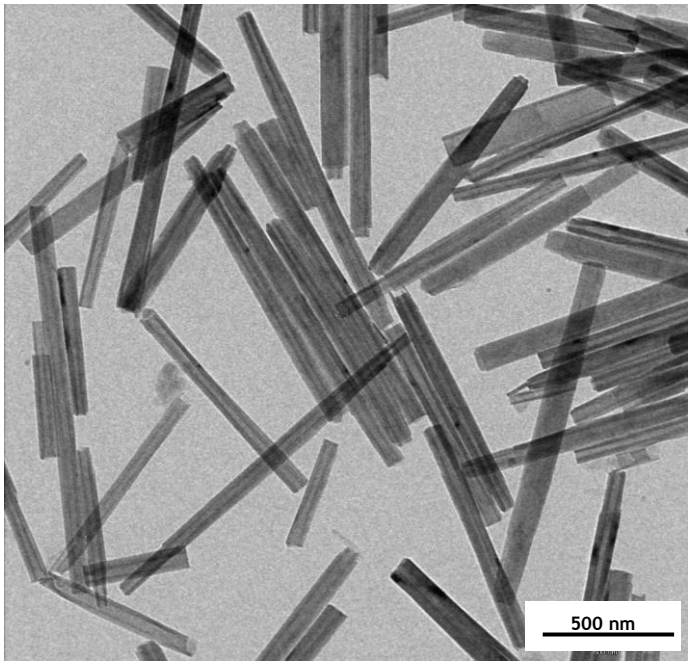

Figure 21. TEM micrographs of A-HNT (Australian HNT).

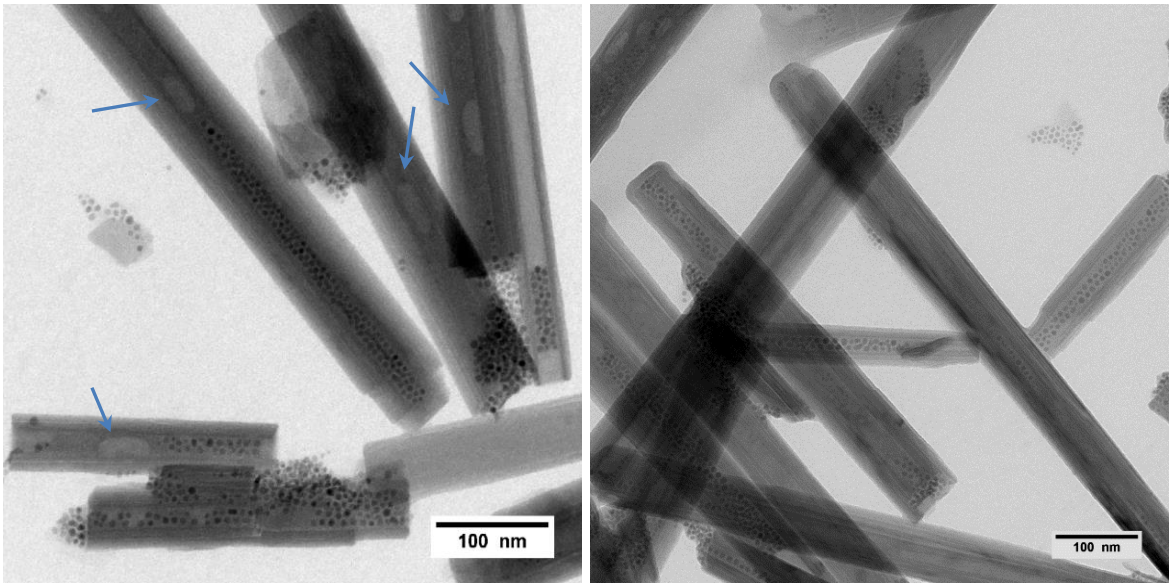

Figure 22 TEM micrographs of SPION-in-A-HNT (A-HNT= Australian Camel lake halloysites). Blue arrows mark the HNT containing possible air bubbles.

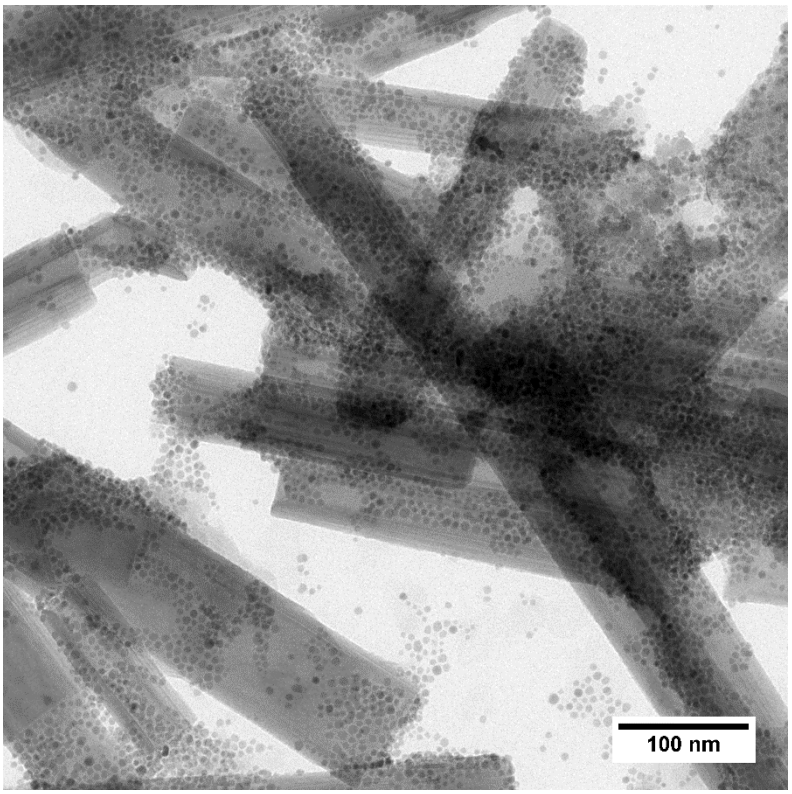

Figure 23. TEM micrographs of A-HNT-TDP treated with a double amount of SPION3@OA in n-hexane and with several repeated vacuum cycles.

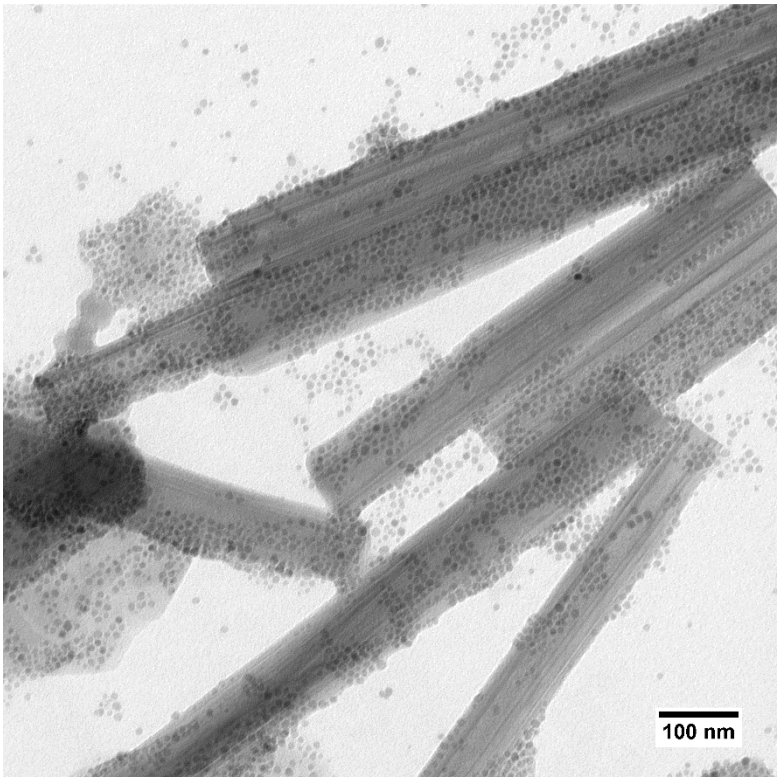

Figure 24. TEM micrographs of A-HNT-TDP subjected to a pre-vacuum-nitrogen cycle and then treated with SPION3@OA in n-hexane and with several repeated vacuum cycles.

2.5 Magnetic properties characterization of SPION-in-HNT nanocomposite.

Magnetic measurements performed on SPION and SPION-in-HNT demonstrated the nanoparticles display the typical superparamagnetic behaviour expected for a set of nanoparticles of this size and that the main magnetic properties have been maintained after the SPION embedding in HNT. The pristine SPION were measured as a hexane solution (SPION-sol) and dried powder (SPION-pow). This last measurement was also used to estimate and remove the diamagnetic contribution of the solvent, thus obtaining reliable magnetization saturation (M_S) value. The M_S of SPIONs was estimated as the magnetic moment recorded at the highest experimental field applied (50 kOe) divided by the iron content of SPION-sol evaluated by AAS analysis (2.2 % w/w). As expected for systems of reduced size, the M_S value of the SPIONs (72 emu/g Fe at 300 K and 82 emu/g Fe at 2.5 K) is lower than the bulk value of magnetite, but it is quite high for 6 nm nanoparticles, where, normally a considerable ratio of disordered spins at the surface to ordered spins in the core is observed.[56] The ZFC/FC magnetization curves (**Figure 25a**) evidenced the superparamagnetic behaviour of the samples, characterized by a maximum in the ZFC curve, the position of which determines, as a rough approximation the blocking temperature (T_B) of the system, and by thermal irreversibility at low temperature. It is interesting to note how the T_B of the pristine SPIONs increases from solution (18.8 K) to powder (32.3 K), while it reaches an intermediate value for SPION-in-HNT (29.3 K). The increase of T_B for a nanoparticle set measured in different conditions is generally ascribed to the enhanced inter-particle interactions.[57] In the case of SPION-sol and SPION-pow, for instance, the dipolar interactions are stronger in the powder sample as the NPs are much closer to each other compared to the solution sample. Assuming that the embedding procedure of SPIONs in HNT induced only negligible modification in the magnetic anisotropy of the pristine SPIONs (see **Figure 25a**), the value of T_B observed for HNT-SPION suggests that the embedded nanoparticles are moderately interacting, as it is between that of SPION-sol (low interactions) and SPION-pow (strong interactions), closer to the latter. This result is consistent with the expected confinement of the SPIONs in the HNT lumen, that implies a reduction of the mean distance among the SPIONs with respect to a diluted solution.

As expected for a superparamagnetic system, the samples present magnetic hysteresis only for temperature below T_B, as shown in **Figure 25b**, where the magnetization curves, M *vs* H, are reported. At low temperature (2.5 K), both samples exhibit similar coercivity (H_C = 370 Oe for SPIONs and H_C = 395 Oe for SPION-in-HNT) and remanence (34 and 32 emu/g Fe, for SPIONs and SPION-in-HNT, respectively), that reduce to zero at high temperature (300 K). The similarity of the curve shape acquired before and after HNT embedding confirms that the loading procedure does not alter significantly the magnetic properties of the pristine SPIONs. The maintenance of the magnetic properties allowed us to accurately estimate the concentration of SPIONs in the SPION-in-HNT simply by the ratio of the saturation magnetization of the two samples. Actually, in our case, the comparison is very accurate, as the same ratio is found at all the magnetic fields because the whole normalized magnetization curves are perfectly superimposable.[58] The iron concentration obtained by the superimposition of the curves at high temperature is 5.3 % w/w, which is very close to the concentration that would be achieved if all the SPIONs in the preparation solution were loaded in the HNT lumen (5.5 % w/w), corresponding to an encapsulation yield of 96 % and to a Fe_3O_4 % w/w of 7.3 %. Furthermore, the total magnetization of the SPION-in-HNT is enough (3.82

emu/g) to guarantee a magnetic response to an appropriate magnetic gradient, allowing the use of the compound in several practical applications. This result underlines the efficacy of the proposed NP embedding procedure.

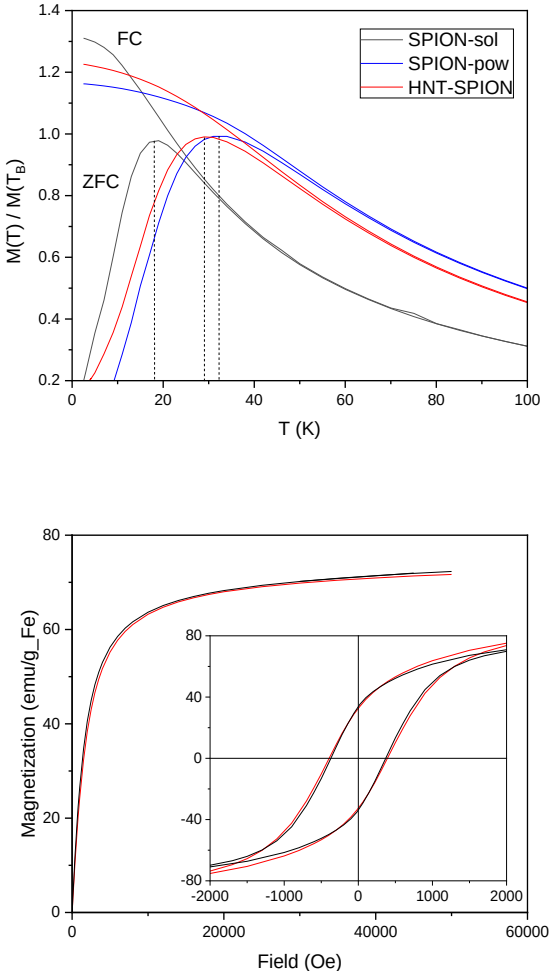

Figure 25 a) ZFC (lower curve) and FC (upper curve) magnetizations acquired with a 50 Oe field. The vertical dashed lines remark the position of the ZFC maxima corresponding to the blocking temperatures (T_B). For a better presentation, each curve was normalized to the magnetization value at the corresponding T_B; b) Magnetization curves at high (300 K, main panel) and low (2.5 K, inset) temperature for SPIONs (black line) and SPION-in-HNT (red line).

3 Conclusions

In summary, we have successfully prepared a novel magnetic halloysite nanocomposite with apolar SPIONs selectively loaded in the inner lumen of pre-functionalized HNT, exploiting vacuum-N_2 cycles. The new SPION-in-HNT nanocomposite has been morphologically characterized by TEM as well as from the magnetic point of view. SPION@OA in the inner lumen of HNT did not change their magnetic properties, retaining the superparamagnetic character at 300 K with a moderate inter-particle interaction once charged into the lumen of the nanotubes, and a sufficient total magnetization such that the SPION-in-HNT obtained with this embedding procedure can respond to an external magnetic stimulus. The SPION-in-HNT

nanocomposite was successfully obtained also using HNT of different source (A-HNT) endowed with a bigger lumen diameter.

Despite this more favorable characteristic for the NP loading, even in this case the NPs did not completely filled all the HNT, suggesting that, rather than the size of the nanoparticles, it is the ability to release the initial air contained in the nanotubes to play a fundamental role in allowing the NP to enter.

Attempts to load pre-formed negatively charged SPIONs, exploiting the opposite charges of the HNT lumen, failed due to an early aggregation of the single NPs once subjected to an external force, which pushed them at the entrance of the lumen.

Finally, the procedure here proposed could be used as a general method for the loading of other kinds of inorganic nanoparticles stabilized with a hydrophobic layer. Depending on the nature of the loaded NPs the applications could span from catalysis to drug delivery or to waste water treatment, just to mention a few.

4 Experimental Part

4.1 Materials and instruments.

Anhydrous $FeCl_3$ and $FeCl_2 \cdot 4H_2O$ (Merck Germany), ethanol 99.8% (Merck UK), oleic acid 90% (Alfa Aesar), n-hexane 96% and acetone (Scharlau), iron acetyl acetonate 97%, 1,2 hexadecandiol 90%, Tetradecylphosphonic acid 97%, DMSA 98%, triethylamine 99%, 16-Phosphonohexadecanoic acid 97%, Protocatechuic acid 97%, Gallic acid >97.5 %, Tetramethylammonium hydroxide pentahydrate 97%, Sodium hydroxide pellets 98%, Oleylamine 70%, diphenyl ether 99%, benzyl ether 98% and halloysite nanotubes HNT (Sigma Aldrich), Australian halloysite clay (A-HNT) provided by prof. John L. Keeling from Camel Lake (Australia), Nile red >99% (Abcr) were all used as received without further purification. Toluene (99.5%, Sigma Aldrich) was distilled from sodium under nitrogen before use. Ultrapure milli-Q water (Millipore, resistivity=18M Ω cm^{-2}) was used for the preparation of the aqueous solutions.

ζ-potential measurements were carried out using a Malvern Zetasizer nano ZS instrument equipped with a 633 nm solid state He–Ne laser at a scattering angle of 173°, typically dissolving samples at a concentration of 1 mg/mL or less at 25 °C. The measurements were averaged on at least three repeated runs.

Iron content on SPION was determined by different methods. AAS analysis was carried out on a Perkin-Elmer Pinaacle 900 instrument for SPION6@OA. For all the other preparations, a spectrophotometric method was employed on an Agilent model 8543 spectrophotometer at room temperature and using disposable cuvettes with 1.0 cm path length. For Fe determination by AAS, few microliters of the particle suspension were digested with 1 mL aqua regia/HCl overnight at room temperature in a 10 mL volumetric flask, and subsequently filled up with MilliQ water. For spectrophotometric analyses few microliters of the particle suspensions were digested with 1 mL aqua regia/HCl at room temperature in a 10 mL volumetric flask. Subsequently, they were filled up with (i) 0.1 mL NH_2OH solution (10% w/w), (ii) 6 mL acetate buffer solution (pH 4.6, 0.15M), (iii) 0.2 mL 1,10-phenantroline solution (0.6% w/w, H_2O/MeOH 10 : 1) (iv) milliQ water until the volume of 10 mL was reached. The absorbance of the band centered at 510 nm due to $Fe(phen)_3^{2+}$ complex was then measured and the concentration of Fe was finally obtained, acquiring a calibration curve, which was obtained with standards prepared with the same procedure starting from a commercial AAS standard solution.

Thermogravimetric analysis (TGA) was carried out in air atmosphere and in the temperature range 50–800 °C with a heating rate of 5 °C·min^{-1}, using a Mettler-Toledo thermogravimetric balance (TGA/DSC 2 Star® System) on ca 10 mg of lyophilized samples.

ATR-FTIR spectra were acquired on a PerkinElmer Frontier instrument equipped with an ATR accessory with a diamond/ZnSe crystal. The IR spectra were registered between 4000 and 400 cm^{-1}.

Transmission Electron Microscopy (TEM) TEM micrographs were collected using a Zeiss Libra 200 FE instrument equipped with an in column pre-aligned omega filter that improves the contrast and a Schottky field emission gun at 200 kV. Alternatively, TEM images were collected using an EFTEM LEO 912AB (Zeiss) at 100 kV. Samples were prepared by dropping a dilute solution of the samples onto 200 mesh carbon-coated copper grids, and after blotting the excess of water, the samples were let drying at least for 24 h in air. The nanoparticle size was measured by Pebbles and Pebbles-Juggler[59] or by Image-J free software. Imaging Platform software (Olympus). For each sample the measured NPs were around 400.

Magnetic measurements were carried out by a SQUID magnetometer from Quantum Design Ltd. Powder samples (SPION-pow and SPION-in-HNT) were prepared by enclosing a small amount of powder in a Teflon tape; solution sample (SPION-sol) was measured in a gel cap. The diamagnetic contribution of Teflon was found negligible, while that of the cap and solvent was evaluated as the magnetization component, linear with the magnetic field, needed to be added to the SPION-sol magnetization in order to obtain the same slope of the SPION-pow curve in the high field region. The magnetization curves were obtained by acquiring the magnetic moment of the sample as a function of the applied magnetic field ranging from 0 to ±50 kOe, at low (2.5 K) and room temperature (300 K). The Zero Field Cooled (ZFC) and Field Cooled (FC) magnetizations were acquired as a function of the temperature applying a 50 Oe probe field after cooling the sample in the absence (ZFC) and presence (FC) of the probe field.

4.2 Synthesis of magnetic nanoparticles and attempts for their loading in the HNT lumen through the electrostatic approach.

SPION@OA and their derivatives after ligand exchange with DMSA, GA, PA and TMAOH are described in the Supporting Information, together with the loading attempts of these negatively charged SPION in HNT and the one-pot procedure with thermal decomposition synthesis of SPION in the presence of HNT.

4.2.1 Synthesis of SPION1@OA by a coprecipitation method in a biphasic system with NaOH.

The synthesis was carried out by following a slightly modified literature procedure.[46] Briefly, in a two-neck round-bottom flask, sodium oleate (4 mmol, 1.218 g), anhydrous $FeCl_3$ (1 mmol, 0.162 g), $FeCl_2{\cdot}4H_2O$ (0.5 mmol, 0.099 g) and NaOH (3mmol, 0.122 g) were dissolved in a mixture of deoxygenated water (by bubbling N_2 gas for 30 min, 3.0 mL), ethanol (3 mL) and toluene (5.25 mL) under nitrogen. The mixture was refluxed at 74 °C for 4 h. Then the final black mixture was left to return to room temperature by removing the heat source. The suspension was precipitated with ethanol and the sediment was isolated by magnetic decantation. The precipitate was dispersed in toluene and centrifuged for 10 min at 7142 rcf to remove all the undispersed residues. The black toluene dispersion was precipitated with ethanol again and the solvent was removed through magnetic separation. Finally, SPIONs were redisposed in 40 mL toluene to form stable colloids and stored under nitrogen at -23 °C for further uses. Fe content by UV-vis spectroscopy was 3.3 mg/mL.

4.2.2 Synthesis of SPION2@OA by a coprecipitation method in a biphasic system without NaOH.

The synthesis was carried out by following the same procedure already reported previously, but in the absence of NaOH.[46] Briefly, in a two-neck round-bottom flask, sodium oleate (8 mmol, 2.44 g), anhydrous $FeCl_3$ (1 mmol, 0.162 g), and $FeCl_2 \cdot 4H_2O$ (0.5 mmol, 0.099 g) were dissolved in a mixture of deoxygenated water (by bubbling N_2 gas for 30 min, 2.25 mL), ethanol (3 mL) and toluene (5.25 mL) under nitrogen atmosphere. The mixture was refluxed at 74 °C for 4 h. Then, the work-up, the recovery and the final storage of the NPs was as for the NPs obtained for coprecipitation in a biphasic system in the presence of NaOH. Fe content by UV-vis spectroscopy was 4 mg/mL.

4.2.3 Synthesis of SPION3@OA by a thermal decomposition method.

The synthesis was carried out by following a slightly modified literature procedure.[47] Birefly, in a two-neck round-bottom flask, $Fe(acac)_3$ (0.353 g, 1 mmol), 1,2-hexadecanediol (1.435 g, 5 mmol), oleic acid (0.952 mL, 3 mmol), and 0.987 mL of oleylamine (3 mmol) were dissolved in 10 mL phenyl ether by magnetic stirring for 10 min under a nitrogen atmosphere. After having removed the magnetic stirrer, the mixture was heated at 15 °C/s from room temperature to 200 °C and left at this final temperature for 35 min. Then, under a blanket of nitrogen, the mixture was further heated up to 265 °C at 15 °C/s and left at this temperature for 35 min. Finally, the black-brown mixture was naturally cooled by removing the heat source to room temperature. The so-obtained suspension was precipitated with ethanol (20 mL), then the black precipitate was separated via centrifugation (10 min at 4226 rcf), then it was dissolved in 20 mL n-hexane in the presence of oleic acid (0.05 mL) and oleylamine (0.05 mL). Centrifugation (10 min at 4226 rcf) was applied to remove any undispersed residue. The SPION@OA were then re-precipitated with 40 mL ethanol, centrifuged (10 min at 4226 rcf) to remove the solvent, then re-dispersed in 15 mL n-hexane and stored under nitrogen at -23 ^{O}C for further uses. Fe content by AAS was 2.2 mg/mL.

4.2.4 Synthesis of SPION4@OA by a thermal decomposition method.

The synthesis was carried out by following a slightly modified literature procedure.[48] Briefly, in a two-neck round-bottom flask, iron-oleate (1.37 g, 1.53 mmol), 1,2-hexadecanediol (1.185 g, 4.596 mmol) and oleic acid (0.448 mL, 1.41 mmol) were dissolved in 7.14 mL diphenyl ether by magnetically stirring for 10 min under a nitrogen atmosphere. The mixture was degassed at 90 °C under vacuum and stirring for 2 h. The mixture was then heated at 10 °C/min from 90 to 260 °C, and left at this final temperature for 30 min under nitrogen. Finally, the black-brown mixture was rapidly cooled by removing the heat source, and water bath till reach to room temperature. The so-obtained suspension was precipitated with acetone (50 mL), and the black precipitate was separated via centrifugation (10 min at 4226 rcf). After that, it was dissolved in 10 mL n-hexane, re-precipitated with 50 mL ethanol, centrifuged (10 min at 4226 rcf), re-dispersed in 35 mL n-hexane, and finally stored under nitrogen at -23 ^{O}C for further uses. Fe content by UV-vis spectroscopy = 1.9 mg/mL.

4.2.5 Ligand exchange OA/DMSA (SPION1@DMSA, SPION2@DMSA, and SPION3@DMSA).

The ligand exchange procedure was carried out following a procedure developed by some of us. [50] A sample of SPION@OA suspended in n-hexane containing a total amount of 5 mg Fe (1.5 mL SPION1, 1.25 mL SPION2, and 2.3 mL SPION3) was treated with 4 mL of acetone and centrifuged (4 min 7197 rcf) to remove the excess of oleic acid. The nanoparticles were re-suspended in 9 mL n-hexane and transferred in a Schlenk tube under nitrogen atmosphere.

To this suspension a solution of DMSA dissolved in acetone (50 mg in 9 mL) was added, followed by 15 µL of triethylamine (TEA). The suspension in the Schlenk tube was then moved to an ultrasonic bath and the reaction mixture was kept at 54 °C for 40 min, maintaining the suspension under nitrogen atmosphere for the whole sonication time. The SPION were then collected with a magnet, re-suspended in 20 mL of acetone and centrifuged for 10 min at a rate of 7197 rcf. The last wash was carried out by re-suspending the pellet in 20 mL of milliQ water and centrifuged again (30 min, 7197 rcf). The washed SPION were finally re-suspended in 10 mL of milliQ water and stored under nitrogen atmosphere at 4 °C or at room temperature for further uses.

4.2.6 Ligand exchange OA/GA (SPION4@GA). [15]

A sample of SPION@OA suspended in n-hexane (2.6 mL, 5 mg/mL Fe) was re-dispersed in 10 mL toluene. Gallic acid (GA) (43.2 mg, 0.254 mmol) was dissolved in a mixture of 110 µL pyridine and 322 µL toluene under 5 min sonication. Then, GA solution was added dropwise into SPION suspension, and the SPIONs precipitated immediately. The SPION@GA were then recovered by a permanent magnet and the supernatant was removed. The magnetic pellet was then re-suspended in 10 mL of 1% sodium carbonate solution, then SPION@GA were washed by adding an excess of ethanol (20 mL) and collecting the precipitating SPIONs by centrifugation (7197 rcf, 2 min). The pellet was then re-suspended in 3 mL water, precipitated again by adding ethanol and collected by centrifugation (7197 rcf, 2 min). Then, the resulting SPION@GA pellet was easily re-dispersed in 10 mL water, and stored at 4 °C for further uses. The same procedure has been used for the exchange OA/PA.

4.2.7 Ligand exchange OA/TMAOH (SPION4@TMAOH). [51]

A sample of SPION@OA was suspended in n-hexane (2.6 mL, 5 mg/mL Fe) and dried under N_2 stream in a glass vial. The solid residue was treated with an aqueous solution $TMAOH \cdot 5H_2O$ (1.25 mL 1.1 M) and ultra-sonicated at 54 °C for 40 min for re-disperse the SPION@TMAOH. After sonication, the suspension was diluted with 10 mL MilliQ water and further sonicated affording a clear brown suspension (final concentration of Fe_3O_4@TMAOH 0.5 mg /mL).

4.2.8 Attempts to load SPION@DMSA into HNT lumen.

Water suspended SPION@DMSA (0.5 mg/mL) at pH 3-4 was mixed with 1 mL of HNT water suspension (10 mg) at the same acid pH value. The mixture was sonicated for 15 min, shaken on a vortex for 10 min, and then the suspension subjected to reduced pressure (30 mmHg) for 30 min at room temperature. The sonication vacuum process was repeated for 5 times, giving rise to a brown HNT adduct affected by an external magnet, which was recovered by centrifugation (3 min, 470 rcf). The same procedure was used for the attempts of loading of the other SPION (SPION@GA, SPION@PA, SPION@TMAOH).

4.3 One-pot procedure with thermal decomposition synthesis of SPION in the presence of HNT.

The synthesis was carried out by following a slightly modified literature procedure, [47] and in the presence of HNT. Birefly, in a two-neck round-bottom flask, under nitrogen atmosphere, $Fe(acac)_3$ (0.353 g, 1 mmol) and HNT (0.706 g) were added to benzyl ether (10 mL) such that the mass ratio Fe: HNT was 1:2. The mixture was magnetically stirred for 10 min, then sonicated for 15 min and subjected to a reduced pressure (~ 1-2 mmHg) under stirring for 30 min. The sonication-vacuum-N_2 cycle was repeated for 2 times more. Finally, 1.435 g of 1,2-hexadecanediol (5 mmol) together with 0.952 mL of oleic acid (3 mmol) and 0.987 mL of oleylamine (3 mmol) were added and mixed under inert atmosphere. The magnetic stirrer was removed and the mixture heated from room temperature to 200 °C at a heating rate of 15 °C/s. Then, the mixture was left at 200 °C for 2 h, and then further heated up to 300 °C at the same rate as before and left at this final temperature for 1 h. At the end of the heating period

the black-dark brown mixture was left to cooling down naturally to room temperature by removing the heat source. The so-obtained suspension was precipitated with ethanol (20 mL), then the black precipitate was recovered by centrifugation (10 min at 4226 rcf). The precipitate was re-suspended in 20 mL n-hexane adding also 50 µL oleic acid and 50 µL oleylamine. Centrifugation (10 min at 4226 rcf) was applied to remove possible free SPION or SPION externally interacting with the HNT. The SPION-in-HNT product was treated with ethanol, and centrifuged again (4226 rcf, 10 min) to remove all the high-boiling solvent or the surfactant excess. Then the solid was re-dispersed in 35 mL n-hexane and left under nitrogen atmosphere. After 2 days of decantation, the black supernatant containing free SPION@OA was carefully removed. The solid residue was dried under vacuum and grinded, thus obtaining a grey and magnetic precipitate.

4.4 Modification of Halloysite Lumen with Tetradecylphosphonic acid (HNT-TDP).[53]

Halloysites (250 mg) were added under stirring to a solution of TDP (0.27837 g, 1 mmol) in 250 mL of 4:1 EtOH: H_2O. The EtOH: H_2O solution was adjusted to pH 4 with HCl 0.1 M. The halloysite suspension was transferred to a 500 mL flask, which was then evacuated using a vacuum-pump. The fizzing of the suspension indicated that air was removed from the halloysite lumen and replaced with TDP solution. The vacuum/nitrogen cycles were repeated 3 times in order to maximize TDP loading. After stirring for a week at room temperature, the modified halloysites were rinsed with EtOH:H_2O for 5 times and recovered by centrifugation, and finally dried at 100 °C overnight under vacuum. The TDP excess was recovered from the gathered supernatants and stored for the next functionalization process. After the functionalization process, colloidal stability of HNT-TDP aqueous suspension was similar to that of untreated HNT at the same pH, indicating that the outermost surface of the clay nanotubes was not hydrophobized. Recovered HNT-TDP ca 250 mg.

4.5 Attempt to Load SPION into unmodified pristine HNT lumen (SPION@OA-in-HNT).

In a Schlenk tube a sample of SPION3@OA (0.5 mL, 2.2 mg/mL) were mixed with 20 mg HNT in 20 mL n-hexane. The suspension was shaken for 1 min by a vortex, then it was cooled at 0 °C, and while standing in the ice bath, it was placed under reduced pressure and magnetic stirring until the solvent was visibly reduced. Then, another 20 mL n-hexane was added. After 1 h of the cycle reducing pressure, the brown color of the supernatant due to the magnetic NPs remained unchanged with respect to the starting color. The HNT/SPION were recovered by centrifugation (3 min, 470 rcf), the supernatant removed and the precipitate washed with 5 mL n-hexane.

4.6 Qualitative assay for lumen hydrophobicity by Nile Red dye.

Nile Red (1 mg, 3.1×10^{-3} mmol) was dissolved in 10 mL ethanol and left under stirring until the compound was completely dissolved. Then, HNT-TDP (20 mg) were added to the alcohol dye solution and the flask was cooled at 0 °C before reducing the pressure by a mechanical pump and leaving the mixture for 2 h. The halloysites were recovered by centrifuging at 4226 rcf for 10 min. The blue-violet pellet was separated from the supernatant and washed with water and recovered by centrifugation. After HNT were dried, the recovered pellet appeared blue under visible light and red-emissive under UV-lamp irradiation. The very same procedure was followed for the loading of Nile Red in pristine HNT. After the washing of the treated HNT with water, the color under visible light irradiation was blue-violet, whilst under UV light irradiation no light emission was detected.

4.7 Preparation of HNT-TDP with SPION selectively loaded in the HNT lumen (SPION@OA-in-HNT-TDP).

In a Schlenk tube SPION3@OA (3.75 mL, 2.2 mg/mL) were mixed with 150 mg HNT-TDP in 150 mL n-hexane. The suspension was shaken for 1 min by a vortex, then the suspension was cooled at 0 °C, and while standing in the ice bath, it was placed under reduced pressure and magnetic stirring until the solvent was visibly reduced. Then, another 150 mL n-hexane were added. The color of the supernatant turned clearer with respect to the beginning (from light brown to beige). The cycle of reduced pressure under stirring was repeated once more, until the supernatant appeared completely clear (about 3 h). The HNT-TDP/SPION were recovered by centrifugation (3 min, 470 rcf), the supernatant removed and the precipitate washed with 5 mL n-hexane.

4.8 Pre-treatment of the HNT mineral to obtain purified HNT in powder.

A piece of mineral clay was cut in thin slices, keeping the part of clay as white as possible. Slices were dried at 50 °C for 1 h. Then, the slices were gently hand-grinded in a mortar. To remove the soluble impurities, 2 g of powder was dispersed in 20 mL distilled water, followed by sonication for 20 min, 20 min stirring, then centrifuge 117 rcf for 20 min. Then, the slurry was re-dispersed in 500 mL distilled water after the pH was adjusted at ca. 7 to achieve a good suspension. The suspension was left to settle down the non-dissolved impurities, then the supernatant containing HNT was transferred in another vial. The adjustment of pH at slightly acidic values (≈4-5) caused the flocculation of HNT. The supernatant was discarded and HNT slurry dried at 60-80 °C, and grinded in a mortar to give a white powder ready for further uses.

5. Bibliography

(1) Vergaro, V.; Abdullayev, E.; Lvov, Y. M.; Zeitoun, A.; Cingolani, R.; Rinaldi, R.; Leporatti, S. Cytocompatibility and Uptake of Halloysite Clay Nanotubes. *Biomacromolecules* **2010**, *11* (3), 820–826. https://doi.org/10.1021/bm9014446.

(2) Szpilska, K.; Czaja, K.; Kudła, S. Halloysite Nanotubes as Polyolefin Fillers. *Polimery* **2015**, *60*, 359–371. https://doi.org/10.14314/polimery.2015.359.

(3) Massaro, M.; Cavallaro, G.; Colletti, C. G.; Lazzara, G.; Milioto, S.; Noto, R.; Riela, S. Chemical Modification of Halloysite Nanotubes for Controlled Loading and Release. *J. Mater. Chem. B* **2018**, *6* (21), 3415–3433. https://doi.org/10.1039/C8TB00543E.

(4) Lvov, Y.; Wang, W.; Zhang, L.; Fakhrullin, R. Halloysite Clay Nanotubes for Loading and Sustained Release of Functional Compounds. *Adv. Mater.* **2016**, *28* (6), 1227–1250. https://doi.org/https://doi.org/10.1002/adma.201502341.

(5) Satish, S.; Tharmavaram, M.; Rawtani, D. Halloysite Nanotubes as a Nature's Boon for Biomedical Applications. *Nanobiomedicine* **2019**, *6*, 1849543519863625–1849543519863625. https://doi.org/10.1177/1849543519863625.

(6) Lee, Y.; Jung, G.-E.; Cho, S. J.; Geckeler, K. E.; Fuchs, H. Cellular Interactions of Doxorubicin-Loaded DNA-Modified Halloysite Nanotubes. *Nanoscale* **2013**, *5* (18), 8577–8585. https://doi.org/10.1039/C3NR02665E.

(7) Tully, J.; Yendluri, R.; Lvov, Y. Halloysite Clay Nanotubes for Enzyme Immobilization. *Biomacromolecules* **2016**, *17* (2), 615–621. https://doi.org/10.1021/acs.biomac.5b01542.

(8) Lun, H.; Ouyang, J.; Yang, H. Natural Halloysite Nanotubes Modified as an Aspirin Carrier. *RSC Adv.* **2014**, *4* (83), 44197–44202. https://doi.org/10.1039/C4RA09006C.

(9) Kırımlıoğlu, G. Y.; Yazan, Y. Development, Characterization and in Vitro Release Characteristics of Rabeprazole Sodium in Halloysite Nanotubes. *Eur Int J Sci Technol* **2016**, *5*, 99–109.

(10) Long, Z.; Zhang, J.; Shen, Y.; Zhou, C.; Liu, M. Polyethyleneimine Grafted Short Halloysite Nanotubes for Gene Delivery. *Mater. Sci. Eng. C* **2017**, *81*, 224–235. https://doi.org/https://doi.org/10.1016/j.msec.2017.07.035.

(11) Shi, Y.-F.; Tian, Z.; Zhang, Y.; Shen, H.-B.; Jia, N.-Q. Functionalized Halloysite Nanotube-Based Carrier for Intracellular Delivery of Antisense Oligonucleotides. *Nanoscale Res. Lett.* **2011**, *6* (1), 608. https://doi.org/10.1186/1556-276X-6-608.
(12) Liu, J.; Zhang, Y.; Zeng, Q.; Zeng, H.; Liu, X.; Wu, P.; Xie, H.; He, L.; Long, Z.; Lu, X.; Xiao, M.; Zhu, Y.; Bo, H.; Cao, K. Delivery of RIPK4 Small Interfering RNA for Bladder Cancer Therapy Using Natural Halloysite Nanotubes. *Sci. Adv.* **2019**, *5* (9), eaaw6499. https://doi.org/10.1126/sciadv.aaw6499.
(13) El-Boubbou, K. Magnetic Iron Oxide Nanoparticles as Drug Carriers: Preparation, Conjugation and Delivery. *Nanomedicine* **2018**, *13* (8), 929–952. https://doi.org/10.2217/nnm-2017-0320.
(14) Ruiz, A.; Morais, P. C.; Bentes de Azevedo, R.; Lacava, Z. G. M.; Villanueva, A.; del Puerto Morales, M. Magnetic Nanoparticles Coated with Dimercaptosuccinic Acid: Development, Characterization, and Application in Biomedicine. *Journal of Nanoparticle Research*. 2014. https://doi.org/10.1007/s11051-014-2589-6.
(15) Hao, R.; Yu, J.; Ge, Z.; Zhao, L.; Sheng, F.; Xu, L.; Li, G.; Hou, Y. Developing Fe3O4 Nanoparticles into an Efficient Multimodality Imaging and Therapeutic Probe. *Nanoscale* **2013**, *5* (23), 11954–11963. https://doi.org/10.1039/C3NR04157C.
(16) Huh, Y.-M.; Jun, Y.; Song, H.-T.; Kim, S.; Choi, J.; Lee, J.-H.; Yoon, S.; Kim, K.-S.; Shin, J.-S.; Suh, J.-S.; Cheon, J. In Vivo Magnetic Resonance Detection of Cancer by Using Multifunctional Magnetic Nanocrystals. *J. Am. Chem. Soc.* **2005**, *127* (35), 12387–12391. https://doi.org/10.1021/ja052337c.
(17) Grillone, A.; Ciofani, G. Magnetic Nanotransducers in Biomedicine. *Chem. – A Eur. J.* **2017**, *23* (64), 16109–16114. https://doi.org/10.1002/chem.201703660.
(18) Zhang, L.; Dong, W.-F.; Sun, H.-B. Multifunctional Superparamagnetic Iron Oxide Nanoparticles: Design, Synthesis and Biomedical Photonic Applications. *Nanoscale* **2013**, *5* (17), 7664–7684. https://doi.org/10.1039/C3NR01616A.
(19) Mazuel, F.; Espinosa, A.; Luciani, N.; Reffay, M.; Le Borgne, R.; Motte, L.; Desboeufs, K.; Michel, A.; Pellegrino, T.; Lalatonne, Y.; Wilhelm, C. Massive Intracellular Biodegradation of Iron Oxide Nanoparticles Evidenced Magnetically at Single-Endosome and Tissue Levels. *ACS Nano* **2016**, *10* (8), 7627–7638. https://doi.org/10.1021/acsnano.6b02876.
(20) Nosrati, H.; Salehiabar, M.; Fridoni, M.; Abdollahifar, M.-A.; Kheiri Manjili, H.; Davaran, S.; Danafar, H. New Insight about Biocompatibility and Biodegradability of Iron Oxide Magnetic Nanoparticles: Stereological and In Vivo MRI Monitor. *Sci. Rep.* **2019**, *9* (1), 7173. https://doi.org/10.1038/s41598-019-43650-4.
(21) Ulbrich, K.; Holá, K.; Šubr, V.; Bakandritsos, A.; Tuček, J.; Zbořil, R. Targeted Drug Delivery with Polymers and Magnetic Nanoparticles: Covalent and Noncovalent Approaches, Release Control, and Clinical Studies. *Chem. Rev.* **2016**, *116* (9), 5338–5431. https://doi.org/10.1021/acs.chemrev.5b00589.
(22) Guo, Y.; Zhang, Y.; Ma, J.; Li, Q.; Li, Y.; Zhou, X.; Zhao, D.; Song, H.; Chen, Q.; Zhu, X. Light/Magnetic Hyperthermia Triggered Drug Released from Multi-Functional Thermo-Sensitive Magnetoliposomes for Precise Cancer Synergetic Theranostics. *J. Control. Release* **2018**, *272*, 145–158. https://doi.org/https://doi.org/10.1016/j.jconrel.2017.04.028.
(23) Sun, Q.; Cheng, D.; Yu, X.; Zhang, Z.; Dai, J.; Li, H.; Liang, B.; Shuai, X. A PH-Sensitive Polymeric Nanovesicle Based on Biodegradable Poly(Ethylene Glycol)-b-Poly(2-(Diisopropylamino)Ethyl Aspartate) as a MRI-Visible Drug Delivery System. *J. Mater. Chem.* **2011**, *21* (39), 15316–15326. https://doi.org/10.1039/C1JM12404H.
(24) Kim, D.-H.; Vitol, E. A.; Liu, J.; Balasubramanian, S.; Gosztola, D. J.; Cohen, E. E.; Novosad, V.; Rozhkova, E. A. Stimuli-Responsive Magnetic Nanomicelles as Multifunctional Heat and Cargo Delivery Vehicles. *Langmuir* **2013**, *29* (24), 7425–7432. https://doi.org/10.1021/la3044158.
(25) Riedinger, A.; Guardia, P.; Curcio, A.; Garcia, M. A.; Cingolani, R.; Manna, L.; Pellegrino, T. Subnanometer Local Temperature Probing and Remotely Controlled Drug Release Based on Azo-Functionalized Iron Oxide Nanoparticles. *Nano Lett.* **2013**, *13* (6), 2399–2406. https://doi.org/10.1021/nl400188q.
(26) Thirunavukkarasu, G. K.; Cherukula, K.; Lee, H.; Jeong, Y. Y.; Park, I.-K.; Lee, J. Y. Magnetic Field-Inducible Drug-Eluting Nanoparticles for Image-Guided Thermo-Chemotherapy. *Biomaterials* **2018**, *180*, 240–252. https://doi.org/https://doi.org/10.1016/j.biomaterials.2018.07.028.
(27) Fizir, M.; Dramou, P.; Zhang, K.; Sun, C.; Pham-Huy, C.; He, H. Polymer Grafted-Magnetic

Halloysite Nanotube for Controlled and Sustained Release of Cationic Drug. *J Colloid Interface Sci* **2017**, *505*, 476–488. https://doi.org/10.1016/j.jcis.2017.04.011.

(28) Wei, Q.; Shi, R.; Lu, D.; Lei, Z. In Situ Formation of Gold Nanoparticles on Magnetic Halloysite Nanotubes via Polydopamine Chemistry for Highly Effective and Recyclable Catalysis. *RSC Adv.* **2016**, *6* (35), 29245–29253. https://doi.org/10.1039/C6RA02789J.

(29) Dai, J.; Wei, X.; Cao, Z.; Zhou, Z.; Yu, P.; Pan, J.; Zou, T.; Li, C.; Yan, Y. Highly-Controllable Imprinted Polymer Nanoshell at the Surface of Magnetic Halloysite Nanotubes for Selective Recognition and Rapid Adsorption of Tetracycline. *RSC Adv.* **2014**, *4* (16), 7967–7978. https://doi.org/10.1039/C3RA45779F.

(30) Xie, Y.; Qian, D.; Wu, D.; Ma, X. Magnetic Halloysite Nanotubes/Iron Oxide Composites for the Adsorption of Dyes. *Chem. Eng. J.* **2011**, *168* (2), 959–963. https://doi.org/https://doi.org/10.1016/j.cej.2011.02.031.

(31) Arshadi, M.; Eskandarloo, H.; Enayati, M.; Godec, M.; Abbaspourrad, A. Highly Water-Dispersible and Antibacterial Magnetic Clay Nanotubes Functionalized with Polyelectrolyte Brushes: High Adsorption Capacity and Selectivity toward Heparin in Batch and Continuous System. *Green Chem.* **2018**, *20* (24), 5491–5508. https://doi.org/10.1039/C8GC02662A.

(32) Maleki, A.; Hajizadeh, Z. Magnetic Aluminosilicate Nanoclay: A Natural and Efficient Nanocatalyst for the Green Synthesis of 4H-Pyran Derivatives. *Silicon* **2019**, *11* (6), 2789–2798. https://doi.org/10.1007/s12633-019-0069-4.

(33) Kadam, A. A.; Jang, J.; Lee, D. S. Supermagnetically Tuned Halloysite Nanotubes Functionalized with Aminosilane for Covalent Laccase Immobilization. *ACS Appl. Mater. Interfaces* **2017**, *9* (18), 15492–15501. https://doi.org/10.1021/acsami.7b02531.

(34) Wan, X.; Zhan, Y.; Long, Z.; Zeng, G.; He, Y. Core@double-Shell Structured Magnetic Halloysite Nanotube Nano-Hybrid as Efficient Recyclable Adsorbent for Methylene Blue Removal. *Chem. Eng. J.* **2017**, *330*, 491–504. https://doi.org/https://doi.org/10.1016/j.cej.2017.07.178.

(35) Duan, J.; Liu, R.; Chen, T.; Zhang, B.; Liu, J. Halloysite Nanotube-Fe3O4 Composite for Removal of Methyl Violet from Aqueous Solutions. *Desalination* **2012**, *293*, 46–52. https://doi.org/https://doi.org/10.1016/j.desal.2012.02.022.

(36) Zheng, P.; Du, Y.; Ma, X. Selective Fabrication of Iron Oxide Particles in Halloysite Lumen. *Mater. Chem. Phys.* **2015**, *151*, 14–17. https://doi.org/https://doi.org/10.1016/j.matchemphys.2014.11.075.

(37) Baaziz, W.; Liu, X.; Florea, I.; Begin-Colin, S.; Pichon, B. P.; Ulhaq, C.; Ersen, O.; Soria-Sánchez, M.; Zafeiratos, S.; Janowska, I.; Begin, D.; Pham-Huu, C. Carbon Nanotube Channels Selectively Filled with Monodispersed Fe3−xO4 Nanoparticles. *J. Mater. Chem. A* **2013**, *1* (44), 13853–13861. https://doi.org/10.1039/C3TA12734F.

(38) Vinokurov, V. A.; Stavitskaya, A. V; Glotov, A. P.; Novikov, A. A.; Zolotukhina, A. V; Kotelev, M. S.; Gushchin, P. A.; Ivanov, E. V; Darrat, Y.; Lvov, Y. M. Nanoparticles Formed onto/into Halloysite Clay Tubules: Architectural Synthesis and Applications. *Chem. Rec.* **2018**, *18* (7–8), 858–867. https://doi.org/https://doi.org/10.1002/tcr.201700089.

(39) Rostamzadeh, T.; Islam Khan, M. S.; Riche', K.; Lvov, Y. M.; Stavitskaya, A. V; Wiley, J. B. Rapid and Controlled In Situ Growth of Noble Metal Nanostructures within Halloysite Clay Nanotubes. *Langmuir* **2017**, *33* (45), 13051–13059. https://doi.org/10.1021/acs.langmuir.7b02402.

(40) Vinokurov, V. A.; Stavitskaya, A. V; Chudakov, Y. A.; Ivanov, E. V; Shrestha, L. K.; Ariga, K.; Darrat, Y. A.; Lvov, Y. M. Formation of Metal Clusters in Halloysite Clay Nanotubes. *Sci. Technol. Adv. Mater.* **2017**, *18* (1), 147–151. https://doi.org/10.1080/14686996.2016.1278352.

(41) Zeng, X.; Wang, Q.; Wang, H.; Yang, Y. Catalytically Active Silver Nanoparticles Loaded in the Lumen of Halloysite Nanotubes via Electrostatic Interactions. *J. Mater. Sci.* **2017**, *52* (14), 8391–8400. https://doi.org/10.1007/s10853-017-1073-y.

(42) Hamdi, J.; Blanco, A. A.; Diehl, B.; Wiley, J. B.; Trudell, M. L. Room-Temperature Aqueous Suzuki–Miyaura Cross-Coupling Reactions Catalyzed via a Recyclable Palladium@Halloysite Nanocomposite. *Org. Lett.* **2019**, *21* (10), 3471–3475. https://doi.org/10.1021/acs.orglett.9b00042.

(43) Wu, S.; Qiu, M.; Guo, B.; Zhang, L.; Lvov, Y. Nanodot-Loaded Clay Nanotubes as Green and Sustained Radical Scavengers for Elastomer. *ACS Sustain. Chem. Eng.* **2017**, *5* (2), 1775–1783. https://doi.org/10.1021/acssuschemeng.6b02523.

(44) Yuan, P.; Tan, D.; Annabi-Bergaya, F. Properties and Applications of Halloysite Nanotubes: Recent Research Advances and Future Prospects. *Appl. Clay Sci.* **2015**, *112–113*, 75–93. https://doi.org/https://doi.org/10.1016/j.clay.2015.05.001.

(45) VEERABADRAN, N. G.; PRICE, R. R.; LVOV, Y. M. CLAY NANOTUBES FOR ENCAPSULATION AND SUSTAINED RELEASE OF DRUGS. *Nano* **2007**, *02* (02), 115–120. https://doi.org/10.1142/S1793292007000441.

(46) Effect of sodium oleate as a buffer on the synthesis of superparamagnetic magnetite colloids - ScienceDirect https://www.sciencedirect.com/science/article/pii/S0021979710002596 (accessed Nov 4, 2019).

(47) Sun, S.; Zeng, H.; Robinson, D. B.; Raoux, S.; Rice, P. M.; Wang, S. X.; Li, G. Monodisperse MFe 2 O 4 (M = Fe, Co, Mn) Nanoparticles. *J. Am. Chem. Soc.* **2004**, *126* (1), 273–279. https://doi.org/10.1021/ja0380852.

(48) Kim, B. H.; Lee, N.; Kim, H.; An, K.; Park, Y. Il; Choi, Y.; Shin, K.; Lee, Y.; Kwon, S. G.; Na, H. Bin; Park, J.-G.; Ahn, T.-Y.; Kim, Y.-W.; Moon, W. K.; Choi, S. H.; Hyeon, T. Large-Scale Synthesis of Uniform and Extremely Small-Sized Iron Oxide Nanoparticles for High-Resolution T1 Magnetic Resonance Imaging Contrast Agents. *J. Am. Chem. Soc.* **2011**, *133* (32), 12624–12631. https://doi.org/10.1021/ja203340u.

(49) Magnetic Iron Oxide Nanoparticles: Synthesis, Characterization and Functionalization for Biomedical Applications in the Central Nervous System https://www.ncbi.nlm.nih.gov/pmc/articles/PMC6384775/ (accessed Nov 4, 2019).

(50) Galli, M.; Guerrini, A.; Cauteruccio, S.; Thakare, P.; Dova, D.; Orsini, F.; Arosio, P.; Carrara, C.; Sangregorio, C.; Lascialfari, A.; Maggioni, D.; Licandro, E. Superparamagnetic Iron Oxide Nanoparticles Functionalized by Peptide Nucleic Acids. *RSC Adv.* **2017**, *7* (25), 15500–15512. https://doi.org/10.1039/C7RA00519A.

(51) Galli, M.; Rossotti, B.; Arosio, P.; Ferretti, A. M.; Panigati, M.; Ranucci, E.; Ferruti, P.; Salvati, A.; Maggioni, D. A New Catechol-Functionalized Polyamidoamine as an Effective SPION Stabilizer. *Colloids Surfaces B Biointerfaces* **2019**, *174* (October 2018), 260–269. https://doi.org/10.1016/j.colsurfb.2018.11.007.

(52) Taroni, T.; Meroni, D.; Fidecka, K.; Maggioni, D.; Longhi, M.; Ardizzone, S. Halloysite Nanotubes Functionalization with Phosphonic Acids: Role of Surface Charge on Molecule Localization and Reversibility. *Appl. Surf. Sci.* **2019**, *486*, 466–473. https://doi.org/https://doi.org/10.1016/j.apsusc.2019.04.264.

(53) Yah, W. O.; Takahara, A.; Lvov, Y. M. Selective Modification of Halloysite Lumen with Octadecylphosphonic Acid: New Inorganic Tubular Micelle. *J. Am. Chem. Soc.* **2012**, *134* (3), 1853–1859. https://doi.org/10.1021/ja210258y.

(54) Malo de Molina, P.; Appavou, M.-S.; Gradzielski, M. Oil-in-Water Microemulsion Droplets of TDMAO/Decane Interconnected by the Telechelic C18-EO150-C18: Clustering and Network Formation. *Soft Matter* **2014**, *10* (28), 5072–5084. https://doi.org/10.1039/C4SM00501E.

(55) Chen, Y.; Zhang, Y.; Liu, J.; Zhang, H.; Wang, K. Preparation and Antibacterial Property of Polyethersulfone Ultrafiltration Hybrid Membrane Containing Halloysite Nanotubes Loaded with Copper Ions. *Chem. Eng. J.* **2012**, *210*, 298–308. https://doi.org/https://doi.org/10.1016/j.cej.2012.08.100.

(56) Kim, T.; Shima, M. Reduced Magnetization in Magnetic Oxide Nanoparticles. *J. Appl. Phys.* **2007**, *101* (9), 09M516. https://doi.org/10.1063/1.2712825.

(57) Mørup, S. Superparamagnetism and Spin Glass Ordering in Magnetic Nanocomposites. *Europhys. Lett.* **1994**, *28* (9), 671–676. https://doi.org/10.1209/0295-5075/28/9/010.

(58) Arosio, P.; Baldi, G.; Federica, C.; Corti, M.; Dessy, A.; Galinetto, P.; Gazzarri, M.; Grandi, M.; Innocenti, C.; Lascialfari, A.; Lorenzi, G.; Orsini, F.; Piras, A.; Ravagli, C.; Sangregorio, C. Magnetism and Spin Dynamics of Novel Encapsulated Iron Oxide Superparamagnetic Nanoparticles. *Dalton Trans.* **2013**, *42*. https://doi.org/10.1039/c3dt32805h.

(59) Mondini, S.; Ferretti, A. M.; Puglisi, A.; Ponti, A. Pebbles and PebbleJuggler: Software for Accurate, Unbiased, and Fast Measurement and Analysis of Nanoparticle Morphology from Transmission Electron Microscopy (TEM) Micrographs. *Nanoscale* **2012**, *4* (17), 5356–5372. https://doi.org/10.1039/C2NR31276J.

Chapter 3

Halloysite nanotubes loaded with Au NPs of different shapes.

1 Introduction

One of the advantages of nanoparticles (NP) is the possibility to integrate several functionalities in one object only, to be exploitable especially in the biomedical field. Functionalities such as drug delivery, delivery tracking/monitoring, imaging, and highly localized treatments can be integrated to take advantage of the properties of the nanomaterials. [1–3] Many of these approaches have been implemented with gold nanoparticles (Au NPs).[4,5] Au NPs have become widely used in the biomedical field thanks to their special electronic, optical, sensing, chemical inertness and their low toxicity. [6,7] Their first use in the biomedical field concerns immunological assays and dates back to the early 70s.[8] Due to their plasmonic properties, the Au NPs can be used as imaging agents[5,7] and in biosensing.[4,5] Additionally, colourimetric sensing, electrical and electrochemical sensing[5] have been demonstrated for different Au NPs. Their applications for drug delivery,[9,10] photothermal therapy and photodynamic therapy have also been realized.[4]

1.1 Optical properties of gold nanoparticles

The first scientist to study the properties of colloidal gold was Faraday who noticed a correlation between the size of the Au nanoparticles and the colour of the suspensions obtained.[11,12] In fact, there is a relationship between the colour of the colloidal suspensions of the Au nanoparticles with the shape, size and medium in which they are dispersed.

They possess bright and intense colours that derive from their surface electrons interaction with an electromagnetic radiation, such as light. At a particular wavelength, called resonance frequency, the nanoparticles absorb the incident radiation, the surface conduction band electrons will tend to oscillate collectively and coherently creating a polarization of the nanoparticle. This phenomenon is known as Surface Plasmon Resonance (SPR, **Figure 1**).

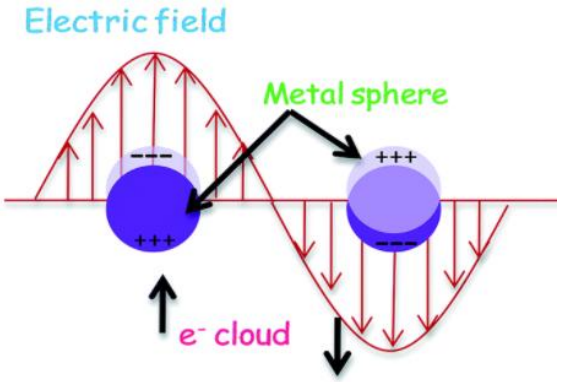

Figure 1 – Electronic oscillation during the SPR phenomenon.[13]

Au NPs are particularly attractive due to their SPR bands which lie in the visible/NIR region. The photon light interacting with Au NPs will be partly scattered in all directions while another part will be absorbed and converted into vibrations of the crystal lattice.[14] Since metal NPs have a very low light emission quantum yield, almost all the absorbed light energy is converted to heat energy,[15] the produced heat able to kill the cancer cells and so used in biomedical applications. Due to the biological window, the region of the electromagnetic spectrum where the absorption of light by water and tissues is minimal, it is important to use NPs with an SPR band possibly centred between 600 and 900 nm. If the diseased tissue is external, also For a more energetic visible SPR band can be useful for the purpose. For example, in one of the first appeared works, El Sayed et al. [16] demonstrated the tumour destruction in mice after illumination with 514 nm visible light using citrate stabilized 40 nm Au NP functionalized with anti-EGFR (Epidermal Grow Factor Receptor) to discriminate between normal and tumour tissue.

1.2 Shapes of gold nanoparticles

Gold NPs are composed of a metallic gold core and can be easily functionalized by adding a monolayer of surface moieties that can act as ligands for active targeting.[2] Although they can be assembled using different chemical, physical and biological methods,[17] Au NPs for biomedical applications are mainly prepared using the colloidal synthesis method using a metal precursor, stabilizer and organic or inorganic reducing agent such as sodium citrate, ascorbate, sodium borohydride, etc.[18] This approach allows to precisely control the optical and electrical properties that strongly depend on the shapes and sizes of the generated Au NP nanostructures (**Figure 2**).

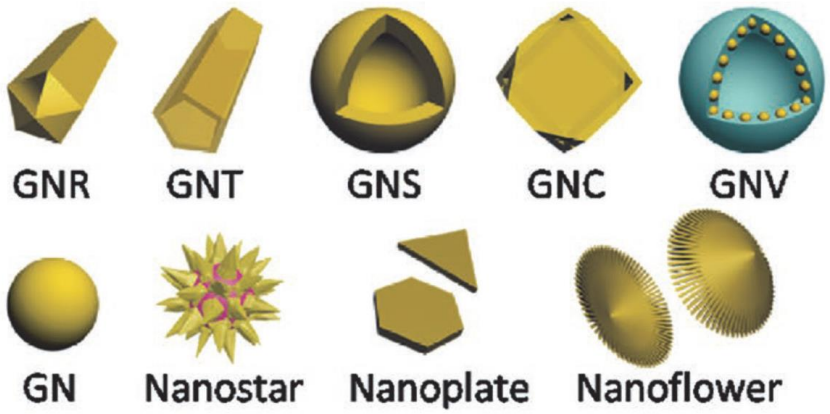

Figure 2 - Schematic images of various AuNPs: nanorods (GNR), nanotubes (GNT), nanoshells, nanocages (GNC), nanovesicles (GNV), nanospheres (GN), nanoplates, nanoflowers.[19]

A relevant characteristic of Au nanoparticles is that of being able to vary the plasmon resonance band based on size and shape. It has been known both theoretically[20] and experimentally[21] that elongated gold nanoparticles feature a SPR band that is red-shifted from the value of spherical gold nanoparticle peak by an amount proportional to their aspect ratio.

In this chapter, through chemical synthetic methods, we prepare gold nanoparticle in spherical and star shapes.

The first and the simplest type of synthesised nanoparticles are spherical gold nanoparticles. The well-known method of Turkevich gold nanoparticle synthesis [22] is based on a reduction reaction of chloroauric acid ($HAuCl_4$) with trisodium citrate solution. Frens [23] has improved this method by allowing particle size control by varying the concentration of citrate.

Recently, branched and star-shaped plasmon-resonant nanoparticles or nanostars (GNS) have attracted a great deal of interest in various biophotonic and biomedical applications due to the tunability of SPR band to the near infrared (NIR) diagnostic/therapeutic window, and the presence of multiple sharp tips that can greatly enhance incident electromagnetic fields.[24] The unique properties of GNS have led to their usage in various applications such as biosensing,[25] photodynamic therapy and photothermolysis,[26,27] visually identifying pathogens,[28] X-ray/CT imaging,[29] targeted delivery and optical imaging.[30,31] There are several strategies for GNS synthesis. In 2003, Chen et al. [32] pioneered the synthesis of branched gold nanoparticles from silver disks in the presence of cetyltrimethylammonium bromide (CTAB) and NaOH. Then, a number of synthesis methods (seedless or seed-mediated) were developed using mainly poly(N-vinylpyrolidone) (PVP) or CTAB as surfactants The applicability of this type of AuNP in biomedicine was limited by the CTAB toxicity, as well as the difficulty in replacing CTAB or PVP during functionalisation, and the aggregation of the GNS after multiple washes. Xie and et al. [33]demonstrated a seedless synthesis method for non-toxic GNS based on $HAuCl_4$ reduction using a 4-(2-hydroxyethyl)-1-piperazineethanesulfonic acid (HEPES) biocompatible solution. We decided to employ this synthetic method in our research (see further). Indeed, this part of our work aimed to extend the halloysite lumen loading to other kinds of NPs for hyperthermia applications, and our attention focused on the loading of gold nanoparticles either in spherical or nanostar shape, and, possibly, selectively in the HNT lumen. In this way, HNT could be used as nanoobjects capable to concentrate many NPs in a restricted space, and this could be useful to improve the hyperthermic abilities of the metallic NPs. Moreover, the co-loading of a drug with the Au NPs could bring to a new nanovector for drug delivery, whose release could be triggered by the light interaction with Au NPs.

2 Results and discussion

The loading of gold NPs into the HNT lumen is dependent on the morphology and polarity of the synthesized NP. We investigated two different shapes of gold nanoparticles, spherical and star. For HNT loaded with spherical Au NPs, we used the same successful approach in the loading of SPION as described in Chapter 2, while the loading of GNS was done by two methods, through electrostatic attraction and an *in situ* GNS formation.

In this chapter, we mainly use the Australian halloysite, simply indicated as HNT, and in few assays, we synthesized HNT-Au adducts using Sigma-Aldrich halloysite and named S-HNT.

2.1 Spherical gold loading attempt

For the loading of spherical Au NPs, we followed the method summarized in **Scheme 1** to load the NP inside the HNT lumen.

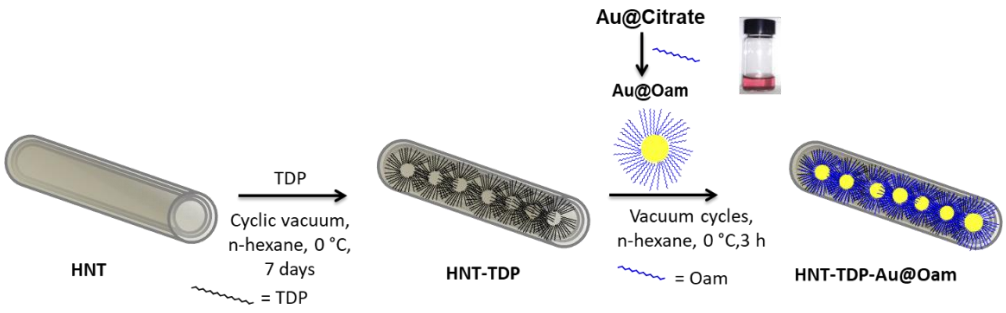

Scheme 1. Schematic depiction of the approach followed in this study to obtain HNT-TDP-Au@Oam nanocomposite with the selective loading of Au in the inner part.

The most used method for the synthesis of spherical Au NPs was devised by Turkevich in 1953 and involves the reduction of tetrachloroauric acid to metallic gold by citrate in an aqueous environment (**Eq. 3.1**).

$$6\,AuCl_4^- + \ C_6H_8O_7 + 5\,H_2O \ \rightarrow 6\,CO_2 + 24\,Cl^- + 6\,Au^0 + 18\,H^+ \qquad (Eq.\,3.1)$$

Subsequently, Turkevich's method was modified, varying the ratio between citrate and $AuCl_4^-$ and obtaining nanoparticles with variable dimensions (between 2 and 150 nm). In our work we follow the literature ratio and method to synthesize nanoparticle below 15 nm[34] to fit the HNT lumen diameter. The Au@citrate NPs showed a hydrodynamic diameter of 8.8 ±4.0 nm from DLS measurements (**Figure 3a**).

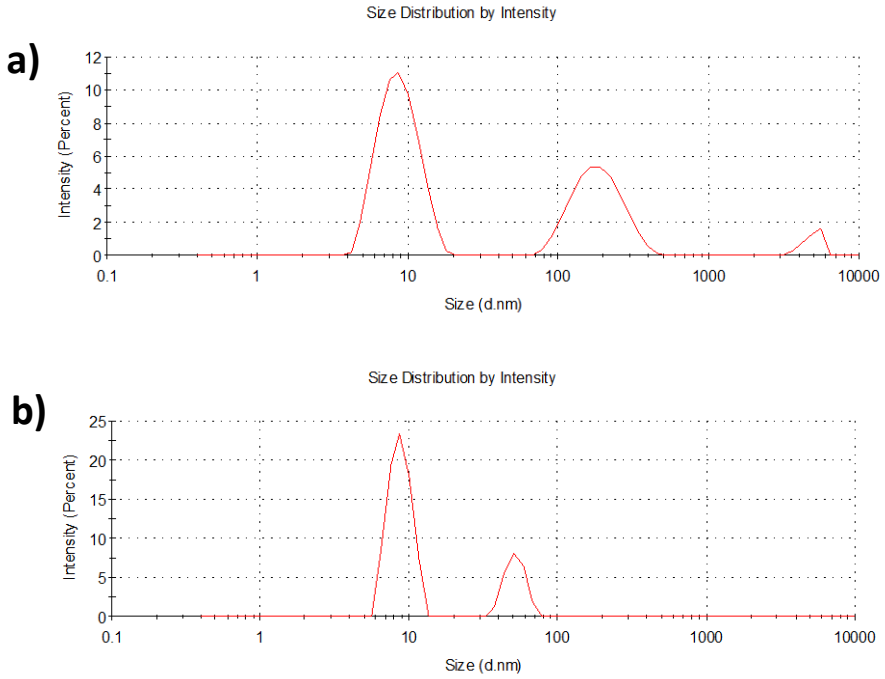

Figure 3. DLS measurements by intensity of (a) an aqueous suspension of Au@citrate NPs (b) an hexane suspenion of Au@OAm after ligand exchange.

To prepare apolar NPs, the citrate layer was removed and substituted with a proper hydrophobic layer of Oleyl amine following a simple literature procedure.[35] After the ligand exchange, the hydrophobic Au@Oam NPs were highly dispersed in n-hexane as showed by DLS measurement (**Figure 3b**). Moreover, they showed an unchanged maximum peak at 520 nm in the visible region, which confirmed that there is no aggregation in Au NPs after the ligand exchange process (**Figure 4**).

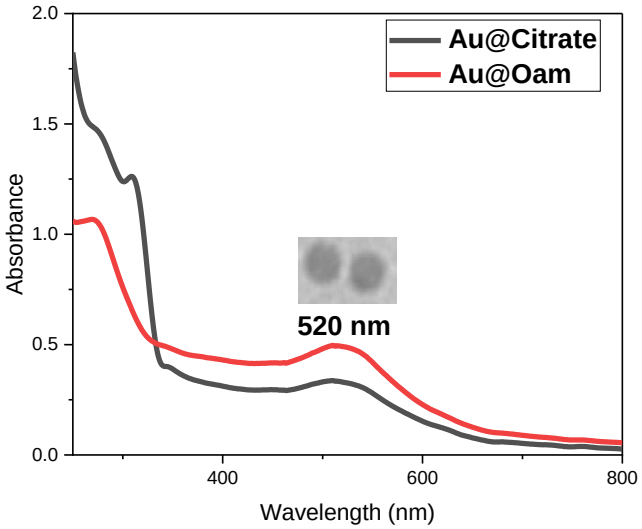

Figure 4. UV–vis absorption spectra recorded for synthesized Au dispersed in water and hexane after ligand exchange.

Similar to the SPION approach used before, the halloysite used for the NP loading were premodified with tetradecylphosphonic acid (TDP),[36] followed by loading the Au@Oam under the vacuum effect. From TEM analysis (**Figure 5**), the loading was successfully observed but only to a low extent due to the very low concentration of the gold suspension compared to the SPION one and giving rise to a Au NPs : HNT ratio equal to 1 : 10 that hampered a massive loading onto HNT, that opposites to highly concentrated Au precursor used in the literature to prepare *in situ* Au NPs inside HNT the ratio was 7.5:10.[37] Moreover since the spherical NP are not that interesting for biomedical purposes, we moved to gold nanostar.

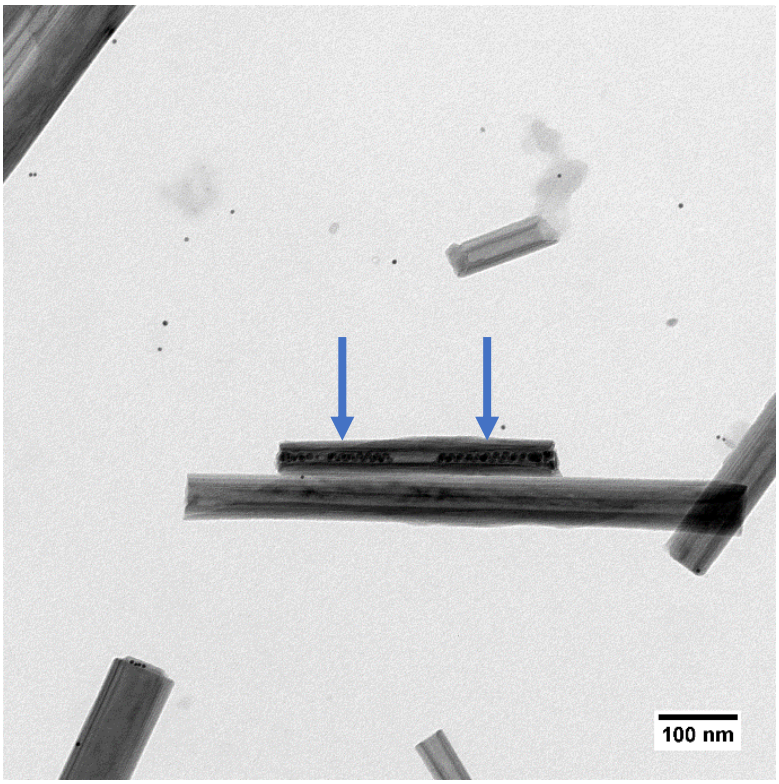

Figure 5. TEM micrographs of Au@Oam loaded to HNT-TDP lumen under vacuum effect.

2.2 Gold star Nanoparticle

Gold nanostars (GNS) were prepared in water by using the nontoxic HEPES solution acting both as a buffer, reducing and stabilizing agent (**Scheme 2**).[33,38,39] The number of GNS tips and their size depend on the [HEPES]/[Au]: by increasing this ratio the tip number and size of GNS increase (**Figure 6**).

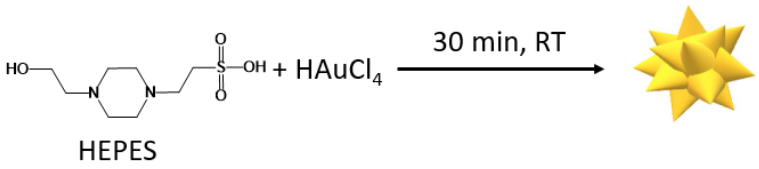

Scheme 2. The synthetic procedure followed in this study to obtain HNT-TDP-Au@Oam nanocomposite with the selective loading of Au in the inner part.

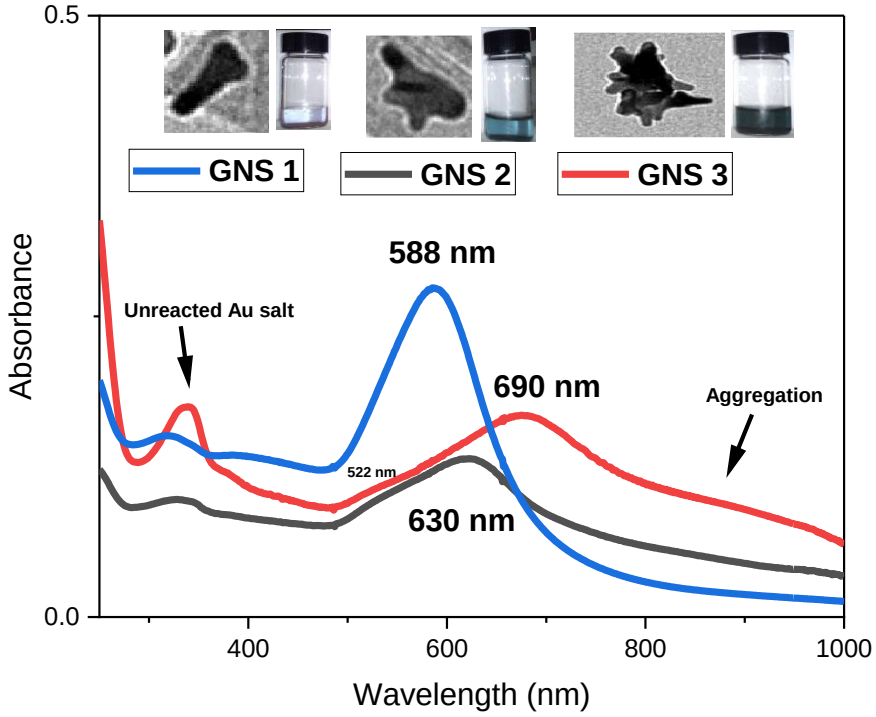

Figure 6. UV-vis absorption spectra recorded for GNS1, 2 and 3 synthesized with [HEPES]/[Au] = 250, 500 and 750 respectively. Insets: TEM micrographs of GNS with colour change under sunlight.

In agreement with literature data,[39] the UV-vis spectra, acquired on solutions containing different HEPES/Au ratios, showed that the longitudinal surface plasmon resonance (LSPR) peak of GNS 1, GNS 2, and GNS 3 lied at 588, 630 and 690 nm respectively. It has been known both theoretically[20] and experimentally[21] that the elongated gold nanoparticles feature a LSPR that red-shifts from ca. 520 nm (the value for spherical gold nanoparticles) by an amount proportional to their aspect ratio. Therefore, the maximum shift showed by the LSPR of GNS 3 suggested the maximum elongation of the tips and/or their amount. The peak at ca. 522 nm is attributable to the transverse plasmon resonance of the tips, as also suggested by previous

works on gold nanorods.[40,41] Because of the high aggregation observed in the case of GNS 3 and low tips number in case of GNS 1, we chose to use GNS 2 for the loading attempts.

DLS and ζ-potential measurements are reported in **Figure 7**, and showed that the hydrodynamic diameter was 12.5 ±2.1 nm while the charge of GNS 2 was equal to -16.5 ±2.2 mV. The negative charge was attributed to the presence of the outer surface stabilizing agent HEPES.

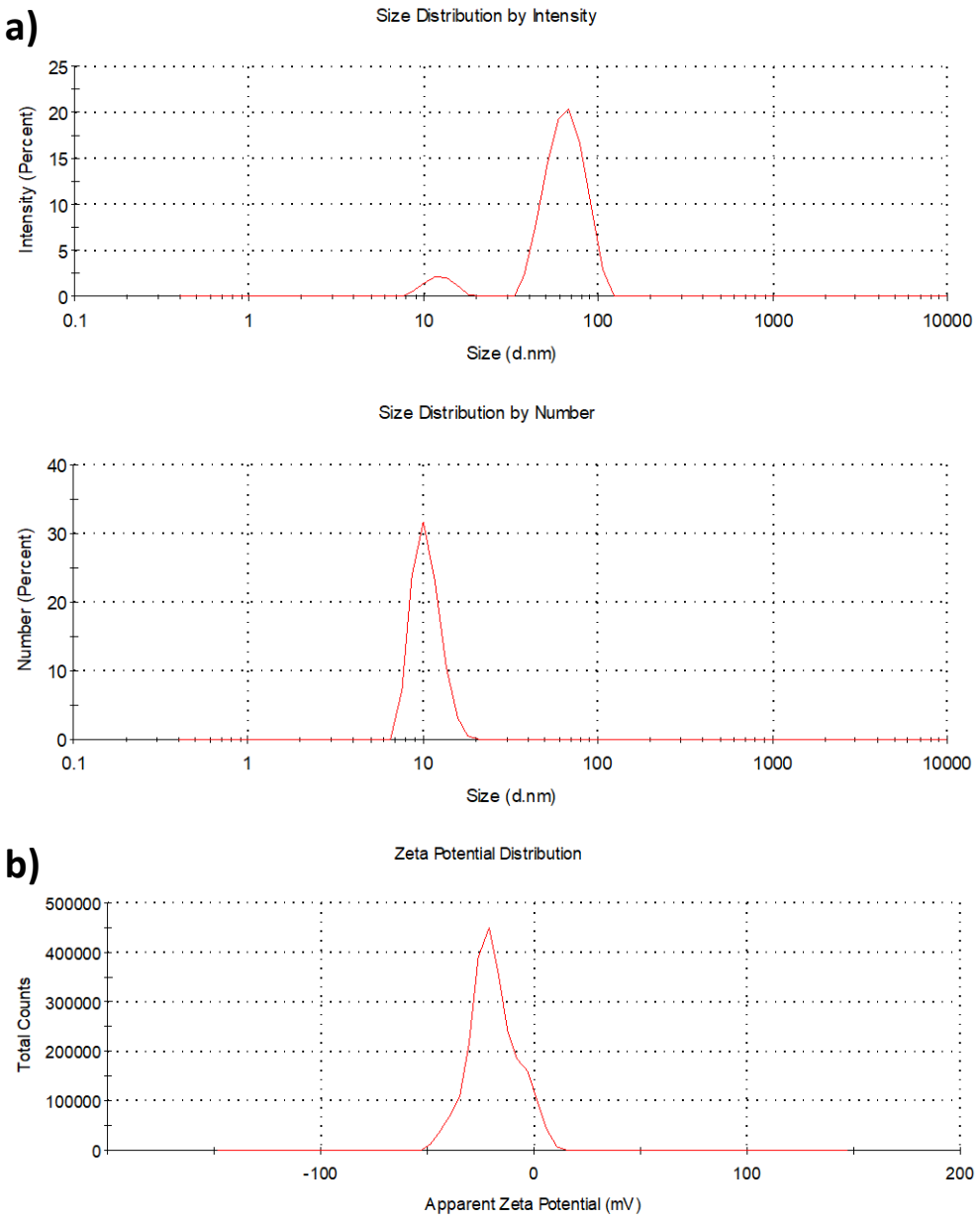

Figure 7. (a)DLS (by intensity and numbers) and (b) ζ-potential analyses of GNS 2 suspension in MilliQ water at pH 7.4.

The loading of GNS2 into lumen of HNT was done following two strategies, either through electrostatic attraction or *in situ* growth.

2.2.1 Electrostatic loading attempt of GNS 2.

The loading of GNS 2 into the lumen of HNT was carried out following the electrostatic method already mentioned in the literature for spherical NPs (**Scheme 3**).[42–44] TEM images (**Figure 8**) confirmed the success of the loading but, the diluted GNS 2 suspension lead to a low loading percentage of GNS especially if we compare these results to other previous works, that anyhow were focused in the loading of spherical nanoparticles.[37]

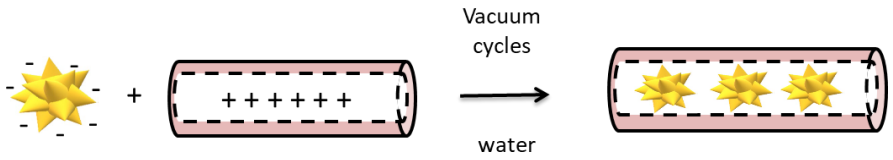

Scheme 3. Schematic depiction of the approach followed to obtain GNS 2-HNT nanocomposite through the electrostatic method.

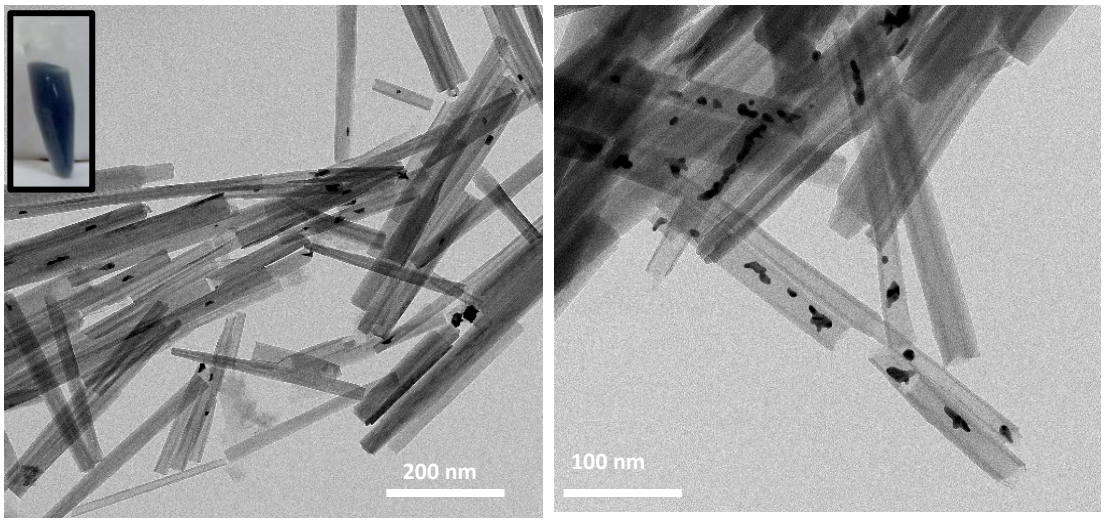

Figure 8. TEM micrographs of GNS 2 loaded to HNT lumen under electrostatic and vacuum effect. Inset the visible color of HNT-GNS adduct after loading.

In order to increase the amount of nanostars per HNT, we attempted to form the gold nanostars directly into the lumen by pre-loading the Au precursor.

2.2.2 insitu loading attempt of GNS 2.

The *in situ* loading of GNS 2 into the HNT lumen was carried out as summarized in **Scheme 4**. The procedure was repeated by employing the American HNT as well as the Australian ones.

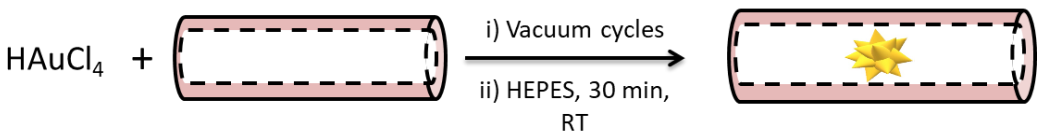

Scheme 4. Schematic depiction of the approach followed to obtain GNS 2-HNT nanocomposite through the *in situ* method.

Panel **(a)** of **Figure 9** shows well that the supernatant after the formation of HNT-GNS was uncoloured, indicating that most of the gold precursor had reacted with HEPES. Analyzing by TEM the HNT-GNS blue pellet recovered after thorough washings (HNT in **Figure 9b and 9c** and S-HNT in **Figure 9d and 9e**) showed that many particles but of spherical shape were formed into the lumen. This can be explained by supposing that the diffusion of HEPES into the lumen could be slow enough to hamper the achievement of the proper concentration ratio with the gold precursor. Moreover, it could be seen that many NPs were forming clusters at the entry of HNT in the case of australian HNT (**Figure 9b and 9c**) while in the case of S-HNT (**Figure 9d and 9e**), the GNS were mostly localized at the outer surface of HNT and heavily captured by impurities of kalone sheets (**Figure 9e**).

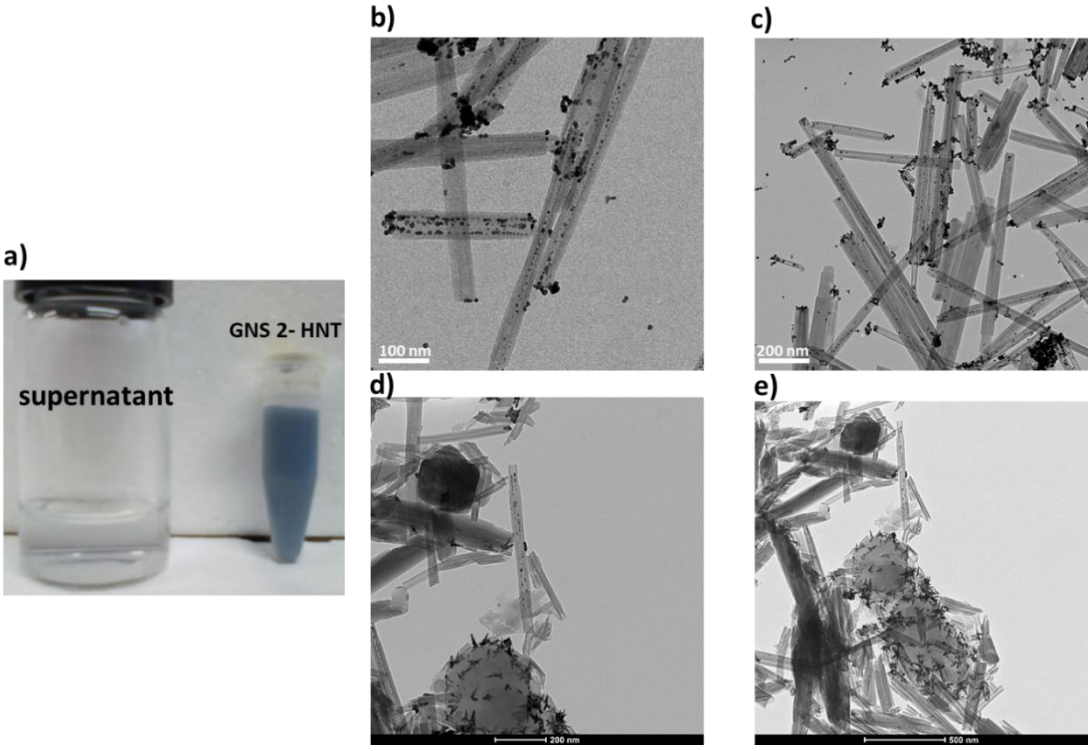

Figure 9. a) visible color of supernatant and GNS 2 -HNT adduct after insitu loading attempt, (b) and (c) TEM micrographs of GNS 2 loaded to austrralian HNT lumen, (d) and (e) TEM micrographs of GNS 2 loaded to sigma HNT lumen through insitu method.

From these last results, we conclude that it was easier to form GNS higher in tips morphology attached to the outer surface than in the inner lumen with the *in situ* method. What could have been done, was the reversal of the reagents: HEPES preloaded in the lumen of the HNTs and $HAuCl_4$ added to the suspension. In this way, the large excess of HEPES should be ensured and the formation of nanostars within the lumen could be feasible.

3 Conclusions

In this work, we tried to load gold nanoparticles into the lumen of HNT, to produce a possible adduct exploitable for optical hypethermia.

The loading of the spherical Au NPs was carried out first of all after having prepared apolar Au NPs that were shown to be loadable into premodified apolar HNT. The loading was scarce due to the very low concentration of the gold NPs suspension. Nevertheless, we demonstrated the feasibility of the method.

Passing considering non-spherical nanoparticles, we prepared GNS in water by using a nontoxic HEPES buffer both as a reducing and stabilizing agent, as described in the literature. The so prepared GNS possessed a surface charge opposite to the one of the HNT lumen, so they were loaded by vacuum cycles exploiting the electrostatic attraction. The loading was successful, but also in this case we found only sporadically GNS into the inner lumen when the loading was conducted in very diluted condition.

We attempted also to form GNS directly into the lumen by pre-loading the Au precursor. When we preloaded HNT with concentrated $HAuCl_4$ solutions we succeed in selectively form NPs in the inner lumen but of spherical shape.

These very preliminary results can be explained first of all by taking into account the big difference between the concentration of the SPION used in Chapter 2 and the gold NPs that are synthesized in very diluted conditions for their nature. Secondly, the inner lumen was not big enough to enable the formation of stars with the chosen synthetic methodology, which mainly resulted sterically hampered in the growth of longer tips.

As a future development, we are planning to modify the outer surface of HNT with 3-mercaptopropyl-trimethoxy silane[45] to covalently bind the GNS to the outer surface of HNT through the thiolic end, which is highly capable to link the gold surface.[46,47]

4 Experimental

4.1 Materials and instruments

Tetradecylphosphonic acid 97%, Sodium tetrachloroaurate(III) hydrate 99.99%, 4-(2-Hydroxyethyl)piperazine-1-ethanesulfonic acid (HEPES) 99%, Sodium hydroxide pellets 98%, Oleylamine 70%, and halloysite nanotubes S-HNT (Sigma Aldrich), n-hexane 96% and acetone (Scharlau), HNO_3 65% and HCl 30% (Merck Germany) were all used as received. Australian halloysite clay (HNT) were provided by prof. John L. Keeling from Camel Lake (Australia). Ultrapure milli-Q water (Millipore, resistivity=18M Ω cm−2) was used for the preparation of the aqueous solutions.

UV-vis absorption spectra were acquired on an Agilent model 8543 spectrophotometer at room temperature and using standard 1.0 cm path length quartz cells .

ζ-potential measurements were carried out using a Malvern Zetasizer nano ZS instrument equipped with a 633 nm solid state He–Ne laser at a scattering angle of 173 at 25 °C. The measurements were averaged on at least three repeated runs.

ATR-FTIR spectra were acquired on a PerkinElmer Frontier instrument equipped with an ATR accessory with a diamond/ZnSe crystal. The IR spectra were registered between 4000 and 400 cm^{-1}.

Transmission Electron Microscopy micrographs were collected using a Zeiss Libra 200 FE instrument equipped with an in column pre-aligned omega filter that improves the contrast and a Schottky field emission gun at 200 kV. Alternatively, TEM images were collected using an EFTEM LEO 912AB (Zeiss) at 100 kV. Samples were prepared by dropping a dilute solution of the samples onto 200 mesh carbon-coated copper grids, and after blotting the excess of water, the samples were let drying at least for 24 h in air.

All glassware was washed with aqua regia ($HCl:HNO_3$ in a 3:1 ratio by volume) and rinsed with ethanol and ultrapure water.

4.2 Synthesis of Au @Citrate.

The synthesis of spherical gold nanoparticles was carried out by following a literature procedure.[34] Briefly, in a 1-neck round-bottom flask (250 mL), a 150 mL of freshly prepared reducing solution of sodium citrate (97.05 mg, 2.2 mM), 96 µL of Tannic acid (2.0 mg, 2.5 mM) and 1.0 ml of potassium carbonate (20.7 mg, 150 mM) was heating under magnetic stirring. When the temperature reached 70 °C, 2 mL of freshly prepared tetrachloroauric acid (12.4 mM) was injected. The colour of the solution changed rapidly in few seconds to black and then to orange-red in the following 3 min. The solution was kept at 70 °C for 10 min more to ensure complete reaction of the gold precursor, followed by DLS and UV characterization. As stated by the literature, the synthetic method gives a 90% yield of spherical gold NP so the expected yield was about 4.4 mg of Au.

4.3 Ligand exchange Citrate/Oleyl amine (Au @Oam).[35]

In 1.0 L separatory funnel, the Au@citrate water suspension of (150.0 mL, 0.03 mg/mL Au) was mixed with 75.0 mL of acetone and shaken for 1 s, followed by adding 75.0 mL of hexane and 680 µL of oleyl amine. After shacking for few minutes, the water-acetone phase became colorless, and the hexane phase turned dark red due to the transfer of gold nanoparticles. All the by-product remained in the water-acetone phase. The recovered hexane layer was analyzed by UV-vis spectroscopy. Next, 16 mL of Au@Oam solution (ca 1.0 mg NPs) were centrifuged at 14000 rpm/45 min (using 2.0 mL Eppendorf), followed by dispersion in 10 mL hexane.

4.4 Attempt to Load Au @Oam into modified HNT lumen (Au @Oam-in-HNT-TDP).

In a Schlenk tube, a sample of Au@Oam (10 mL, 0.1 mg/mL) were mixed with 10 mg HNT-TDP [36] (whose synthetic procedure was explained in Chapter 2).The suspension was shaken for 1 min by a vortex, then it was cooled at 0 °C, and while standing in the ice bath, it was placed under reduced pressure and magnetic stirring until the solvent was visibly reduced. Then, another 20 mL n-hexane was added. After 2 h of the cycle reducing pressure, the colour of the supernatant turned clearer compared to the starting red colour. The HNT-TDP/ Au@Oam were recovered by centrifugation (3 min, 2000 rpm), the supernatant removed, and the precipitate washed with 5 mL n-hexane.

4.5 Synthesis of GNS 1,2 and 3.

The synthesis of gold nanostars of different size was carried out by following a literature procedure.[33,38,39] Briefly, 2.2 M stock solution of HEPES was prepared by dissolving the 12.65 g HEPES buffer salt in 25.0 mL Milli-Q water, followed by pH adjusting using a concentrated solution of NaOH until pH reached 7.4 value. GNS 1, 2 and 3 were synthesized by adding to 75 mM of HEPES an amount of gold(III) chloride trihydrate so that a final concentration of 0.30, 0.15 and 0.10 mM was reached, respectively. The mixture was kept for 30 min without shaking, and meanwhile, the suspension colour changed from light yellow to light purple and finally to greenish-blue.

4.6 Electrostatic loading of GNS 2 into HNT lumen.

10 mg of HNT were added to 5.0 mL of a water suspension of GNS 2 (ca. 1.0 mg) at pH 7.4. The mixture was sonicated for 15 min, shaken on a vortex for 10 min, and then the suspension subjected to reduced pressure (30 mmHg) for 30 min at room temperature. The sonication vacuum process was repeated 5 times, giving rise to a blue HNT adduct, which was recovered by centrifugation (3 min, 2000 rpm).

4.7 *Insitu* procedure to synthesis GNS 2 in the presence of HNT.

9 mg of HNT or S-HNT added to 5 mL of 4.4 mM of gold(III) chloride trihydrate solution, such that the mass ratio Au:HNT was 1:2. The mixture magnetically stirred for 10 min, then sonicated for 15 min and subjected to a reduced pressure (~ 1-2 mmHg) under stirring for 1 h. The sonication-vacuum-N_2 cycle was repeated 2 times more. The mixture vial was kept in the dark and left at room temperature under stirring for 1 night. To theses mixture, 5 mL of HEPES 2.2 M were added, followed by simple shaking for 1 min and left unstirred for 30 min, forming at the end a blue HNT adduct, which was recovered by centrifugation (3 min, 2000 rpm), and washed with 5 mL of water. The supernatant recovered was completely colourless.

5 Bibliography

(1) Siddique, S.; Chow, J. C. L. Application of Nanomaterials in Biomedical Imaging and Cancer Therapy. *Nanomaterials* **2020**, *10* (9), 1700. https://doi.org/10.3390/nano10091700.

(2) Lombardo, D.; Kiselev, M. A.; Caccamo, M. T. Smart Nanoparticles for Drug Delivery Application: Development of Versatile Nanocarrier Platforms in Biotechnology and Nanomedicine. *J. Nanomater.* **2019**, *2019*, 3702518. https://doi.org/10.1155/2019/3702518.

(3) Mudshinge, S. R.; Deore, A. B.; Patil, S.; Bhalgat, C. M. Nanoparticles: Emerging Carriers for Drug Delivery. *Saudi Pharm. J.* **2011**, *19* (3), 129–141. https://doi.org/https://doi.org/10.1016/j.jsps.2011.04.001.

(4) Khlebtsov, N.; Bogatyrev, V.; Dykman, L.; Khlebtsov, B.; Staroverov, S.; Shirokov, A.; Matora, L.; Khanadeev, V.; Pylaev, T.; Tsyganova, N.; Terentyuk, G. Analytical and Theranostic Applications of Gold Nanoparticles and Multifunctional Nanocomposites. *Theranostics* **2013**, *3* (3), 167–180. https://doi.org/10.7150/thno.5716.

(5) Saha, K.; Agasti, S. S.; Kim, C.; Li, X.; Rotello, V. M. Gold Nanoparticles in Chemical and Biological Sensing. *Chem. Rev.* **2012**, *112* (5), 2739–2779. https://doi.org/10.1021/cr2001178.

(6) Singh, P.; Pandit, S.; Mokkapati, V. R. S. S.; Garg, A.; Ravikumar, V.; Mijakovic, I. Gold Nanoparticles in Diagnostics and Therapeutics for Human Cancer. *Int. J. Mol. Sci.* **2018**, *19* (7), 1979. https://doi.org/10.3390/ijms19071979.

(7) Mahan, M. M.; Doiron, A. L. Gold Nanoparticles as X-Ray, CT, and Multimodal Imaging Contrast Agents: Formulation, Targeting, and Methodology. *J. Nanomater.* **2018**, *2018*, 5837276. https://doi.org/10.1155/2018/5837276.

(8) Faulk, W. P.; Taylor, G. M. An Immunocolloid Method for the Electron Microscope. *Immunochemistry* **1971**.

(9) Ghosh, P.; Han, G.; De, M.; Kim, C. K.; Rotello, V. M. Gold Nanoparticles in Delivery Applications. *Adv. Drug Deliv. Rev.* **2008**, *60* (11), 1307–1315.

(10) Kong, F.-Y.; Zhang, J.-W.; Li, R.-F.; Wang, Z.-X.; Wang, W.-J.; Wang, W. Unique Roles of Gold Nanoparticles in Drug Delivery, Targeting and Imaging Applications. *Molecules* **2017**, *22* (9), 1445.

(11) Thompson, D. Michael Faraday's Recognition of Ruby Gold: The Birth of Modern Nanotechnology. *Gold Bull. - GOLD BULL* **2007**, *40*, 267–269. https://doi.org/10.1007/BF03215598.

(12) Tweney, R. Discovering Discovery: How Faraday Found the First Metallic Colloid. *Perspect. Sci.* **2006**, *14*, 97–121. https://doi.org/10.1162/posc.2006.14.1.97.

(13) Jana, J.; Ganguly, M.; Pal, T. Enlightening Surface Plasmon Resonance Effect of Metal Nanoparticles for Practical Spectroscopic Application. *RSC Adv.* **2016**, *6* (89), 86174–86211.

https://doi.org/10.1039/C6RA14173K.
(14) Eustis, S.; El-Sayed, M. A. Why Gold Nanoparticles Are More Precious than Pretty Gold: Noble Metal Surface Plasmon Resonance and Its Enhancement of the Radiative and Nonradiative Properties of Nanocrystals of Different Shapes. *Chem. Soc. Rev.* **2006**. https://doi.org/10.1039/b514191e.
(15) Yeshchenko, O. A.; Kutsevol, N. V; Naumenko, A. P. Light-Induced Heating of Gold Nanoparticles in Colloidal Solution: Dependence on Detuning from Surface Plasmon Resonance. *Plasmonics* **2016**, *11* (1), 345–350. https://doi.org/10.1007/s11468-015-0034-z.
(16) Dickerson, E. B.; Dreaden, E. C.; Huang, X.; El-Sayed, I. H.; Chu, H.; Pushpanketh, S.; McDonald, J. F.; El-Sayed, M. A. Gold Nanorod Assisted Near-Infrared Plasmonic Photothermal Therapy (PPTT) of Squamous Cell Carcinoma in Mice. *Cancer Lett.* **2008**. https://doi.org/10.1016/j.canlet.2008.04.026.
(17) Alaqad, K.; Saleh, T. Gold and Silver Nanoparticles: Synthesis Methods, Characterization Routes and Applications towards Drugs. *J. Environ. Anal. Toxicol.* **2016**, *6*. https://doi.org/10.4172/2161-0525.1000384.
(18) Jiang, X.-M.; Wang, L.-M.; Wang, J.; Chen, C.-Y. Gold Nanomaterials: Preparation, Chemical Modification, Biomedical Applications and Potential Risk Assessment. *Appl. Biochem. Biotechnol.* **2012**, *166* (6), 1533–1551. https://doi.org/10.1007/s12010-012-9548-4.
(19) Chen, W.; Zhang, S.; Yu, Y.; Zhang, H.; He, Q. Structural-Engineering Rationales of Gold Nanoparticles for Cancer Theranostics. *Adv. Mater.* **2016**, *28* (39), 8567–8585. https://doi.org/https://doi.org/10.1002/adma.201602080.
(20) Link, S.; El-Sayed, M. A. Spectral Properties and Relaxation Dynamics of Surface Plasmon Electronic Oscillations in Gold and Silver Nanodots and Nanorods. *J. Phys. Chem. B* **1999**, *103* (40), 8410–8426. https://doi.org/10.1021/jp9917648.
(21) Nikoobakht, B.; El-Sayed, M. A. Preparation and Growth Mechanism of Gold Nanorods (NRs) Using Seed-Mediated Growth Method. *Chem. Mater.* **2003**, *15* (10), 1957–1962. https://doi.org/10.1021/cm020732l.
(22) Turkevich, J.; Stevenson, P. C.; Hillier, J. A Study of the Nucleation and Growth Processes in the Synthesis of Colloidal Gold. *Discuss. Faraday Soc.* **1951**, *11* (0), 55–75. https://doi.org/10.1039/DF9511100055.
(23) FRENS, G. Controlled Nucleation for the Regulation of the Particle Size in Monodisperse Gold Suspensions. *Nat. Phys. Sci.* **1973**, *241* (105), 20–22. https://doi.org/10.1038/physci241020a0.
(24) LI, S. I. Y. U. E.; WANG, M. I. N. BRANCHED METAL NANOPARTICLES: A REVIEW ON WET-CHEMICAL SYNTHESIS AND BIOMEDICAL APPLICATIONS. *Nano Life* **2012**, *02* (01), 1230002. https://doi.org/10.1142/S1793984411000311.
(25) Jana, D.; Matti, C.; He, J.; Sagle, L. Capping Agent-Free Gold Nanostars Show Greatly Increased Versatility and Sensitivity for Biosensing. *Anal. Chem.* **2015**, *87* (7), 3964–3972. https://doi.org/10.1021/acs.analchem.5b00014.
(26) Yuan, H.; Khoury, C. G.; Wilson, C. M.; Grant, G. A.; Bennett, A. J.; Vo-Dinh, T. In Vivo Particle Tracking and Photothermal Ablation Using Plasmon-Resonant Gold Nanostars. *Nanomedicine Nanotechnology, Biol. Med.* **2012**, *8* (8), 1355–1363. https://doi.org/https://doi.org/10.1016/j.nano.2012.02.005.
(27) Rodríguez-Oliveros, R.; Sánchez-Gil, J. A. Gold Nanostars as Thermoplasmonic Nanoparticles for Optical Heating. *Opt. Express* **2012**, *20* (1), 621–626. https://doi.org/10.1364/OE.20.000621.
(28) Verma, M. S.; Chen, P. Z.; Jones, L.; Gu, F. X. "Chemical Nose" for the Visual Identification of Emerging Ocular Pathogens Using Gold Nanostars. *Biosens. Bioelectron.* **2014**, *61*, 386–390. https://doi.org/https://doi.org/10.1016/j.bios.2014.05.045.
(29) Tian, Y.; Luo, S.; Yan, H.; Teng, Z.; Pan, Y.; Zeng, L.; Wu, J.; Li, Y.; Liu, Y.; Wang, S.; Lu, G. Gold Nanostars Functionalized with Amine-Terminated PEG for X-Ray/CT Imaging and Photothermal Therapy. *J. Mater. Chem. B* **2015**, *3* (21), 4330–4337. https://doi.org/10.1039/C5TB00509D.
(30) Hutter, E.; Boridy, S.; Labrecque, S.; Lalancette-Hébert, M.; Kriz, J.; Winnik, F. M.; Maysinger, D. Microglial Response to Gold Nanoparticles. *ACS Nano* **2010**, *4* (5), 2595–2606. https://doi.org/10.1021/nn901869f.
(31) Dam, D. H. M.; Lee, J. H.; Sisco, P. N.; Co, D. T.; Zhang, M.; Wasielewski, M. R.; Odom, T. W. Direct Observation of Nanoparticle–Cancer Cell Nucleus Interactions. *ACS Nano* **2012**, *6* (4),

3318–3326. https://doi.org/10.1021/nn300296p.
(32) Chen, S.; Wang, Z. L.; Ballato, J.; Foulger, S. H.; Carroll, D. L. Monopod, Bipod, Tripod, and Tetrapod Gold Nanocrystals. *J. Am. Chem. Soc.* **2003**, *125* (52), 16186–16187. https://doi.org/10.1021/ja038927x.
(33) Xie, J.; Lee, J. Y.; Wang, D. I. C. Seedless, Surfactantless, High-Yield Synthesis of Branched Gold Nanocrystals in HEPES Buffer Solution. *Chem. Mater.* **2007**, *19* (11), 2823–2830. https://doi.org/10.1021/cm0700100.
(34) Piella, J.; Bastús, N. G.; Puntes, V. Size-Controlled Synthesis of Sub-10-Nanometer Citrate-Stabilized Gold Nanoparticles and Related Optical Properties. *Chem. Mater.* **2016**, *28* (4), 1066–1075. https://doi.org/10.1021/acs.chemmater.5b04406.
(35) Martin, M. N.; Basham, J. I.; Chando, P.; Eah, S.-K. Charged Gold Nanoparticles in Non-Polar Solvents: 10-Min Synthesis and 2D Self-Assembly. *Langmuir* **2010**, *26* (10), 7410–7417. https://doi.org/10.1021/la100591h.
(36) Yah, W. O.; Takahara, A.; Lvov, Y. M. Selective Modification of Halloysite Lumen with Octadecylphosphonic Acid: New Inorganic Tubular Micelle. *J. Am. Chem. Soc.* **2012**, *134* (3), 1853–1859. https://doi.org/10.1021/ja210258y.
(37) Rostamzadeh, T.; Islam Khan, M. S.; Riche', K.; Lvov, Y. M.; Stavitskaya, A. V; Wiley, J. B. Rapid and Controlled In Situ Growth of Noble Metal Nanostructures within Halloysite Clay Nanotubes. *Langmuir* **2017**, *33* (45), 13051–13059. https://doi.org/10.1021/acs.langmuir.7b02402.
(38) Chandra, K.; Culver, K. S. B.; Werner, S. E.; Lee, R. C.; Odom, T. W. Manipulating the Anisotropic Structure of Gold Nanostars Using Good's Buffers. *Chem. Mater.* **2016**, *28* (18), 6763–6769. https://doi.org/10.1021/acs.chemmater.6b03242.
(39) de Puig, H.; Tam, J. O.; Yen, C.-W.; Gehrke, L.; Hamad-Schifferli, K. Extinction Coefficient of Gold Nanostars. *J. Phys. Chem. C* **2015**, *119* (30), 17408–17415. https://doi.org/10.1021/acs.jpcc.5b03624.
(40) McMillan, B. G.; Berlouis, L. E. A.; Cruickshank, F. R.; Pugh, D.; Brevet, P.-F. Transverse and Longitudinal Surface Plasmon Resonances of a Hexagonal Array of Gold Nanorods Embedded in an Alumina Matrix. *Appl. Phys. Lett.* **2005**, *86* (21), 211912. https://doi.org/10.1063/1.1939070.
(41) Shi, W.; Casas, J.; Venkataramasubramani, M.; Tang, L. Synthesis and Characterization of Gold Nanoparticles with Plasmon Absorbance Wavelength Tunable from Visible to Near Infrared Region. *ISRN Nanomater.* **2012**, *2012*, 659043. https://doi.org/10.5402/2012/659043.
(42) Hamdi, J.; Blanco, A. A.; Diehl, B.; Wiley, J. B.; Trudell, M. L. Room-Temperature Aqueous Suzuki–Miyaura Cross-Coupling Reactions Catalyzed via a Recyclable Palladium@Halloysite Nanocomposite. *Org. Lett.* **2019**, *21* (10), 3471–3475. https://doi.org/10.1021/acs.orglett.9b00042.
(43) Zeng, X.; Wang, Q.; Wang, H.; Yang, Y. Catalytically Active Silver Nanoparticles Loaded in the Lumen of Halloysite Nanotubes via Electrostatic Interactions. *J. Mater. Sci.* **2017**, *52* (14), 8391–8400. https://doi.org/10.1007/s10853-017-1073-y.
(44) Wu, S.; Qiu, M.; Guo, B.; Zhang, L.; Lvov, Y. Nanodot-Loaded Clay Nanotubes as Green and Sustained Radical Scavengers for Elastomer. *ACS Sustain. Chem. Eng.* **2017**, *5* (2), 1775–1783. https://doi.org/10.1021/acssuschemeng.6b02523.
(45) Osipova, V. A.; Pestov, A. V; Mekhaev, A. V; Abuelsoad, A. M. A.; Tambasova, D. P.; Antonov, D. O.; Kovaleva, E. G. Functionalization of Halloysite by 3-Aminopropyltriethoxysilane in Various Solvents. *Pet. Chem.* **2020**, *60* (5), 597–600. https://doi.org/10.1134/S0965544120050072.
(46) Häkkinen, H. The Gold–Sulfur Interface at the Nanoscale. *Nat. Chem.* **2012**, *4* (6), 443–455. https://doi.org/10.1038/nchem.1352.
(47) Pakiari, A. H.; Jamshidi, Z. Nature and Strength of M−S Bonds (M = Au, Ag, and Cu) in Binary Alloy Gold Clusters. *J. Phys. Chem. A* **2010**, *114* (34), 9212–9221. https://doi.org/10.1021/jp100423b.

Chapter 4

Halloysites as a vector for porphyrin-based photosensitizers for singlet oxygen ($^1O_2$) generation.

1 Introduction

1.1 Principles of Photodynamic therapy

The association of light and chemicals to treat diseases is referred as photochemotherapy. A particular form of photochemotherapy is photodynamic therapy (PDT). PDT is a therapy used to cause the death of cancer cells as well as of pathogens in localized infections. It is based on the exploitation of three main components: visible or near-infrared (NIR) radiation, a molecule that acts as photosensitizer (PS) and molecular oxygen present in tissues.[1]
Once the PS has been accumulated at the tumour level, it is irradiated with a proper light source and, absorbing a photon of light, it passes from the ground state to a short-lived excited singlet state ($^1PS^*$, **Figure 1**) as a first step. At this point, the PS can either return to the fundamental ground state ($^1PS^0$) by fluorescence (a property that can be clinically exploited for imaging and photodetection) or can switch by intersystem crossing to an excited triplet state ($^3PS^*$) characterized by longer lifetimes.[2]

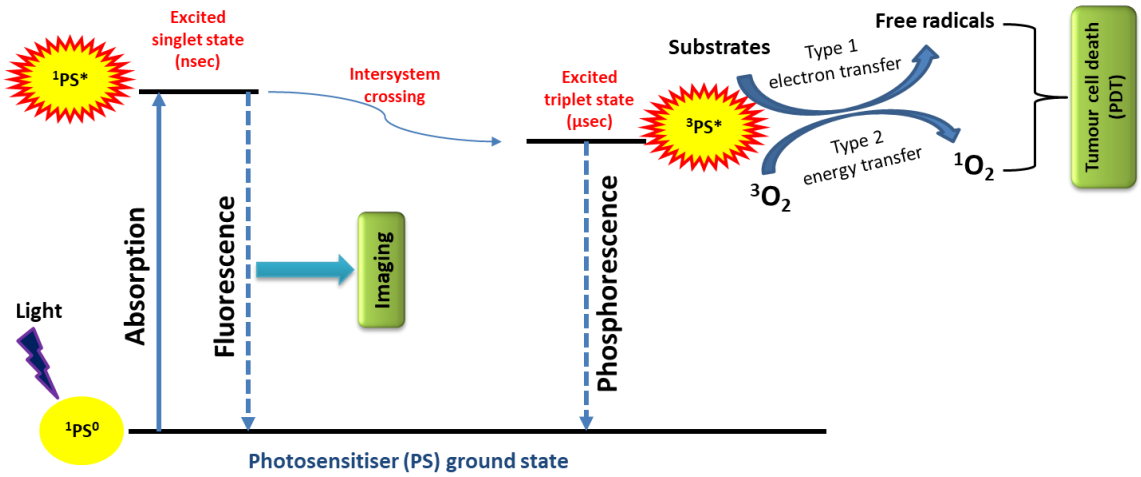

Figure 1 Schematic illustration of a typical photodynamic reaction.

Again, $^3PS^*$ can come back to the ground state by phosphorescence. Otherwise, it can interact with H_2O, O_2 or a biomolecule such as the cell membrane or a protein, and transfer an electron to form a radical species, such as superoxide anion radicals $O_2^{\bullet-}$, hydroxyl radicals $HO^{\bullet}$, and hydrogen peroxides H_2O_2. This electron transfer mechanism is referred to as Type I PDT.

Alternatively, (Type II PDT), the energy of $^3PS^*$ is transferred to molecular oxygen (which is a triplet when in its ground state), which is then converted into singlet oxygen ($^1O_2^*$), which is a highly cytotoxic species. This last transition requires small energy of ca. 22 kcal mol^{-1}, which

corresponds to a wavelength of 1274 nm.[3,4] The highly reactive species formed as a result of the type I and type II reactions are highly cytotoxic and capable of damaging nucleic acids, lipids and proteins. It is necessary to underline, however, that most of the studies indicate type II reactions[5] as the most active ones. Since singlet oxygen has very short lifetimes due to its reactivity (3.5 μs in H_2O and 0.2 μs inside cells)[6,7] hence it can act in a limited radius around the PS site (about 10 nm in diameter). in this way, only cancer cells or infected tissues are destroyed,[4,8] provided that the PS has reached and accumulated at the target site.

1.2 Photosensitizers

Many requirements should be kept in mind for the choice of a PS to be suitable for PDT. A good PS must have the following features:[9] i) it must be chemically pure with ease of large-scale production by the availability of the starting materials; ii) it must have good affinity with tumour tissues and give strong absorption in the visible or NIR with a high extinction coefficient (ε_{max}) in the region 600–800 nm, which is the so-called "therapeutic window". Indeed, in this range, the absorption from tissues is at the minimum and hence the light can deeply penetrate. Secondly, the energy associated with the light is low enough to be safe for healthy tissues.[10] iii) it should not strongly absorb light of the region 400–600 nm so that the risk of generalized photosensitivity caused by sunlight would be as small as possible.[11] iv) it should satisfy specific photophysical characteristics (high quantum yield of production of $^1O_2$*, the lifetime of ^{3}PS* relatively long).[12] v) it should be stable, non-toxic and resistant to degradation as photobleaching. Indeed, photobleaching should be avoided since it can shorten the duration of generalized photosensitivity after PDT) [13-14]
However, many PS that do not satisfy all these features, have been approved for clinical use, and they largely belong to the first and second generation of PS.[15]

The *first generation of photosensitizers* was based on Photofrin and hematoporphyrin derivatives (HPD). Photofrin was approved by Canada for the treatment of bladder cancer and by US FDA for treating oesophagal cancer and lung cancer. [16] HPD were approved for use in clinical applications in Russia, Brazil and EU.[17-18] The limitation of the first generation of PS, including its complexity, is mostly due to the strong absorption around 400 nm (the Soret band) and only much smaller absorption bands at longer wavelengths (Q-bands), and its tendency to be retained in the skin, thus producing cutaneous photosensitivity and prolonged cutaneous phototoxicity.[9]

The *second generation of photosensitizers* was based on porphyrinoid compounds, such as chlorines, bacteriochlorins, phthalocyanines, pheophorbides, acteriopheophorbies and texaphyrins as well as nonporphyrinoid. Compounds like 5-aminolevulinic acid (ALA) are known as second generation PS and have been developed to overcome the disadvantages of first-generation compounds. These PS usually have higher absorption at wavelengths longer than 630 nm, as well as high extinction coefficients, they also possess higher $^1O_2$ quantum yields, their toxicity in the absence of light is null and have higher tumour-to-normal tissue concentration compared to HpD.[14] ALA is the first prodrug of a second-generation photosensitizer for which all the clinical trial phases were passed and so it became available on the market was obtained, the others have been studied in phase I, II, or III of clinical trials for various indications.[12-13]

In the *third generation of photosensitizers,* the research is now focusing on further improving the second-generation of photosensitizers, in that they can i) be activated with the light of a longer wavelength, ii) provoke shorter generalized photosensitivity, and more importantly, iii) have better tumour specificity. These results could be achieved either by modifying the PS with targeting agents (such as antibody conjugation) or by encapsulating the PS into carriers (such as liposomes, micelles, and nanoparticles) that can transport the drug efficiently in blood from the administration site to the target tissue.[15]

The majority of PS currently in use for PDT studies are cyclic tetrapyrrolic structures, that is porphyrins and their analogues.[1,12,19,20]

1.3 Porphyrins

Porphyrins are heterocyclic molecules consisting of a tetra-pyrrolic ring, in which the four pyrrolic units are joined together in the α positions with CH methyl bridges (known as *meso* carbons). Porphyrins can be functionalized with different substitutes on pyrrolic rings and/or *meso* positions, or they can act as macrocyclic ligands to form coordination compounds (metalloporphyrin).[1,12,19–23]

Porphyrins are an important class of naturally occurring macrocyclic molecules found in biological compounds that play a very important role in the metabolism of living organisms. Porphyrins are present in natural systems as iron-containing complexes at haemoglobin level (heme) as well as magnesium-containing reduced porphyrin (or chlorine) found in chlorophyll.[24] Porphyrins are not cytotoxic species in the absence of light and this makes them ideal candidates for singlet oxygen production in biological systems.

Porphyrins are classified as regular or irregular on the bases of their absorption spectra, which means that while regular metalloporphyrins have a contribution to the absorption bands only from the π molecular orbitals of the porphyrin, in the irregular ones there is also a contribution from the metal centred d-orbitals. The regular porphyrins possess at room temperature and in solution a very strong absorption at ca 420 nm, which is indicated as B or Soret band ($S_2 \leftarrow S_0$ transition). Also, there are other much weaker absorption bands indicated as Q-bands starting from ca 500 to 650 nm ($S_1 \leftarrow S_0$ transitions). While in the free-base porphyrins the Q bands are four because of the transitions between the first two electronic states S_0 and S_1 together with two

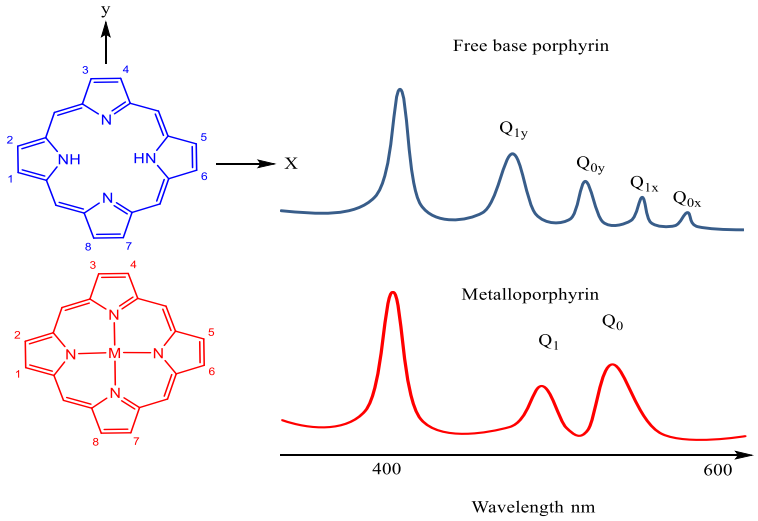

Figure 2a Schematic representation of the UV-vis spectrum of porphyrin free and coordinated to the metal. The x and y subscripts refer to the orientation (polarization) of the electric vector of the absorbed light with respect to the axes shown on the chemical structure diagram for free base porphyrin.

transitions from vibrational excited states (two 0-0 transitions and two overtones 1-0 - or vibronic bands - see **Figure 2a**), in the case of the metalloporphyrins these last two transitions are not active, so that only two Q bands are observable.

Porphyrins are also classified on the bases of their absorption according to the relative intensity of the Q bands[25]: etio- if the order is IV > III > II > I, rhodo- if the relative intensities is III > IV > II > I and a phyllo- if the order is IV > II > III > I (see **Figure 2b)**

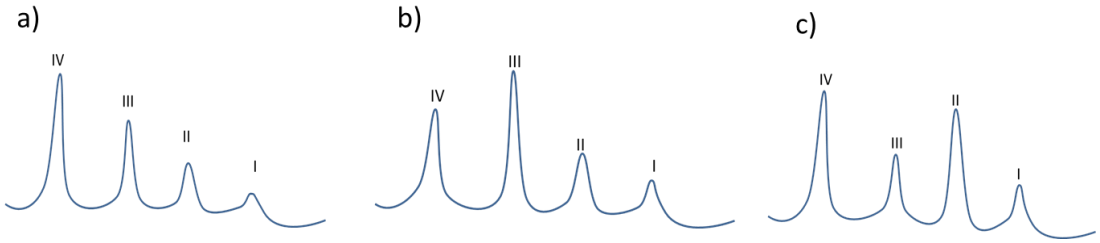

Figure 2b Schematic representation of the Q bands region of a UV-vis of (a) etio- (b) rhodo- and (c) phyllo-porphyrin.

Nevertheless it is already known that the relative intensity of the Q-bands in the etio-porphyrine is depending from the meso-substituents.[26]

Moreover, many porphyrins give rise to the formation of supramolecular self-assemblies, forming eventually porphyrin nanostructures.[27] Porphyrin nanomaterials exhibit unique physical properties which can be employed in many applications, especially for photocatalysis.[28]

In this current work, we focused on the perfluorinated and apolar porphyrin 5,10,15,20-tetrakis(perfluorophenyl)porphyrin (H_2TPPF_{20}) (**Figure 3** in blue) and its Zn complex [5,10,15,20-tetrakis(perfluorophenyl) porphyrinato]zinc(II) ($ZnTPPF_{20}$) (**Figure 3** in red). Indeed, the free base is particularly apolar, so it could act as a good model for apolar drugs that suffer from solubility problems in a water environment.

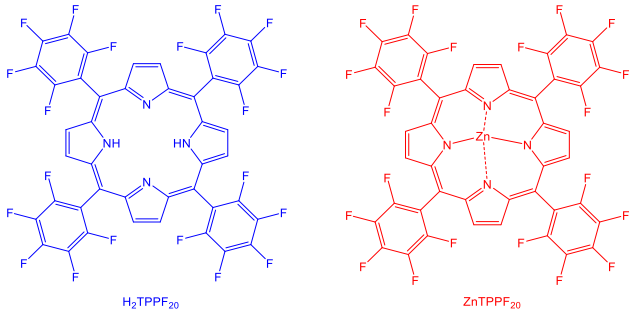

Figure 3 Chemical structure of porphyrins used in our work: the free base form (blue) and its Zn-coordinated form (red).

1.4 H_2TPPF_{20} and $ZnTPPF_{20}$

It is already known that, being unsoluble in water, 5,10,15,20-tetrakis(pentafluorophenyl)porphyrin (H_2TPPF_{20}) self assembles in water as reported in the literature.[28] The UV-vis absorption spectrum of H_2TPPF_{20} in THF is reported in **Figure 4a**, while the Soret band of H_2TPPF_{20} in THF and THF/water is zoomed in in **Figure 4b**. The whole

spectrum (**Figure 4a**) shows, apart the Soret band, three Q bands only, being the fourth one too low in intensity to be detected.

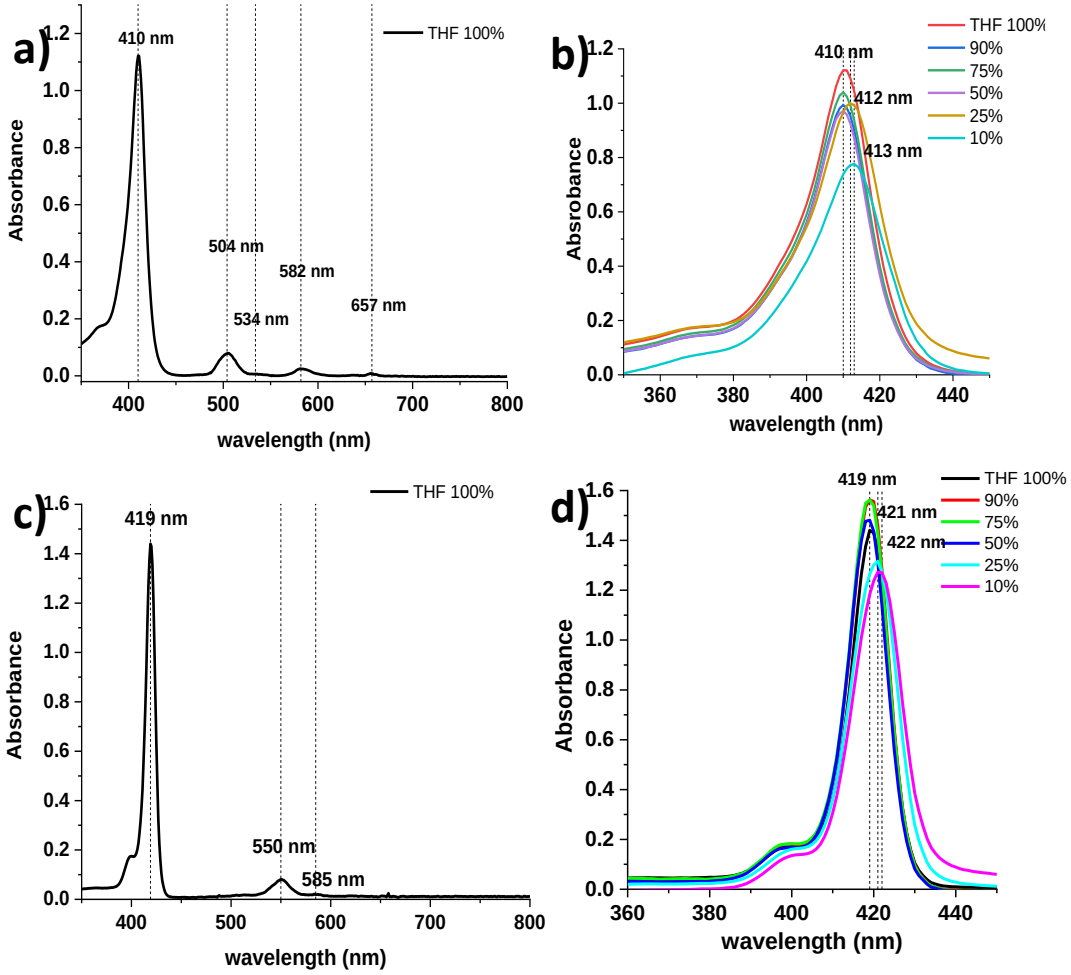

Figure 4 UV-vis absorption spectra of H_2TPPF_{20} in pure THF (**a**) and mixtures THF/H_2O with increasing amounts of water (**b**, region of the Soret band). UV-vis absorption spectra of Zn-$TPPF_{20}$ in pure THF (**c**) and mixtures THF/H_2O with increasing amounts of water (**d**, region of the Soret band).

It is known that as the water content is increased the aggregation increases as well. In THF, H_2TPPF_{20} is completely soluble and the spectrum of the single molecule is observable with the Soret band centred at 410 nm, which remains unchanged until 50% of water is added. For the ratio THF/water 25:75 the Soret band is red-shifted by 2 nm and by another 1 nm for the ratio THF/water 10:90, indicating the formation of a J-aggregate as suggested in the literature.[28] The same shift has been observed for Zn-$TPPF_{20}$ in the same solvent mixtures (**Figure 4c** and **d**).

In addition, an important feature that makes porphyrins suitable to act as photosensitizers is the lifetime of the triplet state ($^3PS^*$) which is relatively long.[1] Perhaps the most serious limitation of these kinds of photosensitisers is the low absorbance of the most red-shifted bands in the electronic spectrum (Q-bands), which is less than ideal for PDT requirements.

The absorption spectrum of H_2TPPF_{20} and $ZnTPPF_{20}$ is similar to that of Photofrin and hematoporphyrin derivative.[12,22,23] It is a so-called etio-type spectrum,[29] containing the strong Soret band, typical of porphyrins, at about 410 nm and the Q-bands of lower intensity at 504, 534, 582, and 657 nm. Absorption at 657 nm is the weakest, but light of this wavelength is

used in PDT, because it penetrates deepest into tissues. Consequently, to achieve a certain therapeutic effect, either large doses of photosensitizer and light are needed, as well as the protection of the drug through a carrier.

Halloysite nano tubes can be used as PS transport platforms as witnessed by many reports describing these vectors that if properly functionalized can accumulate in cancer cells without affecting the healthy ones. Moreover, the use of hydrophilic and biocompatible vectors allow to transport insoluble PS (H_2TPPF_{20}) in a biological environment.

The aim of this work is to develop modified Halloysite nanotubes for the in situ delivery of a suitable photosensitizer for photodynamic therapy. The final goal would be to synthesize a halloysite nanotubes internally functionalized with photosensitizers together with SPION to ensure controlled and selective release triggered through the application of an external magnetic field, that stimulates SPION that in turn provoke the drug release with the application of an external stimulus.

2 Results and discussion

First of all, we assessed the ability of our system to generate singlet oxygen, not for verifying the photosensitizer properties that were already known,[30–32] but rather to ascertain that the power and the emission spectrum of the used led light was the proper one to stimulate the PS. Then we passed to the loading setup, aimed to load selectively in the inner lumen the PS, and after the characterization we passed finally to study the release of the loaded porphyrins, comparing different samples.

2.1 Photoreaction of H_2TPPF_{20} and $ZnTPPF_{20}$ with 1,5-Dihydroxynaphthalene as a Reporter of $^1O_2$ Formation

The ability of H_2TPPF_{20} and $ZnTPPF_{20}$ to act as sensitizers for $^1O_2$ generation was assessed by using 1,5-dihydroxynaphtalene (DHN) as an indirect reporter of singlet oxygen. DHN reacts promptly, quantitatively and selectively with $^1O_2$ forming the oxidized species Juglone (5-hydroxy-1,4-naphthalenedione)[33,34] according to **Scheme 1**:

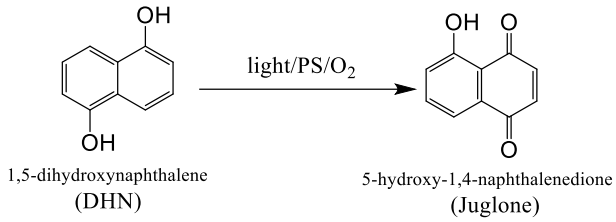

Scheme 1. Photochemical reaction used to monitor $^1O_2$ formation in the presence of an effective PS.

The reaction progress was monitored by UV–vis absorption spectroscopy following the decrease in the DHN band at 300 nm and the concomitant increase of the large Juglone band centred at 427 nm, which in our case was partly overlapped with the very strong Soret band of the PS (**Figure 5**). This reaction occurs without the formation of long-lived intermediates or by-products as indicated by the two isosbestic points at 280 and 330 nm observed in the spectra recorded during the irradiation.

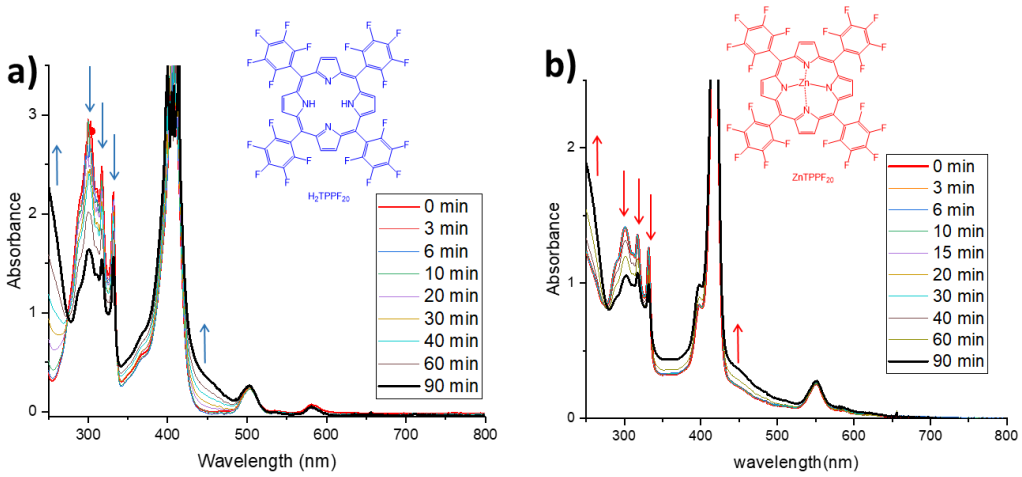

Figure 5 UV–vis absorption spectra recorded at different times of irradiation of LED lamp on solutions containing (a) H_2TPPF_{20} (1.9×10^{-5} M) or (b) $ZnTPPF_{20}$ (1.8×10^{-5} M) and DHN (3.7×10^{-4} M) in 2.6 mL of EtOH bubbled with O_2 for 10 min.

Figure 6 shows the first-order semilogarithmic plots for the reaction of equation **4.1**, sensitized by either H_2TPPF_{20} and $ZnTPPF_{20}$.

$$DHN + {}^1O_2 \rightarrow juglone + \frac{1}{2}\ {}^3O_2 \qquad \text{(Eq. 4.1)}$$

We carried out the experiments by mixing an ethanol DHN solution with one of either H_2TPPF_{20} or $ZnTPPF_{20}$, and after being saturated with O_2, it was irradiated for a total time of 90 min monitoring the evolution of the species by UV-vis spectroscopy.

The disappearance of DHN followed a pseudo-first order kinetic low, which is due to the adoptable steady-state approximation to the oxygen concentration, and the reaction rate can be related to the DHN concentration with a kinetic equation equal to $r = k_{obs}[DHN]$, whose integrated equation is (**Eq. 4.2**)

$$ln\frac{A_t}{A_0} = -k_{obs}t \qquad (Eq.\ 4.2)$$

The pseudo first-order semilogarithmic plots for DHN photo-oxidation in the presence of the investigated sensitizers are shown in **Figure 6**, where the values of $\ln(A_t/A_0)$ decrease linearly over time. While in the case of $ZnTPPF_{20}$ the slope (k_{obs}) is -0.028 min^{-1} compared to -0.051 min^{-1} for H_2TPPF_{20}.

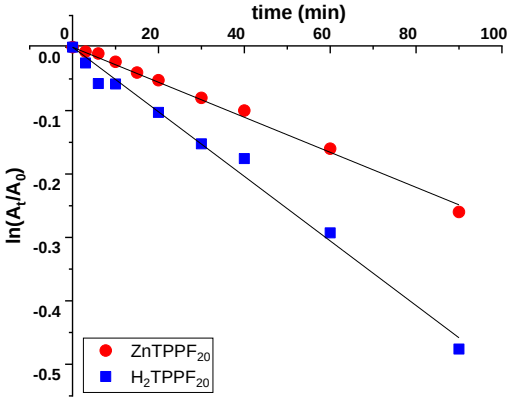

Figure 6 Photo-oxidation of DHN in the presence of photosensitizers H_2TPPF_{20} and $ZnTPPF_{20}$. A_t and A_0 represent the absorbance measured at 300 nm (the maximum of the DHN absorption band) at time t and time 0, respectively.

2.2 Drug loading

We carried out the loading of the PS by using the vacuum/nitrogen cycles strategy,[37] by dissolving the porphyrins in a proper solvent in the presence of the suspended pristine HNT or tetradecyl phosphonic acid-modified HNT (HNT-TDP).[38,39] After centrifugation and several washings of the recovered pellets, we observed that a colour change occurred, and from the white colour of the bulk HNT there was a turn to the colours listed in **Table 1**. The pictures of the samples observed under sunlight are reported in **Figure 7**. All the sample treated with porphyrins were luminescent under UV-lamp irradiation. Besides the loaded samples, we have also prepared two ground samples, grinding in a mortar the pristine HNT with either H_2TPPF_{20} or $ZnTPPF_{20}$.

Table 1 Colour change of loaded sample in the visible light and under UV lamp

Content	Colour under visible light	Colour under UV-lamp
H_2TPPF_{20}	deep purple	red
Zn-$TPPF_{20}$	Violet	orange
H_2TPPF_{20} -HNT	Very Pale yellow	red
Zn-$TPPF_{20}$-HNT	Very Pale pink	orange
H_2TPPF_{20} -HNT-TDP	Pale yellow	red
Zn-$TPPF_{20}$-HNT-TDP	Pale pink	orange

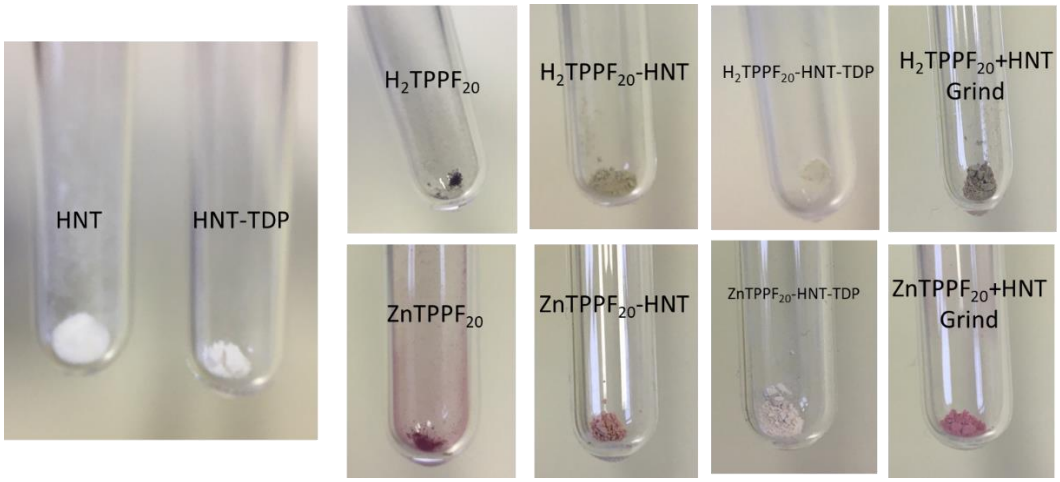

Figure 7. Digital pictures of the HNT samples before and after the interaction with H_2TPPF_{20} and Zn-$TPPF_{20}$, as indicated by the label, together with two samples of H_2TPPF_{20} and Zn-$TPPF_{20}$ alone.

2.3 Dextrin HNT capping

In order to avoid a burst release in the very first few minutes once the HNT-composites were re-suspended in water, we carried out a capping step with a pH sensitive polymer such dextrin is. After drying the loaded samples, the capping process was carried out as already described in the literature (see Experimental Part).[37,40] The success of the HNT capping process with dextrin was assessed by TEM analysis (**Figure 8**) together with thermogravimetric analysis (TGA, see below). The polymer was not easily detectable in the TEM images. Nevertheless, a careful comparison of the non-capped and capped HNT helped in recognizing the dextrin cap (highlighted with blue arrows in the images) at the entry of HNT tube and on the outer surface as a curved light-gray layer. Also TEM shows the presence of drug in inner lumen as blue arrows indicate.

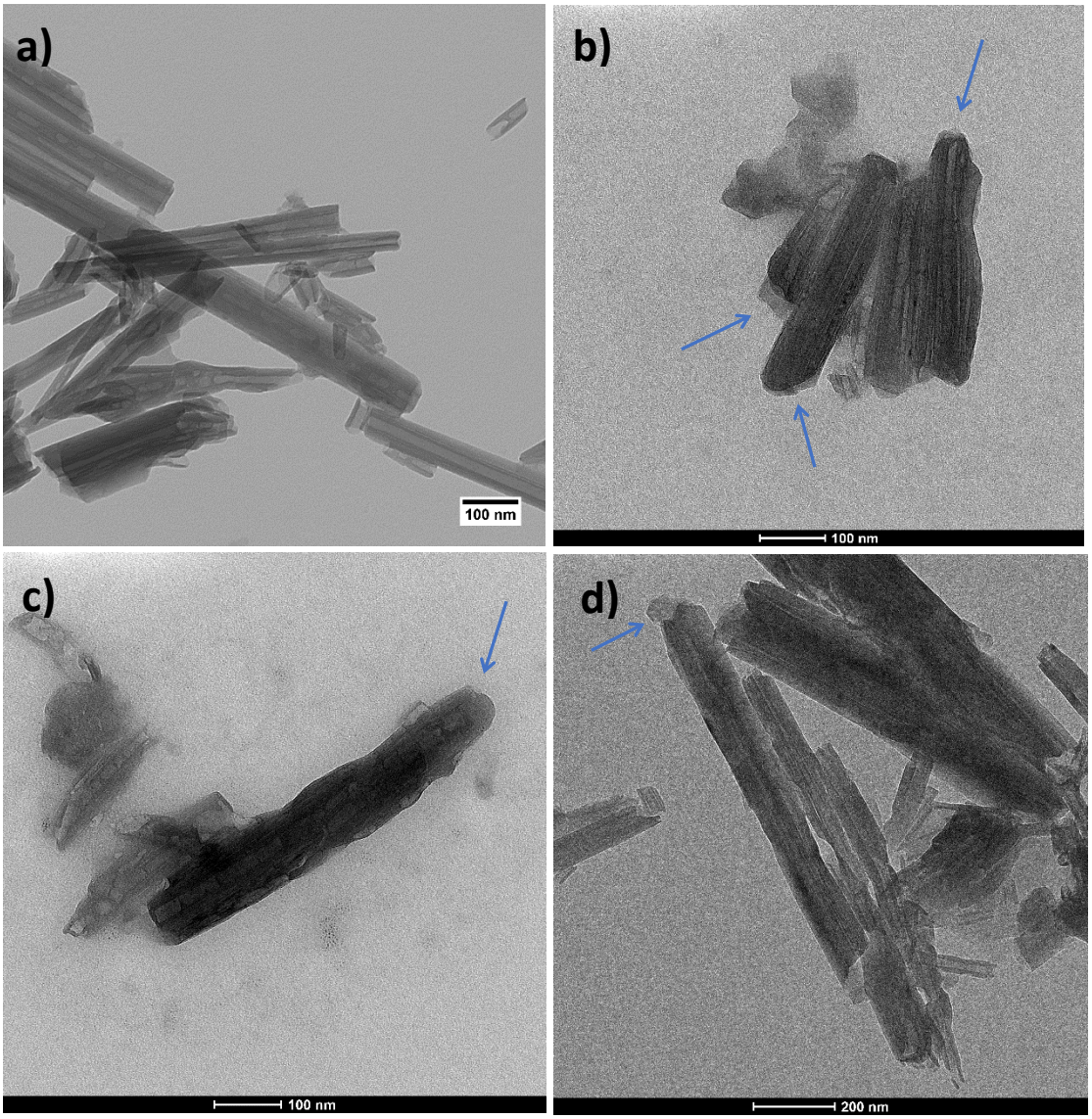

Figure 8. TEM images for a) HNT-TDP - Zn-$TPPF_{20}$ b) capped H_2TPPF_{20}-HNT c) capped H_2TPPF_{20}-HNT-TDP and d) capped $ZnTPPF_{20}$-HNT-TDP. Blue arrows indicate the dextrin cap. Notice the bubbles in the inner lumen indicating the drug loading.

2.4 Characterization of HNT-porphyrin derivatives

2.4.1 Infrared spectroscopy

To spectroscopically investigate on the adducts, confirm the success of the loading, and get some hints about the localization (in the inner lumen or on outer HNT surface), we started collecting ATR-FTIR spectra on the neat powders. The H_2TPPF_{20} and Zn-$TPPF_{20}$ are easily distinguishable by FTIR spectroscopy, being absent the N-H weak vibration stretching bands at 3320 and 3100 cm^{-1} in the case of the Zn-$TPPF_{20}$ (**Figure 9**) while the band at 2920 cm^{-1} is attributed to CH (pyrrole) and present in both the species.[29,41,42]

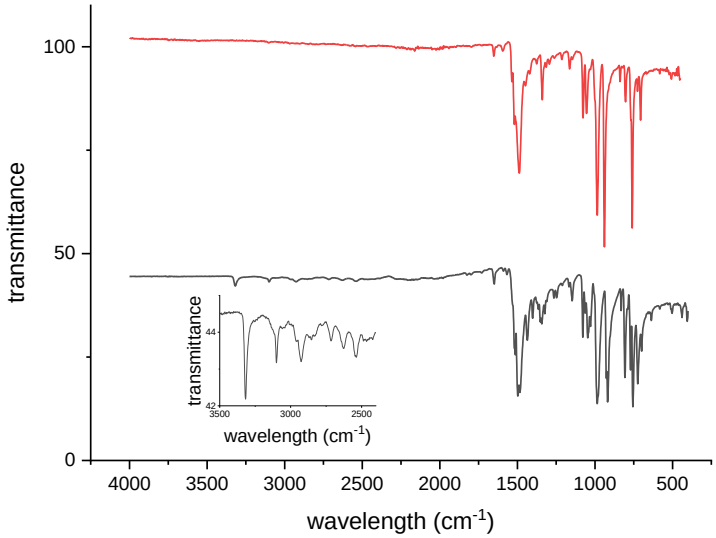

Figure 9. ATR-FTIR spectra of H_2TPPF_{20} (gray trace) and Zn-$TPPF_{20}$ (red).

Unfortunately, these peaks resulted undetectable when we analyzed the several prepared HNT-adducts both due to their low intensity and to the accidental overlap with the OH broad peak of dextrin in the capped samples, with the inner trapped water of HNT in all the samples, and with the CH of TDP where present. More useful for the identification of the porphyrin was the region between 1600 and 1400 cm^{-1}. The strong band at ca. 1600 cm^{-1} is attributed to the symmetric angular deformation in the N–H plane of the pyrrole ring.[42] The bands at 1520 and 1513 cm^{-1} are due to the C-C and the C-N of pyrrole ring, respectively[43] and the bands centred at 1500 and 1480 are attributed to the stretching of the C=C and the C-C bonds of the fluorinated benzene ring.[43–45] These bands were observed in porphyrin ground samples only, while in the loaded samples even these peaks were undetectable due to the low detection limit of this spectroscopy (**Figure 10,** red rectangles). Also in the case of Zn-$TPPF_{20}$ (**Figure 10** bottom) the major peaks (1590, 1530, 1520, 1490 and 1340 cm^{-1} for C=C C=N, C-C and C-N of pyrrole and fluorinated benzene ring)[43–45] were not detectable for the loaded samples.

Even more so for HNT treated with TDP and HNT coated with dextrin (**Figure 11**) where the content of porphyrins is lower, the signals of these last were undetectable.

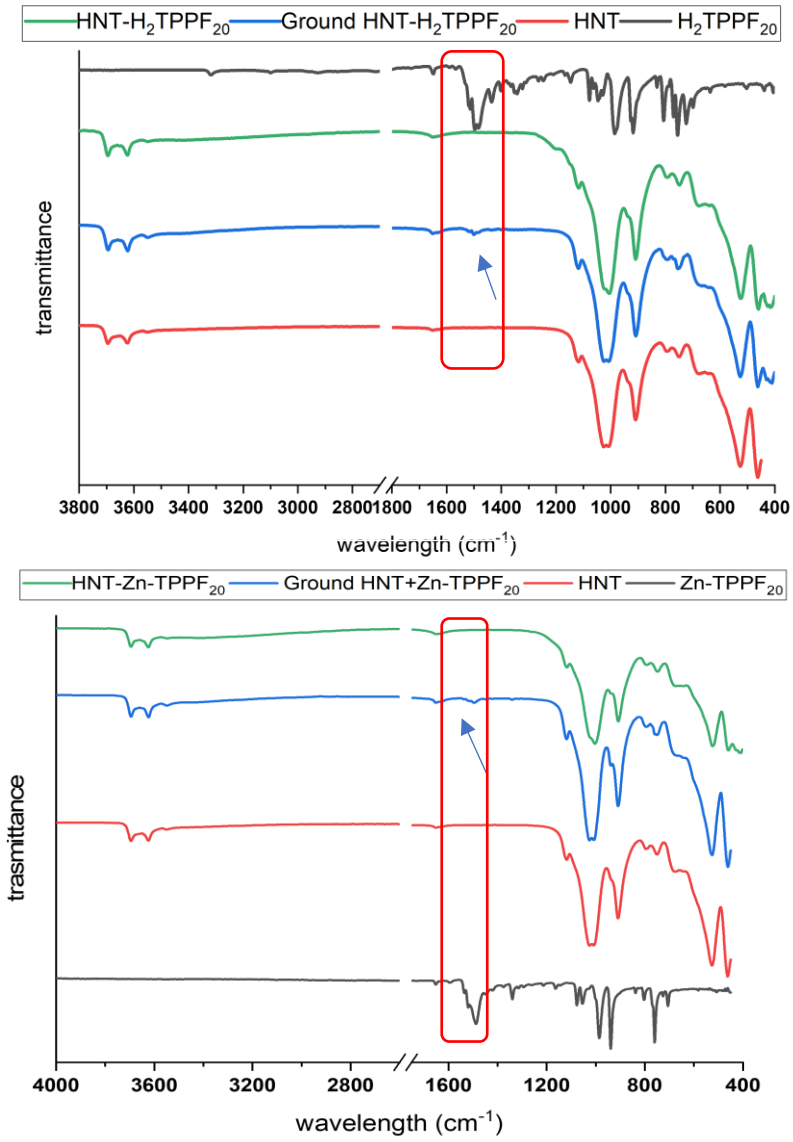

Figure 10. ATR-FTIR spectra of pristine halloysite (red), the porphyrins (gray traces), the ground samples (blue) and the loaded with H_2TPPF_{20} and (d) Zn-$TPPF_{20}$ (green).

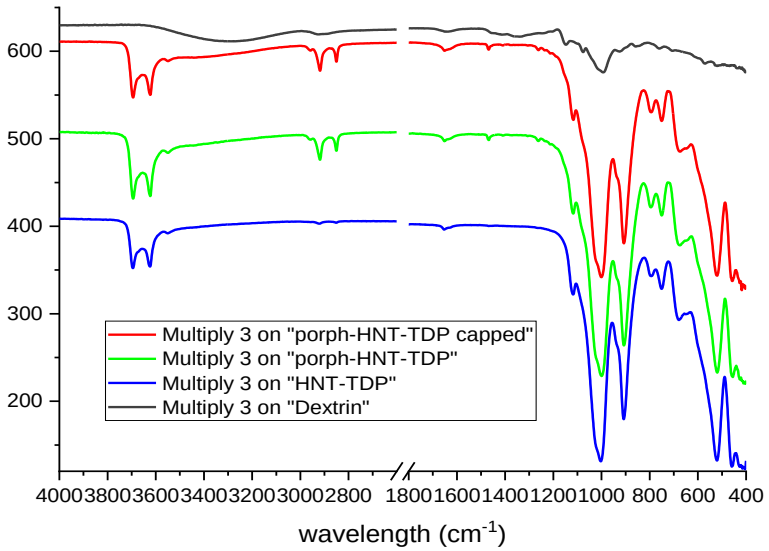

Figure 11. ATR-FTIR spectra of dextrin (grey), HNT modified with TDP (blue) and the same HNT-TDP after loading with H_2TPPF_{20} before (green) and after the capping with dextrin (red).

2.4.2 Diffuse reflectance UV spectroscopy

Diffuse reflectance ultraviolet spectroscopy (DRUV) was taken into account as an alternative technique much more sensitive than ATR-FTIR for the characterization of HNT samples.

The DRUV spectra of HNT and HNT-TDP (traces blue and red, respectively of **Figure 12**) showed a marked absorption peak in the UV region (peaking at ca 260 nm) typical of this type of inorganic oxide matrixes. Moreover, they showed also three typical peaks at 1408 nm, 1920 nm, 2208 nm attributed to the water[46] possibly present both externally, internally and in the interlayer districts (**Figure 12**, zoomed in panels **e** and **f**). In the same region and for the TDP-containing samples only, a band peaking at 1733 nm was attributed to TDP. As it is clear from the comparison of the DRUV spectra reported in **Figure 12**, while for the pristine HNT and HNT-TDP there wasn't an absorption peak in the range 400-700 nm, the H_2TPPF_{20} and Zn-$TPPF_{20}$ exhibited the characteristic B and Q bands of porphyrins,[47–49] confirming the presence of H_2TPPF_{20} and Zn-$TPPF_{20}$ in all the four loaded samples. The H_2TPPF_2 absorption spectrum (**Figure 12a**) shows the typical 5 bands, the B band at 419 nm (S0→S2 transition) and the weaker Q-bands(**Figure 12c)** at 505, 538, 582 and636 nm (S0→S1 transition). These bands are quite similar to the ones of the porphyrin dissolved in THF (see **Figure 4a**), except for the last Q band that results in blue-shifted of ca. 20 nm. On the contrary, the two loaded samples HNT-H_2TPPF_{20} and HNT-TDP-H_2TPPF_{20} present also the fourth Q-band at the very same wavelength as the porphyrin in solution (652 nm). This similarity with the spectrum in solution suggests that the molecules are not packed as in the solid-state, and this could suggest an inner lumen localization. Passing from the free-base to the Zn-porphyrin the ring symmetry of the planar macrocycle increases from D_{2h} to D_{4h}, and this simplifies the solution spectrum, and only two Q-Bands are observed at 550 and 585 nm (**Figure 4c**). In the DRUV spectrum of Zn-porphyrin, apart from the two Q-bands at 543 and 583 nm a third evident transition is present at 630 nm is visible (**Figure 12d**). This band together with other overlapped bands to the principal absorption ascribable to the metalloporphyrin, are very similar to those of the free base. Also in this case, the two loaded samples showed a significant shift of the Q-bands: the first one becomes equal to the one observed in solution (550 nm), the second one is present for the HNT-Zn-$TPPF_{20}$ spectrum (ca. 583 nm) while completely disappears for the HNT-TDP-Zn$TPPF_{20}$ sample for which a new band a 622 nm becomes much evident. In conclusion, the whole evidence is that for the loaded samples the absorption profiles of the Q bands are quite different from the ones of the solid phase and resembles more the solution situation, and this can suggest that the inner lumen loaded molecules are not able to crystallize as the neat powder and they retain a more disordered or amorphous state.

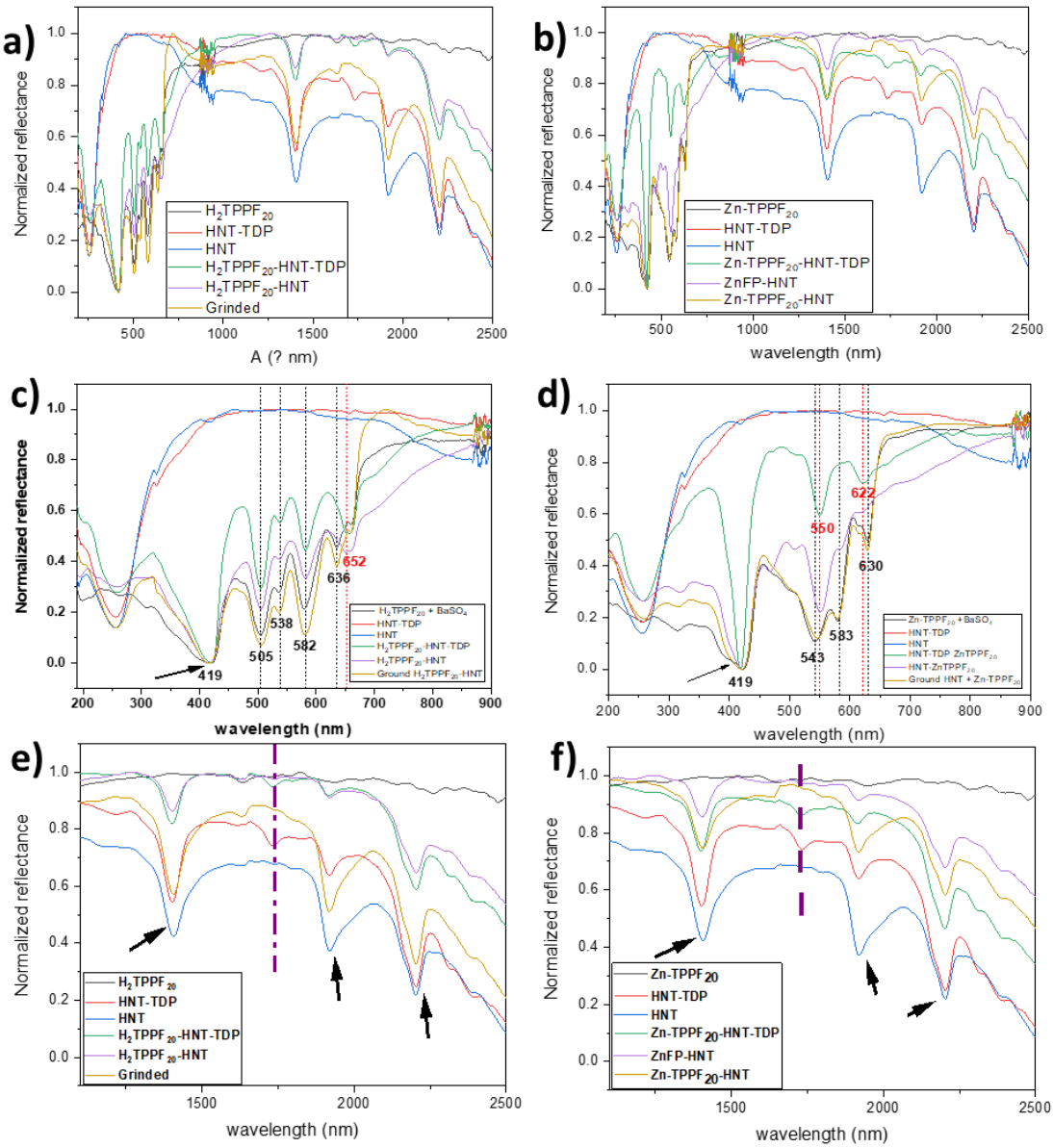

Figure 12 Diffuse reflectance ultraviolet spectra (DRUV) of halloysite pristine and modified with TDP loaded with H_2TPPF_{20} (left column) or Zn-$TPPF_{20}$ (right column).

2.4.3 Thermogravimetric analysis

The loading percentage of H_2TPPF_{20} and $ZnTPPF_{20}$ was estimated gravimetrically through TGA-DTGA analysis (**Figure 13**), whose results are summarized in **Table 2**. All the analyses were carried out under air flux.

The TG profile of the two ground samples (**Figure 13a** and **13b**) showed, apart from the initial weight loss due to hydration water (common to all the samples), the interlayer water and the OH dehydration typical of the HNT (onset temperature 410 °C, see Chapter 2), a weight loss due to the thermo-oxidative degradation of porphyrin and metalloporphyrin, respectively, characterized by an onset temperature of 290 °C and an inflection point at ca. 375 °C.

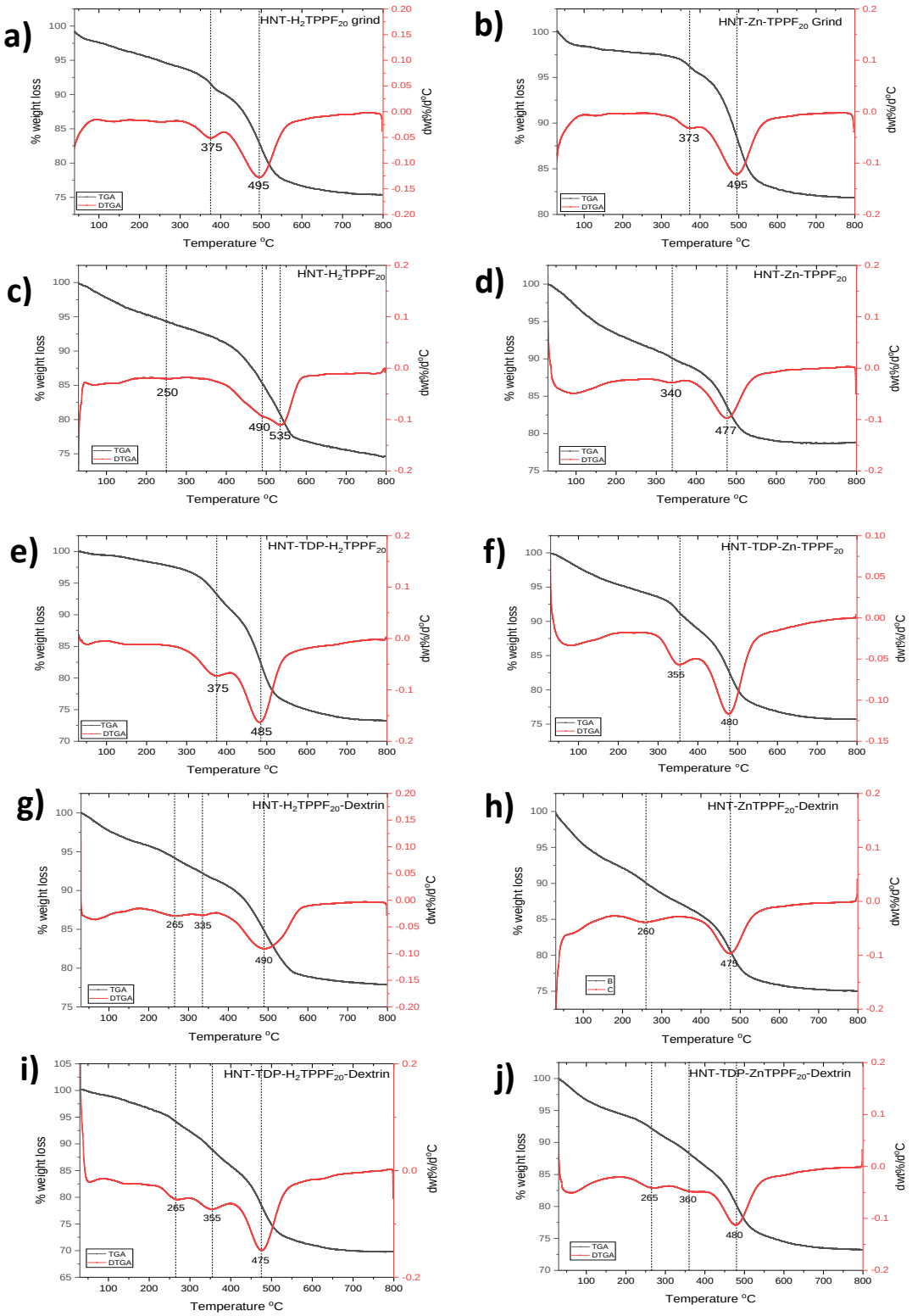

Figure 13. TGA-DTGA of ground HNT with H_2TPPF_{20} and Zn-$TPPF_{20}$ (panels a and b, respectively), and pristine halloysite and modified with TDP before and after dextrin capping loaded with H_2TPPF_{20} (left column) or Zn-$TPPF_{20}$ (right column).

The comparison of these TG curves with the ones of the loaded samples (**Figure 13c** and **d**) highlighted some differences, in particular with the loaded sample HNT-H_2TPPF_{20} (**Figure 13c**) Indeed, in this case, it is noticeable the presence of some THF still present due to the loading

procedure that could even be intercalated into the interlayers. Also the interlayer water is contributing to this first part of the curve. This provoked first of all an inclination of the plateau prior to the thermo-oxidation of the porphyrin. More interesting is the shift of the thermo-oxidation of both the porphyrin and of the OH dihydroxylation of the inner lumen. The slowdown of both the processes could be interpreted as evidence of the localization of the porphyrin in the inner lumen. On the contrary, the thermal degradation processes in the analogue Zn-based sample, the loaded HNT-ZnTPPF$_{20}$, appeared to be slightly accelerated, maybe caused by a catalytic effect due to the presence of the metal centre. The estimation of the H_2TPPF$_{20}$ loaded mass % for the loaded HNT-H_2TPPF$_{20}$ was made by subtracting the OH dihydroxylation contribution to the whole step proportionally corrected. This way we concluded that H_2TPPF$_{20}$ accounted for **3.1%**. In the case of the loaded sample HNT-ZnTPPF$_{20}$, the amount was directly measurable from the separated peak presenting an inflection point at 340 °C, and that accounted for the **3.2%** of weight loss.

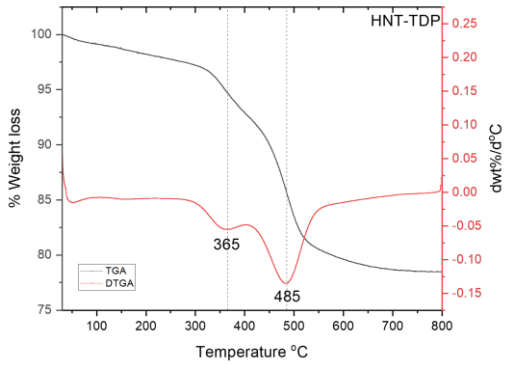

Figure 14. TGA and DTGA profiles of HNT-TDP.

In the case of TDP-containing samples, there was an overlapping of the weight loss step due to the oxidation of TDP and the one of the porphyrins. The step due to porphyrin (see above) differs from that of the TDP (see **Figure 14**) in that the latter has a slightly lower onset temperature (275 °C) with an inflection point at 365 °C. This similarity in the degradation range of porphyrins and TDP complicated the quantification estimation of porphyrin present in those samples in which HNT was functionalized with TDP (**Figure 13e** and **13f**). For this reason, we opted for a calculation that provided the quantification of the loaded drug by difference with the HNT-TDP precursor after a proportional adjustment. This procedure accounted for **3.4%** of porphyrin and only **1.5%** of Zn-porphyrin when the lumen was functionalized by TDP. This can be explained by the higher polarity of the Zn-porphyrin compared to the free base form, and hence the lower affinity with the apolar lumen.

The last four samples were the ones treated with dextrin, used as a stopper for the entry of the lumen (**Figure 13g-l**). The dextrin can be easily recognized by the DTGA profile. Indeed, in all the four analyses, a peak centred at ca 265 °C (corresponding to the inflection point) was diagnostic for its presence. The amount of porphyrin or Zn-porphyrin in these final samples resulted generally decreased compared to their precursors. The loss of the drug has been attributed due to the stirring step, during which the release from the HNT lumen can occur. Only in the case of the loaded HNT-TDP- H_2TPPF$_{20}$-dextrin sample, there was any loss, indicating the high affinity of the apolar inner lumen and the perfluorinated free-base porphyrin. The % amounts in each sample are summarized in **Table 2**.

Table 2 Drug content % estimated through TGA -DTGA analysis for different loaded samples

Sample content	Drug %	TDP%	Dextrin%	Loading efficiency %
HNT- H_2TPPF_{20}	3.1	-	-	62
HNT-TDP- H_2TPPF_{20}	3.5	5.7	-	70
HNT- H_2TPPF_{20}-Dextrin	3.0	-	2.9	60
HNT-TDP- H_2TPPF_{20}-Dextrin	3.5	5.2	4.25	70
HNT- Zn-PPF_{20}	3.2	-	-	64
HNT-TDP- $ZnTPPF_{20}$	1.52	4.4	-	30
HNT- $ZnTPPF_{20}$-Dextrin	2.9	-	2.3	58
HNT-TDP- $ZnTPPF_{20}$-Dextrin	1.35	4.4	2.01	27

2.5 Emission of H_2TPPF_{20} and $ZnTPPF_{20}$

As to the luminescence of this free-base porphyrin, it has been already described in the literature[28] dissolved in THF as well as in its aggregated form as the amount of water was increased. The photoluminescence emission spectrum of H_2TPPF_{20} in THF showed three main emission bands centred at 637, 657 and 704 nm (**Figure 15**). On increasing the amount of water, and in particular for 80% water content, the spectrum completely changed, being almost totally quenched the transition at 637 and 704 nm, while remaining visible the middle transition even if slightly red-shifted at ca 670 nm. The heavy change of the emission profile is ascribed to the aggregation towards the formation of J-aggregates. [28,50]

First of all, we characterized the emission of H_2TPPF_{20} and the $ZnTPPF_{20}$ in the solid phase, to be compared with the adducts of these two porphyrins with both pristine HNT and pre-functionalized HNT with TDP (HNT-TDP). The emission spectrum of H_2TPPF_{20} and the one of the metal-porphyrin Zn-$TPPF_{20}$ are reported in **Figure 16**.

The emission profile of solid H_2TPPF_{20} presented two main bands at 664 and 703 nm that resembled the one of the aggregate observed in the mixture THF/H_2O 80:20 rather than the emission profile of the isolated molecules in THF solution.[50]

As expected, the emission spectrum of H_2TPPF_{20} did not change upon varying the excitation wavelength (**Figure 17**, presenting always the two main peaks and some minor shoulder bands possibly due to excited vibronic transitions. In the case of $ZnTPPF_{20}$ the excitation wavelength modulated the emission intensity only of the transition at lower energy (689 nm), while the transition at 634 nm passing from 423 to 470 nm remains constant (**Figure 17**).[51]

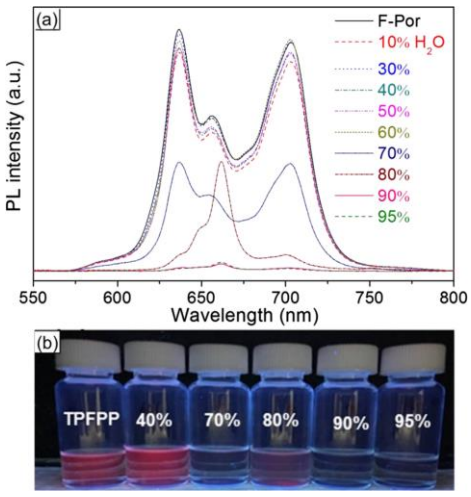

Figure 15 (a) Emission spectra of monomeric H_2TPPF_{20} (black line) and H_2TPPF_{20} upon the addition of H_2O from 10 to 95% (λ_{ex}=407 nm). (b) Picture of H_2TPPF_{20} in THF and THF/H_2O irradiated by UV light. [28]

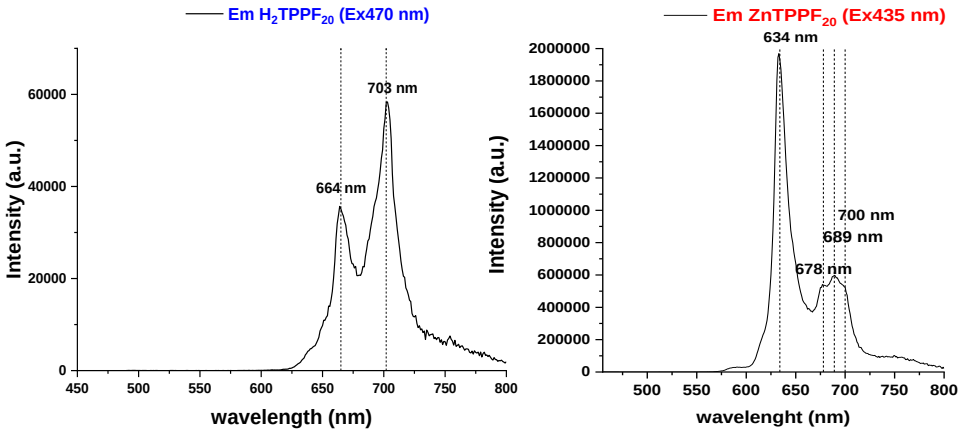

Figure 16. Solid state emission spectra of H_2TPPF_{20} and Zn-$TPPF_{20}$ (λ_{ex} = 470 nm and 435 nm, respectively).

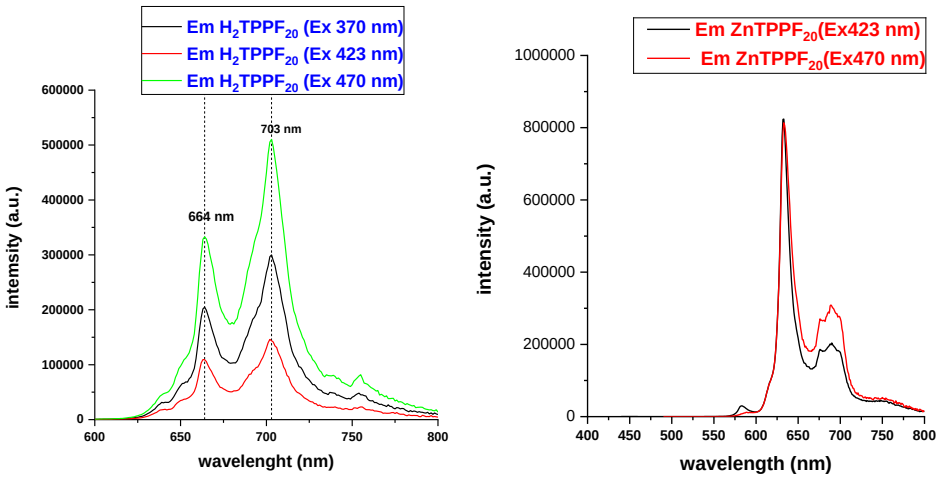

Figure 17. Solid state emission spectra of (Left) H_2TPPF_{20} (λ_{ex} = 370, 423, and 470 nm) and (right) Zn-$TPPF_{20}$(λ_{ex} = 423, and 470 nm) respectively.

The excitation profiles of the free base and Zn-porphyrin complex are reported in the following **Figure 18**. Their profile with a sort of extended plateau is normal when aggregates are present.

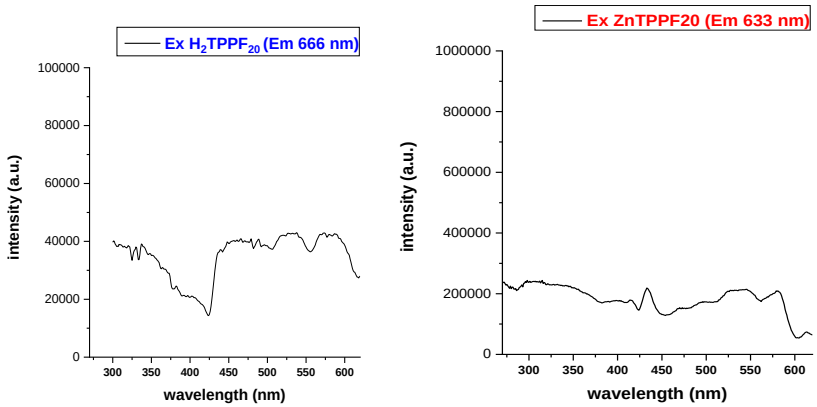

Figure 18. Excitation profiles of H_2TPPF_{20} (λ_{em} = 666 nm) and Zn-$TPPF_{20}$ (λ_{em} = 633 nm).

In order to understand if the loading of the porphyrin by vacuum/N_2 cycles afforded the HNT-porphyrin composite in which the porphyrin was loaded selectively into the HNT inner

lumen, we analyzed the emission spectra of the loaded HNT-porphyrin together with a sample of HNT mechanically mixed with H_2TPPF_{20} by grinding them into a mortar. This way, we were sure that the interaction of porphyrin with HNT, if any, was only with the silica-based external part of the nano-clay. Moreover, we tried also to verify if the employment of the pre-functionalized HNT-TDP was more effective for the inner loading due to the apolar internal environment formed by the tails of TDP. In the next **Figure 19** the emission spectra of loaded HNT- H_2TPPF_{20} (c), HNT-TDP- H_2TPPF_{20} (d)and the ground HNT + H_2TPPF_{20} (b) are shown.

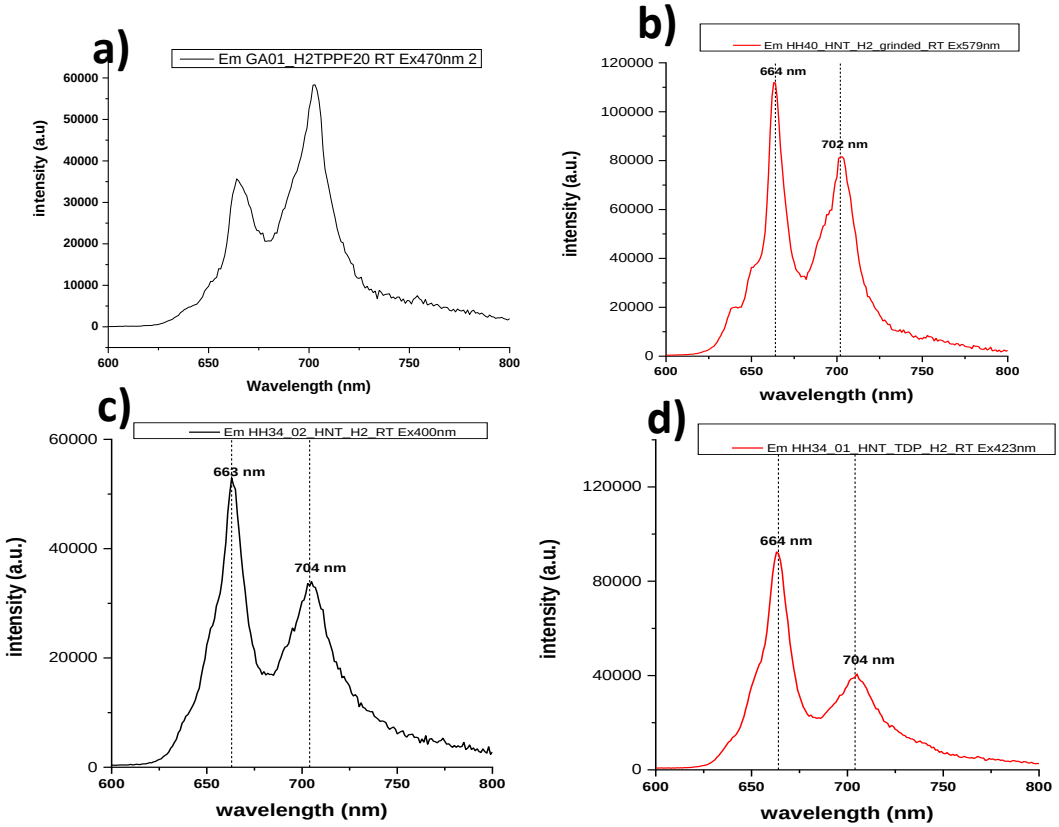

Figure 19. Emission spectra of a) H_2TPPF_{20} (λ_{ex} = 470 nm) b) dry HNT mixed with solid H_2TPPF_{20} (λ_{ex} = 579 nm) c) HNT loaded with H_2TPPF_{20} (λ_{ex} = 400 nm) d) HNT-TDP loaded with H_2TPPF_{20} (λ_{ex} = 423 nm)

The emission spectra of all the samples were acquired exciting at three distinct wavelengths and in any case, a dependence from the excitation wavelength was detected as expected by Kasha's rule. The differences between the four species were minimal, but by comparing the spectra of the four different situations into which the porphyrin can be found (**see Figure 20**), we can list: i) the relative intensity of the two main bands in the three HNT-Porphyrin adducts increase by passing from the ground sample to HNT-porphyrin to HNT-TDP-porphyrin; ii) the sample of neat porphyrin shows an inverted relative intensity of the two bands.

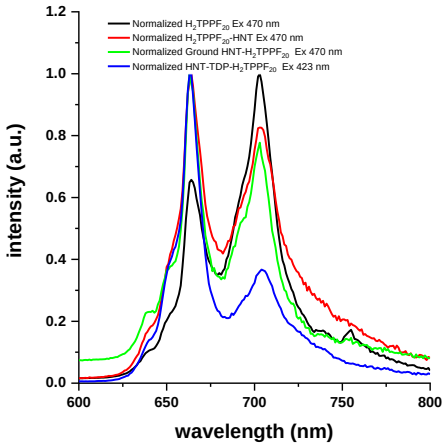

Figure 20. Superposition of the normalized emission spectra of H_2TPPF_{20} alone, loaded HNT-H_2TPPF_{20}, HNT-TDP-H_2TPPF_{20} and the ground HNT + H_2TPPF_{20}.

The spectra on the solid form is not resembling the spectrum of the aggregates in solution reported in the literature (see **Figure 15**). This means that in the solid-state there are other interactions. These interaction are partially removed when the porphyrin interacts with the HNT. The comparison of these solid-state emission spectra with the one in solution seems to indicate that in the case of the loaded HNT-TDP there was a sort of concentrated solution.

The same spectra were acquired on the Zn-porphyrin-containing samples (**Figure 21 and 22**).

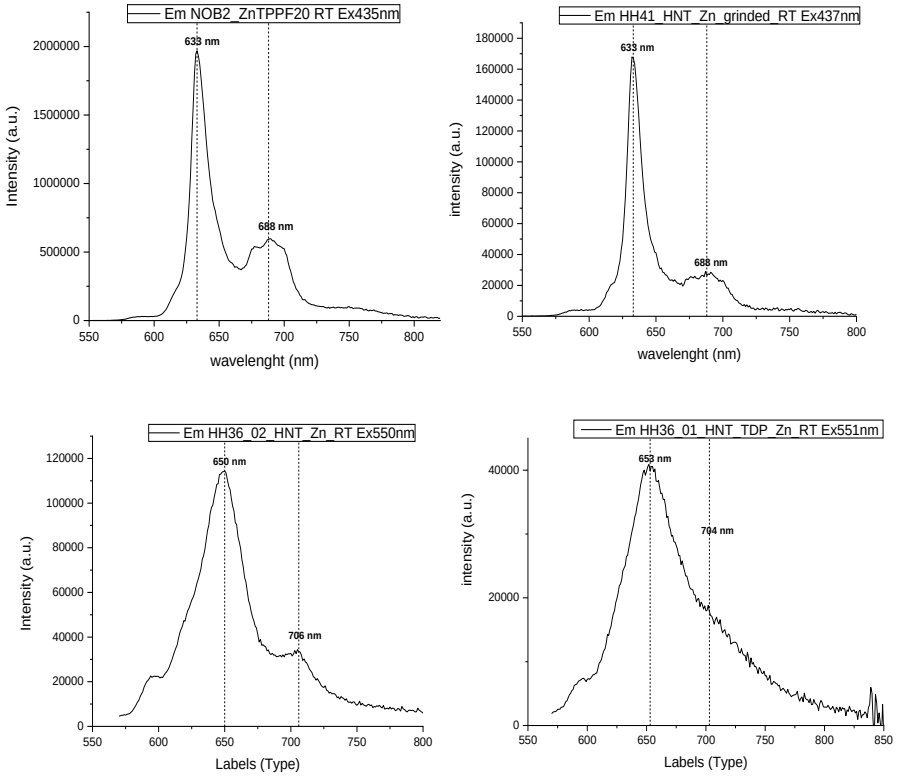

Figure 21. Emission spectra of a) $ZnTPPF_{20}$ (λ_{ex} = 435 nm) b) dry HNT mixed with solid $ZnTPPF_{20}$ (λ_{ex} = 437 nm) c) HNT loaded with $ZnTPPF_{20}$ (λ_{ex} = 550 nm) d) HNT-TDP loaded with $ZnTPPF_{20}$ (λ_{ex} = 551 nm)

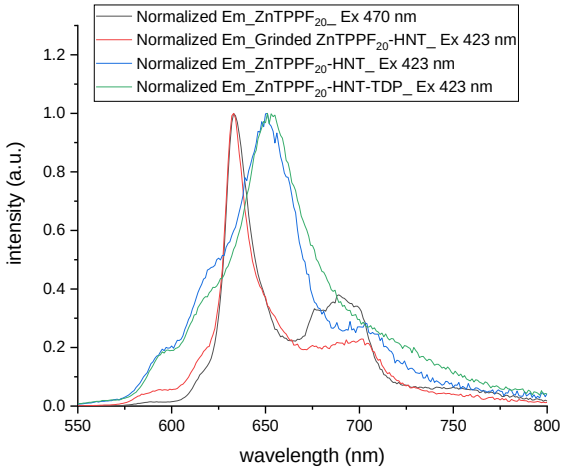

Figure 22. Superposition of the normalized emission spectra of $ZnTPPF_{20}$ alone (black), loaded HNT-$ZnTPPF_{20}$ (blue), HNT-TDP- $ZnTPPF_{20}$ (green) and the ground HNT + $ZnTPPF_{20}$ (red).

The evident difference in the emission spectra is not deriving from an interaction between the external silica of HNT with Zn-porphyrin as suggested by the good superposition of the peaks of Zn-porphyrin and the ground HNT + Zn-porphyrin sample. On the contrary, comparing the spectra of the two samples with loaded Zn-porphyrin in pristine HNT or modified HNT-TDP, it is visible a clear shift of the most intense peak (from 633 to 650 nm) and a concomitant broadening of the band, whereas the less intense transition is not anymore clearly visible but remains as a shoulder of the main peak. Also in this case, it is as when loaded into the HNT-TDP lumen the Zn-porphyrin was diluted compared to the emission profile of the pure metalloporphyrin in the solid-state.

2.6 Drug release

The controlled release of the loaded drug (H_2TPPF_{20} and Zn-$TPPF_{20}$) from HNT composite was studied in THF solution mixed with 50 % water to facilitate the release of hydrophobic drug H_2TPPF_{20} under study. **Figure 23** represented the release process and analysis through UV-visible spectroscopy through the intervals time. The Normalized release profile of the drug from halloysite samples before and after dextrin capping presented in **Figure 24**. Calculation of the amount of drug released over time intervals was done taking into account the dilution factor (see Experimental part).

As noted, compared to non-capped samples, dextrin capping retard the complete release of the drug. For all sample profile, there is an initial release burst within 15 min, then samples divided for two groups non-capped above the capped halloysite composite. The first sample reaching the maximum release % was the Zn-$TPPF_{20}$ from pristine halloysite but the release of H_2TPPF_{20} from capped halloysite modified with TDP required more time compared to the other samples and that could owe to the hydrophobicity of the inner lumen.

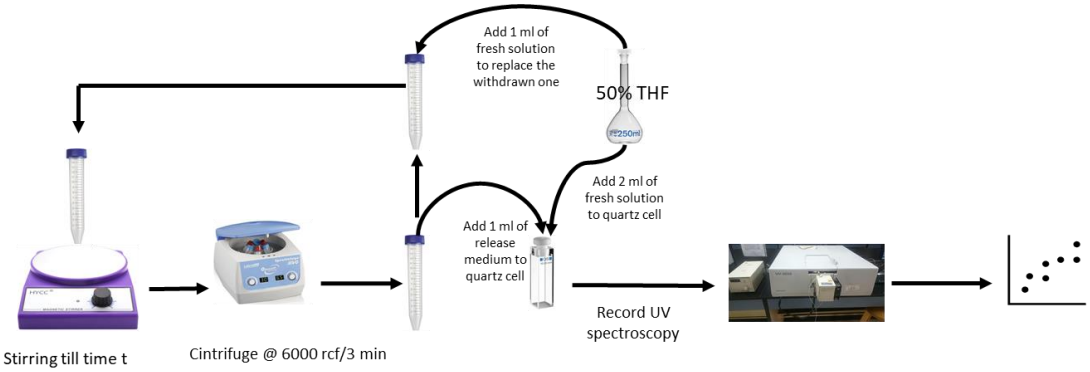

Figure 23 skitch summarize the process of Drug detection during release process

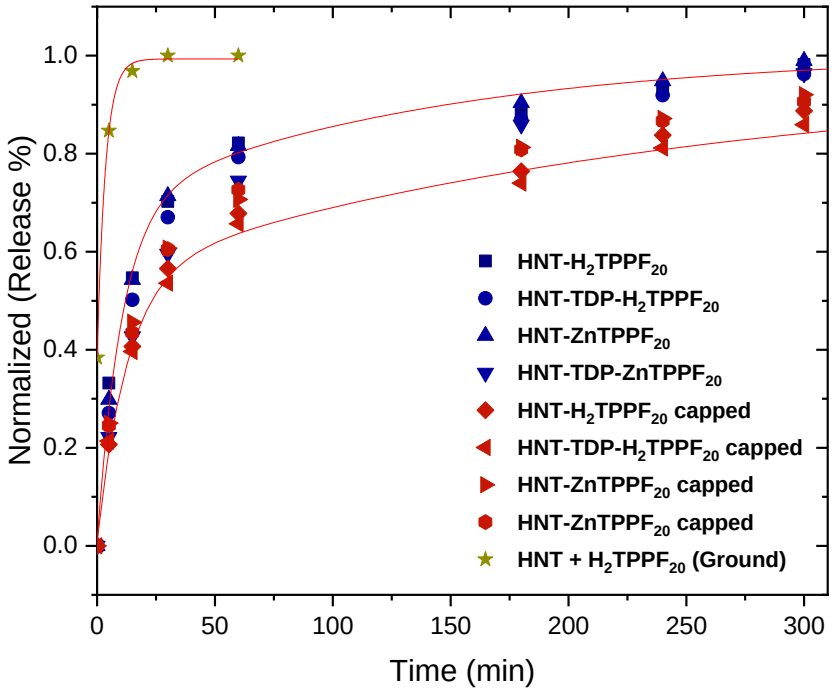

Figure 24. Release of H_2TPPF_{20} and $ZnTPPF_{20}$ from the loaded sample before and after capping with dextrin

To obtain a good fitting of the release profiles (**Figure 24**) and gain insights on the release kinetics, we had to employ a sum of two first-order kinetics,[52] which revealed to be the only model able to well describe the release profile (**Eq. 4. 3**).

$$R = M_1(1-e^{-k1*t}) + M_2(1-e^{-k2*t}) \qquad \text{(Eq. 4.3)}$$

Where M is the amount of active agent (amount loaded within lumen) released at specific time, and k is the release rate constant.

This can be explained by taking into account the presence of two distinct release sites, being evident that the first part of the release kinetic (30 min) is a burst release, much faster than what showed by the second part of the curve.

2.7 SPION addition

The second part of this project with Halloysites was devoted to the co-loading of porphyrins with magnetic nanoparticles (SPION). The aim pursued was to load in the inner lumen the SPION together with the porphyrin to trigger the PS release by an external magnetic stimulus, which in principle would have led to a local overheating and hence the possible release of the PS.

As previously presented (Chapter 2), the selective loading of SPION@OA into the HNT inner lumen was achieved by premodification of the inner lumen with the apolar molecule TDP. For the co-loading we employed the very same strategy to enable the loading of both the apolar free-base perfluorinated porphyrin and the SPION stabilized by a layer of oleic acid (OA). The SPION@OA employed here are the very same as one of the samples (SPION3@OA) already used in Chapter 2.

At the beginning, we used a step by step loading, where we started loading H_2TPPF_{20} leading to a pale yellow adduct, followed by a second SPION@OA loading step. As showed by TEM analysis (**Figure 25**), the step by step loading was not successful in co-loading both the porphyrins and the SPION in the inner lumen. We reasoned that this was possibly due to the necessity to have air bubbles[53] in order to push the SPION to come in, but these were already completely removed by the first loading step. We only succeeded in the formation of an adduct (SPION-HNT-TDP-H_2TPPF_{20}) where SPION were completely covering the outer surface of HNT. These adducts could still be useful for biomedical purposes being SPION contrast agents for MRI and also useful as therapeutic agents in the magnetic hyperthermia. In the future, we will further characterize these adducts and employe them in biological tests.

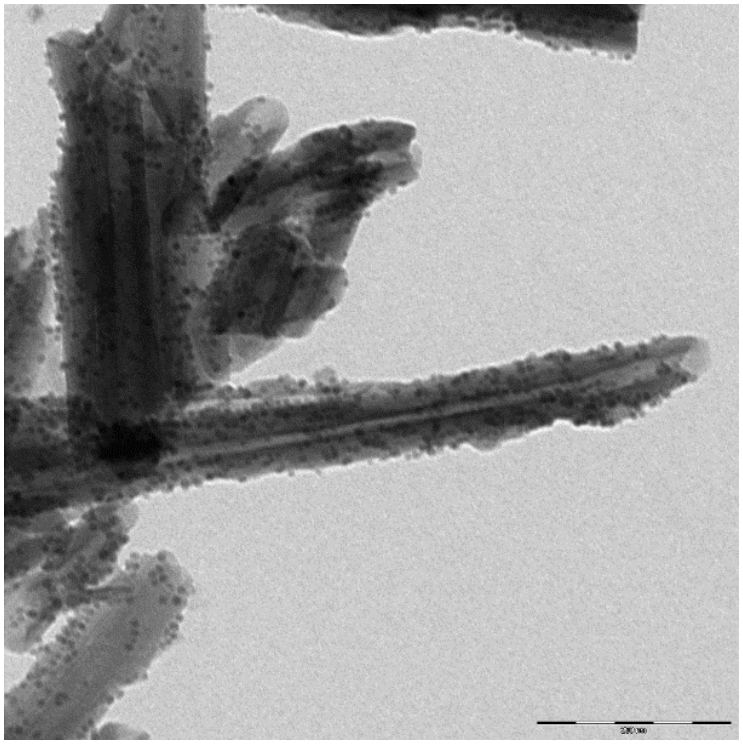

Figure 25. TEM image of SPION-HNT-TDP-H_2TPPF_{20} loaded by the step-by-step method.

The other way pursued for the loading of both SPION and H_2TPPF_{20} was through an *in situ* method, in which both SPION@OA and H_2TPPF_{20} were contemporarily dispersed in n-hexane in the presence of HNT-TDP, followed by vacuum/N_2 cycles. Under UV lamp irradiation, the luminescence of porphyrin became invisible. This induced us to think that SPION were acting as luminescence quenchers[54] due to electronic coupling and energy transfer between magnetic cores and H_2TPPF_{20} leading to a decrease in the quantum emission yield of the porphyrin.

DRUV spectrum (**Figure 26**) of the so obtained sample showed the porphyrin B-band and very poorly the Q bands since the very wide band of SPION nanoparticles dominated the absorption spectrum. Anyhow the presence of the B-band is enough to confirm the porphyrin was loaded together with the SPION.

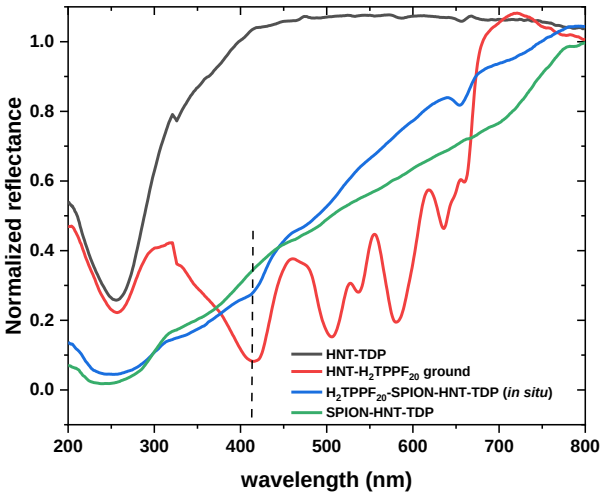

Figure 26. DRUV spectrum of the sample SPION-HNT-TDP-H_2TPPF_{20} loaded by the *one-pot* method (blue curve). A comparison is reported with the SPION/HNT-TDP (green), the ground HNT-porphyrin (red) and the HNT-TDP samples with enlargement of the region of wavelengths characteristic of H_2TPPF_{20} (190-800 nm). The dashed line indicates the intense Soret band.

For further and more reliable confirmation of the presence of SPION and H_2TPPF_{20} within HNT-TDP, some TEM images were captured (**Figure 27**). Even if TEM is not easy to identify a molecule The TEM allowed to identify porphyrins inside the nanotubes through the observation of few grey spots (**Figure 27**, violet arrows). It is noted that there are few SPION present in the HNT lumen (**Figure 27**, blue arrows), and on the contrary, most of them are located outside. Most likely, in simultaneous loading there can be a competition between SPION and porphyrins that hamper both to be effectively loaded.

Hence, we concluded that also the *one-pot* loading did not give the expected outcomes due to the competition between SPION and porphyrins. Further future developments are required to allow both elements to enter the lumen efficiently. A possible way to overcome the co-loading issue in the inner lumen could consist of bonding PS to SPION surface either electrostatically or by a breakable covalent bond as a consequence of an external stimulus.

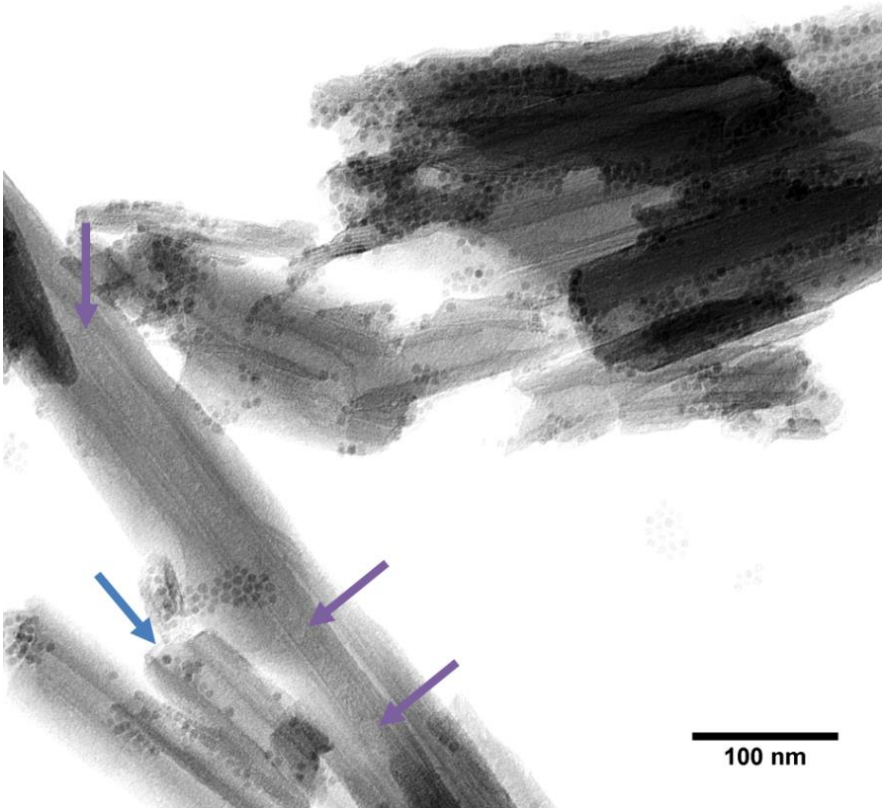

Figure 27. TEM micrograph of the SPION-HNT-TDP-H_2TPPF_{20} loaded by the *one-pot* method. Violet and blue arrows indicate the drug and SPION, respectively, lying in the inner lumen of HNT.

3 Conclusions

The primary goal of this work was the preparation and characterization of new HNT adducts with a luminescent apolar molecule able to act as photosensitizers for photodynamic therapy. The two chosen luminescent molecules were the perfluorinated porphyrin and its Zn complex, used as a model for apolar drugs. It was also ascertained that in our conditions these molecules were able to behave as photosensitizers for the production of singlet oxygen and so they were both effective PDT agents.

The loaded HNT into the inner lumen of both the perfluorinated porphyrin and Zn-porphyrin was obtained by successive vacuum/N_2 cycles studying, by comparison, the efficiency of the loading dependently to the HNT different polarity.

All the synthesized adducts were completely characterized by several techniques such as ATR-FTIR, DRUV and fluorescence spectroscopies as well as the TEM and TGA. Besides the estimation of the amount of loaded drug in the various samples, we tried to evidence the differences throughout the several samples and ascertain if the loading was effectively reaching the inner lumen as desired. In particular, the DRUV and emission spectroscopies were indicative of significant differences between the loaded and the ground samples, together with the TEM microscopy.

Finally, we found that to modulate and slowing down the release of the porphyrin from HNT, the use of dextrin stoppers for the HNT open sides could be helpful. By following the kinetic

of porphyrin release through UV-vis spectroscopy we concluded that as expected the capping dextrin plays a major role in the release process, but we cannot exclude a minor role also due to the apolar TDP layer, being able to establish weak apolar interactions with the porphyrin molecules in the inner lumen. Many efforts will be devoted in the future to test these HNT-adducts in vitro and in vivo as well as to improve the sustained release.

Finally, only very preliminary results have been obtained about the co-loading of SPION and porphyrins. Up to now, we were able to externally decorate the HNT with SPION, and load in the lumen the molecular drug. This could be a valuable product if used as a theranostic agent, exploiting the drug payload together with the magnetic properties of SPION possibly for both diagnosis (MRI contrast agent) and magnetic hyperthermia. For the future, we also aim to pursue the initial purpose of finding an effective way to co-load SPION and drug in the inner lumen, for triggering with an external stimulus the controlled release of the HNT payload. For that, new strategies should be taken into account as, for example, the breakable linkage of the drug to the SPION surface.

4 Experimental Part

4.1 Materials and instruments

5,10,15,20-tetrakis(perfluorophenyl)porphyrin (H_2TPPF_{20}) and [5,10,15,20-tetrakis(perfluorophenyl) porphyrinato]zinc(ii) ($ZnTPPF_{20}$) provided by prof Francesca Tessore group.[55] Tetradecylphosphonic acid 97%, Methanol 99.8%, 1,5-Dihydroxynaphthalene 97%, Halloysite nanotubes HNT (Sigma Aldrich), n-hexane 96% (Scharlau), Tetrahydrofuran THF (Merck), ethanol 99.8% (Merck UK), dextrin from potato starch (Millipore). Ultrapure milli-Q water (Millipore, resistivity=18M Ω cm^{-2}) was used for the preparation of the aqueous solutions.

ATR-FTIR spectra were acquired on a PerkinElmer Frontier instrument equipped with an ATR accessory with a diamond/ZnSe crystal. The IR spectra were registered between 4000 and 400 cm^{-1}.

Transmission Electron Microscopy (TEM) experiments were carried out using a FEI Tecnai F20 Field Emission Gun electron microscope with a 200 kV accelerating voltage. The samples were first dispersed in isopropanol and sonicated for a couple of minutes. A drop was then placed onto a 300 mesh carbon-coated copper grid. The nanoparticle size was measured by Image-J free software, for each sample, the measured NPs were around 1000.

Thermogravimetric analysis (TGA) was carried out in air atmosphere and in the temperature range 50–800 °C with a heating rate of 5 °C·min^{-1}, using a Mettler-Toledo thermogravimetric balance (TGA/DSC 2 Star® System) on ca 10 mg of lyophilized samples.

Diffused Reflectance UV spectroscopy (DRUV) was carried out by using a double beam UV–vis–NIR scanning spectrophotometer (Shimadzu UV-3600 plus, Tokyo, Japan) equipped with a diffuse reflectance accessory (integrating sphere from BIS- 603) in the wavelength range 220–2600 nm. The finely ground powder samples were uniformly pressed in a circular disk (with an external diameter of 0.5 cm) included in the sample holder. The latter was inserted in a special quartz cuvette and then fixed on a window of the integrating sphere for the reflectance measurements. $BaSO_4$ was the reflectance reference compound used.

4.2 Photoreaction of H_2TPPF_{20} and $ZnTPPF_{20}$ with DHN

H_2TPPF_{20} (1.0 mg) (5.1×10^{-4}M) was dissolved in 50 µL of DMSO, then it was transferred in a volumetric flask (2 mL), and was made up to volume by adding EtOH. In another volumetric flask (10 mL) a stock solution of DHN was prepared by dissolving 17.0 mg DHN in EtOH (1.0 ×

10^{-3}M) that was further diluted to 3.7×10^{-4}M. Then, in a quartz cuvette (Quartz SUPRASIL®), 2.5 mL of the diluted DHN solution (3.7×10^{-4}M) were mixed with 100 µL of H_2TPPF_{20} solution. Before irradiation, the solution was saturated with O_2 by bubbling directly in the cuvette for ca. 10 min. The solution was then irradiated through a LED light source (Megamanlamp ® PAR16 GU10 LR0707-SP) and spectra were collected every 3 min for the first 10 min, then at the following time points: 10, 20, 30, 40, 60, and 90 min. The same procedure was followed for the photoreaction involving **$ZnTPPF_{20}$ as PS** using 1.0 mg of **$ZnTPPF_{20}$** in 2.0 mL of pure ETOH (4.8×10^{-4}M).

4.3 Loading step

7.5 milligrams of a photosensitizer (**H_2TPPF_{20}** or **$ZnTPPF_{20}$**) were dissolved in 5 mL of THF. Then, the solution was added with a THF suspension of pristine HNT or modified with TDP (150 mg in 5 mL). The loading of porphyrins was achieved by applying vacuum/N_2cycles for 3 h. During the loading process, when the suspension was near to dryness, other THF was added, to restore the starting volume. This volume restoration was repeated 5 times over the 3 h. Then, the suspension was left under vacuum until the solvent volume was reduced to ca. 4 mL and the mixture was left under stirring at room temperature for 24 h.

The loaded HNT were recovered by centrifugation (5 min at 6000 rcf), then the recovered pellet was washed once with THF, centrifuged once more, dryed at 50 °C for 3 h, and finally gently ground to obtain a fine powder.

4.4 Capping step

For the HNT capping we following a procedure described in the literature.[37,40] Briefly 70 mg of loaded HNT samples were added to 7 mL of an aqueous dextrin solution (10 mg/mL). The mixture was left under vacuum/N_2 cycles for 2 h, then centrifuged at 7197 rcf for 3 min, and the recovered pelled washed with 3 mL milliQ water, and finally dryed by an air flux preserving the sample from the light.

4.5 Determination of the molar extintion coefficient of H_2TPPF_{20} or $ZnTPPF_{20}$ and the UV-vis detection limit

A stock solution of the photosensitizer was prepared by dissolving 1 mg of **H_2TPPF_{20}** or **$ZnTPPF_{20}$** in 250 µL of pure THF, and then added with a mixture 1:1 H_2O/THF up to a total volume of 5 mL (ca. 2×10^{-1} mM). Then, from this stock solution, diluted solutions were subsequently prepared at different concentration values (10^{-1}, 5×10^{-2}, 10^{-2}, 5×10^{-3}, 2.5×10^{-3}, 10^{-3}, 5×10^{-4}, 10^{-4}, 5×10^{-5} mM). For each concentration, a UV-vis spectrum was recorded until the obtainment of the molar extinction coefficients of the Sorbet bands (λmax = 410 and 419 nm for porphyrin and Zn porphyrin, respectively), and a rough detection limit concentration value was estimated.

4.6 Release step

20 milligrams of a loaded sample were added to a plastic Eppendorf centrifuge tube and dispersed in 3 mL of a mixture H_2O:THF 1:1 and equipped with a micro-magnetic stir bar. The suspension was started to be stirred at 1000 rpm and room temperature. Then, at fixed times, the suspension was centrifuged at 6000 rcf/3 min, and 1 mL of the supernatant was withdrawn and the content analyzed after diluting at a total volume of 2.5 mL. To keep constant the volume of the release medium, 1 mL of fresh solution (THF 50%) was added each time to replace the withdrawn one. The UV-vis spectra were recorded at 0.5,15, 30, 60, 180, 240, 300 and 1400 min.

Calculation of the amount of drug released in the intervals was done considering the dilution factor employing the following equations (**Eq. 4.4** and **Eq. 4.5**):

- mmol released in each interval time t =

$$\frac{((((\frac{\text{Absorbance @ time t}}{\text{absorbitivity of drug at analsysis } \lambda} * 3)_{\substack{\text{amount inside} \\ \text{quartz cuvette}}} * 3)_{\substack{\text{total amount inside} \\ \text{eppandorf @ time t}}})_{\textbf{measured amount at time t}} - (\sum_{i=1}^{i=t-1} (\frac{2}{3})^{i} * \text{actual amount released}_{t-i}))}{1000} \quad (Eq.\ 4.4)$$

- Percentage of drug released at time t=

$$\left(\frac{\sum_{t=0}^{t=i} \text{The mmol released each interval time}_i}{\text{maximum amount in mmol loaded in 20 mg}}\right) * 100 \qquad \text{(Eq. 4.5)}$$

4.7 Step by step HNT loading of porphyrin and SPION

2.5 milligrams of **H_2TPPF_{20}** were dissolved in 50 mL n-hexane and then stirred for 30 min until complete dissolution was observed. Then, 50 mg of modified halloysite with TDP were added to the solution. The loading of porphyrins was achieved by applying vacuum/N_2 cycles for 2 h. During the loading process, when the suspension was near to dryness, other hexane was added, to restore the starting volume.

Then to the same suspension, 0.75 mL of an n-hexane suspension of SPION (containing ca. 2mg of Fe) was added, followed by repeating the vacuum/N_2 cycles for 2 h further. Then, the suspension was left under vacuum until the solvent volume was reduced to ca. 4 mL.

The loaded HNT adducts were recovered by centrifugation (5 min at 2000 rcf), then the recovered pellet was washed once with hexane, and the HNT-porphyrin SPION adduct was magnetically recovered, removing the clear n-hexane supernatant. Finally, the pellet was gently dried by a nitrogen flux.

4.8 *One-pot* loading of porphyrin and SPION

2.5 milligrams of **H_2TPPF_{20}** were dissolved in 50 mL of hexane followed by stirring for 30 min until complete dissolution was observed. Then to the solution, 50 mg of modified halloysite with TDP were added. Then to the same mixture, 0.75 mL of SPION (ca. 2mg Fe) were added, followed by the vacuum/N_2 cycles for 2 h. During the loading process, when the suspension was near to dryness, other hexane was added, to restore the starting volume.

Then, the suspension was left under vacuum until the solvent volume was reduced to ≈ 4 mL. The loaded HNT adduct were recovered by centrifugation (5 min at 2000 rcf), then the recovered pellet was washed once with hexane and magnetically recovered. Finally, the pellet was gently dried by a nitrogen flux.

5 Bibliography

(1) DeRosa, M. C.; Crutchley, R. J. Photosensitized Singlet Oxygen and Its Applications. *Coord. Chem. Rev.* **2002**, *233–234*, 351–371. https://doi.org/https://doi.org/10.1016/S0010-8545(02)00034-6.

(2) Castano, A. P.; Demidova, T. N.; Hamblin, M. R. Mechanisms in Photodynamic Therapy: Part One—Photosensitizers, Photochemistry and Cellular Localization. *Photodiagnosis Photodyn. Ther.* **2004**, *1* (4), 279–293. https://doi.org/https://doi.org/10.1016/S1572-1000(05)00007-4.

(3) Foote, C. S. Mechanisms of Photooxygenation. *Prog. Clin. Biol. Res.* **1984**, *170*, 3.

(4) Macdonald, I. J.; Dougherty, T. J. Basic Principles of Photodynamic Therapy. *J. Porphyr. Phthalocyanines* **2001**, *5* (2), 105–129. https://doi.org/https://doi.org/10.1002/jpp.328.

(5) Ding, H.; Yu, H.; Dong, Y.; Tian, R.; Huang, G.; Boothman, D. A.; Sumer, B. D.; Gao, J. Photoactivation Switch from Type II to Type I Reactions by Electron-Rich Micelles for

Improved Photodynamic Therapy of Cancer Cells under Hypoxia. *J. Control. Release* **2011**, *156* (3), 276–280. https://doi.org/https://doi.org/10.1016/j.jconrel.2011.08.019.
(6) Hatz, S.; Lambert, J. D. C.; Ogilby, P. R. Measuring the Lifetime of Singlet Oxygen in a Single Cell: Addressing the Issue of Cell Viability. *Photochem. Photobiol. Sci.* **2007**, *6* (10), 1106–1116. https://doi.org/10.1039/B707313E.
(7) petr Zimcik, M. M. Photodynamic Therapy. In *Dyes and Pigments: New Research*; Lang, A. R., Ed.; Nova Science Publishers, 2009; pp 1–62.
(8) Maiya, B. G. Photodynamic Therapy (PDT). *Resonance* **2000**, *5* (4), 6–18. https://doi.org/10.1007/BF02837901.
(9) Allison, R. R.; Downie, G. H.; Cuenca, R.; Hu, X.-H.; Childs, C. J. H.; Sibata, C. H. Photosensitizers in Clinical PDT. *Photodiagnosis Photodyn. Ther.* **2004**, *1* (1), 27–42. https://doi.org/https://doi.org/10.1016/S1572-1000(04)00007-9.
(10) Sharman, W. M.; Allen, C. M.; van Lier, J. E. B. T.-M. in E. [35] Role of Activated Oxygen Species in Photodynamic Therapy. In *Singlet Oxygen, UV-A, and Ozone*; Academic Press, 2000; Vol. 319, pp 376–400. https://doi.org/https://doi.org/10.1016/S0076-6879(00)19037-8.
(11) MacRobert, A. J.; Bown, S. G.; Phillips, D. What Are the Ideal Photoproperties for a Sensitizer? *Ciba Foundation Symposium 146 - Photosensitizing Compounds: Their Chemistry, Biology and Clinical Use*. September 28, 2007, pp 4–16. https://doi.org/https://doi.org/10.1002/9780470513842.ch2.
(12) Nyman, E. S.; Hynninen, P. H. Research Advances in the Use of Tetrapyrrolic Photosensitizers for Photodynamic Therapy. *J. Photochem. Photobiol. B Biol.* **2004**, *73* (1), 1–28. https://doi.org/https://doi.org/10.1016/j.jphotobiol.2003.10.002.
(13) Ormond, A. B.; Freeman, H. S. Dye Sensitizers for Photodynamic Therapy. *Mater. (Basel, Switzerland)* **2013**, *6* (3), 817–840. https://doi.org/10.3390/ma6030817.
(14) Bonnett, R. Photodynamic Therapy in Historical Perspective. *Rev. Contemp. Pharmacother.* **1999**, *10* (1), 1–17.
(15) Lucky, S. S.; Soo, K. C.; Zhang, Y. Nanoparticles in Photodynamic Therapy. *Chem. Rev.* **2015**, *115* (4), 1990–2042. https://doi.org/10.1021/cr5004198.
(16) Usuda, J.; Kato, H.; Okunaka, T.; Furukawa, K.; Tsutsui, H.; Yamada, K.; Suga, Y.; Honda, H.; Nagatsuka, Y.; Ohira, T.; Tsuboi, M.; Hirano, T. Photodynamic Therapy (PDT) for Lung Cancers. *J. Thorac. Oncol.* **2006**, *1* (5), 489–493. https://doi.org/10.1016/S1556-0864(15)31616-6.
(17) Trindade, F. Z.; Pavarina, A. C.; Ribeiro, A. P. D.; Bagnato, V. S.; Vergani, C. E.; de Souza Costa, C. A. Toxicity of Photodynamic Therapy with LED Associated to Photogem®: An in Vivo Study. *Lasers Med. Sci.* **2012**, *27* (2), 403–411. https://doi.org/10.1007/s10103-011-0909-y.
(18) Beneš, J.; Zeman, J.; Zadinova, M.; Sunka, P.; Lukes, P.; Kolářová, H. Effects of Tandem Shock Waves Combined with Photosan and Cytostatics on the Growth of Tumours. *Folia Biol. (Praha).* **2011**, *57*, 255–260.
(19) Benov, L. Photodynamic Therapy: Current Status and Future Directions. *Med. Princ. Pract.* **2015**, *24 Suppl 1* (Suppl 1), 14–28. https://doi.org/10.1159/000362416.
(20) Hirth, A.; Michelsen, U.; Wöhrle, D. Photodynamische Tumortherapie. *Chemie unserer Zeit* **1999**, *33* (2), 84–94. https://doi.org/https://doi.org/10.1002/ciuz.19990330204.
(21) Samaroo, D.; Vinodu, M.; Chen, X.; Drain, C. M. Meso-Tetra(Pentafluorophenyl)Porphyrin as an Efficient Platform for Combinatorial Synthesis and the Selection of New Photodynamic Therapeutics Using a Cancer Cell Line. *J. Comb. Chem.* **2007**, *9* (6), 998–1011. https://doi.org/10.1021/cc070067j.
(22) Kou, J.; Dou, D.; Yang, L. Porphyrin Photosensitizers in Photodynamic Therapy and Its Applications. *Oncotarget; Vol 8, No 46* **2017**.
(23) Nicosia, A.; Vento, F.; Satriano, C.; Villari, V.; Micali, N.; Cucci, L. M.; Sanfilippo, V.; Mineo, P. G. Light-Triggered Polymeric Nanobombs for Targeted Cell Death. *ACS Appl. Nano Mater.* **2020**, *3* (2), 1950–1960. https://doi.org/10.1021/acsanm.9b02552.
(24) Smith, K. M. 1.23 - Porphyrins; McCleverty, J. A., Meyer, T. J. B. T.-C. C. C. I. I., Eds.; Pergamon: Oxford, 2003; pp 493–506. https://doi.org/https://doi.org/10.1016/B0-08-043748-6/01050-1.
(25) Stern, A.; Deželić, M. Über Die Lichtabsorption Der Porphyrine. XII. *Zeitschrift für Phys. Chemie* **1937**, *180A* (1), 131–138. https://doi.org/doi:10.1515/zpch-1937-18011.
(26) Lopes, J. M. S.; Reis, J. R. T.; Machado, A. E. H.; Leite, T. H. O.; Batista, A. A.; Acunha, T. V; Iglesias, B. A.; Araujo, P. T.; Barbosa Neto, N. M. Influence of the Meso-Substituents on the Spectral Features of Free-Base Porphyrin. *Spectrochim. Acta Part A Mol. Biomol. Spectrosc.*

2020, *238*, 118389. https://doi.org/https://doi.org/10.1016/j.saa.2020.118389.
(27) Elemans, J. A. A. W.; van Hameren, R.; Nolte, R. J. M.; Rowan, A. E. Molecular Materials by Self-Assembly of Porphyrins, Phthalocyanines, and Perylenes. *Adv. Mater.* **2006**, *18* (10), 1251–1266. https://doi.org/https://doi.org/10.1002/adma.200502498.
(28) Aljabri, M. D.; La, D. D.; Jadhav, R. W.; Jones, L. A.; Nguyen, D. D.; Chang, S. W.; Tran, L. D.; Bhosale, S. V. Supramolecular Nanomaterials with Photocatalytic Activity Obtained via Self-Assembly of a Fluorinated Porphyrin Derivative. *Fuel* **2019**, *254*, 115639. https://doi.org/https://doi.org/10.1016/j.fuel.2019.115639.
(29) Rimington, C.; Mason, S. F.; Kennard, O. Porphin. *Spectrochim. Acta* **1958**, *12* (1), 65–77. https://doi.org/https://doi.org/10.1016/0371-1951(58)80128-9.
(30) Grancho, J. C. P.; Pereira, M. M.; Miguel, M. da G.; Gonsalves, A. M. R.; Burrows, H. D. Synthesis, Spectra and Photophysics of Some Free Base Tetrafluoroalkyl and Tetrafluoroaryl Porphyrins with Potential Applications in Imaging¶. *Photochem. Photobiol.* **2002**, *75* (3), 249–256. https://doi.org/https://doi.org/10.1562/0031-8655(2002)0750249SSAPOS2.0.CO2.
(31) Cavaleiro, J. A. S.; Görner, H.; Lacerda, P. S. S.; MacDonald, J. G.; Mark, G.; Neves, M. G. P. M. S.; Nohr, R. S.; Schuchmann, H.-P.; von Sonntag, C.; Tomé, A. C. Singlet Oxygen Formation and Photostability of Meso-Tetraarylporphyrin Derivatives and Their Copper Complexes. *J. Photochem. Photobiol. A Chem.* **2001**, *144* (2), 131–140. https://doi.org/https://doi.org/10.1016/S1010-6030(01)00540-8.
(32) Kashiwagi, Y.; Imahori, H.; Araki, Y.; Ito, O.; Yamada, K.; Sakata, Y.; Fukuzumi, S. Strong Inhibition of Singlet Oxygen Sensitization in Pyridylferrocene−Fluorinated Zinc Porphyrin Supramolecular Complexes. *J. Phys. Chem. A* **2003**, *107* (29), 5515–5522. https://doi.org/10.1021/jp034920q.
(33) Takizawa, S.; Aboshi, R.; Murata, S. Photooxidation of 1,5-Dihydroxynaphthalene with Iridium Complexes as Singlet Oxygen Sensitizers. *Photochem. Photobiol. Sci.* **2011**, *10* (6), 895–903. https://doi.org/10.1039/C0PP00265H.
(34) Wu, W.; Yang, P.; Ma, L.; Lalevée, J.; Zhao, J. Visible-Light Harvesting PtII Complexes as Singlet Oxygen Photosensitizers for Photooxidation of 1,5-Dihydroxynaphthalene. *Eur. J. Inorg. Chem.* **2013**, *2013* (2), 228–231. https://doi.org/https://doi.org/10.1002/ejic.201200665.
(35) Bajju, G. D.; Kundan, S.; Bhagat, M.; Gupta, D.; Kapahi, A.; Devi, G. Synthesis and Spectroscopic and Biological Activities of Zn(II) Porphyrin with Oxygen Donors. *Bioinorg. Chem. Appl.* **2014**, *2014*, 782762. https://doi.org/10.1155/2014/782762.
(36) Nardo, J. V; Dawson, J. H. Spectroscopic Evidence for the Coordination of Oxygen Donor Ligands to Tetraphenylporphinatozinc. *Inorganica Chim. Acta* **1986**, *123* (1), 9–13. https://doi.org/https://doi.org/10.1016/S0020-1693(00)81308-0.
(37) Dzamukova, M. R.; Naumenko, E. A.; Lvov, Y. M.; Fakhrullin, R. F. Enzyme-Activated Intracellular Drug Delivery with Tubule Clay Nanoformulation. *Sci. Rep.* **2015**, *5* (1), 10560. https://doi.org/10.1038/srep10560.
(38) Yah, W. O.; Takahara, A.; Lvov, Y. M. Selective Modification of Halloysite Lumen with Octadecylphosphonic Acid: New Inorganic Tubular Micelle. *J. Am. Chem. Soc.* **2012**, *134* (3), 1853–1859. https://doi.org/10.1021/ja210258y.
(39) Hamza, H.; Ferretti, A. M.; Innocenti, C.; Fidecka, K.; Licandro, E.; Sangregorio, C.; Maggioni, D. An Approach for Magnetic Halloysite Nanocomposite with Selective Loading of Superparamagnetic Magnetite Nanoparticles in the Lumen. *Inorg. Chem.* **2020**. https://doi.org/10.1021/acs.inorgchem.0c01039.
(40) Fakhrullina, G.; Khakimova, E.; Akhatova, F.; Lazzara, G.; Parisi, F.; Fakhrullin, R. Selective Antimicrobial Effects of Curcumin@Halloysite Nanoformulation: A Caenorhabditis Elegans Study. *ACS Appl. Mater. Interfaces* **2019**, *11* (26), 23050–23064. https://doi.org/10.1021/acsami.9b07499.
(41) De Luca, G.; Romeo, A.; Scolaro, L. M.; Ricciardi, G.; Rosa, A. Sitting-Atop Metallo-Porphyrin Complexes: Experimental and Theoretical Investigations on Such Elusive Species. *Inorg. Chem.* **2009**, *48* (17), 8493–8507. https://doi.org/10.1021/ic9012153.
(42) Castro, K. A. D. F.; Silva, S.; Pereira, P. M. R.; Simões, M. M. Q.; Neves, M. da G. P. M. S.; Cavaleiro, J. A. S.; Wypych, F.; Tomé, J. P. C.; Nakagaki, S. Galactodendritic Porphyrinic Conjugates as New Biomimetic Catalysts for Oxidation Reactions. *Inorg. Chem.* **2015**, *54* (9), 4382–4393. https://doi.org/10.1021/acs.inorgchem.5b00196.
(43) Şen, P.; Hirel, C.; Andraud, C.; Aronica, C.; Bretonnière, Y.; Mohammed, A.; Ågren, H.; Minaev,

B.; Minaeva, V.; Baryshnikov, G.; Lee, H.-H.; Duboisset, J.; Lindgren, M. Fluorescence and FTIR Spectra Analysis of Trans-A_2B_2-Substituted Di- and Tetra-Phenyl Porphyrins. *Mater. (Basel, Switzerland)* **2010**, *3* (8), 4446–4475. https://doi.org/10.3390/ma3084446.

(44) Krishnakumar, V.; Mathammal, R. A Joint FTIR, FT-Raman and Scaled Quantum Mechanical Study of 1,3-Dibromo-2,4,5,6-Tetra-Fluoro Benzene (DTB) and 1,2,3,4,5-Pentafluoro Benzene (PB). *J. Raman Spectrosc.* **2009**, *40* (9), 1104–1109. https://doi.org/https://doi.org/10.1002/jrs.2236.

(45) Bufaroosha, M.; Neyadi, S. S. Al; Alnaqbi, M. A. R.; Marzouk, S. A. M.; Al-Hemyari, A.; Abuhattab, B. Y.; Adi, D. A. An Undergraduate Experiment Using Microwave-Assisted Synthesis of First Raw Metalloporphyrins: Characterizations and Spectroscopic Study. *World J. Chem. Educ.* **2019**, *7* (3), 225–231. https://doi.org/10.12691/wjce-7-3-6.

(46) Seelig, H.; Hoehn, A.; Stodieck, L.; Klaus, D.; III, W.; Emery, W. The Assessment of Leaf Water Content Using Leaf Reflectance Ratios in the Visible, near-, and Short-Wave-Infrared. *Int. J. Remote Sens.* **2008**, *29*. https://doi.org/10.1080/01431160701772500.

(47) Yu, M.; Li, J.; Sun, W.; Jiang, M.; Zhang, F. Preparation, Characterization, and Photocatalytic Properties of Composite Materials of Copper(II) Porphyrin/TiO2. *J. Mater. Sci.* **2014**, *49* (16), 5519–5528. https://doi.org/10.1007/s10853-014-8132-4.

(48) Cherian, S.; Wamser, C. C. Adsorption and Photoactivity of Tetra(4-Carboxyphenyl)Porphyrin (TCPP) on Nanoparticulate TiO2. *J. Phys. Chem. B* **2000**, *104* (15), 3624–3629. https://doi.org/10.1021/jp994459v.

(49) Gallagher, A. T.; Lee, J. Y.; Kathiresan, V.; Anderson, J. S.; Hoffman, B. M.; Harris, T. D. A Structurally-Characterized Peroxomanganese(Iv) Porphyrin from Reversible O2 Binding within a Metal–Organic Framework. *Chem. Sci.* **2018**, *9* (6), 1596–1603. https://doi.org/10.1039/C7SC03739B.

(50) Fagadar-Cosma, E.; Enache, C.; Ramona, T.; Armeanu, I.; Mosoarca, E.; Dana, V.; Costisor, O. UV-VIS and Fluorescence Spectra of Meso-Tetraphenylporphyrin and Meso-Tetrakis-(4-Methoxyphenyl) Porphyrin in THF and THF-Water Systems. The Influence of PH. *Rev. Chim.* **2007**, *58*, 451–455.

(51) Suslick, K. S.; Watson, P. A. The Photochemistry of Chromium, Manganese, and Iron Porphyrin Complexes. *New J. Chem.* **1992**, *16*, 633–642.

(52) Wei, W.; Minullina, R.; Abdullayev, E.; Fakhrullin, R.; Mills, D.; Lvov, Y. Enhanced Efficiency of Antiseptics with Sustained Release from Clay Nanotubes. *RSC Adv.* **2014**, *4* (1), 488–494. https://doi.org/10.1039/C3RA45011B.

(53) Lisuzzo, L.; Cavallaro, G.; Pasbakhsh, P.; Milioto, S.; Lazzara, G. Why Does Vacuum Drive to the Loading of Halloysite Nanotubes? The Key Role of Water Confinement. *J. Colloid Interface Sci.* **2019**, *547*, 361–369. https://doi.org/https://doi.org/10.1016/j.jcis.2019.04.012.

(54) Yu, C.-J.; Wu, S.-M.; Tseng, W.-L. Magnetite Nanoparticle-Induced Fluorescence Quenching of Adenosine Triphosphate–BODIPY Conjugates: Application to Adenosine Triphosphate and Pyrophosphate Sensing. *Anal. Chem.* **2013**, *85* (18), 8559–8565. https://doi.org/10.1021/ac400919j.

(55) Orbelli Biroli, A.; Tessore, F.; Di Carlo, G.; Pizzotti, M.; Benazzi, E.; Gentile, F.; Berardi, S.; Bignozzi, C. A.; Argazzi, R.; Natali, M.; Sartorel, A.; Caramori, S. Fluorinated ZnII Porphyrins for Dye-Sensitized Aqueous Photoelectrosynthetic Cells. *ACS Appl. Mater. Interfaces* **2019**, *11* (36), 32895–32908. https://doi.org/10.1021/acsami.9b08042.

Chapter 5

Halloysite nanotubes decorated with a Ru-based photosensitizer as organic-inorganic hybrid PDT agent with potentialities as dual drug vector.

1 Introduction

Metal coordination and organometallic complexes have been used for centuries in medicine because they offer a wide range of oxidation states, coordination numbers, and geometries, yielding virtually unlimited structural and chemical space. Currently, they have been used as anticancer, antimicrobial, and diagnostic agents. [1] The properties of the "d" block transition metal complexes can be changed drastically or fine-tuned, owing to their modular three-dimensional structure that a wise selection of ligand-metal combinations can easily modify. These combinations can be designed with appropriate geometry for specific interactions with biological targets.[2]

The pioneer in the study of metal chelates as antitumor agents with copper and dimethylglyoxime was Takamiya et al., followed by the use of other metals such as platinum and palladium in coordination with 6-mercaptopurine reported by Yung-Kang Wei and Francis in 1962. [3] Later, their FDA approval in 1978 led to discovering other platinum-based compounds such as Oxaliplatin and Carboplatin, presently used at the clinical level.[4] Despite the success of platinum-based anticancer drugs, there remains a usual fear that metals are too toxic to be considered in pharmaceutical formulations.[5]

A significant change in organometallic for therapeutic purpose came in 1979 when Koepf et al. first reported the anticancer activity of titanocene dichloride, which later became available for clinical trials in 1993.[4]

Ruthenium chloro-amine complexes were firstly studied by Durig et al. highlighted the inhibition activity of Ru complexes toward the growth of *E.coli.*[3], followed by the antitumor activity introduced by Clark *et al*. However, these compounds were not suitable for clinical evaluation due to their poor solubility in water.[6] The three main properties that make Ru complexes well suited to the medicinal application are their slow rate of ligand exchange[7], range of accessible oxidation states and the ability of ruthenium to mimic iron in binding to certain biological molecules.[8]

Ruthenium polyazine complexes were initially developed for their characteristic photophysical, photochemical, and redox properties for solar energy conversion purposes. Later these complexes were also used as DNA probes.[9] These complexes showed specific binding to B-DNA,[10] due to the interaction between the ligand and phosphate backbone.[11]

As already discussed in the previous chapter, photodynamic therapy (PDT) is a treatment modality that utilizes light, a photosensitizer (PS), and molecular oxygen. There is a variety of

PSs already under study.[12,13] In contrast to the π-π* excited states that lead to PDT effects in organic photosensitizers, metallo-based PSs can be designed to provide diverse excited-state configurations (**Scheme 1**). These configurations can be centred entirely on the metal (metal-centred, MC), within a single ligand (intraligand, IL), or involve both the metal and the ligand(s) in charge-transfer states, metal-to-ligand charge transfer (MLCT) or ligand-to-metal charge transfer (LMCT). It is also possible to have a charge-transfer excited state within a single ligand (intraligand transfer, ILCT), between two different ligands (ligand-to-ligand charge transfer, LLCT), or between two metal atoms in the case of a multimetallic complex (metal-to-metal charge transfer, MMCT). These excited states are further described by multiplicity, usually singlet or triplet. Triplet states are generally more easily accessed in metal complexes due to enhanced spin-orbit coupling induced by heavy atoms. This is an important consideration for at least two reasons. First, triplet states tend to be longer-lived, permitting the increased probability of a reaction between the sensitizer and a substrate. Second, oxygen-dependent and oxygen-independent phototoxic mechanisms originate from triplet states.

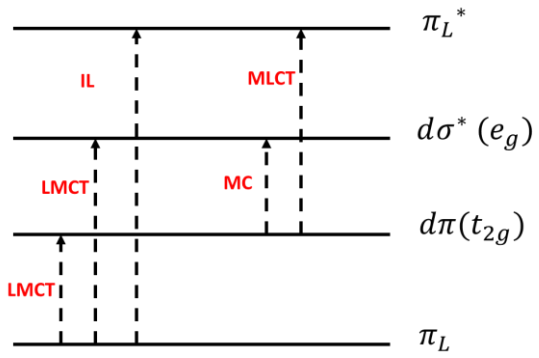

Scheme 1. Some of the electronic transitions available to transition metal complexes.

Ruthenium (II) polyazine complexes show promise as PDT agents and selected for our study because of (i) the kinetically inert character of the low-spin d^6 species, (ii) their intense metal to ligand charge-transfer (MLCT) band in the visible spectrum with luminescent emission in the red –NIR region of the spectrum (iii) they can be excited by both one-photon and two-photon excitation mechanisms exploiting the long-lived triplet metal-to-ligand charge transfer state (^{3}MLCT) and since (iv) many chemical and spectroscopic properties of the poly polyazine complexes have been established, so a series of Ru polyazine based complexes have already reached the clinical trials as new photosensitizers for PDT.[14–16]

The electronic structure of the ground and excited states of Ruthenium (II) polyazine has been examined in detail in many literatures.[17–19] As a summary, the ligand-centred π *-orbitals are lower in energy than the metalcentred σ *-(eg)-orbitals. Therefore, upon excitation of Ru complex an electron from the ground state orbital (π_M) of ruthenium is promoted to a ligand orbital ($\pi_L{}^*$) localised on one of the azine rings. This electron movement assigned as (^{1}MLCT).

So our goal starts with the development of a hybrid system as a novel photosensitizer that can be further developed towards a dual nano-platform where the photosensitizer is attached to the external halloysite (HNT) surface through a covalent bond, hence leaving the inner lumen free to be eventually loaded with a second drug (**Scheme 2**), potentially able to synergically enhance the therapeutic effect on an unhealthy or infected tissue.

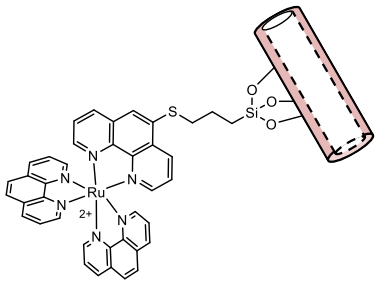

HNT-**5**

Scheme 2. Schematic representation of the chemical structure of purposed Ru PS attached to HNT surface.

2 Results and discussion

The trisphenanthroline Ru(II) complex -HNT adduct can be easily obtained by reacting the non-luminescent precursor $[Ru(phen)_2((CF_3)_2SO_3)_2]$ with the third phenanthroline ligand, which promptly substitutes the labile triflate anions. The third ligand synthesized by our group ended with trimethoxy silyl groups which can be easily bound to the HNT surface. We used two alternative routes to reach our goal: a) a pre-reaction of the phenanthroline-silane ligand followed by the complexation of the "phen" pendant to the metal ion; b) a pre-complexation of the ligand with the Ru precursor followed by the interaction with the Halloysites.

2.1 Synthesis of 1,10-phenanthroline-5,6-epoxide (compound 1)

The synthetic procedure was taken from the literature,[20] and consists of the oxidation of the central ring by employing commercial bleach at controlled slightly basic pH (**Scheme 3**). Moreover, the reaction proceeds in a biphasic environment, so the tetrabutylammonium bisulfate was used as phase transfer agent.

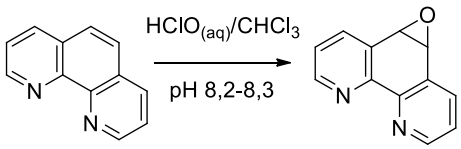

1

Scheme 3. Synthesis of the precursor 1,10-Phenanthroline-5,6-epoxide.

The pH is the most important parameter to check since the occurrence of the reaction depends on it.[21] Indeed, as already reported, in dependence on the pH, the reaction can proceed by favouring chlorine-based products, as indicated in the following **Scheme 4**.

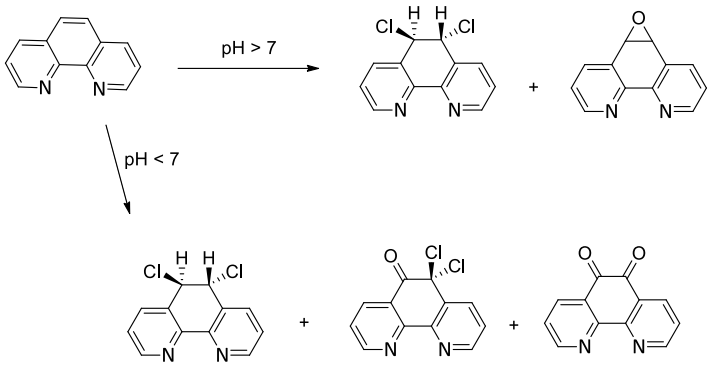

Scheme 4. The pH control pathway representation of 1,10-phenanthroline oxidation

The purification of the product was carried out by gravimetric chromatography after the proper eluting mixture was found. Comparing the first two TLC (see **Figure 1**) it is evident that NH_3, as expected, increased the run rate of both the components, while with the same mixture in the absence of NH_3, the R_f for compound **1** was too slow. Only by mixing ethyl acetate and MeOH with both NH_3 and a slight amount of n-hexane, a sufficient separation of the two stains without decreasing too much the R_f was obtained.

Proton NMR spectrum of the crude product showed two sets of signals (blue trace in **Figure 2**), in agreement with TLC, containing the two species after separated by chromatography. After the chromatographic separation, the two fractions showed very similar ^{1}H NMR splitting pattern, indicating that, as compound **1**, also the by-product must be highly symmetric and with a non-aromatic central ring. Thus, the by-product could be the chlorinated by-product indicated in **Scheme 4**.

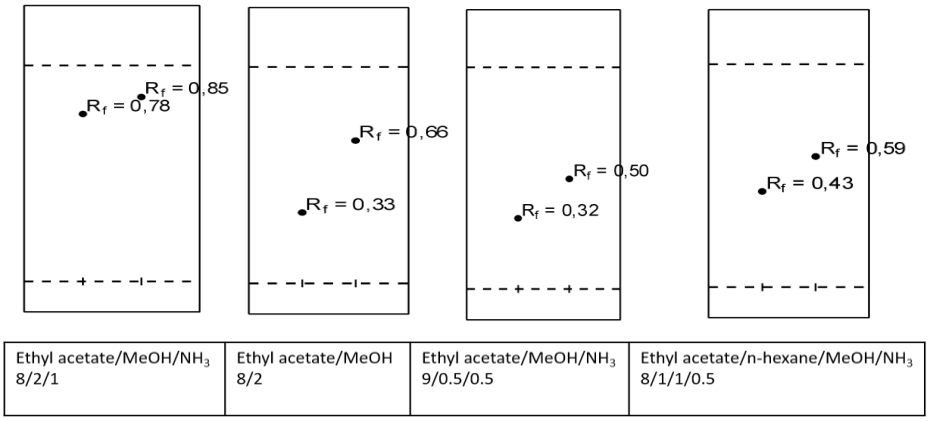

Figure 1. Schematic representation of TLC with used mixture eluent.

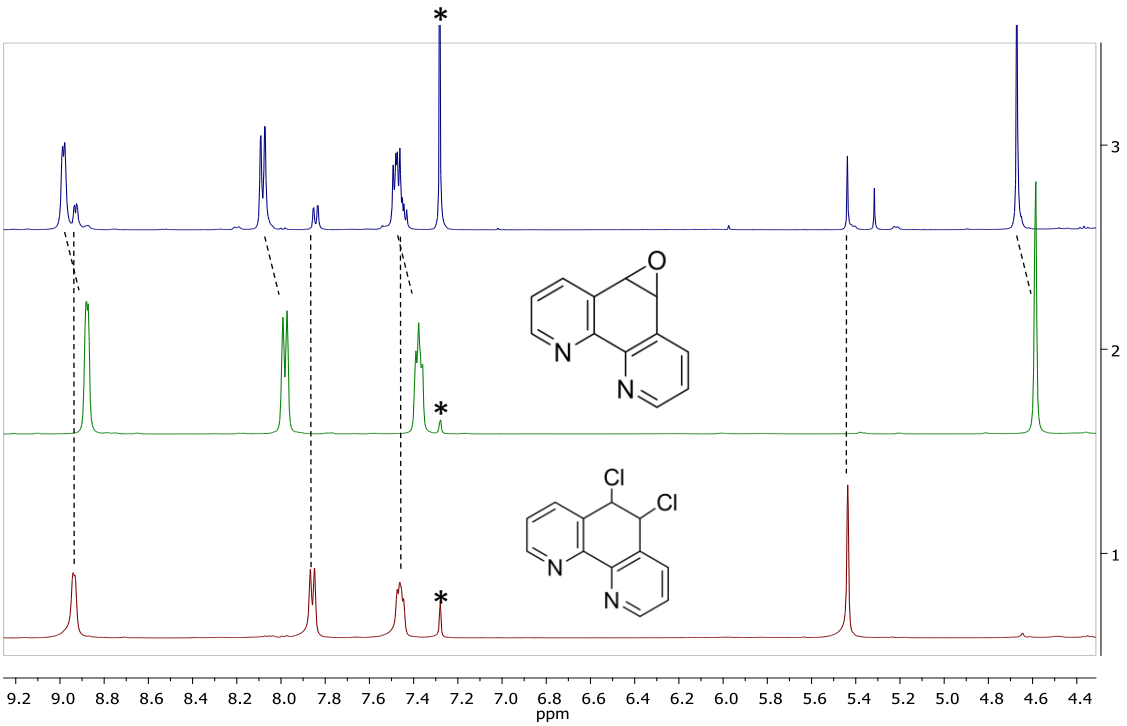

Figure 2. ^{1}H NMR spectra of the crude product of the synthesis of compound **1** (blue trace), of compound **1** after chromatographic separation (green trace), and the unknown by-product after chromatographic separation tentatively attributed to 5,6-dichloro-5,6-dihydro-1,10-phenanthroline (red trace) (9.4 T, 300 K, $CDCl_3$ = *). The shift of the signals of compound **1** is due to a difference in concentration.

2.2 Synthesis of 5-((3-(trimethoxysilyl)propyl)thio)-1,10-phenanthroline (Compound 3)

The epoxy-phenanthroline derivative is a key intermediate since it easily reacts with many nucleophiles, and in particular, it is promptly reacted with mercapto groups, leading to the opening of the epoxy ring and forming the transition intermediate **2** (**Scheme 5**). Moreover, the restoration of the aromaticity of the central ring is the driving force that leads to the formation of the final compound **3** by dehydration (**Scheme 5**).

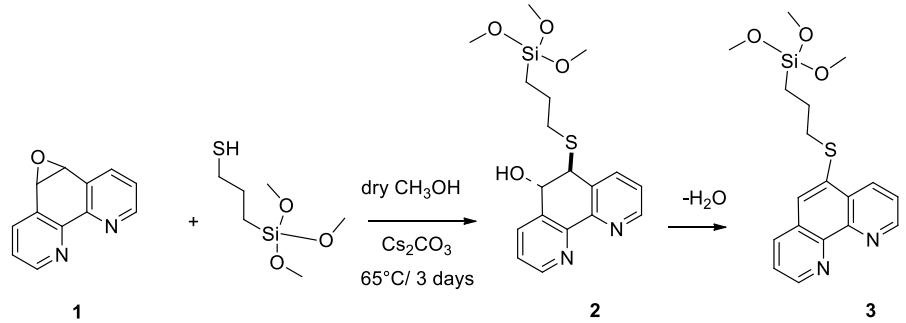

Scheme 5. Schematic depiction of the synthesis of compound **3** starting from phenanthroline-epoxide **1**.

^{1}H NMR spectrum of the crude product is reported in **Figure 3**. It shows a set of signals compatible with a phenanthroline re-aromatized ring. Indeed, while in the aliphatic region there are the three typical signals of the silane propyl chain, in the aromatic region the presence of seven signals of equal integrated intensity states that the mercaptopropylsilane made a nucleophilic attack at one of the epoxide carbons, then followed by dehydration towards the restoration of the aromaticity of the central substituted ring. The methoxy groups that give a signal at 3.54 ppm tend to hydrolyse very easily, and indeed, the lower integrated intensity indicates that partly the methoxy groups hydrolyzed to OH. The crude product was judged to be sufficiently pure and due to the instability of the product, we decided to go further without any other manipulation and estimating the concentration on the bases of the nominal amount of the precursors.

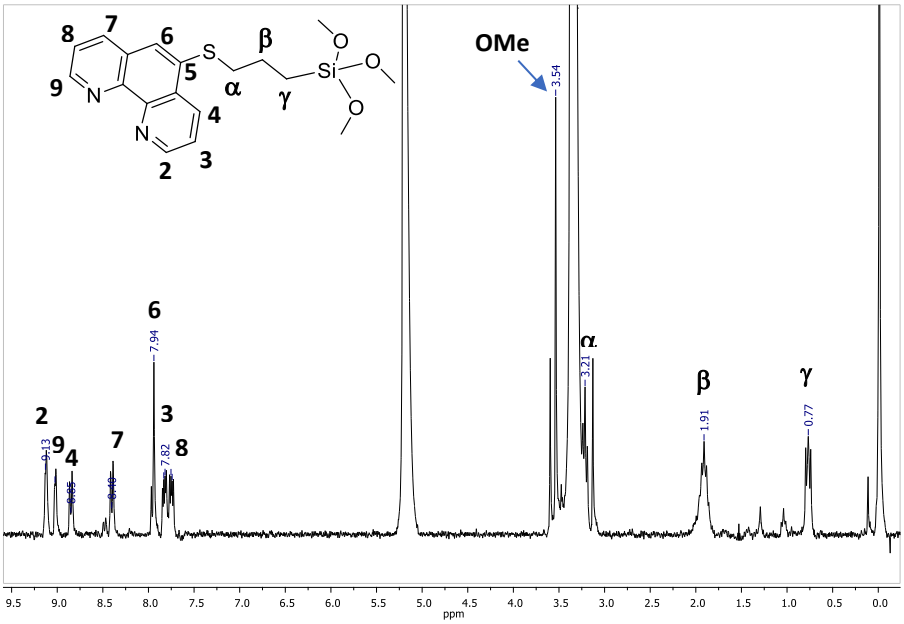

Figure 3. ^{1}H NMR spectrum of compound **3** (9.4 T, 300 K, CD_2Cl_2).

2.3 Functionalization of HNT with Ru-trisphenanthroline complexes

First of all, to enhance the stability of halloysite nanotubes (by Sigma-Aldrich) in water and to increase the reactivity toward the silane group of compound **3**, the pristine HNT were pretreated with NaOH to enhance the amount of surface OH (see Experimental part), as shown in **Scheme 6**.[22,23]

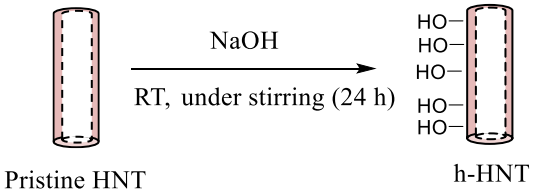

Scheme 6. Hydroxylation of pristine HNT.

To effectively conjugate a Ru-photosensitizer to the hydroxylated HNT (h-HNT) external surface, we used two alternative ways, from now on called Pre-reaction and Pre-complexation.

2.3.1 Formation of HNT-5 through Pre-reaction method

The pre-reaction method for the functionalization of h-HNT consisted of 2 separated following steps: the reaction of the external h-HNT surface with compound **3** followed by the chelation of a suitable Ru precursor on the HNT surface.

At starting, the HNT-**3** adduct was prepared as shown in **Scheme 7**, through the hydrolysis of the methoxy groups of **3** and the consequent condensation with the surface OH of between h-HNT,[24] with the concomitant expulsion of one water molecule per condensed Si-O group. The reaction was carried out in a slightly basic aqueous medium to enhance the interaction between the siloxane group and the outer surface of halloysites.[25]

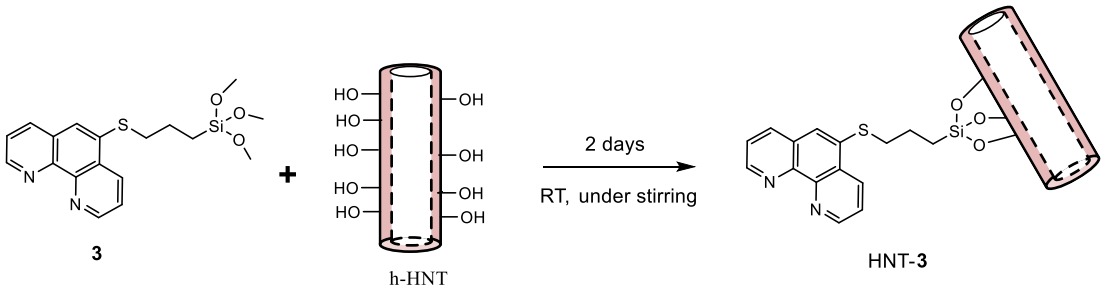

Scheme 7. Schematic description of the synthesis of HNT-**3** adduct.

The FTIR analysis on the solid HNT-**3** intermediate (**Figure 4**) showed small but significant differences compared to the one of the pristine HNT (**Figure 5**). In the HNT-**3** adduct, we can see the typical stretching bands due to the inner Al-μ_2-OH at 3695 cm^{-1} and interlayer Al-μ_2-OH at 3621 cm^{-1} that did not result decreased as expected in the case of reaction with the silane, suggesting that compound **3** interacted mostly with the outer surface. On the contrary, the inner Al_2OH increased after the pre-treatment with NaOH, as well as the outer Si-OH vibrations that are responsible for the very large band centred at ca 3420 cm^{-1}. The weaker band centred at 3550 cm^{-1} attributed to the stretching of the intercalated water molecules were still present but less evident.[26] The presence of the silane molecule was revealed by the stretching mode of the aliphatic groups of the silane chain that were poor but still visible at 2930 cm^{-1}, while in the range between 1800 and 1200 cm^{-1}, overlapped with bending mode bands of water and OH groups, there were sharper and weaker peaks attributable to the aromatic fingerprint bands (inset of **Figure 5**). It is likely that, because of the absence of enough water molecules, compound **3** could not hydrolyze thoroughly. The unhydrolyzed methoxy groups (CH_3O) are visible in the spectra by the deformation vibration band (1255 cm^{-1}), whose presence suggests their uncomplete hydrolysis. The fraction of hydrolyzed compound **3** species not only react with the surface OH groups on HNT but also condense one to each other to form a surface cross-linked structure.[24] All the other bands in the range 1200-400 cm^{-1} are pretty similar in the two samples, and typical of the various vibrational modes of silica and alumina layers of HNT (see **Table 1** for attributions).[24,27–30]

Anyhow, from this analysis we cannot exclude that part of compound **3** was not reacted with the inner alumina, since it is possible that by diffusion it reached the inner lumen. Nevertheless, we think that without vacuum cycles this could be less probable and that most of compound **3** reacted with the exposed outer OH groups.

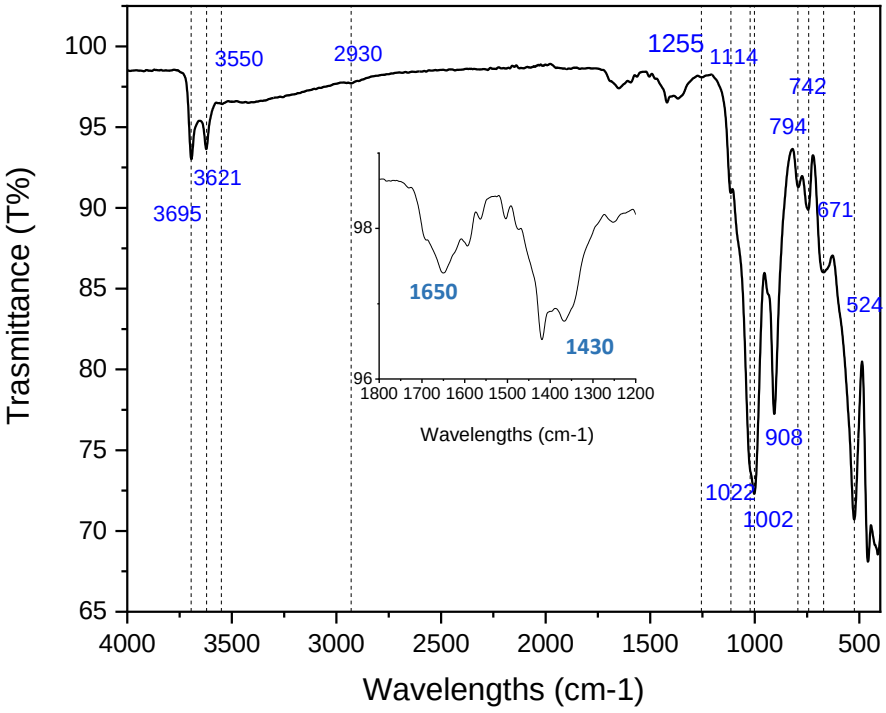

Figure 4. ATR-FTIR spectrum of HNT-**3**

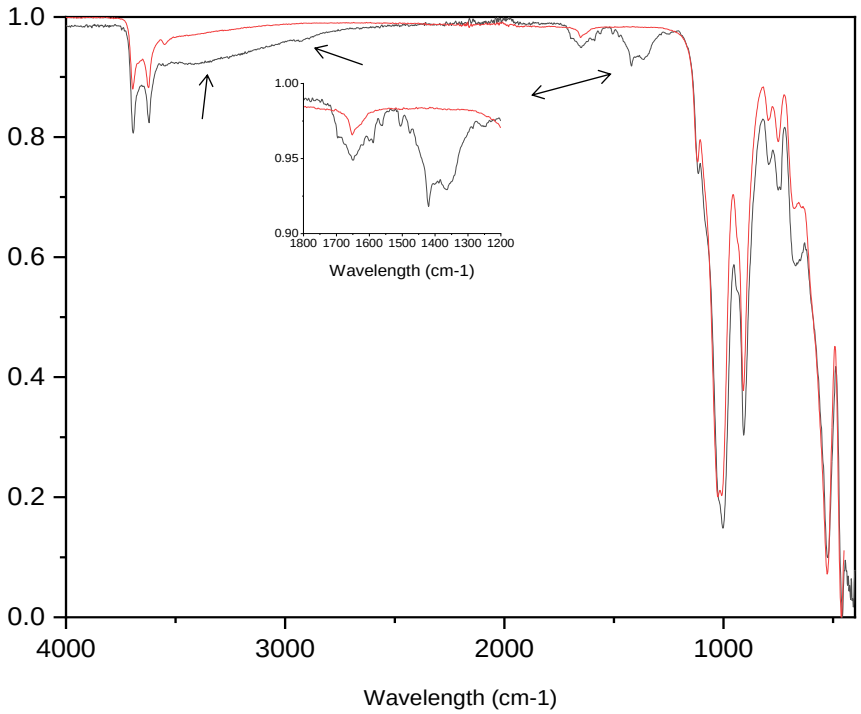

Figure 5. Comparison of ATR-FTIR spectra of HNT-**3** and pristine HNT.

Table 1. ATR-FTIR bands and their attribution for HNT-**3**

Wavenumber (cm^{-1})	Attribution
3695	inner-surface AlO-H stretching
3621	inner AlO-H stretching
3550	OH stretching of water present in the HNT interlayers
2930	CH_2 stretching vibrations of silane
1800-1200	aromatic fingerprints
1347	deformation (scissoring) of Si-CH
1255	deformation (scissoring) of C-H in CH_3
1114	perpendicular Si-O stretching
1088 and 1022	in-plane Si-O stretching
1028	Si-O-Si deformation
1007	Si–O stretching band of HNT silica layer
940	O-H deformation of inner - surface hydroxyl groups
908	O-H deformation of inner hydroxyl groups
794	symmetric stretching of Si–O–Si
742	perpendicular stretching of Si–O–Al
671	alcohol-OH out of plane
524	deformation of of Si–O–Al
460	deformation of Si–O–Si
428	deformation of Si–O

As shown in **Scheme 8**, the HNT-**3** adduct was reacted with the Ru precursor $Ru(phen)_2(OTf)_2$ (**4**) in a mixture of water/methanol at a slightly basic pH (≈ 7.5-8.0). In this condition, no protonation of N of phenanthroline was occurring, so that the complexation was facilitated. Moreover, at this pH value, the positive charge of the HNT inner lumen was still preserved, and so there was active electrostatic repulsion towards the $Ru(phen)_2^{2+}$ precursor. The reaction was easily followed since while the precursor is not luminescent, the substitution at the metal of the two labile triflate anions with a third phenanthroline ligand led to an orange luminescence emission. Even after several washings by centrifugation, the luminescence was observed coming by the collected HNT pellet, demonstrating that complexation reaction did occur at the HNT surface, giving rise to the formation of the adduct HNT-**5**. The ATR-FTIR analysis did not reveal evident peaks attributable to HNT-**5**, except for the fingerprint region due to the bending of the aromatic CH bonds.

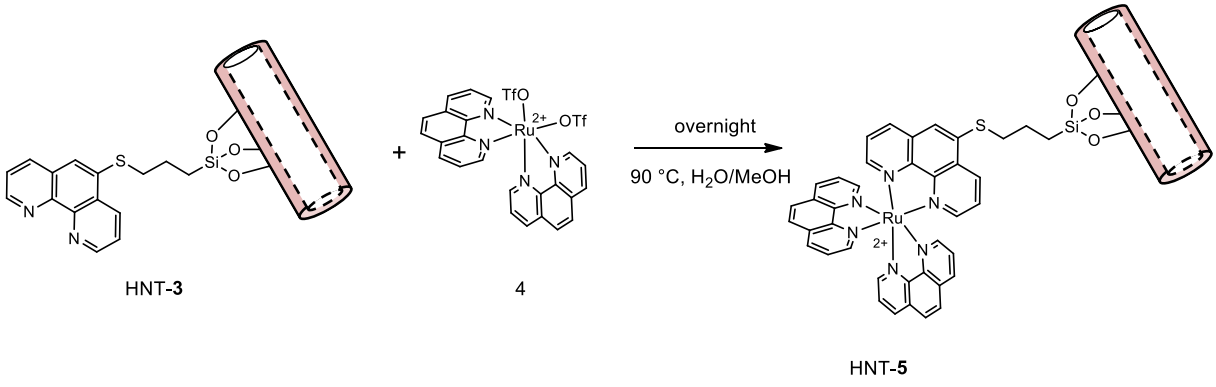

Scheme 8 Schematic description of the synthesis of HNT-5 adduct through pre-reaction method.

2.3.2 Formation of HNT-5 through Pre-complexation method

The second pursued synthetic way consisted of the preventive preparation of the luminescent Ru-based complex, to be reacted with the h-HNT only at a later time (**Scheme 9**).

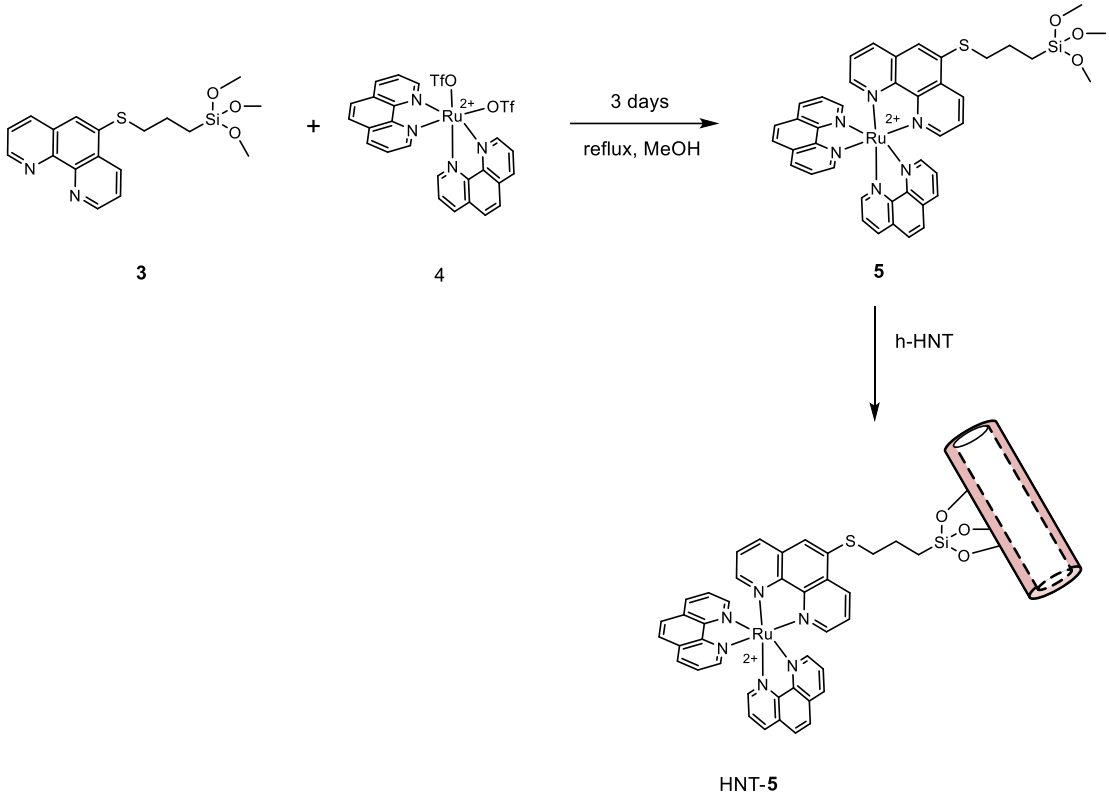

3 4 **5** HNT-**5**

Scheme 9 Schematic description of the synthesis of HNT-5 adduct through pre-complexation method.

As for compound **3**, also complex **5** for the same reasons could not be purified by chromatography due to the high instability and reactivity of the trimethoxysilyl moiety. After three days at reflux, methanol was evaporated to dryness and the residue immediately re-dissolved in MeOD for the NMR analysis. The ^{1}H NMR spectrum is reported in **Figure 6**.

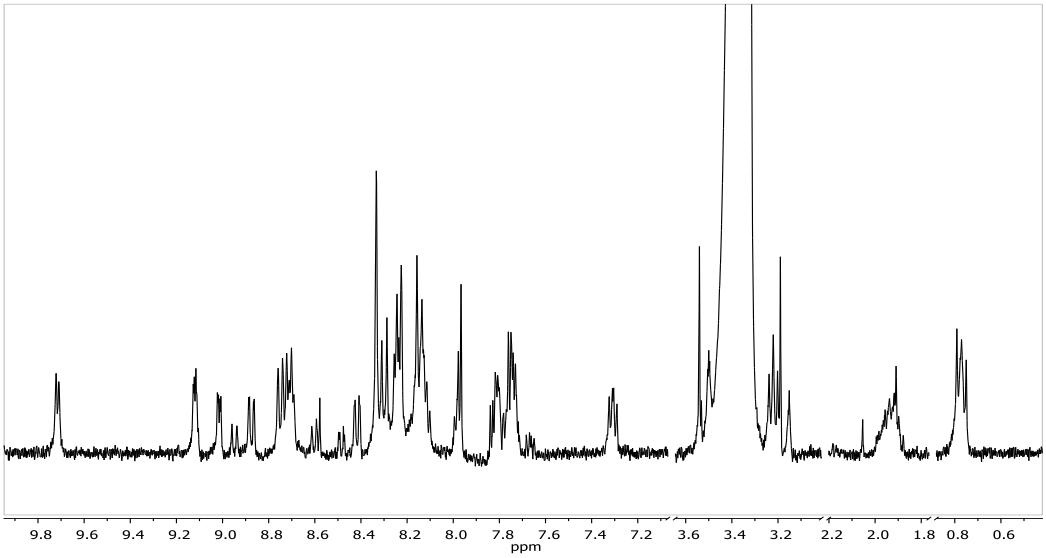

Figure 6. ^{1}H NMR spectrum of compound **5** (MeOD, 400 MHz, 300 K).

On the bases of the symmetry of compound **5**, the expected aromatic signals are 7 of equal integrated intensity (1, in **Figure 7** indicated with the green square symbols) and 8 signals of doubled intensity for the two unsubstituted phenanthroline ligands (**Figure 7**, red circle symbols), since the asymmetry of ligand **3** is enough far away to affect the chemical shift of the two phenanthrolines, thus they result isochronous.

To assign all the aromatic resonances, we compared first of all the ^{1}H NMR spectra of ligand **3**, the mixture of ligand **3** together with *trans*-Ru(phen)$_2$(OTf)$_2$ complex at t = 0 and the same mixture at t = 72 h (**Figure 7**).

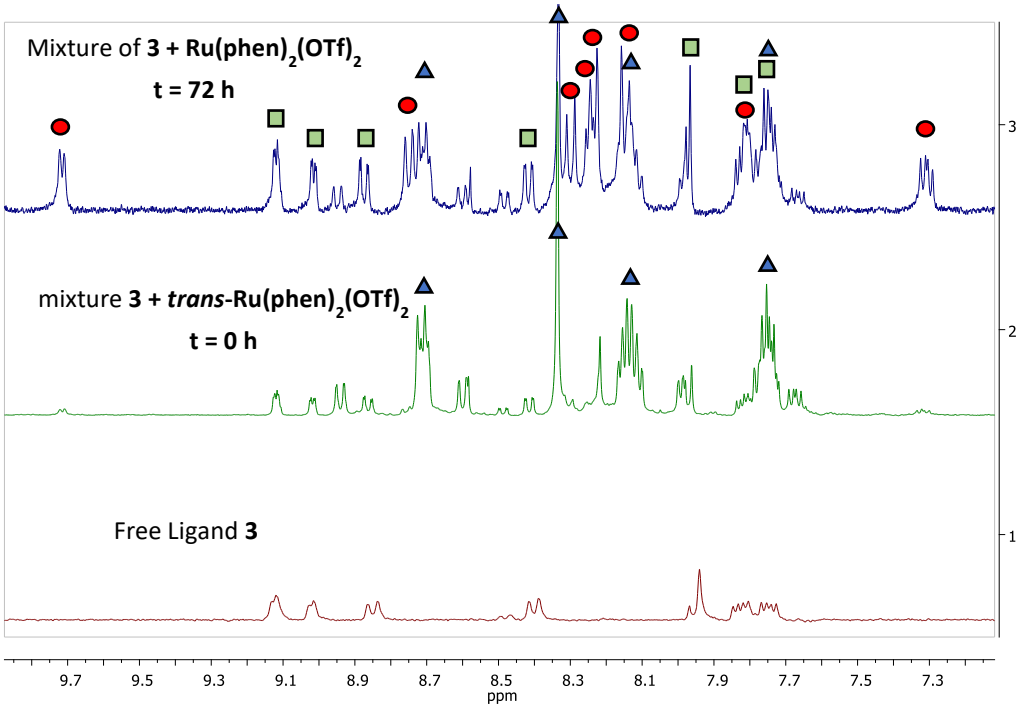

Figure 7. Aromatic region of ^{1}H NMR spectra (MeOD, 400 MHz, 300 K) of (1) compound **3**; (2) mixture of *trans*-Ru(phen)$_2$(OTf)$_2$ and compound **3** at t = 0; (3) the same mixture at t = 72 h.

The first consideration concerns the Ru precursor. The ^{1}H NMR showed four signals only, which are compatible with the *trans* isomer, while the Ru complex synthesized (**4**) was originally the *cis*. The isomerization from *cis* to *trans* is induced by the exposure to sunlight and depends on both the exposure time and the light intensity, while the inverse transformation reaction from *trans* to *cis* is induced by prolonged heating.[31] Thus, in our synthesis the first step necessary for the complexation reaction was the isomerization step from *trans* to *cis* (**Scheme 10**).

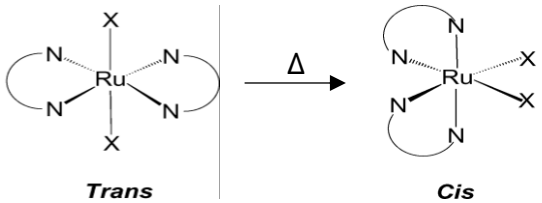

Scheme 10. Schematic depiction of the isomerization trans-cis around the Ru(II) centre activated by heating.

Simultaneously with the *cis*- isomer formation, the reaction of compound **3** started to take place. **Figure 8 and 9** report the 2D NMR homonuclear ^{1}H COSY and ^{1}H NOESY experiments, through which the assignment of all the signal of the desired product was obtained.

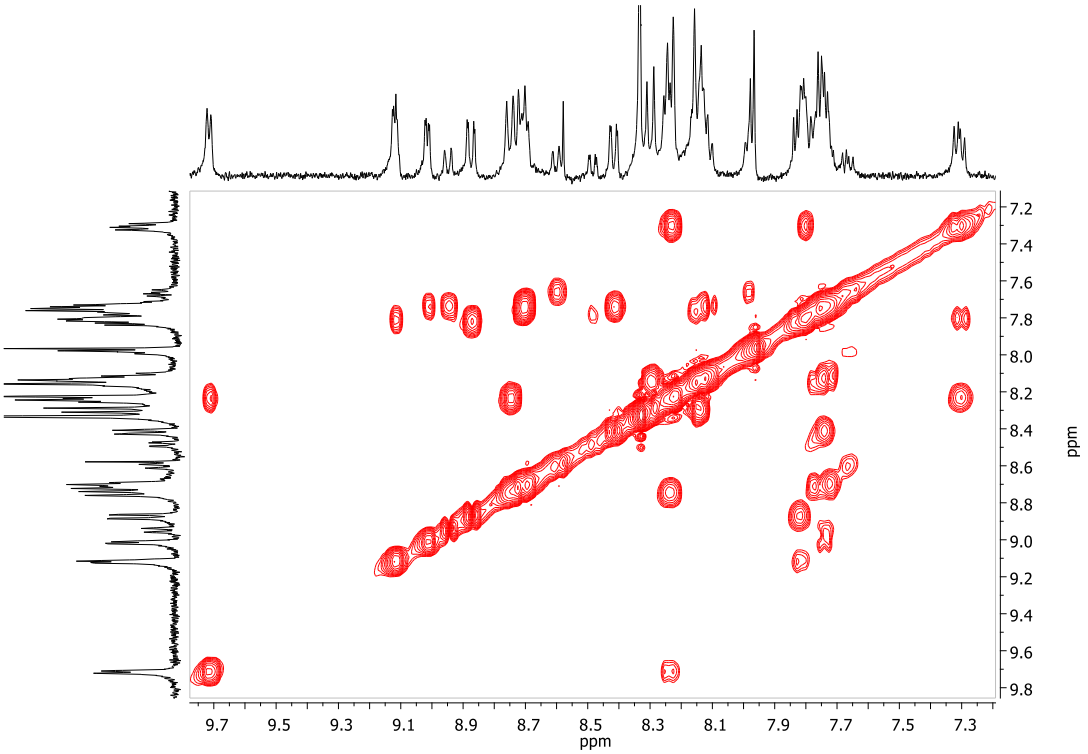

Figure 8.2D- NMR ^{1}H-COSY experiment (MeOD, 400 MHz, 300 K) of compound **5**.

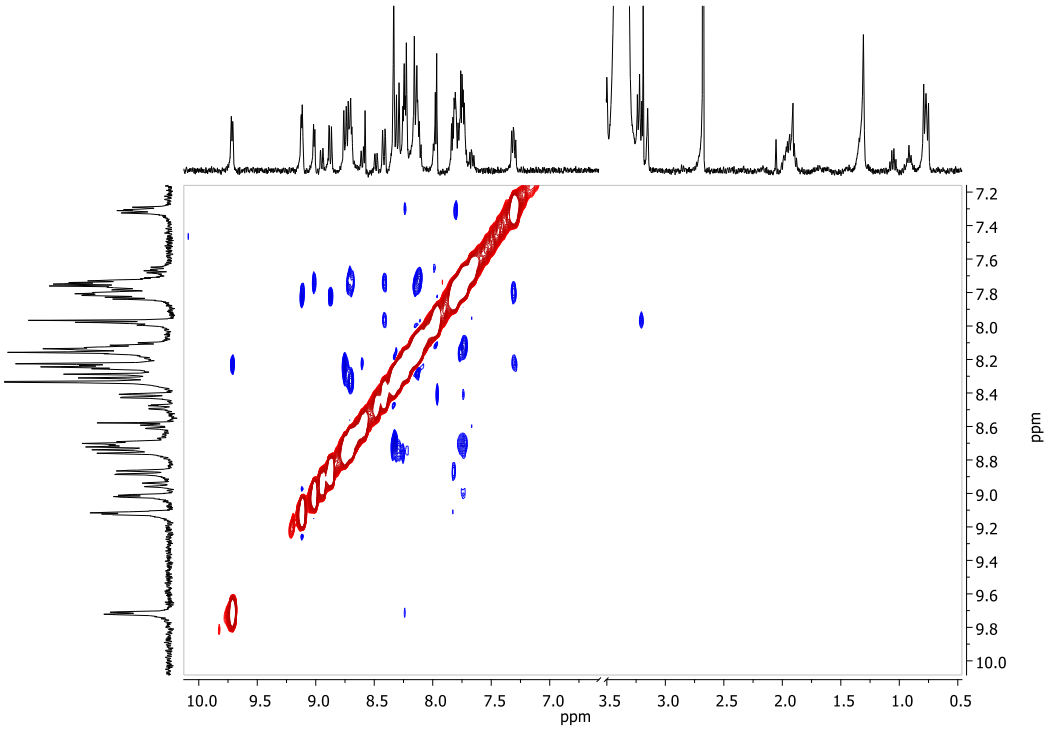

Figure 9.2D- NMR ^{1}H-NOESY experiment (MeOD, 400 MHz, 300 K) of compound **5**.

Together with the appearance of the NMR signals attributable to the desired product, an orange luminescence started to be visible when the sample was observed under UV-lamp irradiation.

The comparison of the ATR-FTIR spectra of HNT-**5** obtained by both the methods (**Figure 10)** did not show any substantial difference, stating that the final products are very similar product. The only difference is the missing of the weak peak at 1255 cm^{-1}, already attributed

to the C-H scissoring of CH_3. This evidence suggests that in this case, a possible oligomerization of **5** could have occurred over HNT surface. [24]

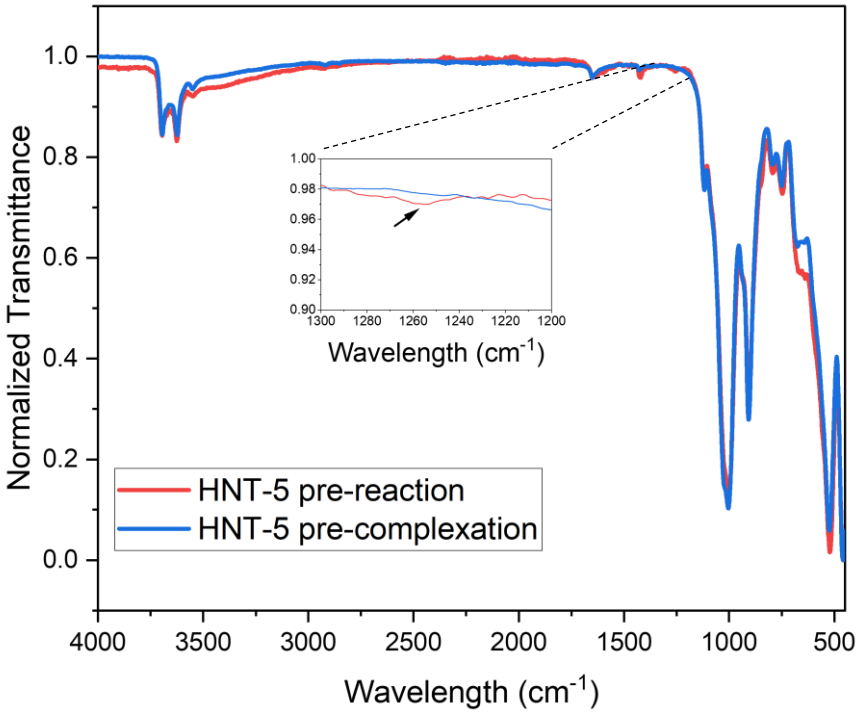

Figure 10. Comparison of normalized ATR-FTIR spectra of HNT-**5** synthesized through pre-reaction and pre complexation. The inset highlights the missing peak at 1255 cm^{-1}.

Two pictures of the samples observed under sunlight or UV-lamp irradiation are reported as well (**Figure 11**). Under UV-lamp we observed that the luminescence emission of HNT-**5** adduct synthesized by the pre-reaction method was much more intense compared to HNT-**5** synthesized with the other route. Also, a simple colloidal stability test (1 mg/mL) show that HNT-**5** was much more stable in the case of the pre-reaction product compared to the pre-complexation one, which completely settled down after 12 h. This colloidal stability could be attributed to the increase in the net charge value of the HNT outer surface measured by ζ-potential (**Figure 12**), passing from negative values for pristine HNT (-25.0 ± 0.7 mV measured at pH 7.0) to + 16.9 ± 1.2 mV for pre-complexation product and + 44.3 ± 3.2 mV in the case of the pre-reaction sample. The observation of a more positive value for HNT-**5** in the case of pre-reaction compared to pre-complexation further confirms the increase of % of Ru interacted with HNT. Also, the positive ζ-potential of HNT-**5** adduct compared to the pristine HNT negative value suggests that the localization of PS is in the outer part of the nanotube. Due to the higher aqueous colloidal stability and obviously for the higher content of Ru PS, we concentrated our attention on HNT-**5** adduct obtained by the pre-reaction route from now on.

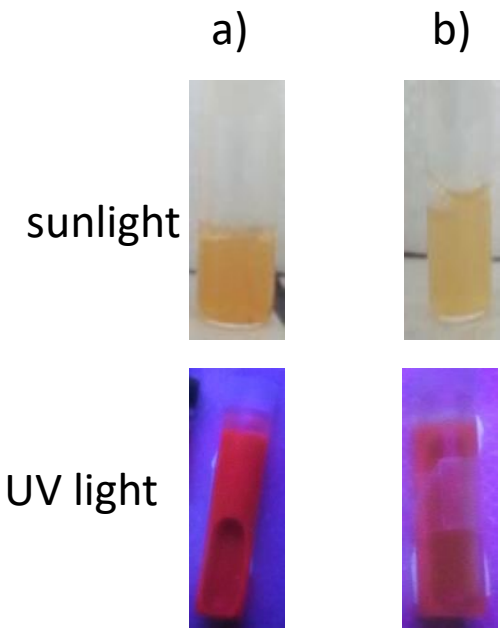

Figure 11. Comparison of the colour of HNT-**5** synthesized through a) pre-reaction and b) pre complexation.

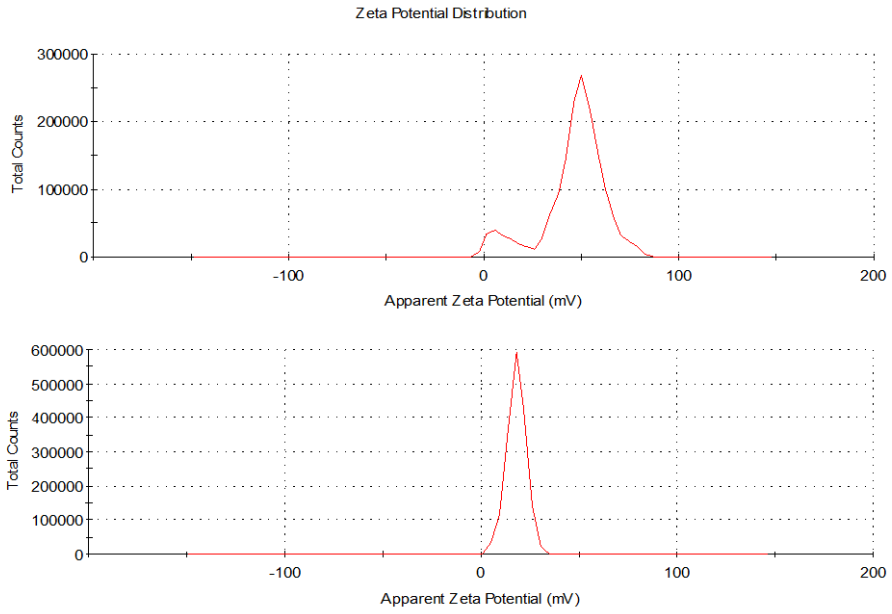

Figure 12. ζ-potential analyses of suspensions (1.0 mg/1.0 ml milliQ water)of HNT-5 synthesized through a) pre-reaction and b) pre complexation.

2.4 Photoreaction of HNT-5 with 1,5-Dihydroxynaphthalene as a Reporter of $^1O_2$ Formation

The ability of Ru complex anchored on the surface of HNT to act as photosensitizers for the $^1O_2$ generation was assessed by using 1,5-dihydroxynaphtalene (DHN) as an indirect reporter of singlet oxygen. DHN reacts promptly, quantitatively and selectively with $^1O_2$ forming the oxidized species Juglone (5-hydroxy-1,4-naphthalenedione),[32,33] according to **Scheme 11**:

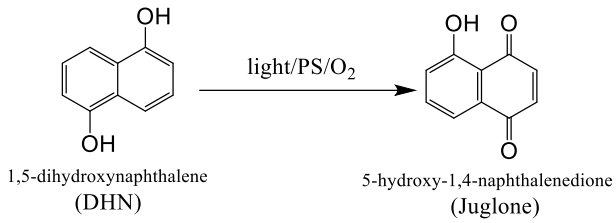

Scheme 11. Photochemical reaction used to monitor $^1O_2$ formation in the presence of an effective PS.

The reaction progress was monitored by UV–vis absorption spectroscopy following the decrease of the DHN band at 299 nm (**Figure 13**). This reaction occurs without the formation of long-lived intermediates or by-products as indicated by the two isosbestic points at 280 and 330 nm observed in the spectra recorded during the irradiation.

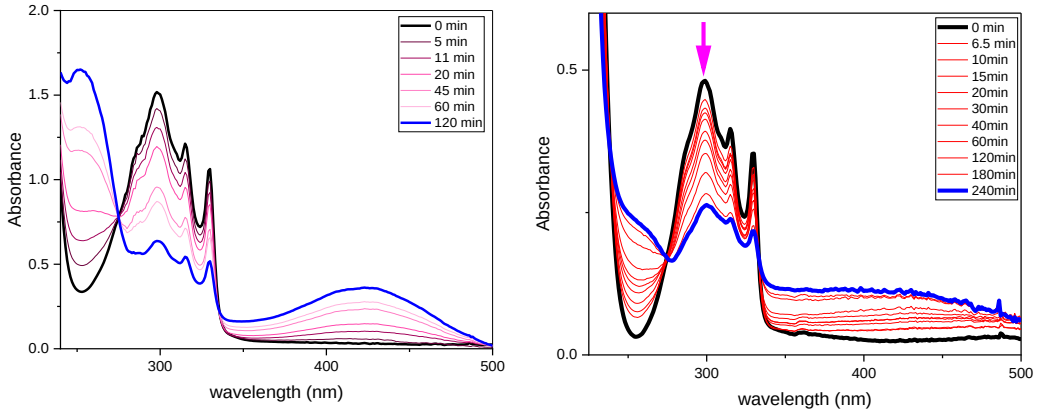

Figure 13 UV–vis absorption spectra recorded at different times of irradiation of LED lamp on solutions containing the standard $Ru(bpy)_3^{2+}$ (left) and HNT-**5** (right) with Ru concentration (1.9 X 10^{-5} M) and DHN (3.7 × 10^{-4} M) in 2.6 mL of MeOH/H_2O (15: 85) bubbled with O_2 for 10 min.

Figure 14 shows the first-order semilogarithmic plots for the reaction of equation 5.1, sensitized by Ru complex on HNT-5.

$$DHN + {}^1O_2 \rightarrow juglone + \frac{1}{2}\,{}^3O_2 \qquad (Eq.\ 5.1)$$

We carried out the experiments by mixing DHN solution with HNT-5 suspension or Ru standard, and after being saturated with O_2, it was irradiated for a total time of 240 min monitoring the evolution of the species by UV-vis spectroscopy.

The disappearance of DHN followed a pseudo-first order kinetic low, which is due to the adoptable steady-state approximation to the oxygen concentration, and the reaction rate can be related to the DHN concentration with a kinetic equation equal to $r = k_{obs}[DHN]$, whose integrated equation is (**Eq. 5.2**)

$$ln\frac{A_t}{A_0} = -k_{obs}t \qquad (Eq.5.2\ )$$

The pseudo first-order semilogarithmic plots for DHN photo-oxidation in the presence of the investigated sensitizers are shown in **Figure 14**, where the values of $\ln(A_t/A_0)$ decrease linearly over time. While in the case of HNT-5 the slope (k_{obs}) is -0.006 min^{-1} compared to -0.01 min^{-1} for Ru standard.

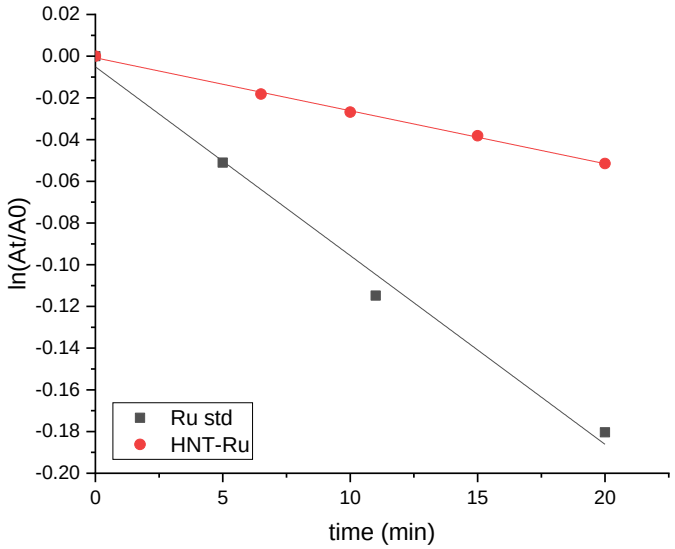

Figure 14 Photo-oxidation of DHN in the presence of photosensitizers HNT-5 and Ru standard. A_t and A_0 represent the absorbance measured at 299 nm (the maximum of the DHN absorption band) at time t and time 0, respectively.

2.5 Emission of HNT-5

It is known, that Ru $(phen)_3^{2+}$ -like complexes exhibit strong luminescence upon excitation in the MLCT region. Their emission band is usually in the range between 585 and 750 nm and strongly depends on ligands structure around the ruthenium centre. [15,17,18]

Figure 15 shows the excitation and emission spectra for Ru PS over HNT-**5** adduct in water. LC (π- π *) transaction was at 261 nm together with the one at 330 nm. The mixed-ligand nature of our Ru complex produced multiple singlet metal-to-ligand charge transfer ^{1}MLCT transitions in the visible region at 436 and 450 nm, which can be assigned to electronic transitions from the Ru (II) based t_2g orbital to the ligand-based π* orbitals. The emission spectrum presents a single broad peak at 645 nm, typical for this class of compounds.[34] The comparison with the free Ru-silane complex in water was prevented by the high reactivity of the silane group that in this medium quickly forms oligomers by the subsequent hydrolysis and condensation steps of the methoxy groups. In the literature usually, it is showed a blue shift of the emission comparing the free with the bound Ru-Silane complex, due to a rigidochromism effect.[35–38]

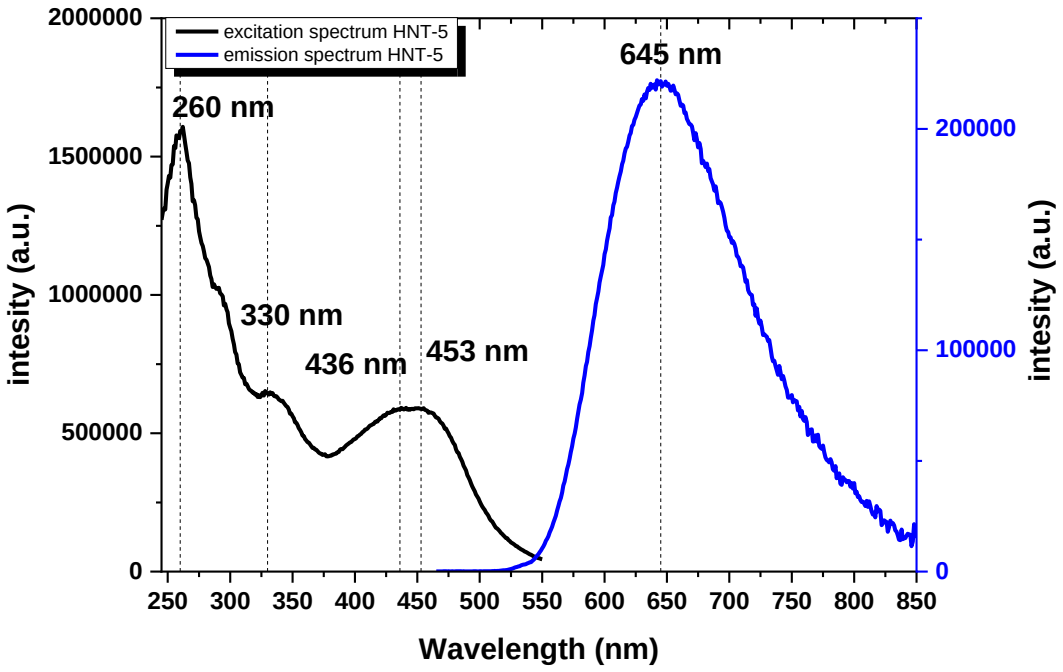

Figure 15 Fluorescence emission (blue line) and excitation (black line) spectra of HNT-**5** in aerated water solutions.

3 Conclusions

PDT activity has been known generally for over a century. While there is no "ideal" photosensitizer, those derived from transition metal complexes offer many advantages, so we aimed to covalently functionalize the halloysite nanotube surface with a novel ruthenium complex photosensitizer belonging to the very well-known family of the Ru-imine complexes.

^{1}H-NMR spectroscopy was used to follow the new ligand synthesis. The phenanthroline-silane new ligand was exploited as a linker between halloysite and the $Ru(phen)_2^{2+}$ precursor. The step of binding was done exploring two distinct paths, that is a pre-reaction of the phenanthroline-silane ligand followed by the complexation of the "phen" pendant to the metal ion or a pre-complexation of the ligand with the Ru precursor followed by the interaction with the halloysite surface.

The photoreaction and emission spectra of the new adduct were studied in an aqueous medium, confirming the suitability of the adduct for PDT application. Moreover, the new product is suitable for future development as a dual drug carrier by the exploitable loading of a second drug into the free lumen.

4 Experimental

4.1 Materials and instruments

The Ru precursor $Ru(phen)_2(OTf)_2$ (**4**) was prepared previously by our group following a the literature procedure.[39]

Halloysite nanotubes HNT, Sodium hydroxide pellets 98%, Cesium carbonate 99%, Magnesium sulfate anhydrous 99%, 1,10-Phenanthroline monohydrate, Methanol anhydrous 99.8%, H_2SO_4 97%, Chloroform 99.5%, Dichloromethane 99.8%, Ethyl acetate anhydrous 99.8%, Tris(2,2-bipyridyl)ruthenium(II) chloride hexahydrate 99.9%, Tetrabutylammonium bisulfate 99%, and 3-(mercaptopropyl)trimethoxysilane 95% were purchased from Sigma Aldrich; n-hexane 96% and acetone were purchased from Scharlau; HNO_3 65% and HCl 30% were purchased from Merck Germany; Ammonia 28% was purchased from Prolabo. The oxydation to epoxyde of the phenanthroline was carried out by employing a commercial bleach (CLOROX). They were all used as received without further purification. Ultrapure milli-Q water (Millipore, resistivity=18M Ω cm^{-2}) was used for the preparation of the aqueous solutions.

NMR experiments were carried out on a Bruker DRX400 spectrometer equipped with a Bruker 5 mm BBI Z-gradient probe-head with a maximum gradient strength of 53.5 G/cm.

UV-vis absorption spectra were acquired on an Agilent model 8543 spectrophotometer at room temperature and using standard quartz cells with a 1.0 cm path length.

ζ-potential measurements were carried out using a Malvern Zetasizer Nano ZS instrument equipped with a 633 nm solid-state He–Ne laser at a scattering angle of 173°, typically dissolving samples at a concentration of 1 mg/mL or less at 25 °C. The measurements were averaged on at least three repeated runs.

ATR-FTIR spectra were acquired on a PerkinElmer Frontier instrument equipped with an ATR accessory with a diamond/ZnSe crystal. The IR spectra were registered between 4000 and 400 cm^{-1}.

Elemental analysis of Ru content on HNT-**5** synthesized by the pre-reaction method was carried out by ICP-AES analysis on a Perkin-Elmer Pinnacle instrument. For Ru determination, 1.11 mg of a lyophilized HNT-**5** sample was digested with an acidic/oxidant mixture composed of 0.6 mL HCl (30%) and 0.3 mL HNO_3 (65%) and warming the mixture by a sand bath at 90 °C for 12 h directly in a 10 mL volumetric flask. The compound HNT-**5** at the end of the digestion process was destroyed and dissolved.

Emission spectra were obtained with an Edinburgh FLS980 spectrofluorimeter equipped with a 450 W xenon arc lamp. Emission spectra were corrected for source intensity (lamp and grating) and emission spectral response (detector and grating) by standard correction curves.

4.2 Synthesis of Compound 1.

In a 250 mL round-bottom flask, tetrabutylammonium bisulphate (800 mg, 2.36 mmol) was dissolved in 46 mL of commercial bleach (CLOROX) at 18 °C. The solution was left under constant stirring and the pH adjusted at 8.2-8.3 by the addition of 1.3 µL H_2SO_4 23%. Then, the solution was added with 1.0 g (5.05 mmol) 1,10-phenanthroline monohydrate previously dissolved in 100 mL CH_2Cl_2. The pH of the solution was constantly monitored and maintained at pH 8.2-8.3 by following additions of a few microliters of NaOH 50%. The reaction was stopped after 1.5 h by separating the organic and aqueous phases, extracting and treating the aqueous phase with CH_2Cl_2 (2 mL x 3). The collected organic fractions were then washed with water (5 mL x 2), anhydrified with anhydrous magnesium sulphate, and the solvent evaporated to dryness. The yellowish solid residue was re-dissolved in chloroform and precipitated by the addition of an excess of acetone (ratio $CHCl_3/CH_3COCH_3$ 1:3). The supernatant was then filtered off and the precipitate collected after being dried under

vacuum. A TLC (eluent mixture: 8 ethyl acetate, 1 n-hexane, 1 MeOH, 0.5 mL NH_3) revealed the presence of a second by-product species (R_f = 0.59), apart the compound of interest **1** (R_f = 0.43). Yield 93.2% (5.5 g). ^{1}H-NMR (**Figure 16**, 400 MHz, $CDCl_3$) δ 4.63 ppm (2H, s, CH(7,8)); 7,38 ppm (2H, dd, CH(1,13), J=7.4, 4.7 Hz); 7,98 ppm (2H, dd, CH(6,14), J=7.4, 1.1 Hz) 8,85 ppm (2H, *ps*d,CH(2,12), J_{app}=3.7 Hz).

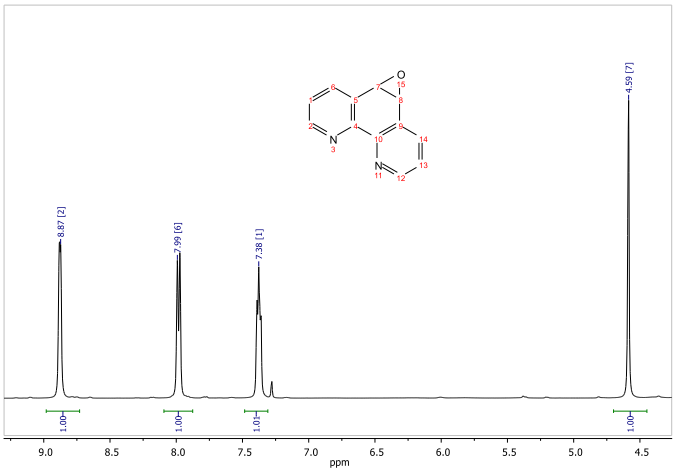

Figure 16–^{1}H-NMR spectrum of compound **1** after the chromatographic separation (9.4 T, 300 K, $CDCl_3$).

4.3 Synthesis of Compound 3.

In a 100 mL two-necked round-bottom flask, compound **1** (51.2 mg, 0.26 mmol) was dissolved in 10 mL of anhydrous methanol under nitrogen. Then, $CsCO_3$ (1.0 g) and 3-(mercaptopropyl)trimethoxysilane (50 mL, 0.27 mmol) were added and the reaction was left to occur at 65 °C for 3 days under stirring and inert atmosphere. The mixture assumed first a brown-yellow colour and at the end turned to light yellow. The crude mixture was filtered on a sintered glass disk filter funnel and the product was stored in methanol solution under nitrogen. Only a small portion of this solution was dried and, immediately after, dissolved in the deuterated solvent for the NMR analysis. ^{1}H-NMR (400 MHz, CD_2Cl_2) δ 9.17 ppm (1H, dd, CH(2), J= 4.1, 1.3 Hz); 9.02 ppm(1H, dd, CH(9), J= 4.2, 1.4 Hz); 8.85 ppm (1H, dd, CH(4), J= 8.3, 1.3 Hz); 8.4 ppm (1H, dd, CH(7) J= 8.2, 1.4 Hz); 7.94 ppm (1H, s, CH(6); J= 8.2, 4.2 Hz); 7.83 ppm (1H, dd, CH(3); J= 8.3, 4.1 Hz); 7.75 ppm (1H, dd, CH(8)); 3.21 ppm (2H, t, CH2 (α) J= 7.4 Hz); 1.91 ppm (1H, tt, CH2 (β) Japp=7.7 Hz); 0.75 ppm (2H, m, CH2 (γ).

4.4 Preparation of hydroxylated HNTs (h-HNTs)

The synthesis of h-HNT was carried out by following the same procedure already reported in the literature.[23] Typically, 100 mg of HNT was dispersed in 5.0 mL milliQ water, followed by adding 3.0 mg NaOH. The mixture was magnetically stirred for 24 h at room temperature. The resultant hydroxylated HNTs (h-HNTs) solid phase was then separated by centrifugation and rinsed several times with water until the pH reached the value of 7. The supernatant was discarded and the HNT slurry dried at 60-80 °C to give a white powder (**h-HNT**) ready for further uses.

4.5 Preparation of HNT-3

50 mg of **h-HNT** was dispersed in 10.0 mL milliQ water. The suspension was adjusted to pH 8.5 with the addition of NaOH 0.1 M, followed by the addition of compound **3** (8.8 mg, 0.0237 mmol). The mixture was magnetically stirred for 48 h at room temperature. The resultant HNT-**3** solid phase was then separated by centrifugation and rinsed several times with water. The prepared HNT-**3** was kept dispersed in 2.0 mL milliQ water with an adjusted pH of 8.0 for

the following complexation step. To record ATR-FTIR spectrum, 0.2 mL of suspension was centrifuged (4226 rcf, 3 min), then dried in an oven at 100 °C for 1.5 h.

4.6 Synthesis of HNT-5 adduct through the pre-reaction method

In a 25 mL two-necked round-bottom flask, under nitrogen atmosphere, the Ru precursor $Ru(phen)_2(OTf)_2$ (**4**, 9.0 mg, 0.01185 mmol) was added to 2.0 mL methanol and stirred until complete dissolution was observed. HNT-**3** was dispersed in 1.8 mL of milliQ water (pH 8.0) and then the suspension was added to the flask, such that the mmol ratio Ru: compound **3** was ca. 1:2. The final volume was adjusted to 10 mL with further addition of milliQ water, then magnetically stirred for 10 min. Finally, the solution mixture was left under stirring in an oil bath at 90 ° C overnight under an inert atmosphere. Once the mixture temperature reached to 90 ° C, the visible color changed from red (non luminescent) to bright orange (luminescent). At the end of the heating period, the mixture was left to cooling down naturally to room temperature by removing the heat source. The so-obtained suspension was recovered by centrifugation (30 min at 4226 rcf), followed by washing with methanol for 3 times to remove unreacted Ru precursor **4** until supernatant was clear. An extra washing step was carried out using milliQ water, followed by dispertion in 0.5 mL milliQ water. Finally, the product was freeze-dried. From ICP-AES analysis, the Ru content % in the lyophilized sample was 0.63% w/w, equal to a yield of complexation of 26%.

4.7 Synthesis of HNT-5 adduct through the pre-complexation method

In a 25 mL two-necked round-bottom flask, under nitrogen atmosphere, the Ru precursor $Ru(phen)_2(OTf)_2$ (**4**, 9.0 mg, 0.01185 mmol) was added to 2.0 mL anhydrous methanol by stirring until complete dissolution was observed. Then, compound **3** (4.4. mg, 0.01185 mmol) was added. The total volume was set to 3 mL with a further addition of anhydrous methanol and homogenized by magnetic stirring for 10 min. Finally, the solution mixture was left under stirring in an oil bath at 90 ° C for 72 h. At the end of the heating period, the mixture was left to cooling down naturally to room temperature by removing the heat source. The product compound **5** presented an intense red-orange luminescence under UV-lamp irradiation. Directly to compound **4**, 50 mg of **h-HNT** dispersed in 10 ml milliQ water (pH= 8.0) were added. The mixture was magnetically stirred overnight at room temperature. The resultant HNT-**5** solid phase was recovered by centrifugation (30 min at 4226 rcf), followed by washing with methanol for 3 times to remove the possible unreacted complex **5**, and finally washed once with milliQ water. The final product was dispersed in 0.5 mL of milliQ water for further uses.

4.8 Photoreaction of HNT-5 and Ru standard with DHN

In a 10 mL volumetric flask, a stock solution of DHN was prepared by dissolving 17.0 mg DHN in MeOH/ H_2O (15:85) mixture (1.0×10^{-3}M) that was further diluted to 3.7×10^{-4}M. Then, in a quartz cuvette (Quartz SUPRASIL®), 2.6 mL of the diluted DHN solution (3.7×10^{-4}M) were mixed with 0.8 mg of HNT-**5** (1.9×10^{-5}M of Ru). Before irradiation, the solution was saturated with O_2 by bubbling directly in the cuvette for ca. 10 min. The solution was then irradiated through a LED light source (Megamanlamp ® PAR16 GU10 LR0707-SP) and spectra were collected at the following time points: 6.5, 10, 15, 20, 30, 40, 60, 120, 180, and 240 min. The blank used to overcome the halloysite scattering was 2.6 mL of the diluted DHN solution (3.7×10^{-4}M) were mixed with 0.8 mg of pristine HNT. The same procedure was followed for the photoreaction involving Ru standard (Tris(2,2-bipyridyl)ruthenium(II) chloride hexahydrate) using 0.23 mL of Ru standard stock (1.1×10^{-4}M) (0.17 mg / 2.0 mL of MeOH/ H_2O), mixed with 0.5 mL of DHN (1.0×10^{-3}M) followed by further dilution in the quartz cuvette with MeOH/ H_2O until a total volume of 2.5 mL was reached to maintain the same ratio of [DHN]/[PS] used in HNT-**5** analysis.

5 Bibliography

(1) Mjos, K. D.; Orvig, C. Metallodrugs in Medicinal Inorganic Chemistry. *Chem. Rev.* **2014**, *114* (8), 4540–4563. https://doi.org/10.1021/cr400460s.

(2) Ndagi, U.; Mhlongo, N.; Soliman, M. E. Metal Complexes in Cancer Therapy - an Update from Drug Design Perspective. *Drug Des. Devel. Ther.* **2017**, *11*, 599–616. https://doi.org/10.2147/DDDT.S119488.

(3) Süss-Fink, G. Arene Ruthenium Complexes as Anticancer Agents. *Dalt. Trans.* **2010**, *39* (7), 1673–1688. https://doi.org/10.1039/B916860P.

(4) Hannon, M. Metal-Based Anticancer Drugs: From a Past Anchored in Platinum Post-Genomic Future and Biology. *Pure Appl. Chem* **2007**, *79*, 2243–2261. https://doi.org/10.1351/pac200779122243.

(5) Hamilton, U. O. and G. A Better Platinum-Based Anticancer Drug Yet to Come? *Anti-Cancer Agents in Medicinal Chemistry*. 2010, pp 293–301. https://doi.org/http://dx.doi.org/10.2174/187152010791162306.

(6) Trondl, R.; Heffeter, P.; Kowol, C. R.; Jakupec, M. A.; Berger, W.; Keppler, B. K. NKP-1339, the First Ruthenium-Based Anticancer Drug on the Edge to Clinical Application. *Chem. Sci.* **2014**, *5* (8), 2925–2932. https://doi.org/10.1039/C3SC53243G.

(7) Reedijk, B. J. Metal-Ligand Exchange Kinetics in Platinum and Ruthenium Complexes. *Platin. Met. Rev.* **2008**, *52* (1), 2–11. https://doi.org/10.1595/147106708X255987.

(8) Allardyce, C.; Dyson, P. Ruthenium in Medicine: Current Clinical Uses and Future Prospects. *Platin. Met. Rev.* **2001**, *45*, 62–69.

(9) Ghesquiere, J.; Gac, S. Le; Marcelis, L.; Mesmaeker, C. M. and A. K.- De. What Does the Future Hold for Photo-Oxidizing RuII Complexes with Polyazaaromatic Ligands in Medicinal Chemistry? *Current Topics in Medicinal Chemistry*. 2012, pp 185–196. https://doi.org/http://dx.doi.org/10.2174/156802612799079008.

(10) Barton, J. K.; Danishefsky, A.; Goldberg, J. Tris(Phenanthroline)Ruthenium(II): Stereoselectivity in Binding to DNA. *J. Am. Chem. Soc.* **1984**, *106* (7), 2172–2176. https://doi.org/10.1021/ja00319a043.

(11) Mesmaeker, A. K.-D.; Orellana, G.; Barton, J. K.; Turro, N. J. LIGAND-DEPENDENT INTERACTION OF RUTHENIUM(II) POLYPYRIDYL COMPLEXES WITH DNA PROBED BY EMISSION SPECTROSCOPY. *Photochem. Photobiol.* **1990**, *52* (3), 461–472. https://doi.org/https://doi.org/10.1111/j.1751-1097.1990.tb01787.x.

(12) Chatterjee, D. K.; Fong, L. S.; Zhang, Y. Nanoparticles in Photodynamic Therapy: An Emerging Paradigm. *Adv. Drug Deliv. Rev.* **2008**, *60* (15), 1627–1637. https://doi.org/https://doi.org/10.1016/j.addr.2008.08.003.

(13) Montaseri, H.; Kruger, C. A.; Abrahamse, H. Review: Organic Nanoparticle Based Active Targeting for Photodynamic Therapy Treatment of Breast Cancer Cells. *Oncotarget; Vol 11, No 22* **2020**.

(14) McKenzie, L. K.; Bryant, H. E.; Weinstein, J. A. Transition Metal Complexes as Photosensitisers in One- and Two-Photon Photodynamic Therapy. *Coord. Chem. Rev.* **2019**, *379*, 2–29. https://doi.org/https://doi.org/10.1016/j.ccr.2018.03.020.

(15) Lemercier, G.; Four, M.; Chevreux, S. Two-Photon Absorption Properties of 1,10-Phenanthroline-Based Ru(II) Complexes and Related Functionalized Nanoparticles for Potential Application in Two-Photon Excitation Photodynamic Therapy and Optical Power Limiting. *Coord. Chem. Rev.* **2018**, *368*, 1–12. https://doi.org/https://doi.org/10.1016/j.ccr.2018.03.019.

(16) Mascheroni, L.; Dozzi, M. V.; Ranucci, E.; Ferruti, P.; Francia, V.; Salvati, A.; Maggioni, D. Tuning Polyamidoamine Design To Increase Uptake and Efficacy of Ruthenium Complexes for Photodynamic Therapy. *Inorg. Chem.* **2019**, *58* (21), 14586–14599. https://doi.org/10.1021/acs.inorgchem.9b02245.

(17) Sutin, N.; Creutz, C. Light Induced Electron Transfer Reactions of Metal Complexes. *Pure Appl. Chem.* **1980**, *52* (12), 2717–2738. https://doi.org/doi:10.1351/pac198052122717.

(18) Alford, P. C.; Cook, M. J.; Lewis, A. P.; McAuliffe, G. S. G.; Skarda, V.; Thomson, A. J.; Glasper, J. L.; Robbins, D. J. Luminescent Metal Complexes. Part 5. Luminescence Properties of Ring-Substituted 1,10-Phenanthroline Tris-Complexes of Ruthenium(II). *J. Chem. Soc. Perkin Trans. 2* **1985**, No. 5, 705–709. https://doi.org/10.1039/P29850000705.

(19) Monro, S.; Colón, K. L.; Yin, H.; Roque 3rd, J.; Konda, P.; Gujar, S.; Thummel, R. P.; Lilge, L.; Cameron, C. G.; McFarland, S. A. Transition Metal Complexes and Photodynamic Therapy from a Tumor-Centered Approach: Challenges, Opportunities, and Highlights from the Development of TLD1433. *Chem. Rev.* **2019**, *119* (2), 797–828. https://doi.org/10.1021/acs.chemrev.8b00211.

(20) Howell, B. A.; Dumitrascu, A. Thermal Stability of Bidendate Nitrogen Ligands Tethered to Multiwall Carbon Nanotubes. *J. Therm. Anal. Calorim.* **2010**, *102* (2), 505–512. https://doi.org/10.1007/s10973-010-0774-0.

(21) Antkowiak, R.; Antkowiak, W. Z. On the Chlorine Addition to the C(5)-C(6) Bridge and the N-Oxidation of 1,10-Phenanthroline. *Heterocycles* **1998**, *47* (2), 893–909. https://doi.org/10.3987/COM-97-S(N)99.

(22) Tharmavaram, M.; Pandey, G.; Rawtani, D. Surface Modified Halloysite Nanotubes: A Flexible Interface for Biological, Environmental and Catalytic Applications. *Adv. Colloid Interface Sci.* **2018**, *261*, 82–101. https://doi.org/https://doi.org/10.1016/j.cis.2018.09.001.

(23) Zeng, S.; Reyes, C.; Liu, J.; Rodgers, P. A.; Wentworth, S. H.; Sun, L. Facile Hydroxylation of Halloysite Nanotubes for Epoxy Nanocomposite Applications. *Polymer (Guildf).* **2014**, *55* (25), 6519–6528. https://doi.org/https://doi.org/10.1016/j.polymer.2014.10.044.

(24) Yuan, P.; Southon, P. D.; Liu, Z.; Green, M. E. R.; Hook, J. M.; Antill, S. J.; Kepert, C. J. Functionalization of Halloysite Clay Nanotubes by Grafting with γ-Aminopropyltriethoxysilane. *J. Phys. Chem. C* **2008**, *112* (40), 15742–15751. https://doi.org/10.1021/jp805657t.

(25) Bretti, C.; Cataldo, S.; Gianguzza, A.; Lando, G.; Lazzara, G.; Pettignano, A.; Sammartano, S. Thermodynamics of Proton Binding of Halloysite Nanotubes. *J. Phys. Chem. C* **2016**, *120* (14), 7849–7859. https://doi.org/10.1021/acs.jpcc.6b01127.

(26) Taroni, T.; Meroni, D.; Fidecka, K.; Maggioni, D.; Longhi, M.; Ardizzone, S. Halloysite Nanotubes Functionalization with Phosphonic Acids: Role of Surface Charge on Molecule Localization and Reversibility. *Appl. Surf. Sci.* **2019**, *486*, 466–473. https://doi.org/https://doi.org/10.1016/j.apsusc.2019.04.264.

(27) Launer, P.; Arkles, B. Infrared Analysis of Organsilicon Compounds: Spectra-Structure Correlations. In *Reprinted from Silicone Compounds Register and Review*; 2008; pp 223–226.

(28) Borrajo, J. P.; Liste, S.; Serra, J.; González, P.; Chiussi, S.; León, B.; Pérez Amor, M.; Ylänen, H. O.; Hupa, M. Influence of the Network Modifier Content on the Bioactivity of Silicate Glasses. *Key Eng. Mater.* **2003**, *254–256*, 23–26. https://doi.org/10.4028/www.scientific.net/KEM.254-256.23.

(29) Li, C.; Zhao, Y.; Zhu, T.; Li, Y.; Ruan, J.; Li, G. Effective Solvent-Free Oxidation of Cyclohexene to Allylic Products with Oxygen by Mesoporous Etched Halloysite Nanotube Supported Co2+. *RSC Adv.* **2018**, *8* (27), 14870–14878. https://doi.org/10.1039/C7RA11245A.

(30) Choo, C. K.; Kong, X. Y.; Goh, T. L.; Ngoh, G. C.; Horri, B. A.; Salamatinia, B. Chitosan/Halloysite Beads Fabricated by Ultrasonic-Assisted Extrusion-Dripping and a Case Study Application for Copper Ion Removal. *Carbohydr. Polym.* **2016**, *138*, 16–26. https://doi.org/https://doi.org/10.1016/j.carbpol.2015.11.060.

(31) Amouri, H.; Waern, J. B.; Caspar, R.; Barbieri, A.; Sabatini, C.; Zanelli, A.; Barigelletti, F. Cis–Trans Photoisomerization in [Ru(DIP)2(MeOH)2][OTf]2: Synthesis, NMR, X-Ray Structure of the Trans-Isomer and Photophysical Properties. *Dalt. Trans.* **2007**, No. 21, 2179–2186. https://doi.org/10.1039/B701089C.

(32) Takizawa, S.; Aboshi, R.; Murata, S. Photooxidation of 1,5-Dihydroxynaphthalene with Iridium Complexes as Singlet Oxygen Sensitizers. *Photochem. Photobiol. Sci.* **2011**, *10* (6), 895–903. https://doi.org/10.1039/C0PP00265H.

(33) Wu, W.; Yang, P.; Ma, L.; Lalevée, J.; Zhao, J. Visible-Light Harvesting PtII Complexes as Singlet Oxygen Photosensitizers for Photooxidation of 1,5-Dihydroxynaphthalene. *Eur. J. Inorg. Chem.* **2013**, *2013* (2), 228–231. https://doi.org/https://doi.org/10.1002/ejic.201200665.

(34) Juris, A.; Balzani, V.; Barigelletti, F.; Campagna, S.; Belser, P.; von Zelewsky, A. Ru(II) Polypyridine Complexes: Photophysics, Photochemistry, Eletrochemistry, and Chemiluminescence. *Coord. Chem. Rev.* **1988**, *84*, 85–277. https://doi.org/https://doi.org/10.1016/0010-8545(88)80032-8.

(35) Sábio, R. M.; Gressier, M.; Caiut, J. M. A.; Menu, M.-J.; Ribeiro, S. J. L. Luminescent Multifunctional Hybrids Obtained by Grafting of Ruthenium Complexes on Mesoporous Silica. *Mater. Lett.* **2016**, *174*, 1–5. https://doi.org/https://doi.org/10.1016/j.matlet.2016.03.058.

(36) Wei, H.; Yin, J.; Wang, E. Bis(2,2′-Bipyridine)(5,6-Epoxy-5,6-Dihydro-[1,10] Phenanthroline)Ruthenium: Synthesis and Electrochemical and Electrochemiluminescence Characterization. *Anal. Chem.* **2008**, *80* (14), 5635–5639. https://doi.org/10.1021/ac8001462.
(37) Matsui, K.; Momose, F. Luminescence Properties of Tris(2,2‘-Bipyridine)Ruthenium(II) in Sol−Gel Systems of SiO2. *Chem. Mater.* **1997**, *9* (11), 2588–2591. https://doi.org/10.1021/cm970186+.
(38) Li, M.-J.; Chen, Z.; Yam, V. W.-W.; Zu, Y. Multifunctional Ruthenium(II) Polypyridine Complex-Based Core–Shell Magnetic Silica Nanocomposites: Magnetism, Luminescence, and Electrochemiluminescence. *ACS Nano* **2008**, *2* (5), 905–912. https://doi.org/10.1021/nn800123w.
(39) Maggioni, D.; Fenili, F.; D’Alfonso, L.; Donghi, D.; Panigati, M.; Zanoni, I.; Marzi, R.; Manfredi, A.; Ferruti, P.; D’Alfonso, G.; Ranucci, E. Luminescent Rhenium and Ruthenium Complexes of an Amphoteric Poly(Amidoamine) Functionalized with 1,10-Phenanthroline. *Inorg. Chem.* **2012**, *51* (23), 12776–12788. https://doi.org/10.1021/ic301616b.

Chapter 6

Cinnamaldehyde hydrogenation using Au-Pt supported over halloysite nanotube catalysts prepared by sol-immobilization

1 Introduction

Society's development in the last 150 years has been possible, in part, thanks to the advancement of the chemistry industry. New and innovative materials have led the technological revolution in health, fuels, food production, and disinfection; central to this is the field of catalysis. An example is the extensive work that resulted in Karl Ziegler and Giulio Natta being awarded the Nobel prize in Chemistry in 1963: the so-called "Ziegler-Natta Catalysts" have entirely revolutionized the polymer industry, and the amount of plastic produced from these catalysts accounts for the largest volume commodity chemicals in the world.[1]

The word "catalysis" was first used to describe the field in 1835 when Jöns Jacob Berzelius defined the "Catalytic Force" as "the property that simple and compound bodies, soluble and insoluble, exercising on other bodies an action very different from chemical affinity".[2,3] Moreover, Berzelius observed that "the body affecting the changes does not take part in the reaction and remains unaltered through the reaction". Nowadays, almost 200 years after the observation of the catalytic force, catalysis is deeply integrated into our everyday lives, and over 90 % of all chemical industrial processes employ catalysts.[4]

A more scientific and modern description of a catalyst is a substance that lowers the activation energy of a reaction, thereby increasing the rate without being consumed, and thus can be reused multiple times. As illustrated in **Figure 1**, only the kinetics of the process is affected, while the thermodynamics remain unaltered, as dictated by the second law of thermodynamics.

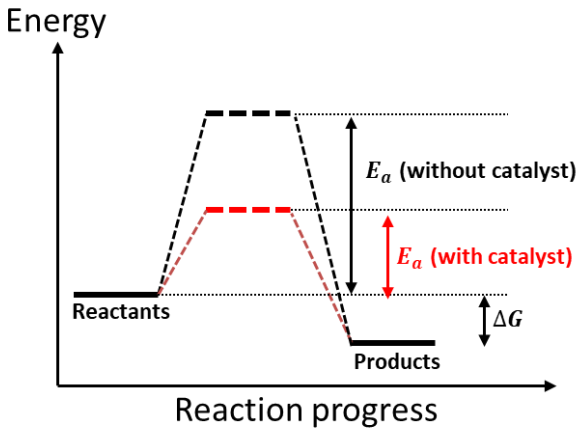

Figure 1 *Potential energy diagram of an un-catalysed and catalysed chemical reaction. The black line represents the un-catalysed reaction pathway, while the red line the catalysed reaction with lower activation energy* E_a

Catalysts can be generally divided into two main groups depending on their chemical phase: if both catalyst and reagents are in the same phase, the catalysis is considered homogeneous, otherwise, when the reactants are in a different phase to the catalyst the system is called heterogeneous.

Homogeneous catalysts are usually coordination complexes composed of a metal centre bonded to organic ligands through a coordinate covalent bond. The nature and the oxidation state of the metal and the electronic properties of the ligands dominate the chemistry of such complexes. Homogeneous systems usually exhibit a higher selectivity than heterogeneous catalysts.[5] Additionally, the probability of interaction between substrate and catalyst is higher in homogeneous catalysis, making these catalysts, in general, more active than their heterogeneous counterparts.[6] Despite this, homogeneous catalysts are often not economically viable at a large scale mainly because of recycling/separation problems and as a result, they represent only 20 % of the total catalytic industrial processes[7]. Hydroformylation of olefins[8], acetic acid synthesis[9] and coupling reactions[10] are examples of industrial reactions that make use of homogeneous catalysts.

Heterogeneous catalysts are usually solid compounds that can be used either in gas or liquid phase reactions. Compared to homogeneous catalysts, they display several advantages, such as cheaper and easier recovery from the reaction medium and higher thermal stability. They find applications in numerous industrial processes such as the Haber-Bosh process (synthesis of ammonia),[11] the catalytic reforming of crude oil and the Fischer-Tropsch process for the synthesis of hydrocarbons from syngas.[12] However, the complexity of the surface chemistry involved, and the challenge to attain a homogeneous population of catalytic sites makes these catalysts generally less active and selective. The adsorption of reactants on the active sites and the consequent desorption of the products is often the rate-limiting step, due to the low availability of active sites on the catalyst surface. For this reason, the catalyst surface area is a critical parameter since it determines the availability and population of catalytic sites.

Currently, about 90% of the chemical industry products are made in catalytic processes; because of the disadvantages presented by the traditionally homogenous catalysts, this study is dedicated to heterogeneous catalysts based on metal nanoparticles (MNPs).[13] MNPs are considered perfect candidates for catalysis because of their very high surface area per volume or density unit compared with bulk metal. Moreover, by controlling the particle size and surface chemistry, the selectivity and activity of the catalysts can often be tuned.[14]

One disadvantage that affects MNPs, however, is their tendency to agglomerate in larger nanostructures, thus limiting their activity; agglomeration phenomena are caused by the intrinsic instability of nanoscopic structures. In order to overcome this problem, MNPs are often supported onto materials with high surface area, thermal stability and chemical resistance, such as carbonaceous materials (activated carbon, carbon nanotubes, graphene, etc.) or metal oxides (silica, alumina, titania, etc.).[15]

Supported metal nanoparticles proved to be effective for a wide range of reactions such as hydrogenations,[16,17] oxidations,[18] C–C coupling,[17,19] hydrochlorination,[20] hydrogen peroxide production,[21] conversion of organosilanes to silanols,[22] and other organic reactions.[23] A particularly hot field of application of supported metal nanoparticles is the conversion of biomass-based materials into biofuels and chemicals. Indeed, biomass materials are one of the most promising renewable feedstocks that are set to completely replace in the future fossil fuels for both energy production and synthesis of fuels and chemicals. In this context,

hydrogenation reactions play a crucial role, since biomass-based raw materials usually have a high oxygen content, as well as a high number of unsaturations; indeed, biomass is mainly composed of carbohydrate polymers (cellulose, hemicellulose) and aromatic polymers (lignin). One of the most used model substrates for catalytic performance in hydrogenation reactions is cinnamaldehyde (CAL). CAL exist in nature in the bark of cinnamon trees. Its low toxicity and well-known properties make it ideal for agriculture as a fungicide.[24] CAL and its derivatives are used extensively in the flavour and fragrance industry[25] as well as a corrosion inhibitor in metal coatings.[26,27] The selective hydrogenation of the vinyl (C=C) or carbonyl (C=O) groups of CAL leads to hydrocinnamaldehyde (HCAL) and cinnamyl alcohol (COH), respectively, which are useful intermediates in pharmaceuticals and perfumery (**Figure 2**).[28,29] Production of COH from CAL has always been a challenge since it is more favourable to produce the saturated aldehyde or the saturated alcohol than to generate the corresponding unsaturated alcohol from a thermodynamic point of view.[30]

Homogeneous and heterogeneous catalysts have been tested to find a catalytic system that is highly selective to the formation of COH. In general, heterogeneous catalysts are highly desirable because they can be easily separated and recycled.

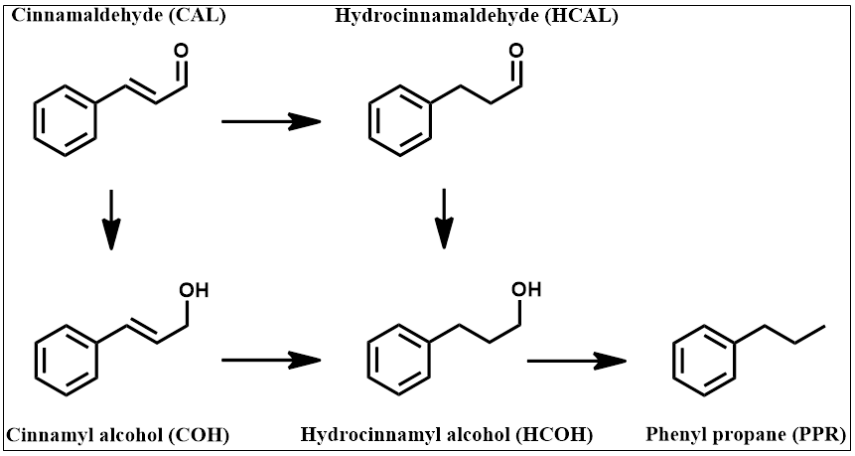

Figure 2 Cinnamaldehyde hydrogenation pathways.

Platinum nanoparticles (Pt NPs) with diameters in the range 3 to 10 nm and supported over silica or TiO_2 have been widely used as heterogeneous catalysts for reactions such as the CO oxidation in catalytic converters, oxidation and reduction reactions in fuel cells, nitric acid production, and hydrogen production[14,31,32] owing to the high catalytic activity of Pt NPs. Most of the studies indicate that the monometallic catalysts have a lower selectivity to the unsaturated alcohol. On the contrary, the presence of promoter metal in bimetallic catalysts showed electronic and chemical properties distinct from those of their parent metals.[33,34] In the case of Pt as base metal, the highest selectivity was found by the addition of Sn or Fe.[35–39] Gold is another metal that has been widely used in numerous reactions, such as selective oxidation of alcohol, hydrocarbons, and sugars, among many others,[40] hydrogen production from wastewater using either enzimes or molecular photosensitizers[41,42] and hydrogen purification by selective oxidation of CO in the presence of H_2 (preferential oxidation, PROX).[43] The advantages of using Au as active metal usually is due to its high selectivity and stability in particular reaction conditions.[44] However, the use of Au NPs for industrial purposes is limited by their tendency to agglomerate, forming clusters, which leads to a loss of catalytic activity.

To overcome this drawback, Au NPs can be anchored to solid supports such as (HNT, TiO_2, ZrO_2, Fe_2O_3, etc).[45–50]

Two metals can be effectively mixed to produce a new material with better activity, selectivity and stability,[51,52] depending on the final composition and its alloy structure. For example, Au–Pt bimetallic nanoparticles can combine optical properties of Au with the catalytic properties of Pt, giving catalytic materials that can enhance their activity when illuminated by electromagnetic radiation.[53]

An efficient catalyst must have the highest possible degree of metal dispersion, smaller particle size, and low loading; this is particularly true especially for expensive noble metals such as platinum and gold. This can be achieved in two ways, firstly by fixing the metal cations into rigid support through organic ligand attachment, subsequently, execute the chemical reduction to produce the supported metal nanoparticles. Another way is to perform metal reduction in solution to obtain zero-oxidation state metal nanoparticles that are then immobilised onto the supporting material.

Halloysite nanotubes (HNT), an aluminosilicate clay, are natural microporous nanotubes. The external surface and the internal lumen of HNT are composed of silicon-oxygen tetrahedra and alumina oxygen octahedra respectively, forming two monolayers faced one to each other (see introduction Chapter 1, §1.2). Because of the economic availability of HNT and the different chemical properties of their surface and lumen, HNT have been used in many applications in the last decade, especially in catalysis.[54–56] Indeed, HNT show some advantages: they are eco-friendly, resistant against organic solvents, with a high thermal and mechanical stability, ease of disposal or reusability, and large surface area without additional material treatment.[57]

The most widely used method for the preparation of supported metal nanoparticles employing HNT as support previews the halloysite external surface modification by a suitable functionality able to interact with the metal salts, then followed by their reduction towards the formation of metal nanoparticles. Alternatively, metal nanoparticles can be immobilized onto the HNT surface by physical adsorption or self-assembly. In this context, Fe, Co, Ni, Au, Ru, and Pd NPs were adsorbed on the halloysite surface, leading to hybrid nanomaterials.[45,58-62]

There are several techniques, described in the literature, for the obtainment of well-dispersed gold and platinum NPs on different supports. One of the most commonly used is the so-called “sol-immobilization method”.[63] Colloidal NPs can be synthesized in solution in the presence of an excess of stabilizing (capping) agents/ligands or surfactants (which can be as polymers, thiols, amines, phosphines, etc.); this provides control of the size and shape of the formed nanoparticles, preventing them from agglomeration. Colloids prepared by reducing the metal precursor by citric acid, $NaBH_4$, or other reducing agents, can be used to prepare metal NPs on oxide-based supports, by deposition from the colloid, to give suitable dispersions of the NPs.

In this chapter, we demonstrate a novel nano-catalyst preparation and characterization based on HNTs and Au-Pt NPs using the above strategy. The prepared catalysts were then tested for the selective hydrogenation of cinnamaldehyde under relatively mild reaction conditions. In this extensive study, we report the effect of the Au/Pt molar ratio on the catalytic activity, selectivity, and stability of the sol-immobilized catalysts.

2 Results and discussion

2.1 Catalyst preparation

The synthesis of Sol-immobilization catalysts was carried out following some literature procedures,[64,65] by performing metal reduction in solution to obtain metal nanoparticles with zero oxidation state. The Au^0 or Pt^0 NPs are then immobilised over the HNT surface to obtain 5 different catalysts: 2 monometallic Au and Pt and 3 bimetallic Au-Pt with different Au-Pt ratios. The change from white of pristine halloysite to violet in case of Au, grey in case of Pt, or dark grey in case of mixed metal support over HNT. These colour changes give us a simple indication of the metal nanoparticle presence, most likely in the outer layer because the lumen loading requires in principle vacuum cycles and it is expected to produce faint colours.

2.2 Catalyst characterization

We prepared a series of Au_xPt_y@HNT catalysts with different metal ratios. The Au-Pt metal deposition, the average metal particle size, and particle size distribution of the catalysts were determined by TEM (**Figure 3a-e** and Table 1). Representative bright-field TEM micrographs of monometallic and bimetallic catalysts are presented in **Figure 4**. The mean particle size of nanoparticles for all catalysts was between ca 2 and 3 nm without any appreciable size variation for different Au/Pt ratios. From TEM images, we could also observe the tendency of NPs to interact with the edge of HNT, especially in unequal ratio bimetallic catalysts (**Figure 3d and 3e**). Nevertheless, $Au_{50}Pt_{50}$ NPs (**Figure 3c**) were also mostly localized inside the lumen, a fact that was completely unexpected due to the adopted loading method. For the other samples it seemed there was no selectivity toward the localization, inside or outside, but with the edges where a possible high concentration of OH groups can be expected that would facilitate the non-covalent interaction of the PVA-covering agent.

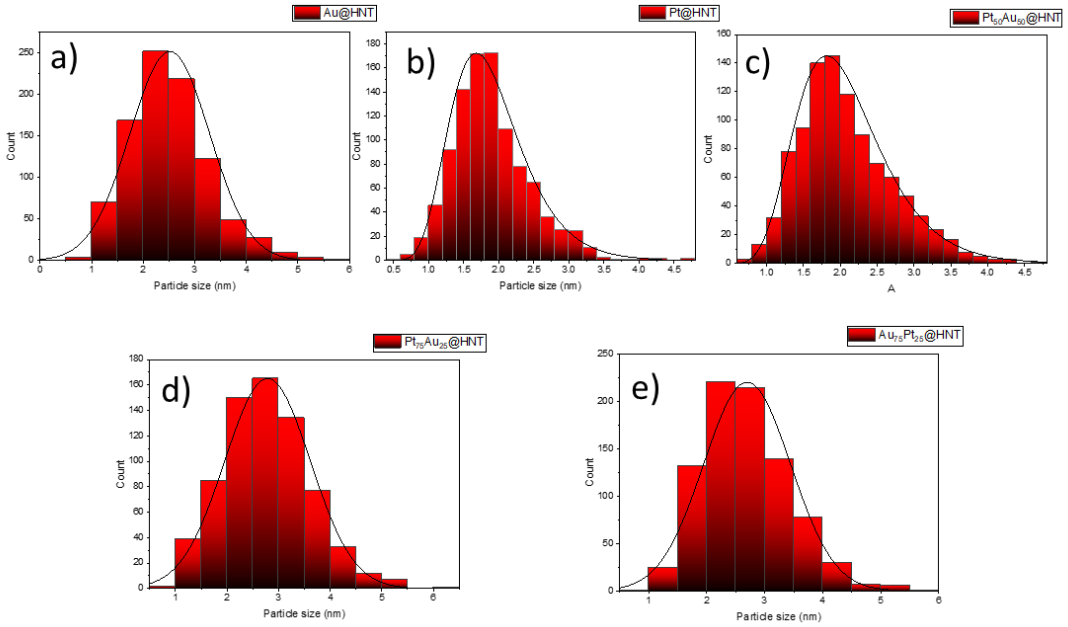

Figure 3 Particle size distribution ranging between 1.9 (±0.6) and 2.8 (±0.8) nm nm of (a) Au@HNT (b) Pt@HNT (c) $Au_{50}Pt_{50}$@HNT (d) $Au_{25}Pt_{75}$@HNT (e) $Au_{75}Pt_{25}$@HNT.

Table 1 Mean, median, minimum and maximum values (nm) obtained by TEM of the supported monometallic and bimetallic catalysts.

	Mean	Standard Deviation	Minimum	Median	Maximum
Au@HNT	2.5	0.8	0.5	2.5	5.7
Pt@HNT	1.9	0.6	0.5	1.8	4.7
$Au_{50}Pt_{50}$@HNT	2.1	0.6	0.6	2.0	4.6
$Au_{25}Pt_{75}$@HNT	2.8	0.8	0.7	2.7	6.1
$Au_{75}Pt_{25}$@HNT	2.7	0.7	0.8	2.6	5.9

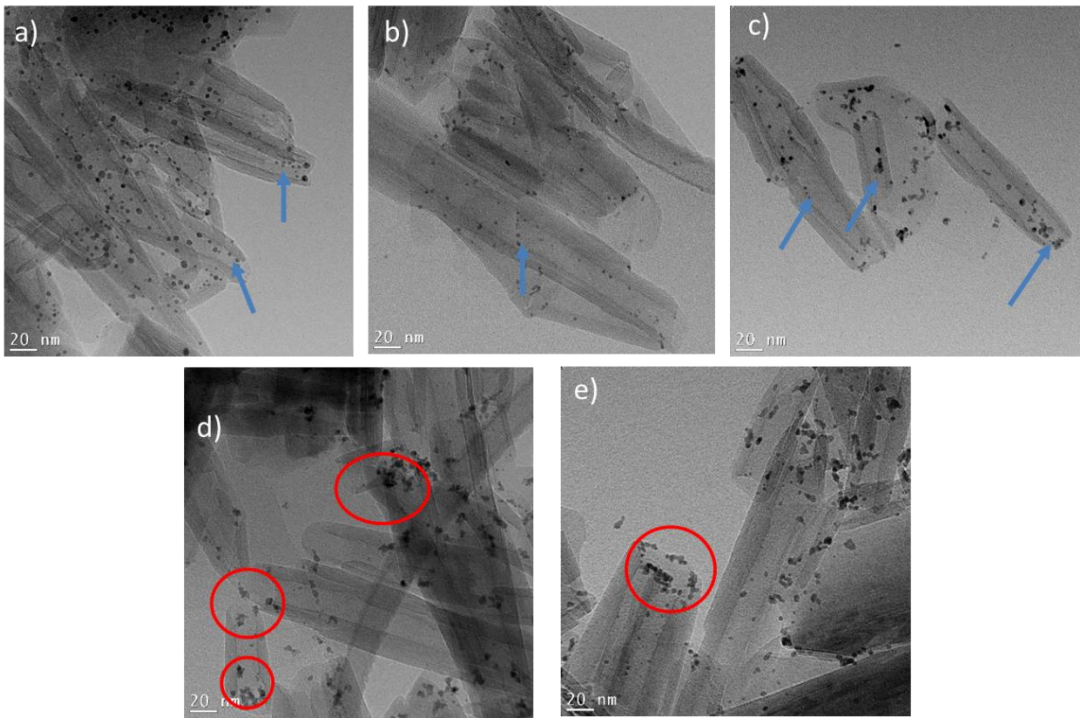

Figure 4 Representative TEM images of the fresh catalysts: (a) Au@HNT (b) Pt@HNT (c) $Au_{50}Pt_{50}$@HNT (d) $Au_{25}Pt_{75}$@HNT (e) $Au_{75}Pt_{25}$@HNT. Blue arrows indicate the NPs selectively adsorbed in the inner lumen location while red circles indicate the preferential nanoparticle adsorption onto HNT edges.

Through the synthetic procedure, the stabilizing agent PVA is used in excess to stabilize MNPs effectively. MNP colloids are deposited on the surface of the support to synthesize a heterogeneous catalyst. Thus, PVA might also form bonds with HNT.[66] FTIR spectrum (**Figure 5a**) showed a red-shift of the Si–O stretching band of HNT silica layer from 1007 cm^{-1} (**Figure 5b** vertical red dashed lines) to 995 cm^{-1}, pointing out a weakening of the force constant due to the hydrogen-bonding interactions between OH defects and PVA surfactant and a corresponding increase of IR intensities.[67] For the same reason, the peak at 909 cm^{-1} (**Figure 5b** vertical blue dashed lines) assigned to the O-H deformation of inner hydroxyl groups of HNT Al-OH, it slightly increased in intensity. These shifts were accompanied by unchanged in-plane Si–O–Si deformations, whose peak remained at 1028 cm^{-1} (**Figure 5b** vertical green dashed lines)).[68,69] These observations are in agreements with TEM images were the MNP were mainly observed inside the inner lumen and at the edge of HNT due to presence of Al-OH or Si-OH, respectively. The few nanoparticles on the HNT surface could owe to the defects

on the surface of HNT either naturally present or formed by the etching action of H_2SO_4 that was used in the preparation procedure.[70–74]

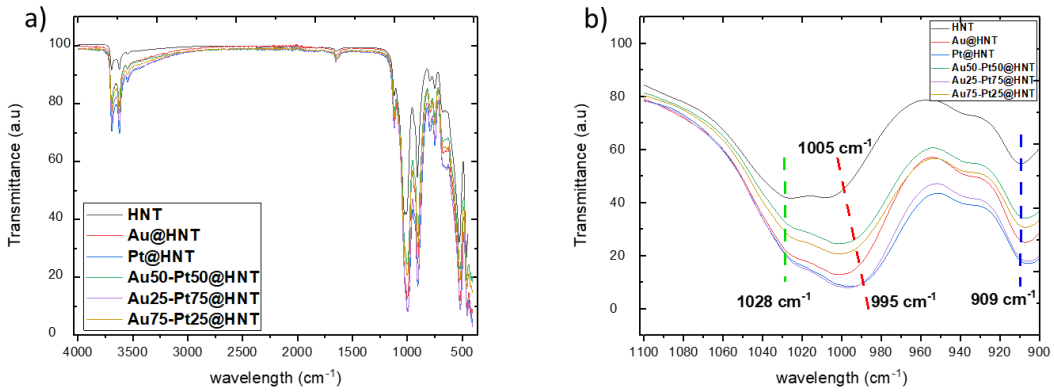

Figure 5 a) ATR-FTIR spectra of freshly prepared catalysts b) magnification of the spectral wavelength region of interest (1100–900 nm).

2.3 Catalytic activity

The selective hydrogenation of α,β-unsaturated ketones and aldehydes to unsaturated alcohols is a critical step in the synthesis of chemical intermediates used in the production of pharmaceuticals, cosmetics, and food flavours.[75,76] Studies have proven that platinum-based bimetallic catalysts have been used for the selective hydrogenation of α,β ethylenic aldehydes. The addition of Ni, Co, and Fe to Pt increases activity and selectivity for unsaturated alcohols. In contrast, the addition of Ga, Sn, and Ge improves selectivity but decreases the catalysts' activity.[38,77–79] Cinnamaldehyde (CAL) is repeatedly taken as a model compound for the hydrogenation of α,β-unsaturated aldehydes. According to the hydrogenation pathway reported in **Figure 2**, CAL can be either partially hydrogenated to hydrocinnamaldehyde (HCAL) and cinnamyl alcohol (COH) or wholly hydrogenated to hydrocinnamyl alcohol (HCOH) followed by phenyl propane (PPR) formation by hydrogenolysis mechanism.

Herein, CAL hydrogenation reaction was carried out at 60 °C and under 7 bar of H_2 using Au_xPt_y@HNT catalysts, where x and y are the relative metal amount in % used during the alloy NPs preparation. **Figure 6** shows that Pt is mandatory for CAL hydrogenation while Au monometallic catalyst is inert for CAL hydrogenation.

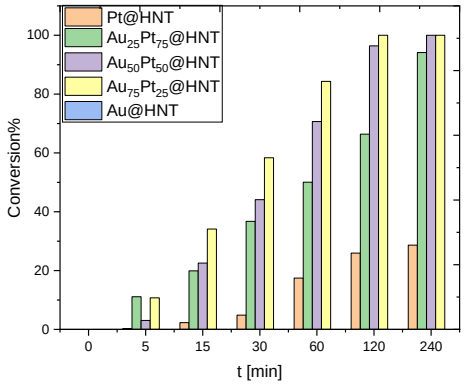

Figure 6 CAL conversion over time with different Au_xPt_y@HNT catalysts. Reaction condition: 7 bar H_2, 60 °C, CAL 0.5 M in toluene, metal: substrate ratio 1:1000.

Some have proposed that the nature of the support influences the activity of gold catalysts, reducible oxides (TiO_2, ZrO_2, Fe_2O_3, etc.) supported gold catalysts selectively hydrogenate the C=O bond. In contrast, inert oxides (such as SiO_2 and Al_2O_3) supporting gold catalysts show no or low selectivity toward C=O hydrogenation.[46–50] In agreement with previous literature, the Au NPs in monometallic catalyst either interacted with silica on the surface and at the edge of HNT or intercalated into the alumina lumen as it is clear from TEM (**Figure 4a**). Bus et al. reported the conversion of CAL with Au/Al_2O_3 to COH with a selectivity of up to 90% at 85 bar H_2 and 100 °C. Nevertheless, it is worth notice that this condition is severe compared to our system.[80]

Figure 7a-d presents the effect of time on hydrogenation reactions of CAL, and the main products observed were cinnamyl alcohol (COH), hydrocinnamaldehyde (HCAL), hydrocinnamyl alcohol (HCOH), and phenylpropane (PPR). Some unknown peaks in the GC chromatogram were observed and are here referred as "mass loss", along with products that cannot be detected or quantified, following the equation 6.1:

$$[mass\ loss]_t = [COH]_t + [HCAL]_t + [HCOH]_t + [PPR]_t - [CAL]_0 \quad (Eq.6.1)$$

Where $[\mathrm{HCAL}]_t, [\mathrm{COH}]_t, [\mathrm{HCOH}]_t$ and $[\mathrm{PPR}]_t$ are the concentration of expected products at time t and $[CAL]_0$ is the substrate concentration at time zero.

In **Figure 6** and **Figure 7a**, we observed that the conversion of monometallic Pt is lower than bimetallic and mainly tend to be selective for hydrogenation of C=C producing unsaturated aldehyde (**Figure 8a**).[81]

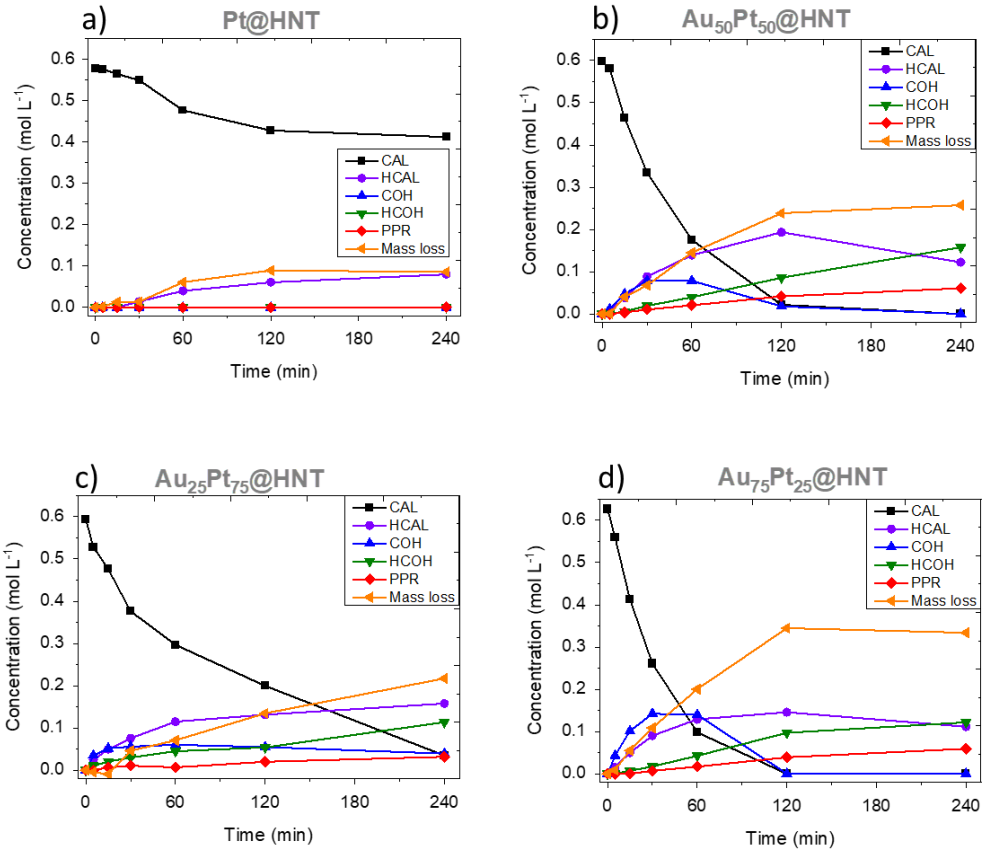

Figure 7 CAL hydrogenation profile of (a) Pt@HNT (b) $Au_{50}Pt_{50}$@HNT (c) $Au_{25}Pt_{75}$@HNT (d) $Au_{75}Pt_{25}$@HNT. Reaction condition: 7 bar H_2, 60 °C, CAL 0.5 M in toluene, metal: substrate ratio 1:1000.

Both the conversion and selectivity for C=O hydrogenation varied to a certain extent after the addition of the second metal Au (**Figure 6**, **Figure 7b-d**, and **Figure 8b-d**). Similarly to what reported by *Wang et al.* with Pt NPs supported onto roughed HNT,[82] our Au_xPt_y@HNT catalyst was highly selective for COH production in just 5 min. In our case, however, we extended the study to longer reaction times and observed the hydrogenation reaction continued until reaching the final predominant products HCOH and PPR. The prepared bimetallic catalysts showed good conversion and selectivity much higher than the one shown by the Pt / SiO_2 catalyst reported in the literature (18 % and 40 %, respectively)[82,83] that, moreover, required also higher reaction conditions (150 °C and 10 bar of H_2).

By comparing the three bimetallic catalysts, we found that the activity and selectivity toward hydrogenation of C=O were increased by increasing the Au/Pt ratio following the trend: $Au_{25}Pt_{75}@HNT \ < \ Au_{50}Pt_{50}@HNT < Au_{75}Pt_{25}@HNT$

Two hypotheses can be drawn to explain the improvements in selectivity. The first is based on the observation that an increased electron density on the base metal (Pt) is caused by the formation of metal alloys or a strong interaction of the promotor (or the support) with the base metal. The increased electron density on the base metal is claimed to decrease the probability for C=C bond adsorption and, at the same time, the interaction of the C=O bond with the polar bimetallic sites is increased. The second explanation is based on the presence of Lewis acid sites at or near the metal particles that may interact with the lone electron pairs of the oxygen of the carbonyl group, and thus would lower the strength of the C=O bond, facilitating a higher rate of hydrogenation.[79,84,85]

Another factor that could be the reason for the higher activity of the bimetallic NPs is the tendency of MNP to interact with the HNT edges or with the HNT outer surface, as highlighted by the red circles in **Figures 4 d-e** (TEM micrographs). In that case, the substrate could interact more easily with the MNP, maximizing the diffusion towards the metal active sites.

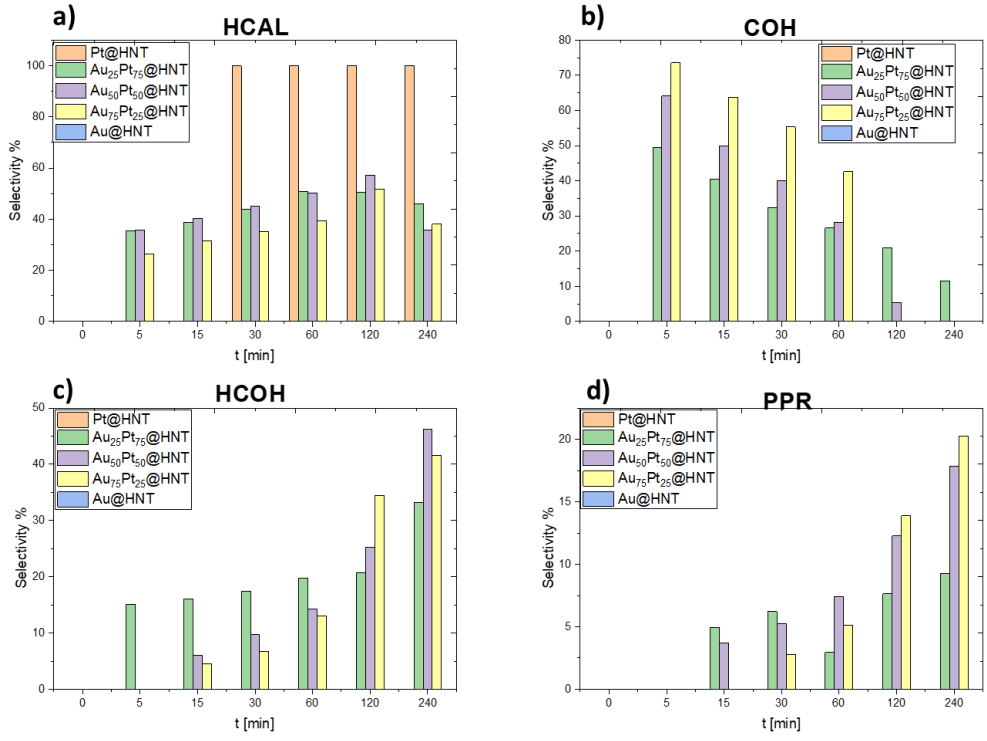

Figure 8 Au/Pt molar ratio effect on selectivity of (a) HCAL (b) COH (c) HCOH (d) PPR. Reaction condition: 7 bar H_2, 60 °C, CAL 0.5 M in toluene, metal: substrate ratio 1:1000.

3 Conclusions

In this study, new synthetic Au-Pt nanoparticles supported over HNT catalysts with different Au-to-Pt molar ratio were prepared via a sol immobilization method. TEM and FTIR analyses were applied to study the particle size and size distribution, as well as the interaction between nanoparticles and the HNT support. TEM images revealed that NPs mostly localized both on the outer surface and especially at the edges of the HNT. Nevertheless, surprisingly the NPs were able by diffusion to reach also the inner part of HNT, and in the case of Au50Pt50 NPs there was a preferential localization in the inner lumen. The catalytic hydrogenation of cinnamaldehyde was investigated using the HNT-Au/Pt NPs. Under mild condition (60 °C, 7 bar of H_2), we have shown that the selectivity towards C=O hydrogenation could be enhanced by increasing the Au/Pt molar ratio, with a maximum of selectivity reached with Au_{75}/Pt_{25} molar ratio. Even though in the absence of Pt, Au NPs were not able to promote catalysis, a small amount of Pt added to gold showed the best performances, while on decreasing the Au content the catalyst abilities became worst.

4 Experimental

4.1 Materials and instruments

$NaAuCl_4 \cdot 2H_2O$ 99.99%, K_2PtCl_4 98% were used as metal precursors, Halloysite used as the support, $NaBH_4$ 99.99% and polyvinyl alcohol (PVA, Mw = 9 000–10 000, 80% hydrolysed) were used as reducing agent and protecting agent respectively (Sigma-Aldrich). Cinnamaldehyde 95%, hydrocinnamaldehyde 98%, hydrocinnamyl alcohol 98% and phenylpropane 98% (Sigma-Aldrich), cinnamyl alcohol 95% (Alfa Aesar) were used as substrates and/or standards, p-xylene 99% (Sigma-Aldrich) as an external standard. Toluene >99%, 2-propanol 99.5% (Sigma-Aldrich) was used as solvent. H_2SO_4 97% (Sigma-Aldrich). Ultrapure milli-Q water (Millipore, resistivity=18M Ω cm^{-2}) was used for the preparation of the aqueous solutions.

ATR-FTIR spectra were acquired on a PerkinElmer Frontier instrument equipped with an ATR accessory with a diamond/ZnSe crystal. The IR spectra were registered between 4000 and 400 cm^{-1}.

Transmission Electron Microscopy (TEM) experiments were carried out using a FEI Tecnai F20 Field Emission Gun electron microscope with a 200 kV accelerating voltage. The samples were first dispersed in isopropanol and sonicated for a couple of minutes. A drop was then placed onto a 300 mesh carbon-coated copper grid. The nanoparticle size was measured by Image-J free software, for each sample the measured NPs were around 1000.

4.2 Catalyst preparation

The synthesis of Sol-immobilization catalysts was carried out by following a slightly modified literature procedure.[64,65]

Preparation of Au/HNT nanocomposite. Solid $NaAuCl_4 \cdot 2H_2O$ (0.051 mmol) and PVA (1 wt %) solution (Au/PVA = 1/0.5 wt/wt) were added to 100 mL of H_2O. After 5 min, a freshly prepared solution of $NaBH_4$ (0.1 M) (Au/$NaBH_4$ 1/5 mol/mol) was added to the yellow solution under vigorous magnetic stirring. The solution turned immediately to dark red, indicating the reduction of the metal precursor. The colloid was left ageing for 30 minutes, after which 1 g of support (HNT) was added along with a couple of drops of concentrated H_2SO_4 in order to maintain the pH of the suspension at ca. 3. The amount of support was calculated as having a total final metal loading of 1 wt %. After 2 h, the slurry was filtered, the catalyst washed

thoroughly with distilled water to remove any leftover PVA and $NaBH_4$ from the reduction and dried at 80 °C for 4 h.

Preparation of Pt/HNT nanocomposite. Solid K_2PtCl_4 (0.051 mmol) and PVA (1 wt %) solution (Pt/PVA = 1/0.5 wt/wt) were added to 100 mL of H_2O. After 5 min, a freshly prepared solution of $NaBH_4$ (0.1 M) (Pt/$NaBH_4$ 1/16 mol/mol) was added to the solution under vigorous magnetic stirring. A small amount of H_2SO_4 was introduced in order to facilitate the next reduction step. The colloid was left ageing for 30 minutes, after which 1 g of support (HNT) was added. No further acid was added at this step since the solution's pH was already at ca. 3. The amount of support was calculated as having a total final metal loading of 1 wt %. After 2 h the slurry was filtered, the catalyst washed thoroughly with distilled water to remove PVA from the catalyst surface and dried at 80 °C for 4 h.

Preparation of Au_xPt_y/HNT **nanocomposite.** For Au/Pt mass ratios of 75:25, 50:50 and 25:75, $NaAuCl_4{\cdot}2H_2O$ (7.5, 5.0 and 2.5 mg) and K_2PtCl_4 (2.5, 5.0 and 7.5 mg) respectively (total metal amount of 10.0 mg), PVA solution (1 wt%) ((Au+Pt)/PVA = 1/0.5 wt/wt) were added to 100 mL of H_2O. After 5 min, a freshly prepared solution of $NaBH_4$ (0.1 M) ((Au+Pt)/$NaBH_4$ 1/16 mol/mol) was added to the solution under vigorous magnetic stirring. A small amount of H_2SO_4 was introduced in order to facilitate the next reduction step. The colloid was left ageing for 30 minutes, after which 1 g of support (HNT) was added. No further acid was added at this step, since the solution's pH was already at ca. 3. The amount of support was calculated as having a total final metal loading of 1 wt %. After 2 h the slurry was filtered, the catalyst washed thoroughly with distilled water to remove PVA from the catalyst surface and dried at 80 °C for 4 h.

4.3 Catalyst testing

The hydrogenation reaction was carried out by following a slightly modified literature procedure.[65,82]

Briefly, the hydrogenation reactions were carried out in a 100 ml stainless autoclave equipped with a glass liner; the catalyst (98mg, typical substrate/metal molar ratio 1000:1), cinnamaldehyde substrate (0.005 mol) were dispersed in 10 ml of toluene. The autoclave was purged with H_2 for 5 cycles. The autoclave was then loaded into a preheated heating block, which was maintained at the desired reaction temperature and pressure (60 °C and 7 H_2 bar). The reaction was started by commencing stirring inside the reactors at 1000 rpm. After the desired reaction time, the autoclave was cooled down in an ice bath for 5 min to quench the reaction. A fixed volume of the mixture (0.2 mL) was then centrifuged and an aliquot of the clear supernatant of the reaction mixture (0.1 mL) was diluted with an external standard solution (0.1 mL of a 0.5 M solution of p-xylene in toluene) for GC measurement. For the quantification of the amounts of reactants consumed and the products generated, GC-FID (Thermo Scientific, TRACE 1300 equipped with an Agilent HP-5 column) was employed and the external calibration method was used. The concentration of any component at any time was calculated according to the following equation 6.2:

$$[Component\ i]_t = \frac{A_{i_t}}{A_{external\ standard_t}} \times \frac{[external\ standard]_t}{Response\ factor\ of\ i} \quad (Eq.6.2)$$

Where A_{i_t} and $A_{external\ standard_t}$ are the area of the measured GC peaks for the component and p-xylene respectively. $Response\ factor\ of\ i$ obtained from measured GC peak of the standard of component (i).

The conversion % at any time was calculated according to the following equation 6.3:

$$Conversion\ \%_t = \left(1 - \frac{[CAL]_t}{[CAL]_0}\right) \times 100 \quad (Eq\ 6.3)$$

Where $[CAL]_t$ & $[CAL]_0$ are the concentration of cinnamaldehyde substrate at time t and at the start, respectively. Through analysis by GC we detected some unknown peaks that could

not be quantified (mass loss) so we use the following equation to calculate the normalized selectivity % of any component at any time (**Eq. 6.4**):

$$Selectivity\%_{i_t} = \frac{[component\ i]_t}{[\mathrm{HCAL}]_t + [\mathrm{COH}]_t + [\mathrm{HCOH}]_t + [\mathrm{PPR}]_t} \qquad (Eq.\,6.4)$$

Where $[\mathrm{HCAL}]_t, [\mathrm{COH}]_t, [\mathrm{HCOH}]_t \& [\mathrm{PPR}]_t$ are the concentration of expected products hydrocinnamaldehyde, cinnamyl alcohol, hydrocinnamyl alcohol and phenylpropane respectively.

5 Bibliography

(1) Fisch, A. G. Ziegler-Natta Catalysts. *Kirk-Othmer Encyclopedia of Chemical Technology*. December 16, 2019, pp 1–22. https://doi.org/https://doi.org/10.1002/0471238961.2609050703050303.a01.pub2.

(2) Robertson, A. J. B. The Early History of Catalysis. *Platin. Met. Rev.* **1975**, *19* (2), 64–69.

(3) Berzelius, Jöns Jacob, F. *Årsberättelse Och Framstegen I Fysik Og Kemi, Afgifven Den 31 Mars*; Norstedt: Stockholm, 1835.

(4) Sá, J.; Szlachetko, J. Heterogeneous Catalysis Experiments at XFELs. Are We Close to Producing a Catalysis Movie? *Catal. Letters* **2014**, *144* (2), 197–203. https://doi.org/10.1007/s10562-013-1171-7.

(5) Liu, Y.; Jiang, Z.; Li, C. Emulsion Catalysis: Interface between Homogeneous and Heterogeneous Catalysis. *Bridg. Heterog. Homog. Catal. Concepts, Strateg. Appl.* **2014**, 283–324.

(6) Cole-Hamilton, D. J.; Tooze, R. P. *Catalyst Separation, Recovery and Recycling: Chemistry and Process Design*; Catalysis by Metal Complexes; Springer Netherlands, 2014.

(7) Homogeneous Catalysis with Transition Metal Catalysts. *Industrial Catalysis*. October 12, 2015, pp 17–46. https://doi.org/https://doi.org/10.1002/9783527684625.ch2.

(8) Kohlpaintner, C.; Schulte, M.; Falbe, J.; Lappe, P.; Weber, J. Aldehydes, Aliphatic and Araliphatic. *Ullmann's Encyclopedia of Industrial Chemistry*. June 15, 2000. https://doi.org/https://doi.org/10.1002/14356007.a01_321.

(9) Cheung, H.; Tanke, R. S.; Torrence, G. P. Acetic Acid. *Ullmann's Encyclopedia of Industrial Chemistry*. June 15, 2000. https://doi.org/https://doi.org/10.1002/14356007.a01_045.

(10) Budarin, V. L.; Shuttleworth, P. S.; Clark, J. H.; Luque, R. Industrial Applications of C-C Coupling Reactions. *Curr. Org. Synth.* **2010**, *7* (6), 614–627.

(11) Appl, M. Ammonia. *Ullmann's Encyclopedia of Industrial Chemistry*. December 15, 2006. https://doi.org/https://doi.org/10.1002/14356007.a02_143.pub2.

(12) Kaneko, T.; Derbyshire, F.; Makino, E.; Gray, D.; Tamura, M.; Li, K. Coal Liquefaction. *Ullmann's Encyclopedia of Industrial Chemistry*. July 15, 2012. https://doi.org/https://doi.org/10.1002/14356007.a07_197.pub2.

(13) Liu, J. Catalysis by Supported Single Metal Atoms. *ACS Catal.* **2017**, *7* (1), 34–59. https://doi.org/10.1021/acscatal.6b01534.

(14) Chen, J.; Lim, B.; Lee, E. P.; Xia, Y. Shape-Controlled Synthesis of Platinum Nanocrystals for Catalytic and Electrocatalytic Applications. *Nano Today* **2009**, *4* (1), 81–95. https://doi.org/https://doi.org/10.1016/j.nantod.2008.09.002.

(15) Corma, A.; Garcia, H. Supported Gold Nanoparticles as Oxidation Catalysts. *Nanoparticles Catal.* **2008**, 389–426.

(16) Ye, X.-R.; Lin, Y.; Wang, C.; Engelhard, M. H.; Wang, Y.; Wai, C. M. Supercritical Fluid Synthesis and Characterization of Catalytic Metal Nanoparticles on Carbon Nanotubes. *J. Mater. Chem.* **2004**, *14* (5), 908–913. https://doi.org/10.1039/B308124A.

(17) Astruc, D.; Lu, F.; Aranzaes, J. R. Nanoparticles as Recyclable Catalysts: The Frontier between Homogeneous and Heterogeneous Catalysis. *Angew. Chemie Int. Ed.* **2005**, *44* (48), 7852–7872. https://doi.org/https://doi.org/10.1002/anie.200500766.

(18) Campelo, J. M.; Conesa, T. D.; Gracia, M. J.; Jurado, M. J.; Luque, R.; Marinas, J. M.; Romero, A. A. Microwave Facile Preparation of Highly Active and Dispersed SBA-12 Supported Metal Nanoparticles. *Green Chem.* **2008**, *10* (8), 853–858. https://doi.org/10.1039/B801754A.

(19) Budarin, V. L.; Clark, J. H.; Luque, R.; Macquarrie, D. J.; White, R. J. Palladium Nanoparticles on

Polysaccharide-Derived Mesoporous Materials and Their Catalytic Performance in C–C Coupling Reactions. *Green Chem.* **2008**, *10* (4), 382–387. https://doi.org/10.1039/B715508E.
(20) Hutchings, G. J. Nanocrystalline Gold and Gold Palladium Alloy Catalysts for Chemical Synthesis. *Chem. Commun.* **2008**, No. 10, 1148–1164. https://doi.org/10.1039/B712305C.
(21) Edwards, J. K.; Carley, A. F.; Herzing, A. A.; Kiely, C. J.; Hutchings, G. J. Direct Synthesis of Hydrogen Peroxide from H2 and O2 Using Supported Au–Pd Catalysts. *Faraday Discuss.* **2008**, *138* (0), 225–239. https://doi.org/10.1039/B705915A.
(22) Chauhan, B. P. S.; Sarkar, A.; Chauhan, M.; Roka, A. Water as Green Oxidant: A Highly Selective Conversion of Organosilanes to Silanols with Water. *Appl. Organomet. Chem.* **2009**, *23* (10), 385–390. https://doi.org/https://doi.org/10.1002/aoc.1528.
(23) S, K.; M, C.; H, S.; Sangeeta; CB, M. A Review: The Uses of Various Nanoparticles in Organic Synthesis. *J. Nanomed. Nanotechnol.* **2020**, *11*. https://doi.org/10.35248/2157-7439.19.10.543.
(24) Shreaz, S.; Wani, W. A.; Behbehani, J. M.; Raja, V.; Irshad, M.; Karched, M.; Ali, I.; Siddiqi, W. A.; Hun, L. T. Cinnamaldehyde and Its Derivatives, a Novel Class of Antifungal Agents. *Fitoterapia* **2016**, *112*, 116–131. https://doi.org/https://doi.org/10.1016/j.fitote.2016.05.016.
(25) Cocchiara, J.; Letizia, C. S.; Lalko, J.; Lapczynski, A.; Api, A. M. Fragrance Material Review on Cinnamaldehyde. *Food Chem. Toxicol.* **2005**, *43* (6), 867–923. https://doi.org/https://doi.org/10.1016/j.fct.2004.09.014.
(26) Keleş, H.; Keleş, M. Electrochemical Investigation of a Schiff Base Synthesized by Cinnamaldehyde as Corrosion Inhibitor on Mild Steel in Acidic Medium. *Res. Chem. Intermed.* **2014**, *40* (1), 193–209. https://doi.org/10.1007/s11164-012-0955-5.
(27) Solmaz, R. Investigation of the Inhibition Effect of 5-((E)-4-Phenylbuta-1,3-Dienylideneamino)-1,3,4-Thiadiazole-2-Thiol Schiff Base on Mild Steel Corrosion in Hydrochloric Acid. *Corros. Sci.* **2010**, *52* (10), 3321–3330. https://doi.org/https://doi.org/10.1016/j.corsci.2010.06.001.
(28) Bohnet, M. Ullmann's Encyclopedia of Industrial Chemistry. 2014.
(29) Könst, W. M. B. Chemistry of Fragrant Substances P.J. Teisseire VCH, Weinheim, 1994 vi + 458 Pages. DM 218.00 / £ 89.00 ISBN 1-56081-610-4 Publishers, Inc. ISBN 3-527-89610-4 VCH Verlagsgesellschaft. *Recl. des Trav. Chim. des Pays-Bas* **1994**, *113* (7-8), 381. https://doi.org/https://doi.org/10.1002/recl.19941130712.
(30) Li, H.; Chen, X.; Wang, M.; Xu, Y. Selective Hydrogenation of Cinnamaldehyde to Cinnamyl Alcohol over an Ultrafine Co-B Amorphous Alloy Catalyst. *Appl. Catal. A Gen.* **2002**, *225* (1), 117–130. https://doi.org/https://doi.org/10.1016/S0926-860X(01)00855-9.
(31) Chen, A.; Holt-Hindle, P. Platinum-Based Nanostructured Materials: Synthesis, Properties, and Applications. *Chem. Rev.* **2010**, *110* (6), 3767–3804. https://doi.org/10.1021/cr9003902.
(32) Khdary, N. H.; Ghanem, M. A. Highly Dispersed Platinum Nanoparticles Supported on Silica as Catalyst for Hydrogen Production. *RSC Adv.* **2014**, *4* (91), 50114–50122. https://doi.org/10.1039/C4RA09341K.
(33) Tsang, S. C.; Cailuo, N.; Oduro, W.; Kong, A. T. S.; Clifton, L.; Yu, K. M. K.; Thiebaut, B.; Cookson, J.; Bishop, P. Engineering Preformed Cobalt-Doped Platinum Nanocatalysts For Ultraselective Hydrogenation. *ACS Nano* **2008**, *2* (12), 2547–2553. https://doi.org/10.1021/nn800400u.
(34) Ponec, V. On the Role of Promoters in Hydrogenations on Metals; α,β-Unsaturated Aldehydes and Ketones. *Appl. Catal. A Gen.* **1997**, *149* (1), 27–48. https://doi.org/https://doi.org/10.1016/S0926-860X(96)00250-5.
(35) Galvagno, S.; Poltarzewski, Z.; Donato, A.; Neri, G.; Pietropaolo, R. Liquid Phase Hydrogenations over Platinum-Tin Catalysts. *J. Mol. Catal.* **1986**, *35* (3), 365–375. https://doi.org/https://doi.org/10.1016/0304-5102(86)87084-5.
(36) Poltarzewski, Z.; Galvagno, S.; Pietropaolo, R.; Staiti, P. Hydrogenation of α,β-Unsaturated Aldehydes over Pt□Sn/Nylon. *J. Catal.* **1986**, *102* (1), 190–198. https://doi.org/https://doi.org/10.1016/0021-9517(86)90153-3.
(37) Marinelli, T. B. L. W.; Ponec, V. A Study on the Selectivity in Acrolein Hydrogenation on Platinum Catalysts: A Model for Hydrogenation of α,β-Unsaturated Aldehydes. *J. Catal.* **1995**, *156* (1), 51–59. https://doi.org/https://doi.org/10.1006/jcat.1995.1230.
(38) Beccat, P.; Bertolini, J. C.; Gauthier, Y.; Massardier, J.; Ruiz, P. Crotonaldehyde and Methylcrotonaldehyde Hydrogenation over Pt(111) and Pt80Fe20(111) Single Crystals. *J. Catal.* **1990**, *126* (2), 451–456. https://doi.org/https://doi.org/10.1016/0021-9517(90)90011-

8.
(39) Richard, D.; Ockelford, J.; Giroir-Fendler, A.; Gallezot, P. Composition and Catalytic Properties in Cinnamaldehyde Hydrogenation of Charcoal-Supported, Platinum Catalysts Modified by FeCl2 Additives. *Catal. Letters* **1989**, *3* (1), 53–58. https://doi.org/10.1007/BF00765054.
(40) Abad, A.; Concepción, P.; Corma, A.; García, H. A Collaborative Effect between Gold and a Support Induces the Selective Oxidation of Alcohols. *Angew. Chemie Int. Ed.* **2005**, *44* (26), 4066–4069. https://doi.org/https://doi.org/10.1002/anie.200500382.
(41) Zhang, Y.; Shen, J. Enhancement Effect of Gold Nanoparticles on Biohydrogen Production from Artificial Wastewater. *Int. J. Hydrogen Energy* **2007**, *32* (1), 17–23. https://doi.org/https://doi.org/10.1016/j.ijhydene.2006.06.004.
(42) Li, D.; Wehrung, J.-F.; Zhao, Y. Gold Nanoparticle-Catalysed Photosensitized Water Reduction for Hydrogen Generation. *J. Mater. Chem. A* **2015**, *3* (9), 5176–5182. https://doi.org/10.1039/C4TA06853J.
(43) Sankar, M.; He, Q.; Engel, R. V; Sainna, M. A.; Logsdail, A. J.; Roldan, A.; Willock, D. J.; Agarwal, N.; Kiely, C. J.; Hutchings, G. J. Role of the Support in Gold-Containing Nanoparticles as Heterogeneous Catalysts. *Chem. Rev.* **2020**, *120* (8), 3890–3938. https://doi.org/10.1021/acs.chemrev.9b00662.
(44) Villa, A.; Dimitratos, N.; Chan-Thaw, C. E.; Hammond, C.; Veith, G. M.; Wang, D.; Manzoli, M.; Prati, L.; Hutchings, G. J. Characterisation of Gold Catalysts. *Chem. Soc. Rev.* **2016**, *45* (18), 4953–4994. https://doi.org/10.1039/C5CS00350D.
(45) Massaro, M.; Colletti, C. G.; Fiore, B.; La Parola, V.; Lazzara, G.; Guernelli, S.; Zaccheroni, N.; Riela, S. Gold Nanoparticles Stabilized by Modified Halloysite Nanotubes for Catalytic Applications. *Appl. Organomet. Chem.* **2019**, *33* (3), e4665–e4665. https://doi.org/https://doi.org/10.1002/aoc.4665.
(46) E. Bailie, J.; J. Hutchings, G. Promotion by Sulfur of Gold Catalysts for Crotyl Alcohol Formation from Crotonaldehyde Hydrogenation. *Chem. Commun.* **1999**, No. 21, 2151–2152. https://doi.org/10.1039/A906538E.
(47) Milone, C.; Ingoglia, R.; Galvagno, S. Gold Supported on Iron Oxy-Hydroxides: A Versatile Tool for the Synthesis of Fine Chemicals. *Gold Bull.* **2006**, *39* (2), 54–65. https://doi.org/10.1007/BF03215277.
(48) Milone, C.; Ingoglia, R.; Schipilliti, L.; Crisafulli, C.; Neri, G.; Galvagno, S. Selective Hydrogenation of α,β-Unsaturated Ketone to α,β-Unsaturated Alcohol on Gold-Supported Iron Oxide Catalysts: Role of the Support. *J. Catal.* **2005**, *236* (1), 80–90. https://doi.org/https://doi.org/10.1016/j.jcat.2005.09.023.
(49) Campo, B. C.; Ivanova, S.; Gigola, C.; Petit, C.; Volpe, M. A. Crotonaldehyde Hydrogenation on Supported Gold Catalysts. *Catal. Today* **2008**, *133–135*, 661–666. https://doi.org/https://doi.org/10.1016/j.cattod.2007.11.043.
(50) Schimpf, S.; Lucas, M.; Mohr, C.; Rodemerck, U.; Brückner, A.; Radnik, J.; Hofmeister, H.; Claus, P. Supported Gold Nanoparticles: In-Depth Catalyst Characterization and Application in Hydrogenation and Oxidation Reactions. *Catal. Today* **2002**, *72* (1), 63–78. https://doi.org/https://doi.org/10.1016/S0920-5861(01)00479-5.
(51) Sankar, M.; Dimitratos, N.; Miedziak, P. J.; Wells, P. P.; Kiely, C. J.; Hutchings, G. J. Designing Bimetallic Catalysts for a Green and Sustainable Future. *Chem. Soc. Rev.* **2012**, *41* (24), 8099–8139. https://doi.org/10.1039/C2CS35296F.
(52) Alonso, D. M.; Wettstein, S. G.; Dumesic, J. A. Bimetallic Catalysts for Upgrading of Biomass to Fuels and Chemicals. *Chem. Soc. Rev.* **2012**, *41* (24), 8075–8098. https://doi.org/10.1039/C2CS35188A.
(53) Gilroy, K. D.; Ruditskiy, A.; Peng, H.-C.; Qin, D.; Xia, Y. Bimetallic Nanocrystals: Syntheses, Properties, and Applications. *Chem. Rev.* **2016**, *116* (18), 10414–10472.
(54) Massaro, M.; Colletti, C. G.; Lazzara, G.; Milioto, S.; Noto, R.; Riela, S. Halloysite Nanotubes as Support for Metal-Based Catalysts. *J. Mater. Chem. A* **2017**, *5* (26), 13276–13293. https://doi.org/10.1039/C7TA02996A.
(55) Ahmad, Y. H.; Mohamed, A. T.; Al-Qaradawi, S. Y. Exploring Halloysite Nanotubes as Catalyst Support for Methane Combustion: Influence of Support Pretreatment. *Appl. Clay Sci.* **2021**, *201*, 105956. https://doi.org/https://doi.org/10.1016/j.clay.2020.105956.
(56) Vinokurov, V. A.; Stavitskaya, A. V; Chudakov, Y. A.; Ivanov, E. V; Shrestha, L. K.; Ariga, K.; Darrat, Y. A.; Lvov, Y. M. Formation of Metal Clusters in Halloysite Clay Nanotubes. *Sci.*

Technol. Adv. Mater. **2017**, *18* (1), 147–151. https://doi.org/10.1080/14686996.2016.1278352.
(57) Massaro, M.; Noto, R.; Riela, S. Past, Present and Future Perspectives on Halloysite Clay Minerals. *Molecules* **2020**, *25* (20), 4863. https://doi.org/10.3390/molecules25204863.
(58) Hajizadeh, Z.; Maleki, A.; Rahimi, J.; Eivazzadeh-Keihan, R. Halloysite Nanotubes Modified by Fe3O4 Nanoparticles and Applied as a Natural and Efficient Nanocatalyst for the SymmetricalHantzsch Reaction. *Silicon* **2020**, *12* (5), 1247–1256. https://doi.org/10.1007/s12633-019-00224-3.
(59) Chen, S.; Li, J.; Zhang, Y.; Zhang, D.; Zhu, J. Effect of Preparation Method on Halloysite Supported Cobalt Catalysts for Fischer-Tropsch Synthesis. *J. Nat. Gas Chem.* **2012**, *21* (4), 426–430. https://doi.org/https://doi.org/10.1016/S1003-9953(11)60386-1.
(60) Li, Y.; Quan, X.; Hu, C.; Li, C. Effective Catalytic Reduction of 4-Nitrophenol to 4-Aminophenol over Etched Halloysite Nanotubes@α-Ni(OH)2. *ACS Appl. Energy Mater.* **2020**, *3* (5), 4756–4766. https://doi.org/10.1021/acsaem.0c00382.
(61) Wang, L.; Chen, J.; Ge, L.; Rudolph, V.; Zhu, Z. Halloysite Nanotube Supported Ru Nanocatalysts Synthesized by the Inclusion of Preformed Ru Nanoparticles for Preferential Oxidation of CO in H2-Rich Atmosphere. *J. Phys. Chem. C* **2013**, *117* (8), 4141–4151. https://doi.org/10.1021/jp312491m.
(62) Zhang, Y.; He, X.; Ouyang, J.; Yang, H. Palladium Nanoparticles Deposited on Silanized Halloysite Nanotubes: Synthesis, Characterization and Enhanced Catalytic Property. *Sci. Rep.* **2013**, *3*, 2948. https://doi.org/10.1038/srep02948.
(63) Rossi, L. M.; Fiorio, J. L.; Garcia, M. A. S.; Ferraz, C. P. The Role and Fate of Capping Ligands in Colloidally Prepared Metal Nanoparticle Catalysts. *Dalt. Trans.* **2018**, *47* (17), 5889–5915. https://doi.org/10.1039/C7DT04728B.
(64) Villa, A.; Jouve, A.; Sanchez Trujillo, F. J.; Motta, D.; Prati, L.; Dimitratos, N. Exploring the Effect of Au/Pt Ratio on Glycerol Oxidation in Presence and Absence of a Base. *Catalysts* . 2018. https://doi.org/10.3390/catal8020054.
(65) Cattaneo, S.; Freakley, S. J.; Morgan, D. J.; Sankar, M.; Dimitratos, N.; Hutchings, G. J. Cinnamaldehyde Hydrogenation Using Au–Pd Catalysts Prepared by Sol Immobilisation. *Catal. Sci. Technol.* **2018**, *8* (6), 1677–1685. https://doi.org/10.1039/C7CY02556D.
(66) Donoeva, B.; de Jongh, P. E. Colloidal Au Catalyst Preparation: Selective Removal of Polyvinylpyrrolidone from Active Au Sites. *ChemCatChem* **2018**, *10* (5), 989–997. https://doi.org/10.1002/cctc.201701760.
(67) Fornaro, T.; Burini, D.; Biczysko, M.; Barone, V. Hydrogen-Bonding Effects on Infrared Spectra from Anharmonic Computations: Uracil–Water Complexes and Uracil Dimers. *J. Phys. Chem. A* **2015**, *119* (18), 4224–4236. https://doi.org/10.1021/acs.jpca.5b01561.
(68) Li, C.; Zhao, Y.; Zhu, T.; Li, Y.; Ruan, J.; Li, G. Effective Solvent-Free Oxidation of Cyclohexene to Allylic Products with Oxygen by Mesoporous Etched Halloysite Nanotube Supported Co2+. *RSC Adv.* **2018**, *8* (27), 14870–14878. https://doi.org/10.1039/C7RA11245A.
(69) Choo, C. K.; Kong, X. Y.; Goh, T. L.; Ngoh, G. C.; Horri, B. A.; Salamatinia, B. Chitosan/Halloysite Beads Fabricated by Ultrasonic-Assisted Extrusion-Dripping and a Case Study Application for Copper Ion Removal. *Carbohydr. Polym.* **2016**, *138*, 16–26. https://doi.org/https://doi.org/10.1016/j.carbpol.2015.11.060.
(70) Gaaz, T. S.; Sulong, A. B.; Kadhum, A. A. H.; Nassir, M. H.; Al-Amiery, A. A. Impact of Sulfuric Acid Treatment of Halloysite on Physico-Chemic Property Modification. *Mater. (Basel, Switzerland)* **2016**, *9* (8), 620. https://doi.org/10.3390/ma9080620.
(71) White, R. D.; Bavykin, D. V; Walsh, F. C. The Stability of Halloysite Nanotubes in Acidic and Alkaline Aqueous Suspensions. *Nanotechnology* **2012**, *23* (6), 65705. https://doi.org/10.1088/0957-4484/23/6/065705.
(72) Abdullayev, E.; Joshi, A.; Wei, W.; Zhao, Y.; Lvov, Y. Enlargement of Halloysite Clay Nanotube Lumen by Selective Etching of Aluminum Oxide. *ACS Nano* **2012**, *6* (8), 7216–7226. https://doi.org/10.1021/nn302328x.
(73) Garcia-Garcia, D.; Ferri, J. M.; Ripoll, L.; Hidalgo, M.; Lopez-Martinez, J.; Balart, R. Characterization of Selectively Etched Halloysite Nanotubes by Acid Treatment. *Appl. Surf. Sci.* **2017**, *422*, 616–625. https://doi.org/https://doi.org/10.1016/j.apsusc.2017.06.104.
(74) Banaś, D.; Kubala-Kukuś, A.; Braziewicz, J.; Majewska, U.; Pajek, M.; Wudarczyk-Moćko, J.; Czech, K.; Garnuszek, M.; Słomkiewicz, P.; Szczepanik, B. Study of Properties of Chemically

Modified Samples of Halloysite Mineral with X-Ray Fluorescence and X-Ray Powder Diffraction Methods. *Radiat. Phys. Chem.* **2013**, *93*, 129–134. https://doi.org/https://doi.org/10.1016/j.radphyschem.2013.05.028.

(75) Augustine, R. L.; Doyle, L. K.; Malhotra, S.; Posner, L. S.; O'Leary, S. T.; Roberto, S. A.; Tanielyan, S. K. Heterogeneous Catalysis in Organic Synthesis. *Catal. Org. React.* **1994**, *62*, 81.

(76) Manyar, H. G.; Yang, B.; Daly, H.; Moor, H.; McMonagle, S.; Tao, Y.; Yadav, G. D.; Goguet, A.; Hu, P.; Hardacre, C. Selective Hydrogenation of α,β-Unsaturated Aldehydes and Ketones Using Novel Manganese Oxide and Platinum Supported on Manganese Oxide Octahedral Molecular Sieves as Catalysts. *ChemCatChem* **2013**, *5* (2), 506–512. https://doi.org/https://doi.org/10.1002/cctc.201200447.

(77) Galvagno, S.; Donato, A.; Neri, G.; Pietropaolo, R.; Pietropaolo, D. Hydrogenation of Cinnamaldehyde over Platinum Catalysts: Influence of Addition of Metal Chlorides. *J. Mol. Catal.* **1989**, *49* (2), 223–232. https://doi.org/https://doi.org/10.1016/0304-5102(89)80053-7.

(78) Neri, G.; Milone, C.; Galvagno, S.; Pijpers, A. P. J.; Schwank, J. Characterization of Pt-Sn/Carbon Hydrogenation Catalysts. *Appl. Catal. A Gen.* **2002**, *227* (1), 105–115. https://doi.org/https://doi.org/10.1016/S0926-860X(01)00927-9.

(79) Englisch, M.; Ranade, V. S.; Lercher, J. A. Hydrogenation of Crotonaldehyde over Pt Based Bimetallic Catalysts. *J. Mol. Catal. A Chem.* **1997**, *121* (1), 69–80. https://doi.org/https://doi.org/10.1016/S1381-1169(96)00450-5.

(80) Bus, E.; Prins, R.; van Bokhoven, J. A. Origin of the Cluster-Size Effect in the Hydrogenation of Cinnamaldehyde over Supported Au Catalysts. *Catal. Commun.* **2007**, *8* (9), 1397–1402. https://doi.org/https://doi.org/10.1016/j.catcom.2006.11.040.

(81) Bidaoui, M.; Especel, C.; Sabour, S.; Benatallah, L.; Saib-Bouchenafa, N.; Royer, S.; Mohammedi, O. Toward the Improvement in Unsaturated Alcohol Selectivity during α,β-Unsaturated Aldehyde Selective Hydrogenation, Using Zn as Promoter of Pt. *J. Mol. Catal. A Chem.* **2015**, *399*, 97–105. https://doi.org/https://doi.org/10.1016/j.molcata.2015.01.010.

(82) Wang, Q.; Wang, Y.; Zhao, Y.; Zhang, B.; Niu, Y.; Xiang, X.; Chen, R. Fabricating Roughened Surfaces on Halloysite Nanotubes via Alkali Etching for Deposition of High-Efficiency Pt Nanocatalysts. *CrystEngComm* **2015**, *17* (16), 3110–3116. https://doi.org/10.1039/C5CE00189G.

(83) Durndell, L. J.; Parlett, C. M. A.; Hondow, N. S.; Isaacs, M. A.; Wilson, K.; Lee, A. F. Selectivity Control in Pt-Catalyzed Cinnamaldehyde Hydrogenation. *Sci. Rep.* **2015**, *5* (1), 9425. https://doi.org/10.1038/srep09425.

(84) Galvagno, S.; Capannelli, G.; Neri, G.; Donato, A.; Pietropaolo, R. Hydrogenation of Cinnamaldehyde over Ru/C Catalysts: Effect of Ru Particle Size. *J. Mol. Catal.* **1991**, *64* (2), 237–246. https://doi.org/https://doi.org/10.1016/0304-5102(91)85115-I.

(85) Simion, A.-M.; Arimura, T.; Simion, C. Reaction of Cinnamaldehyde and Derivatives with Raney Ni–Al Alloy and Al Powder in Water. Reduction or Oxido-Reduction? *Comptes Rendus Chim.* **2013**, *16* (5), 476–481. https://doi.org/https://doi.org/10.1016/j.crci.2012.11.022.

Part Two
Ceria-based nanocomposites for environment toxicological studies

Chapter 7

Natural molecule coatings modify the fate of Cerium dioxide nanoparticles in water: synthesis and eco-toxicity

Sara Villa, Daniela Maggioni, Valeria di Nica, Hady Hamza, Stefano Magni, Bianca Morosetti, Camilla Carla Parenti, Antonio Finizio, Andrea Binelli, Camilla Della Torre
Environmental Research, 10 Jun 2020, 188:109778.
Bianca Morosetti, Rosa Freitas, Eduarda Pereira, Hady Hamza, Madalena Andrade, Francesca Coppola, Daniela Maggioni, Camilla Della Torre
Environmental Pollution, Volume 257, February 2020, 113597.
Camilla Della Torre.; Daniela Maggioni.; Lara Nigro.; Fiorenza Farè.; Hady Hamza.; Giuseppe Protano.; Stefano Magni.; Manuela Fontana.; Nicoletta Riccardi.; Matteo Chiara.; Donatella Caruso.; Andrea Binelli
Sci. Total Environ. 2021, 773, 145612.

1. Introduction

1.1 Nanotechnology

One of the most rapidly developing research fields of the 21st century.[1] It involves studying, producing, and manipulating structures, devices, materials, or particles with at least one dimension that falls within the range of 1–100 nm length. The unique physicochemical properties of nanoparticles (NPs), substantially different from those of the same bulk materials, made them attractive for a broad range of technological applications and consumer goods.[2–5] The massive use of products containing nanomaterials (NMs) on a large scale leads to a relevant voluntary or involuntary release of these contaminants in the environment, reaching different types of ecosystem compartments (water, sediments, and biota).[6] This has raised concern about the possible harmful consequence of NPs on natural ecosystems. In particular, the marine ecosystem represents the final sink of the released NPs in soils and waterways; moreover, it suffers also from the immediate release of NPs developed for marine applications.[6–9]

An essential feature of NPs lies in the fact that they do not follow elemental physico-chemical features of other classes of human-made pollutants, thus creating new challenges in ecotoxicology and risk assessment.[10–12] Upon being released in the environment, NPs undergo several transformations such as aggregation, dissolution, redox reactions. Among these transformations, due to their high surface-area-to-volume ratio, NPs can be covered by a corona of biological macromolecules from the surroundings, called eco-corona, which might affect their transport and bioavailability in natural [12–15] The combined effects of biological contaminants and NPs on organisms can be categorized as synergistic, antagonistic, or independent, depending on contaminant composition, the type of NP, and the different water media where the interactions are [16–25]

In water, one of the main biological components is the natural organic matter (NOM). The NOM

is constituted by humic substances, proteins, exudates, and polysaccharide acid compounds.[26] These organic substances can alter the NP aggregation state in the water column and the consequent impacts on biological [27–29], some studies have shown a reduced aggregation of NPs in freshwater due to the presence of NOM, which increases the particle ζ-potential, thus increasing electrostatic repulsion.[30,31]

While the surface modifications effect is widely considered in toxicological/pharmacological studies, it is barely addressed in nano-ecotoxicological research. Also, most of the available studies investigating the combined effects of NPs and pollutants dealt with,[16,32] assessing this topic is essential to properly predict the risk related to the presence of NPs in the environment since organisms are exposed to complex mixtures of contaminants in natural conditions.[12,14,33–36]

1.2 Cerium oxide nanoparticles (CeO_2 NPs)

Ceria NPs are one of the most promising NPs extensively used in several applications such as paint coating, polishing powder, catalyst in diesel fuel oil, luminescent materials, UV absorbents, coatings, glass polishers, oxygen gas sensors, fuel cells, fuel additives and antioxidant agents in biomedicine (**Figure 1**).[37–42] The use of CeO_2 NPs is foreseen to further increase in the next years with a forecasted estimated upper limit of production volumes at 10,000 t/a in 2050.[10] The consequent release of CeO_2 NPs in 2050 is estimated to be up to 300 t/a in the ecosphere (waters, soil, air) and up to 4000 t/a in technosphere (i.e. landfills, waste treatment).[10]

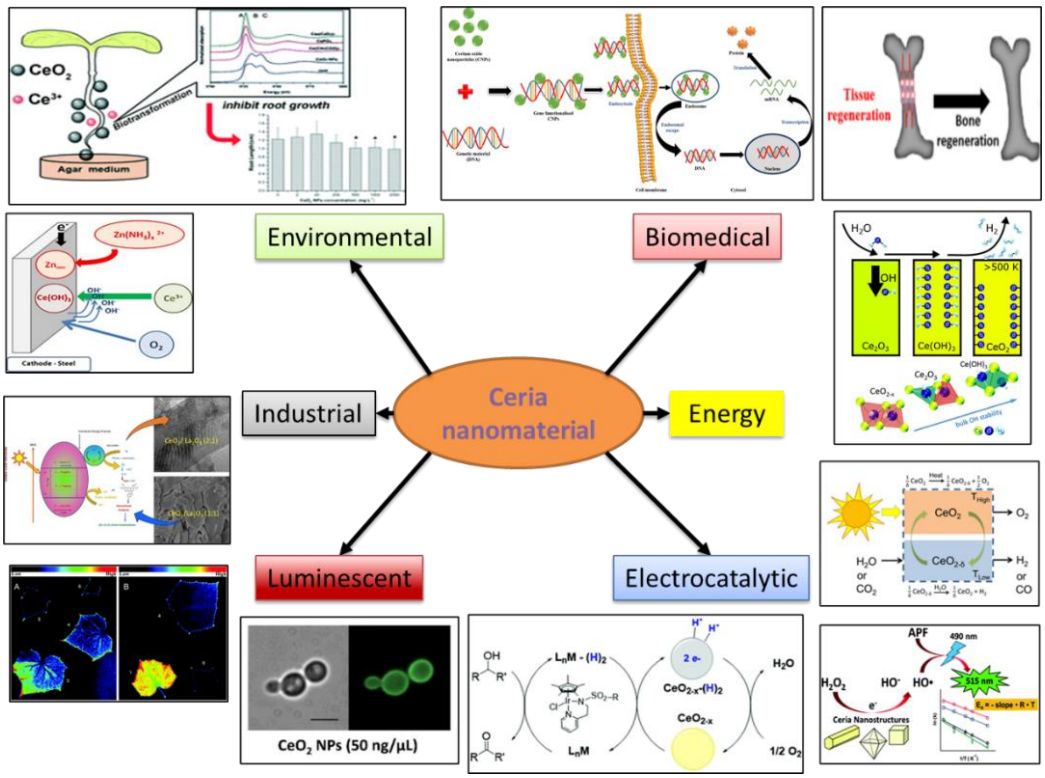

Figure 1. Schematic representation of the applications of Nanoceria.

The actual levels of CeO_2 NPs in the natural ecosystem are still unknown, but several models attempted to establish a predicted environmental concentration in natural matrices. The CeO_2 NPs concentration in water is expected to be in the range of ng/L in surface water[43] and pg/L in seawater.[44,45] A calculation of predicted environmental concentrations (PECs) as high as 1 µg/L in surface waters has been suggested in some worst-case scenario such as effluents of wastewater treatment plant.[10,46–48]

1.2.1 Techniques of ceria preparation

There are many methods for the synthesis of Ceria NPs nanoparticles for different applications. Those synthetic strategies are fundamental (**Figure 2**), as the physicochemical characteristics of the nanoparticles such as surface chemistry, morphology, size/aggregation, and zeta potential depend upon them. These features determine the behavior especially in the medical field of application, as the final properties affect the interaction at the biological interface. So, first of all, here in the following we discuss the various methods which have been used in the literature to synthesize nanoceria.

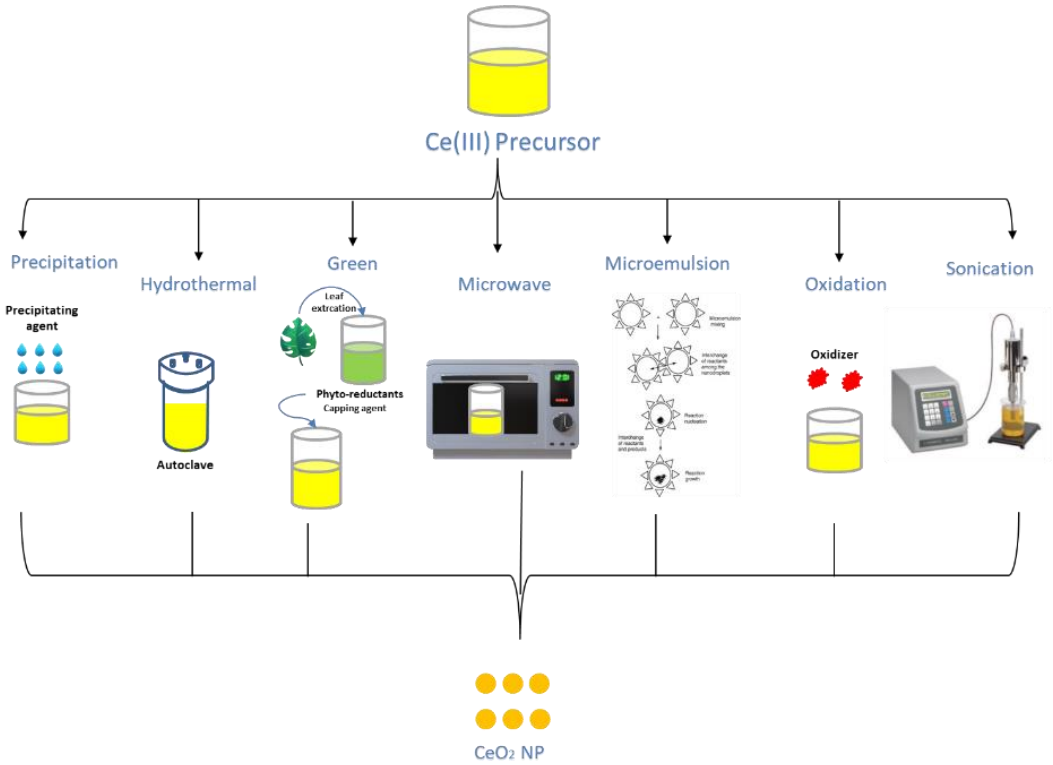

Figure 2. Different methods for the synthesis of nanoceria.

Precipitation method. The most common synthetic method for Ceria NPs consists in a simple precipitation gained by the addition of a base such as sodium hydroxide or ammonia into the solution of cerium (III) ions precursor, which usually is cerium nitrate hexahydrate. In this method,

CeO_2 NPs can be synthesized with different properties by controlling several parameters such as the temperature, the stirring rate, the type of atmosphere in the reaction chamber, and the medium pH. Moreover, depending on these parameters, the shape and diameter of the obtained NPs could be both spherical with a size ranging between 3-27 nm,[49–51] polyhedral with a mean size of 6-21 nm[52] and cubic with an edge length ranging between 19-33 nm.[53] In general, the size of ceria NPs decreases as oxygen content increases and/or the temperature of the reaction atmosphere decreases.[52] Also, spherical NP size decreases as the pH of the medium increases towards pH 12.[53] Most of the literature states that spherical NPs were predominantly the final product using cerium nitrate hexahydrate as a precursor.[49–51,54,55]

Hydrothermal method. This synthetic procedure consists of a reaction under pressure carried out by the use of an autoclave where a solution of the cerium precursor and reducing agent are mixed and warmed under controlled pressure. By controlling the autoclave temperature, the hydrothermal method enhances nanoparticle production with catalytic behaviour.[56] The high concentration of oxygen on the surface of the nanoparticles enhances the catalytic activity especially the one of nanorods that results is much higher than for nanocubes. For some biological application is important to verify the impact of morphology and size. It is now clear from the literature that altering the synthetic parameter such as the temperature, the type of solvents, the stabilizing agents, and the concentration will change the morphology and size.[57–59]

Green method. The harmful effects of the toxic chemicals used in the chemical preparation methods pushed the researchers to use “green chemistry” methods for ceria preparation. The green process is an easy, safer, reliable, efficient, and eco-friendly method since the use or production of toxic substances is sensibly reduced. In this method, high temperature, pressure, and energy are not required. The main substances involved in nanoceria synthesis by this method are plant extracts, sugars, biodegradable polymers, and microorganisms that will act as reducing and capping agents.[60,61]

Microwave-assisted method. The microwave-assisted method is more efficient than any other conventional heating methods because the microwaves interact directly with the solvent and reactant molecules present in the reaction mixture. The energy-transfer takes place quickly, leading to a rapid rise in the temperature of the system. In this method, the reaction is rapidly completed, and spotless products with a high yield are obtained.[62,63] Different morphology of ceria nanoparticles could be obtained by controlling the microwave power.[64–67]

Micro-emulsion methods. Micro-emulsions are colloidal solutions that consist of two immiscible solvents (water and oil), a surfactant and a co-surfactant. They can be prepared rapidly by stirring the mentioned components, and the formed microemulsions are thermodynamically stable solutions. Microemulsions are of different types such as oil-in-water (O/W) microemulsions or water-in-oil (W/O) reverse microemulsions.[68,69] The size of ceria nanoparticles can be controlled by changing the cerium source and solvents used in the synthesis.[70–72]

Direct oxidation method. In the direct oxidation method, the cerium source is mixed with an oxidizer like hydrogen peroxide in an acidic medium or ammonia in basic conditions. As the oxidizer concentration increases, the size of nanoceria decreases.[73] However, in both media, the size of nanoceria remains small (3–5 nm), but the basic medium shows less aggregation compared to the acidic one.[74–76]

Sonochemical method. In the sonochemical method, the reaction is carried out by applying a high-intensity ultrasound wave, which forms acoustic cavitation, i.e., formation, growth, and collapse of bubbles, developing very high local temperature and pressure that start a chemical reaction. These reactions are swift, and no external activation energy and pressure are applied.[64,77–79] Some researchers[77] stated that adding additives to the reaction container would reduce the size of ceria NPs and prevent aggregate formation.

Besides the above-discussed methods, some researchers have also reported other methods for ceria NPs preparation, as ball milling,[80] flame spray pyrolysis,[81] and solution plasma process.[82]

1.2.2 Environmental Toxicity of Ceria

Ecotoxicological studies have described the adverse effects of CeO_2 NPs on different marine taxa such as bacteria, algae, bivalves, echinoderms and it was reported that CeO_2 NPs may target the organism at different biological scales,[83–91] inducing oxidative stress,[84,85,92,93] immunomodulation,[83,94–96] alteration of feeding and swimming capacity,[93,97] reducing growth or development, and increasing lethality.[98–100]

Nonetheless, the cellular mechanisms underpinning the toxicity of CeO_2 NPs are far to be understood. Concerning oxidative stress, CeO_2 NPs have either pro-oxidant or antioxidant properties. Indeed, several studies showed that CeO_2 NPs can act as reactive oxygen species (ROS) scavengers protecting cells from oxidative damages, mimicking the activity of the catalase (CAT) and superoxy-dismutase (SOD) enzymes.[101,102] This property is due to the contemporary presence of Ce^{3+}/Ce^{4+} on the surface of NPs, and the presence of redox reaction between Ce^{3+}/Ce^{4+} generates oxygen vacancies which confer catalytic and electrical properties and biological reactivity.[103,104] On the contrary, other studies showed the ability of CeO_2 NPs to trigger an imbalance of the oxidative status in different models.[105] Most of the evidence arose from ecotoxicity tests carried out on pristine NPs. Nevertheless, several studies emphasized that environmental modifications might affect the physico-chemical features of CeO_2 NPs[106,107], which in turn influence bioavailability and toxic outcomes for aquatic organisms.[108] In particular, the surface interactions of CeO_2 NPs with organic and inorganic molecules can enhance stability in water and modify biological consequences to organisms.

1.2.3 Influence of natural functionalization on the ecotoxicity of Cerium dioxide nanoparticles for aquatic models (Tap water study)

Several studies showed that the interaction of CeO_2 NPs with NOM modifies the surface properties and behaviour of Ceria in water media. For instance, poly (acrylic acid)-stabilized CeO_2 NPs remained more dispersed in water and generated higher toxicity in the freshwater algae *Pseudokirchneriella subcapitata* than non-stabilized CeO_2 NPs.[109] Citrate coated CeO_2 NPs resulted more stable in the water column compared to bare CeO_2 NPs in a simulated pond ecosystem. [110] A further investigation on the bivalve mussel *Dreissena polymorpha* showed that this coating enhanced the accumulation of CeO_2 NPs.[108]. Besides, the citrate coated CeO_2 NPs reduced significantly the expression of piGST gene and CAT activity and increased the lysosomal system.

While the interaction of CeO_2 NPs with alginate has been described[111], the influence on biological impacts of these NPs are largely unknown except for a study performed on the algae *P. subcapitata*, which showed that NOM enhanced the stability of CeO_2 NPs in suspension and decreased their toxicity. [112]

In this view, the study was to perform an ecotoxicological evaluation of CeO_2 NPs with different surface modifications, representing NPs bio-interaction with molecules naturally occurring in the water environment, to identify the influence of biomolecule coatings on nanoceria fate and toxicity for aquatic organisms.

To this aim, CeO_2 NPs were *ad hoc* synthesized with two different coating agents such as Alginate and Chitosan. Alginate and Chitosan were selected as representative of biomolecules present in natural aquatic systems. Alginate is a natural polysaccharide that represents up to 30% of NOM in lake water[113] and is a model of extracellular polymeric substances produced by biofilm. [114] Chitosan is a biopolymer, a chitin derivative that is produced from crustacean shells, which is the second most abundant natural polysaccharide on earth. [115]The impacts of bare and coated CeO_2 NPs were assessed in the marine bacteria *Aliivibrio fischeri*, in the freshwater crustacean *Daphnia magna*. To assess NP bioavailability, different toxicity endpoints were evaluated such as the inhibition of luminescence in *A. fischeri* and imbalance of antioxidant mechanism, inhibition of acetylcholinesterase activity, swimming performance in *D. magna*. Such metrics would allow linking the effects observed at the molecular-cellular level to toxic outcomes at the individual level (**Table 1**).

Table 1. Summary for environmental study cases of ceria nanoparticle

Type of studied interaction	Ceria/Natural organic matter		Ceria/Mercury at different Temperature
Medium	Tap water		Saltwater
Model	*Aliivibrio fischeri* bacteria 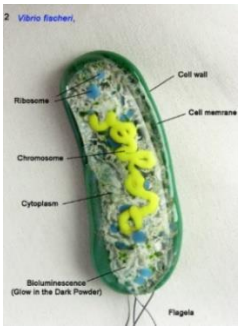	*Daphnia magna* 	*Mytilus galloprovincialis* 
Parameter	luminescence activity	Mortality	Toxicity

1.2.4 Influence of Cerium dioxide on the ecotoxicity of heavy metals under warming conditions (Saltwater study)

Cerium-based oxides and their composites were reported to be reliable adsorbents for metal traces.[116] Indeed, CeO_2 NPs have been employed for sorption from water media of many different cations, such as As^{5+}, As^{3+}, Cr^{6+}, Pb^{2+}, Cd^{2+}, F^-, Hg^0, Hg^{2+} and U^{6+}.[117] Although the potential use of these NPs can be a promising solution for water decontamination, several crucial issues should be addressed regarding this application, such as the possible occurrence of unexpected effects due to the interactions between NPs, including CeO_2 NPs, and metals. Among metals, mercury (Hg) ranks in the third position in the priority list of substances that can potentially threat human health by ATSDR [118] due to its persistence in the environment and its propensity to bio-accumulate in the organism.[119]

Mercury has been found in coastal ecosystems since decades ago, derived from many activities, including the chloro-alkali industry.[120] Although in recent years some of these activities have been limited, Hg has been used in novel applications, including fluorescent lamps, together with rare earth elements as Ce.[121] In coastal waters, Hg was detected in concentrations up to µg/L,[122] whereas in open sea Hg concentrations were estimated to be in the range of 0.5–3.0 ng/L.[123] The capacity of Hg to affect biological processes, including biochemical mechanisms involved in organisms' oxidative stress status, was assessed by several authors.[124,125] The negative impacts that Hg has on energy metabolism, physiological mechanisms and reproduction were also ascertained.[125]

Besides pollution, coastal ecosystems are affected by the ever-increasing threat posed by the changing climate. Indeed, the adverse effects of contaminants could be further amplified if combined with other environmental stressors such as global warming.[126] Several studies highlighted that an increase in **water temperature** can affect the bioaccumulation of pollutants, including metals, but also to modify organism' susceptibility to contaminants.[127,128] However, the effect of increasing temperature on NPs is still barely investigated[129], and less is known on the influence of temperature rise on the combined effects between NPs and metals.[130]

The goal of this study is to assess the potential interaction between CeO_2 NPs and the toxic metal Hg under the temperature representative of current conditions at the sampling area, and the temperature increase forecasted to occur at the end of the 21st century.[131] The marine bivalve Mytilus galloprovincialis was selected for this study since it has been widely used as bioindicator species for a vast variety of pollutants, including metals as Hg, metalloids and nanoparticles.[132–134] Mussels were exposed to CeO_2 NPs and Hg individually and in combination at 17 and 22 °C, for twenty-eight days. Several biochemical endpoints were evaluated such as electron transport system (ETS) activity, as markers of energy alteration and metabolism; glutathione reductase (GR) and glutathione-s-transferases (GSTs) activities, as markers of oxidative stress. Moreover, reduced glutathione (GSH) content was evaluated to measure mussel's redox balance.

2 Result and Discussion

2.1 Ceria nanocomposite characterization

We prepared CeO_2 NPs with some modification of literature procedure[135] resumed in **Scheme 1.** From these naked NPs, the Chitosan and Alginate nanocomposites have been obtained. Alginate is a negatively charged polymeric species in a wide range of pH due to carboxylate functionalities present in each repeating unit. On the contrary, Chitosan is a polymer characterized by amine groups that are mainly protonated until pH 7-8. The ζ-potential curves for the two natural polymers in MilliQ water (**Figure 3)**, together with the chemical structure sketching the repeating unit) showed the different overall charge of these two natural macromolecules in the pH range 3.10.

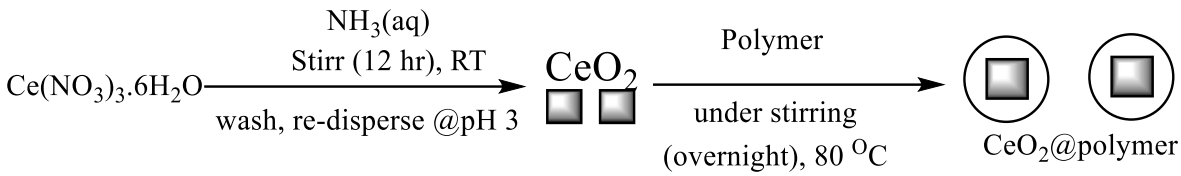

Scheme 1. Synthesis of Ce NPs coated with Chitosan and Alginate

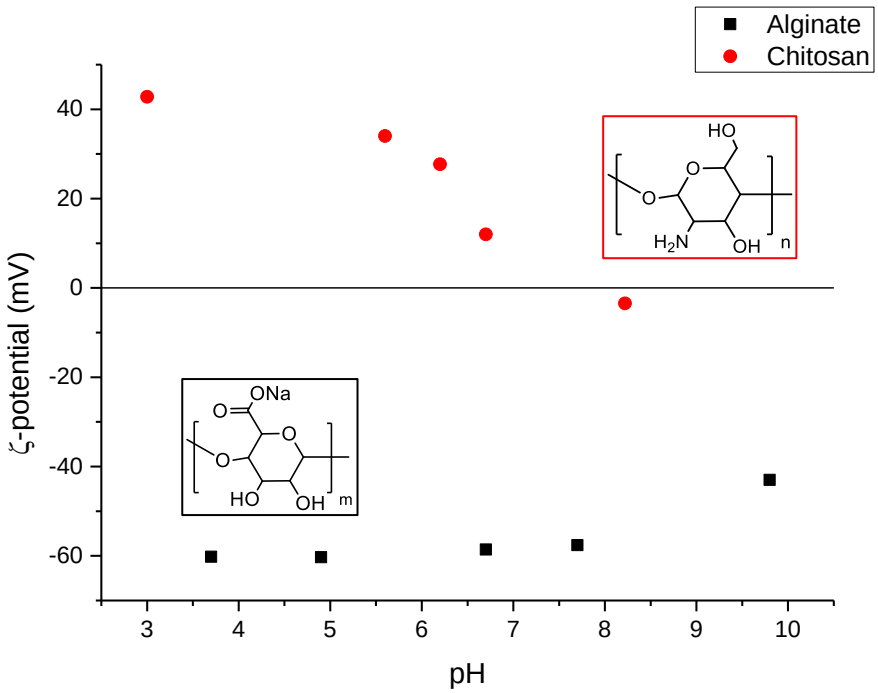

Figure 3. ζ-potential vs pH curves for Alginate and Chitosan polymers. In the boxes, the sketches of the polymer repeating units are shown.

The full characterization of NPs highlighted that the coating with natural polymers altered the

stability and hydrodynamic behaviour of the NPs in water, with CeO_2@Alginate being more prone to sedimentation compared to the other two NPs.

The three synthesized nanoceria showed some differences in size, shape, or aggregation state (**Figure 4**). TEM images of naked CeO_2 showed some aggregates, but most of the freshly prepared NPs appeared well spread on the sample holder with a mean diameter centred at ~5 nm (**Figure 4a)**.

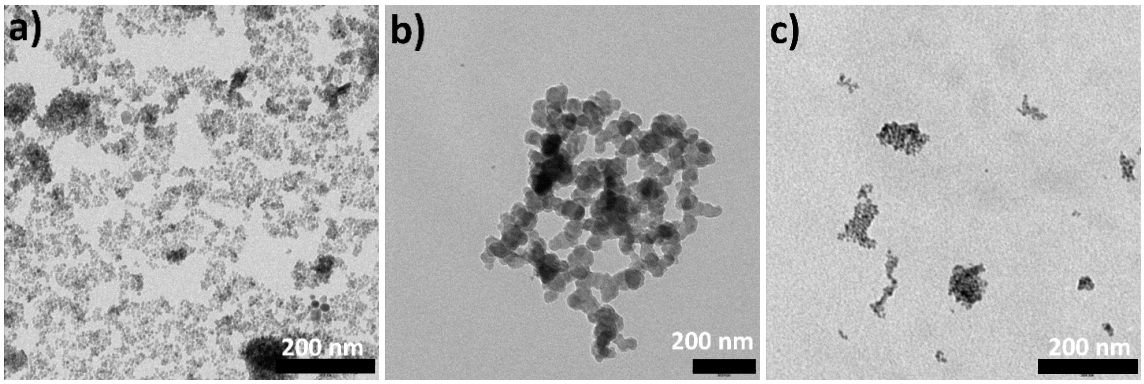

Figure 4. TEM micrographs of (a) naked CeO_2 NPs; (b) CeO_2@Alginate NPs; (c) CeO_2@Chitosan NPs.

In contrast, CeO_2@Chitosan (**Figure 4c**) NPs appeared in the TEM micrographs as irregular NP clusters composed of NPs identical in size with the naked NPs, and the Chitosan shell was not visible. The CeO_2@Alginate was composed of particles with rounded shapes and larger sizes (~50 nm) (**Figure 4b**). In this nanocomposite, we can observe the Alginate shell surrounding the NPs in the TEM images (see **Figure 5**), which explains the observed differences by TEM both in shape and size.

To confirm the formation of the coating and quantify it, we carried out thermogravimetric analysis (TGA). While in the TG profile of naked ceria a continuous mass loss until 800 °C was present, for both the Chitosan and Alginate derivatives, there was a defined weight loss step (from 150 to 400 °C), stating the presence of the polymer together with Ceria NPs. The starting weight loss was due to the loss of hydration water (~2% and ~9% for Chitosan and Alginate, respectively). Then, while in the CeO_2@Chitosan curve the decomposition of the polymer accounts for only ~9% of weight loss (T onset = 230 °C), for CeO_2@Alginate, the percentage of polymer reached ~49% (T onset = 210 °C), in line with what was observed by TEM, which showed that the Alginate amount surrounding the Ceria NPs, compared to that of Chitosan, was much higher (**Figure 6**).

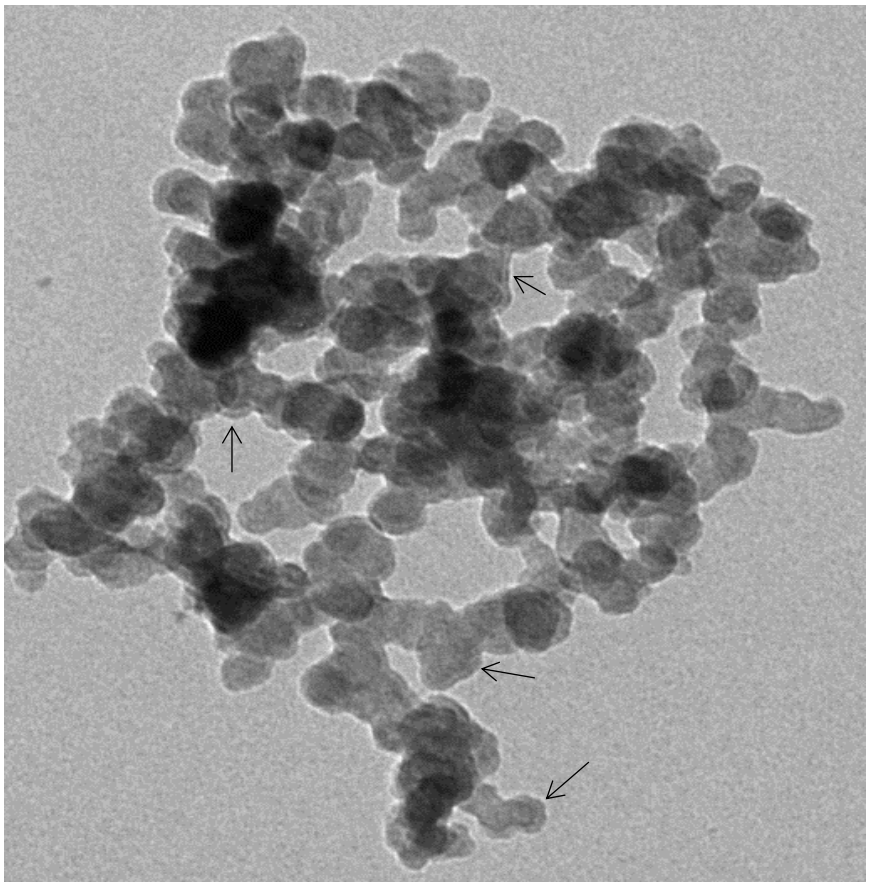

Figure 5. Magnification of panel (B) of **Figure 4**. The arrows are indicating some parts of the sample in which is more evident the presence of a lighter shell.

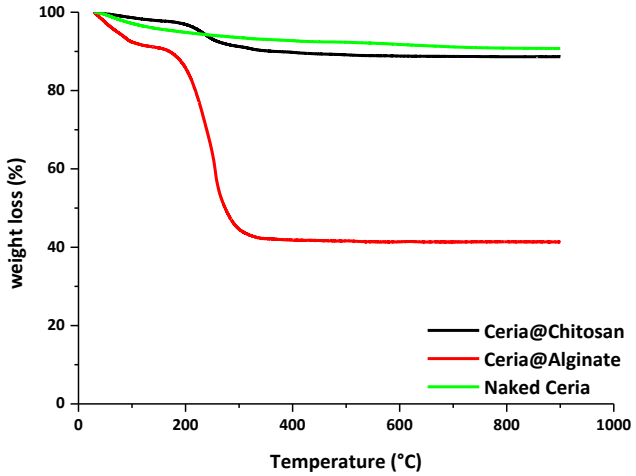

Figure 6. TGA curves for the three Ceria-based samples carried out in air at a heating rate of 10 °C min^{-1}.

Another indicator of the presence of polymers on Ceria NPs was observed in FTIR-ATR spectroscopy. The spectra are reported in **Figure 7** (panel (a) Chitosan; panel (b) Alginate), in

which a comparison between naked Ceria NPs, the polymers and the relative Ceria derivatives are reported. The attribution of the bands relative to the various species is reported in **Table 2**. From this comparison, it can be seen that in the blue traces, the signals of Chitosan (**Figure 7a**) and Alginate (**Figure 7b**) are evident (vertical green dashed lines) together with the intense and partially visible band of the Ceria lattice (750-400 cm^{-1}).

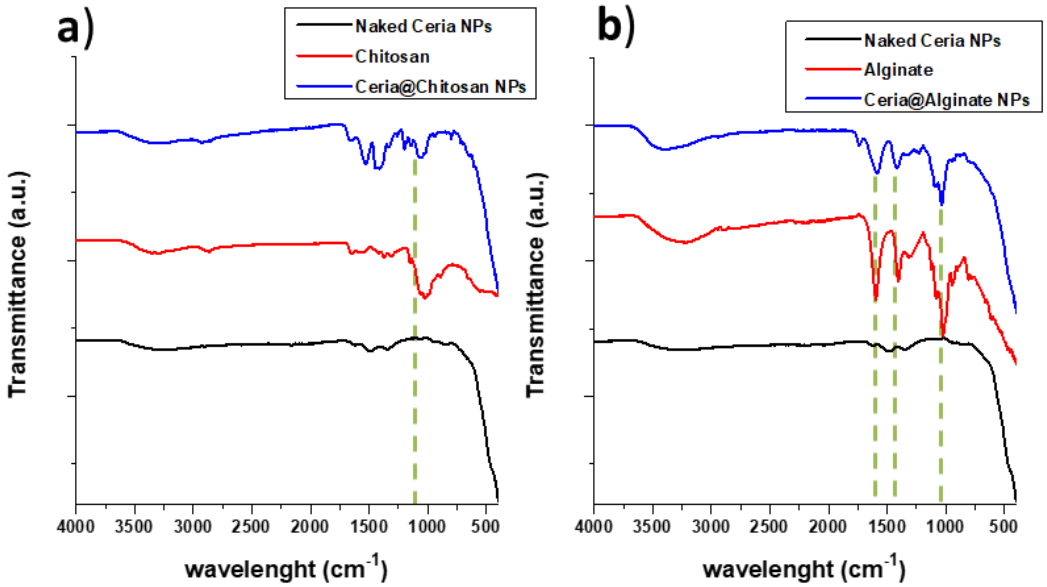

Figure 7. ATR-FTIR spectra of naked CeO_2 NPs (black traces), Chitosan (red trace panel a), Alginate (red trace panel b), and the two nanocomposites CeO_2@Chitosan (blue trace panel a) and CeO_2@Alginate (blue trace panel b).

Table 2. FTIR-ATR bands and their attribution for the various species studied.

Species	Wavenumber (cm^{-1})	Attribution
CeO_2 NPs	3300	ν_{OH} stretching mode of surface OH and adsorbed H_2O
	1622	δ_{OH} bending mode of adsorbed water
	1348 and 1494	$\nu_{C\text{-}O}$ carbonate ions interacting with the NPs surface Ce cations
	750-400	$\nu_{Ce\text{-}O}$ Ceria NPs lattice
Chitosan	3359	ν_{OH} and ν_{NH} stretching modes of axial OH and NH amine groups
	2919 and 2867	symmetric and asymmetric ν_{CH} of the aliphatic groups
	1655	ν_{CO} stretching mode of acetamido groups (amide I) present in some of the repetition units of chitosan
	1570	δ_{NH} bending of amino groups
	1422 and 1477 (sh)	ν_{CN} stretching mode and δ_{NH} bending of amino groups
	1380	δ_{CH} symmetrical deformation of CH_3
	1150-900	vibrations of glycosidic bonds, C-O and C-O-C stretching
CeO_2@Chitosan	3340	ν_{OH} and ν_{NH} stretching modes of axial OH and NH amine groups
	2920 and 2849	symmetric and asymmetric ν_{CH} of the aliphatic groups of Chitosan and possible acetate residues
	1655	ν_{CO} stretching mode of acetamido groups (amide I) present in some of the repetition units of chitosan

	1534 and 1407	ν_{CO} symmetroc and asymmetric stretching of COO^- groups of acetate deriving from acetic acid used for the dissolution of Chitosan.
	1146 and 1050	vibrations of glycosidic bonds, C-O and C-O-C stretching
	750-400	ν_{Ce-O} Ceria NPs lattice
Alginate	3223	ν_{OH} stretching modes of axial OH
	2955 and 2885	symmetric and asymmetric ν_{CH} of the aliphatic groups of Alginate
	1606 and 1415	Characteristic peaks of Alginate attributed to asymmetric and symmetric stretching vibrations of carboxylate salt ion
	1130 - 938	attributed to the ν_{C-O} stretching of pyranosyl ring with contributions from C–C–H and C–O–H deformation
CeO_2@Alginate	3388	ν_{OH} stretching modes of axial OH
	2952-2882	symmetric and asymmetric ν_{CH} of the aliphatic groups of Alginate
	1595 and1429	asymmetric and symmetric stretching vibrations of carboxylate salt ion of alginate (the shift owing to chelation with Ceria NPs surface
	1131 - 935	attributed to the ν_{C-O} stretching of pyranosyl ring with contributions from C–C–H and C–O–H deformation
	800-400	ν_{Ce-O} Ceria NPs lattice

The three samples suspended in milliQ water appeared different to the naked eye. While CeO_2@Chitosan NPs were well suspended, both the naked Ceria and CeO_2@Alginate NPs showed a certain amount of precipitate settling down over time, with the CeO_2@Alginate the sample having the highest visible sediment formation.

First, we tentatively tried to characterize the three samples by DLS in milliQ water at a concentration as low as 0.1 mg/mL, but the insufficiency of the results, due to a very low scattering power, prompted us to increase the concentration to 1 mg/mL. At these concentration levels, the analyses were robust and reproducible but far from the concentrations used for the assessment of the effects on bacteria as well as on animal models. Nevertheless, DLS is a useful tool to compare the colloidal behaviour of the different nano-derivatives and to collect information on their actual state, provided that the suspension is stable enough.

The DLS results (**Table 3**) in milliQ water showed that CeO_2@Chitosan NPs present only one peak, which was centered at ~200 nm, while in the case of the naked Ceria two populations were detected (at ~150 and ~400 nm), indicating that incipient aggregation began to occur. The instability over time of some suspensions produced DLS outputs that were not always representative of the whole sample since even during the short time of the measurements, dynamic aggregation events occurred, as in the case of the Alginate derivative, which showed the most aggregated situation. This last sample started to flocculate in a few minutes, and one of the two peaks detected by DLS was centered at much higher sizes (~790 nm). This behaviour can be ascribed to the ability of this polymer species to crosslink several NPs to each other. Hence, it is clear that the hydrodynamic diameter is representative of just the fraction of material remaining in suspension.

Through measurements of the ζ -potential, the surface charge was also investigated. As expected, the different coatings heavily modified the surface charge, from the negative value -28 mV for CeO_2@Alginate to positive values for Naked Ceria (+36.7 mV) and Ceria@Chitosan (+42.8 mV).

Table 3. Hydrodynamic diameters (nm) and z-potential values of the three CeO2 NPs in milliQ water, tap water and NaCl water

Type of tested water	Sample	Dynamic light scattering			ζ potential (mV)
		d_h (nm, intensities)	Vol %	Numb. %	
MilliQ	Naked Ceria (1 mg/mL)	146 ± 15	78.3	100	+36.7 ± 2.3
		400 ± 75	21.7	0	
	CeO_2@Chitosan (1 mg/mL)	209 ± 46	100	100	+42.8 ± 3.2
	CeO_2@Alginate (1 mg/mL)	786 ± 115	79	2	-28 ± 2.2
		144 ± 14	21	98	
Tap water (San Benedetto®)	Naked Ceria (1 mg/mL)	973 ± 115	100	100	-12 ±2.8
	CeO_2@Chitosan (1 mg/mL)	506 ± 20	100	100	-2.7 ± 2.4
	CeO_2@Alginate (1 mg/mL)	210 ± 25	66	98	-17.0 ± 2.0
		790 ± 150	33	2	
NaCl water (northwest coast of Portugal)	Naked Ceria (0.1 mg/mL)	1590 ± 110	100	100	+ 2.8
	CeO_2@Chitosan (1 mg/mL)	780 ± 80	100	100	+ 20.2
	CeO_2@Alginate (0.05 mg/mL)	1857 ± 200	100	100	-18.2

In tap water, all the CeO_2 NPs exhibited increased aggregation and colloidal instability (see sizes in **Table 3**). In general, the increase of the ionic strength affects the diffused layer at the NP surface by reducing it, thus lowering the ζ -potential values and consequently enhancing aggregation. Moreover, in the case of Alginate, Ca^{2+} ions can heavily affect the aggregation crosslink of different chains since carboxylate groups effectively bind this cation. In this medium, the hydrodynamic diameter of naked Ceria resulted close to micron size, CeO_2@Chitosan formed aggregates of ~506 nm, while CeO_2@Alginate copiously precipitated, leaving in suspension few smaller aggregates as 98% of the population showed a hydrodynamic diameter of ~210 nm. Also, NPs showed a consistent ζ -potential change in tap water (whose natural pH is 7.9). Naked Ceria acquired a negative surface charge (-12 mV), the CeO_2@Chitosan z-potential was approximately zero (-2.7 mV), while CeO_2@Alginate still showed a negative surface charge (-17.0 mV). All of these values were within the range of +20/-20 mV and very near zero, which explains the deterioration of the colloidal stability.

A much greater instability was finally observed in NaCl water media, where larger hydrodynamic diameters were observed for all NPs, again affecting the Alginate derivative more than the Chitosan derivative, with the following descending order: CeO_2@Alginate > naked Ceria > CeO_2@Chitosan. The Naked Ceria and CeO_2@Chitosan acquired a positive surface charge, while

the CeO_2@Alginate ζ -potential was still negative (-18.2 mV).

We also evaluated the sedimentation of the NPs by absorption UV-vis spectroscopy, following the decrease over time of the absorption band at ~300 nm in the ceria matrix. Due to the high sensitivity of this spectroscopic technique, these measurements were carried out at a concentration as low as 0.01 mg mL^{-1} to still detect the adsorption band of ceria while implementing similar concentration conditions used in the biological tests. In tap water and at this low concentration, the Ceria@Chitosan derivative was more stable and decreased slowly and almost linearly, and a similar profile was also observed for the naked Ceria (**Figure 8**). In contrast, the CeO_2@Alginate NPs were prone to aggregate and flocculate much faster, and in 50 min their concentration was halved (**Figure 8**).

The results showed that in tap water, the coating with Chitosan seemed to increase the dispersion and stability of CeO_2 NPs, while the coating with Alginate enhanced sedimentation, leaving smaller aggregates in the water column compared to those of the other NPs.

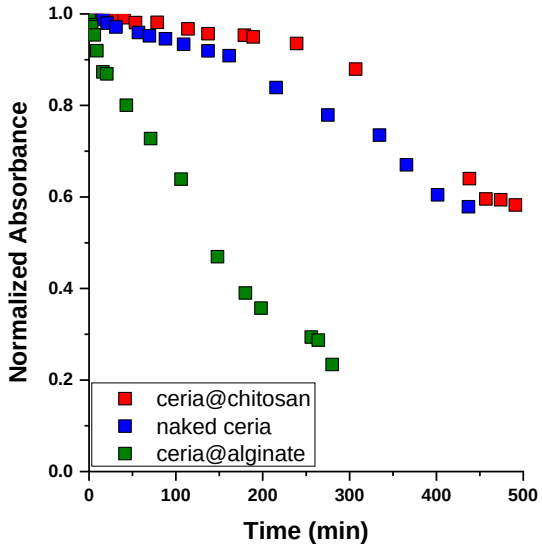

Figure. 8. Sedimentation test, followed by UVevis spectroscopy, of the three Ceria NP suspensions in tap water, monitored by the absorbance peak variation of the Ceria core (λ_{max} = 300-305 nm) over time.

A different trend was observed in salt water, where the very high ionic strength provokes substantial aggregation of all the NPs, in agreement with previous observations.[136,137] The most evident and fast aggregation was observed, once more, for Alginate derivative (hydrodynamic diameter of ~1860 nm, surface charge of-18 mV), followed by the Naked NPs (~1590 nm, ~ zero charge) and the Chitosan derivative (~780 nm, +20 mV) which, once more, resulted in the most stable among the three. Overall, the evidence underlined that the interaction with biomolecules influenced the fate of CeO_2 NPs, and this could reflect the bioavailability of the NPs to aquatic organisms.

2.2 Study of the interaction of Ceria nanoparticles and natural organic matter on *Aliivibrio fischeri* and *Daphnia magna*

Passing from the characterization of the material to the biological tests, the biologist involved in this collaboration observed the effects of Ceria NPs starting from the measurement of the bacteria inhibition. Here in the following are resumed the most important results that the biologists obtained using the Ceria NPs we prepared.

By measuring the bacteria luminescence activity (Microtox bioassay), they conclude that no significant effect was observed on luminescence activity measured on bacterium *A. fischeri*. as the percentage of inhibition was always maintained below 20% in bacteria exposed to all CeO_2 NPs **(Figure. 9).** The absence of toxic effects observed in the study could therefore be related to the lower concentrations of CeO_2 NPs tested in the short exposure time (1.0 mg/L), compared to the studied inhibition in higher concentration as 5.0-70 mg/L.[85,138]

Effects on *D. magna* did not induce significant acute toxic effects as immobilization/mortality was below 10% in all replicates. In order to assess whether the different coating may interfere with cellular pathways, the activity of enzymes involved in the antioxidant response machinery was investigated. They observed (**Figure 10**) an increase in the reactive oxygen species (ROS) levels paralleled the induced Glutathione-S-transferase (GST) activity. For that, CeO_2@Alginate NP triggers oxidative stress on *D. Magna*. On the contrary, CeO_2@Chitosan NPs induced hyperactivity behavior by increasing average speed and acceleration **(Figure 10**).

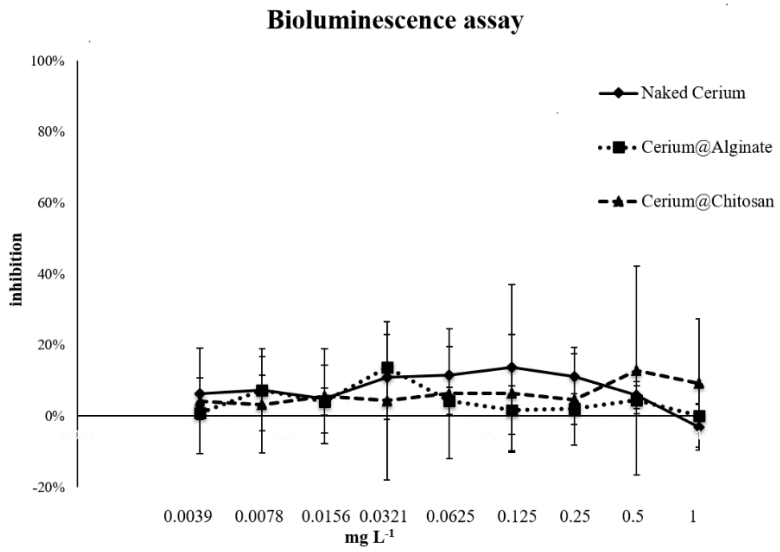

Figure 9. Concentration-response curve of the three CeO2 NPs tested with *Aliivibrio fischeri*.

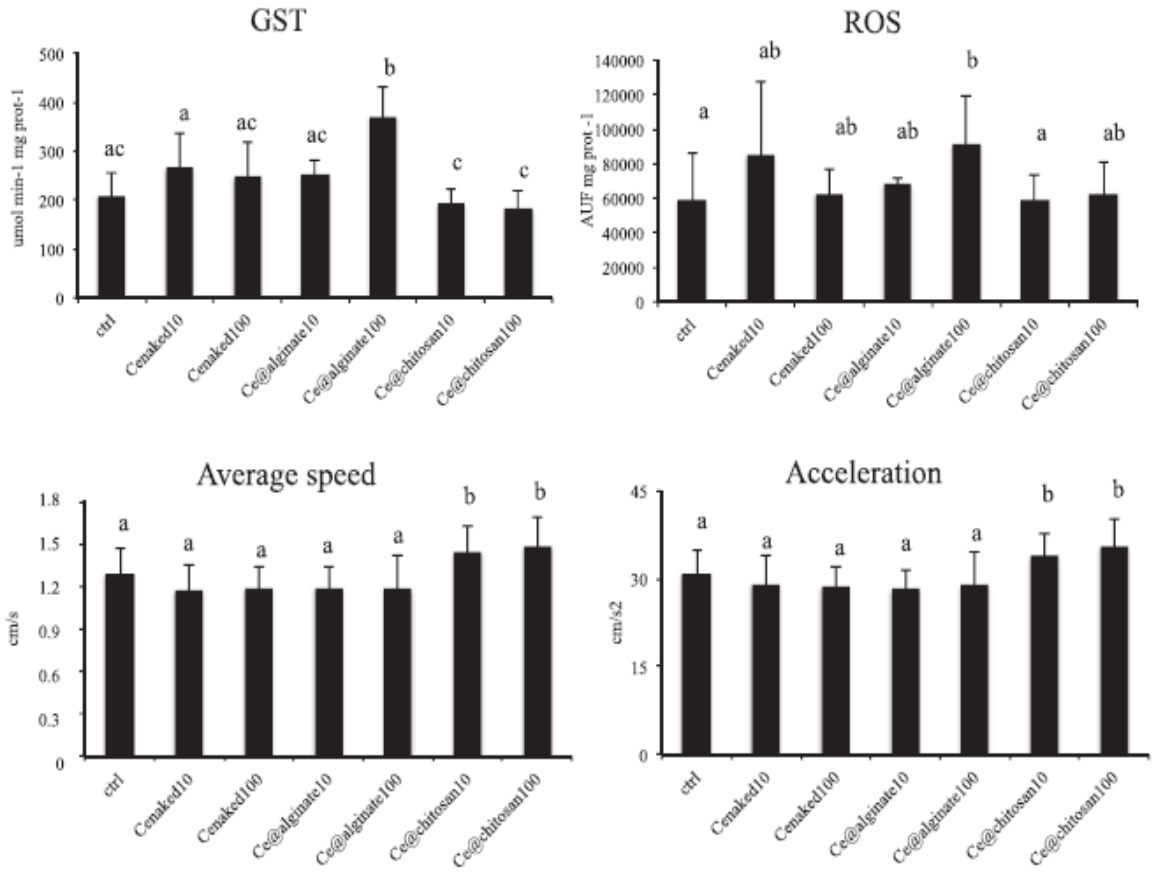

Figure. 10. Activity of GST, amount of ROS, Swimming activity and swimming velocity measured in D. magna exposed to the three CeO_2 NPs at 10 and 100 µg L^{-1} for 48 h. Data are expressed as Mean ± SD (N =5). Different letters indicate significantly different values $p < 0.05$.

2.3 Study of the interaction of Ceria nanoparticles and mercury on *Mytilus galloprovincialis* at different temperatures

2.3.1 Mercury and cerium quantification in seawater and mussels' soft tissues

Concerning the Hg concentration in water, no differences were observed between Hg levels measured in the aquaria contaminated with the metal alone with compared to Hg + CeO_2 NPs at 17 °C and 22. °C **(Table 4).** The measurement of Ce levels in water confirmed fast sedimentation of the NPs since no differences were observed between the concentration of the CTL and the NP contaminated waters at both temperatures.

However, given the low concentration of NPs used in this study, this data should be considered with caution.

The amount of Hg in soft tissue confirmed the uptake and bioaccumulation of the metal by mussels **(Table 5)**. The concentration of Hg was significantly higher in the group exposed to Hg

alone and combined with CeO_2 NPs than to CTL, both at 17 and 22 °C. The co-exposure to Hg and CeO_2 NPs did not affect metal accumulation at 17 °C, while a slight increase of metal content was observed in mussels exposed to Hg + CeO_2 NPs at 22 °C compared to the exposure to the metal alone as well as to the metal NPs combination at 17 °C. The tissue level of Ce did not show any significant differences among exposure conditions.

Table 4. Hg and CeO_2 NPs concentrations in exposure water (µg/L) expressed as mean ± standard deviation. **< lod** means below the detection limit.

Conditions	Hg µg/L		Ce µg/L	
	17 °C	*22 °C*	*17 °C*	*22 °C*
CTL	1.14 ± 0.20	1.5 ± 0.1	0.15 ± 0.21	0.156 ± 0.21
CeO_2 NPs	-	-	0.008 ± 0.02	0.01 ± 0.04
Hg	4.12 ± 0.51	2.1 ± 0.4	< lod	< lod
Hg + CeO_2 NPs	2.95 ± 1.38	4.6 ± 1.4	< lod	< lod

Table 5. Hg and Ce concentrations (µg/g) in M. galloprovincialis exposed to CTL, Hg and CeO_2 NPs individually and in combination (mean ± standard deviation). Different letter means statistically difference ($p < 0.05$).

Conditions	Hg µg/g		Ce µg/g	
	17 °C	*22 °C*	*17 °C*	*22 °C*
CTL	0.15 ± 0.01	0.13 ± 0.01	0.28 ± 0.09	0.32 ± 0.12
Ce NPs	-	-	0.43 ± 0.12	0.24 ± 0.03
Hg	4.93 ± 1.11	4.44 ± 0.95	-	-
Hg + Ce NPs	4.98 ± 1.39	7.66 ± 1.37	0.30 ± 0.18	0.34 ± 0.15

2.3.2 Effect of interaction of Ceria nanoparticles with mercury interaction at different temperature

The observed decrease of Hg toxicity in the presence of CeO_2 NPs could be due to the adsorption of the metal on NPs that undergoing fast agglomeration and sedimentation might reduce the bioavailability for the organisms. Indeed, some studies reported the ability of Cerium-based nanomaterials to adsorb other metals such as As and Cr.[117,139] As an example of successful use for the removal of Hg from water medium, a nano ceria-impregnated silica–iron oxide material[139] and a composite of ceria–zirconia–titania for the removal of metallic Hg exploiting a catalytic oxidation method.[140] To test this hypothesis, the influence of nano ceria on Hg bioavailability and bioaccumulation was assessed. Results showed that the Hg levels were only slightly reduced in water in the presence of Ce NPs and the bioaccumulation was similar in the organisms exposed to the metal alone and in combination with NPs **(Table 4 and 5)**. Therefore, a physico-chemical interaction in water medium is unlikely to occur, but rather an antagonistic effect could take place on biological target inside the organism, potentially affecting the metabolism of the metal. In support to this hypothesis, the marked differences between Hg alone and Hg + NPs were observed on GSH and enzymes involved in its pathway, such as GR and GSTs **(Figure. 11A-C**). Due to the crucial role of GSH in Hg detoxification, it is possible that the combination with Ce NPs allows Hg to bypass the GSH response mechanism. Nevertheless, this hypothesis needs further confirmations. The presence of the NPs could also alter the biodistribution of the metal in the

organism. In particular, biodistribution is essential for determining the adverse effects triggered by pollutants, as different compartments in the organism could show different sensitivity to contaminants. For instance, TiO_2 NPs not only adsorbed and enhanced the accumulation of As in *Artemia salina*, but also modified the subcellular allocation of As in the organism.[18]

The effects caused by temperature increase override those caused by pollutants (both acting individually or in combination). Indeed, control organisms showed a significant loss of metabolic performance, shifting from 17 °C to 22 °C. As a consequence of this metabolic depression also the activity of antioxidant capacity was lowered. Similarly to the present study,[124] exposed *M. galloprovincialis* to Hg under warming conditions (21 °C) and detected a limited capacity to activate the antioxidant defenses due to the reduced metabolic capacity. Also, the study by Coppola et al.[127] showed that the rise of temperature from 17 °C to 22 °C reduced the ETS **(Figure 11D**). activity preventing the bioaccumulation of Hg in *M. galloprovincialis*. In line with the present results, those authors pointed out that the adverse outcomes induced by temperature overcame the metal effects. Moreover, Andrade et al.[129] evidenced that the exposure of M. galloprovincialis to tidal regime and to an increased temperature (21 °C) resulted in lower metabolic capacity. This may be due to a closure of the valves and metabolic depression put in place as the organism defense response under heat stress. An increase of the frequency and duration of valve closure in response to thermal stress was already documented in the freshwater mussel Unio tumidus.[141] A similar behavior was observed also in M. galloprovincialis, which under heat stress exhibited valve closure and metabolic depression.[142]

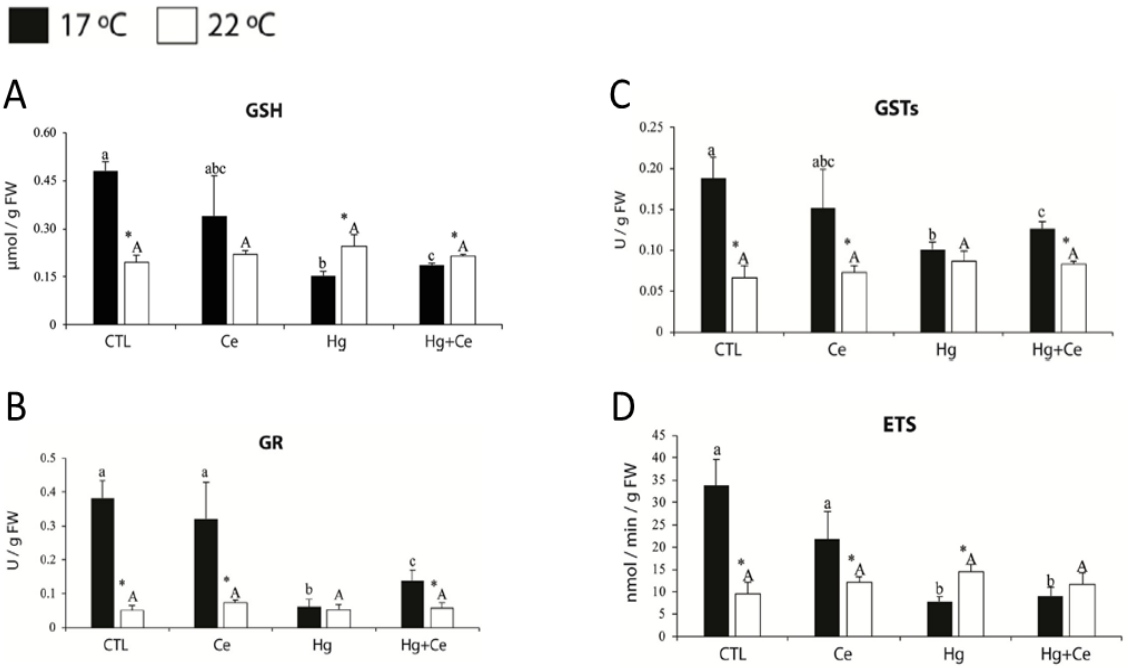

Figure. 11. A: Glutathione (GSH) content; B: Glutathione reductase (GR) activity;C: Glutathione S-transferases (GSTs) activity and D: Electron transport system (ETS) activity; (mean +standard deviation) (n =9), in M. galloprovincialis exposed to CTL, as well as Ce NPs and Hg individually and in combination. Significant differences ($p < 0.05$) among exposure conditions were represented with different lowercase letters for groups exposed at 17 °C and uppercase letters for groups exposed at 22 °C. Besides, an asterisk represents significant differences between groups exposed to different temperatures (17 °C and 22 °C).

3 Conclusion

Our study highlighted that the fate CeO_2 NPs in water is highly dependent from the characteristics of the receiving water bodies (e.g. pH, ionic strength), by inducing changes on the ζ-potential. These changes influence the processes of aggregation/agglomeration, sedimentation and dissolution of the different forms of CeO_2 NPs. All CeO_2 NPs, at the tested concentrations, showed no acute effects (neither photoinhibition in *A. fischeri* nor mortality in *D. magna*) were observed on the tested organisms.

Also the present study represents the first attempt to assess the combined effects of CeO_2 NPs and Hg using on valuable marine species such as *M. galloprovincialis*. Furthermore, the potential influence of sea warming on this interaction was evaluated. The CeO_2 NPs did not affect significantly the mussel metabolic metabolism and oxidative status. On the contrary, Hg induced a general metabolic depression and inhibition of antioxidant enzymes in organisms. A slight antagonistic effect of the two pollutants was observed, even if the effects of the metal prevailed on the NPs. The present results highlighted also that warming conditions do affect metabolic performance and reduce neurological functions of mussels. These effects might lead to negative repercussion on key physiological functions such as feeding, growth and reproduction, ultimately affecting mussel population health.

4 Experimental

4.1 Material and instruments

Cerium(III) nitrate hexahydrate 99%, Alginic acid sodium salt from brown algae, Chitosan, Acetic acid 99% (Sigma Aldrich), HCl 30% (Merck Germany), Ammonia 28% (Prolabo) were all used as received without further purification. Ultrapure milli-Q water (Millipore, resistivity=18M Ω cm−2) was used for the preparation of the aqueous solutions.

The morphology of the CeO_2 NPs was observed with Zeiss LEO 912 ab Energy Filtering TEM operating at 100 kV using a CCD-BM/ 1 K system. TEM samples were prepared by depositing a drop of diluted aqueous ceria suspensions on a carbon-coated copper grid (CF300-Cu), allowing the contact for 15 min and then carefully removing the drop from the surface grid, and allowing it to dry at room temperature overnight.

Hydrodynamic size and ζ-potential were carried out on a Zetasizer nano ZS instrument (Malvern) equipped with a 633 nm solid state He–Ne laser at a scattering angle of 173°, operating at 25 °C. The size and charge analyses were averaged from at least three repeated measurements.
Typically, dissolving samples at a concentration of $1 mg mL^{-1}$ or less in dependence on the conductivity of the solution and/or the scattering power. The size and charge analyses were averaged from at least three repeated measurements.

The stability over time of the colloidal suspensions was carried out by acquiring UV-vis absorption spectra on an Agilent model 8543 spectrophotometer at room temperature and using standard quartz cells with a 1.0 cm path length.

Thermogravimetric analysis (TGA) was carried out using a Mettler-Toledo thermogravimetric

balance (TGA/DSC 2 Star® System), analysing ~ 10-15 mg of lyophilized samples operating in air and spanning in the temperature range of 50-800 °C with a heating rate of 5 °C min^{-1}.
Infrared spectra were acquired for lyophilized samples on a PerkinElmer Frontier spectrometer equipped with an ATR accessory with a diamond/ZnSe crystal.

4.2 Nanoparticle synthesis

4.2.1 Ceria nanoparticle

The CeO_2 NPs (Naked Ceria) were prepared by modifying a literature procedure[135] as follow:
A cerium(III) nitrate aqueous solution (200 mL, 0.1 M) was added to 1 L of 3 M ammonia under continuous magnetic stirring at room temperature. The obtained violet precipitate was allowed to age for 12 h, until a colour change from violet to light yellow was observed. The aged precipitate was separated from the supernatant, then added with 300 mL milliQ water and the suspension bubbled with a N_2 flux for 30 min to remove the excess ammonia. The precipitate was left to settle down and the supernatant removed. The last bubbling and washing steps were repeated 3 times. The so obtained NPs were finally re-dispersed in 350 mL milliQ water adjusting the pH at 3 with a further addition of HCl to increase the long term stability in suspension and avoid an early aggregation, and storing the suspension at 4 °C. The final concentrations of ceria NPs (9.3 mg mL^{-1}) was determined on the basis of thermogravimetric analysis (TGA) carried out with a lyophilized sample of a known suspension volume.

4.2.2 Ceria chitosan[143,144]

The preparation of ceria-chitosan NPs (Ce@Chitosan) was carried out starting from freshly prepared naked CeO_2 NPs. An aliquot of ceria NPs colloid (53.8 mL containing 0.5 g CeO_2) was diluted at 500 mL with milliQ water. Then, a solution of chitosan (1.0 g dissolved in 400 mL of 1% (v/v) acetic acid) was added to CeO_2 NPs suspension under constant magnetic stirring at 80 °C, and kept in that condition overnight. The excess of chitosan, not interacting with ceria NPs, was removed by centrifugation (2935 rcf for 1 h, × 3 times). The Ce@Chitosan nanocomposite was finally re-dispersed in milliQ water. The portion of settled-down NPs were separated from stable suspended ones, and stored at 4 °C. The final concentrations of Ce@Chitosan NPs (13.0 mg mL^{-1}) was determined on the basis of thermogravimetric analysis (TGA) carried out with a lyophilized sample of a known suspension volume.

4.2.3 Ceria-Alginate

The preparation of Ce@Alginate nanocomposite, freshly prepared naked CeO_2 NPs (48.4 mL of colloid containing 0.45 g of CeO_2) were diluted to 450 mL with milliQ water. Then, a clear solution of sodium alginate (0.9 g in 400 mL 1% (v/v) acetic acid solution dissolved at 80 °C under sonication for 1 h) was added under magnetic stirring and at 80 °C, and kept in that condition overnight. The excess of sodium alginate was removed by repeated centrifugations (2935 rcf for 1 h, × 3 times). The CeO_2@alginate nanocomposite was finally re-dispersed in milliQ water and retained only the stable part of the so-obtained colloid and stored at 4 °C. The final concentrations of Ce@Alginate NPs (10.1mg mL^{-1}) was determined on the basis of thermogravimetric analysis (TGA) carried out with a lyophilized sample of a known suspension volume.

Experimental part of biology is reported in literature.[145–147]

5 Bibliography

(1) Aithal, P. S.; Aithal, S. A Review on Anticipated Breakthrough Technologies of 21st Century. *Int. J. Res. Dev. Technol. Manag. Sci.* **2015**, *21* (6).

(2) Kotagiri, N.; Sudlow, G. P.; Akers, W. J.; Achilefu, S. Breaking the Depth Dependency of Phototherapy with Cerenkov Radiation and Low-Radiance-Responsive Nanophotosensitizers. *Nat. Nanotechnol.* **2015**, *10* (4), 370–379. https://doi.org/10.1038/nnano.2015.17.

(3) Shehada, N.; Brönstrup, G.; Funka, K.; Christiansen, S.; Leja, M.; Haick, H. Ultrasensitive Silicon Nanowire for Real-World Gas Sensing: Noninvasive Diagnosis of Cancer from Breath Volatolome. *Nano Lett.* **2015**, *15* (2), 1288–1295. https://doi.org/10.1021/nl504482t.

(4) Piccinno, F.; Gottschalk, F.; Seeger, S.; Nowack, B. Industrial Production Quantities and Uses of Ten Engineered Nanomaterials in Europe and the World. *J. Nanoparticle Res.* **2012**, *14* (9), 1109. https://doi.org/10.1007/s11051-012-1109-9.

(5) Vance, M. E.; Kuiken, T.; Vejerano, E. P.; McGinnis, S. P.; Hochella Jr, M. F.; Rejeski, D.; Hull, M. S. Nanotechnology in the Real World: Redeveloping the Nanomaterial Consumer Products Inventory. *Beilstein J. Nanotechnol.* **2015**, *6* (1), 1769–1780.

(6) Selck, H.; Handy, R. D.; Fernandes, T. F.; Klaine, S. J.; Petersen, E. J. Nanomaterials in the Aquatic Environment: A European Union-United States Perspective on the Status of Ecotoxicity Testing, Research Priorities, and Challenges Ahead. *Environ. Toxicol. Chem.* **2016**, *35* (5), 1055–1067. https://doi.org/10.1002/etc.3385.

(7) Corsi, I.; Cherr, G. N.; Lenihan, H. S.; Labille, J.; Hassellov, M.; Canesi, L.; Dondero, F.; Frenzilli, G.; Hristozov, D.; Puntes, V.; Della Torre, C.; Pinsino, A.; Libralato, G.; Marcomini, A.; Sabbioni, E.; Matranga, V. Common Strategies and Technologies for the Ecosafety Assessment and Design of Nanomaterials Entering the Marine Environment. *ACS Nano* **2014**, *8* (10), 9694–9709. https://doi.org/10.1021/nn504684k.

(8) Klaine, S. J.; Koelmans, A. A.; Horne, N.; Carley, S.; Handy, R. D.; Kapustka, L.; Nowack, B.; von der Kammer, F. Paradigms to Assess the Environmental Impact of Manufactured Nanomaterials. *Environ. Toxicol. Chem.* **2012**, *31* (1), 3–14.

(9) Klaine, S. J.; Alvarez, P. J. J.; Batley, G. E.; Fernandes, T. F.; Handy, R. D.; Lyon, D. Y.; Mahendra, S.; McLaughlin, M. J.; Lead, J. R. Nanomaterials in the Environment: Behavior, Fate, Bioavailability, and Effects. *Environ. Toxicol. Chem.* **2008**, *27* (9), 1825–1851. https://doi.org/https://doi.org/10.1897/08-090.1.

(10) Giese, B.; Klaessig, F.; Park, B.; Kaegi, R.; Steinfeldt, M.; Wigger, H.; von Gleich, A.; Gottschalk, F. Risks, Release and Concentrations of Engineered Nanomaterial in the Environment. *Sci. Rep.* **2018**, *8* (1), 1–18.

(11) Gottschalk, F.; Sun, T.; Nowack, B. Environmental Concentrations of Engineered Nanomaterials: Review of Modeling and Analytical Studies. *Environ. Pollut.* **2013**, *181*, 287–300. https://doi.org/https://doi.org/10.1016/j.envpol.2013.06.003.

(12) Zhang, J.; Guo, W.; Li, Q.; Wang, Z.; Liu, S. The Effects and the Potential Mechanism of Environmental Transformation of Metal Nanoparticles on Their Toxicity in Organisms. *Environ. Sci. Nano* **2018**, *5* (11), 2482–2499. https://doi.org/10.1039/C8EN00688A.

(13) Surette, M. C.; Nason, J. A. Nanoparticle Aggregation in a Freshwater River: The Role of Engineered Surface Coatings. *Environ. Sci. Nano* **2019**, *6* (2), 540–553. https://doi.org/10.1039/C8EN01021H.

(14) Canesi, L.; Corsi, I. Effects of Nanomaterials on Marine Invertebrates. *Sci. Total Environ.* **2016**, *565*, 933–940. https://doi.org/https://doi.org/10.1016/j.scitotenv.2016.01.085.

(15) Navarro, E.; Baun, A.; Behra, R.; Hartmann, N. B.; Filser, J.; Miao, A.-J.; Quigg, A.; Santschi, P. H.; Sigg, L. Environmental Behavior and Ecotoxicity of Engineered Nanoparticles to Algae, Plants, and Fungi. *Ecotoxicology* **2008**, *17* (5), 372–386. https://doi.org/10.1007/s10646-008-0214-0.

(16) Canesi, L.; Ciacci, C.; Balbi, T. Interactive Effects of Nanoparticles with Other Contaminants in Aquatic Organisms: Friend or Foe? *Mar. Environ. Res.* **2015**, *111*, 128–134. https://doi.org/https://doi.org/10.1016/j.marenvres.2015.03.010.

(17) Amde, M.; Liu, J.; Tan, Z.-Q.; Bekana, D. Transformation and Bioavailability of Metal Oxide Nanoparticles in Aquatic and Terrestrial Environments. A Review. *Environ. Pollut.* **2017**, *230*, 250–267. https://doi.org/https://doi.org/10.1016/j.envpol.2017.06.064.

(18) Liu, Y.; Nie, Y.; Wang, J.; Wang, J.; Wang, X.; Chen, S.; Zhao, G.; Wu, L.; Xu, A. Mechanisms Involved in the Impact of Engineered Nanomaterials on the Joint Toxicity with Environmental Pollutants. *Ecotoxicol. Environ. Saf.* **2018**, *162*, 92–102. https://doi.org/https://doi.org/10.1016/j.ecoenv.2018.06.079.

(19) Naasz, S.; Altenburger, R.; Kühnel, D. Environmental Mixtures of Nanomaterials and Chemicals: The Trojan-Horse Phenomenon and Its Relevance for Ecotoxicity. *Sci. Total Environ.* **2018**, *635*, 1170–1181. https://doi.org/https://doi.org/10.1016/j.scitotenv.2018.04.180.

(20) Lundqvist, M.; Stigler, J.; Elia, G.; Lynch, I.; Cedervall, T.; Dawson, K. A. Nanoparticle Size and Surface Properties Determine the Protein Corona with Possible Implications for Biological Impacts. *Proc. Natl. Acad. Sci.* **2008**, *105* (38), 14265 LP – 14270. https://doi.org/10.1073/pnas.0805135105.

(21) Qiu, Y.; Liu, Y.; Wang, L.; Xu, L.; Bai, R.; Ji, Y.; Wu, X.; Zhao, Y.; Li, Y.; Chen, C. Surface Chemistry and Aspect Ratio Mediated Cellular Uptake of Au Nanorods. *Biomaterials* **2010**, *31* (30), 7606–7619. https://doi.org/https://doi.org/10.1016/j.biomaterials.2010.06.051.

(22) Hajipour, M. J.; Laurent, S.; Aghaie, A.; Rezaee, F.; Mahmoudi, M. Personalized Protein Coronas: A "Key" Factor at the Nanobiointerface. *Biomater. Sci.* **2014**, *2* (9), 1210–1221. https://doi.org/10.1039/C4BM00131A.

(23) Mahmoudi, M.; Abdelmonem, A. M.; Behzadi, S.; Clement, J. H.; Dutz, S.; Ejtehadi, M. R.; Hartmann, R.; Kantner, K.; Linne, U.; Maffre, P.; Metzler, S.; Moghadam, M. K.; Pfeiffer, C.; Rezaei, M.; Ruiz-Lozano, P.; Serpooshan, V.; Shokrgozar, M. A.; Nienhaus, G. U.; Parak, W. J. Temperature: The "Ignored" Factor at the NanoBio Interface. *ACS Nano* **2013**, *7* (8), 6555–6562. https://doi.org/10.1021/nn305337c.

(24) Pozzi, D.; Caracciolo, G.; Capriotti, A. L.; Cavaliere, C.; La Barbera, G.; Anchordoquy, T. J.; Laganà, A. Surface Chemistry and Serum Type Both Determine the Nanoparticle-Protein Corona. *J. Proteomics* **2015**, *119*, 209–217. https://doi.org/10.1016/j.jprot.2015.02.009.

(25) Tenzer, S.; Docter, D.; Kuharev, J.; Musyanovych, A.; Fetz, V.; Hecht, R.; Schlenk, F.; Fischer, D.; Kiouptsi, K.; Reinhardt, C.; Landfester, K.; Schild, H.; Maskos, M.; Knauer, S. K.; Stauber, R. H. Rapid Formation of Plasma Protein Corona Critically Affects Nanoparticle Pathophysiology. *Nat. Nanotechnol.* **2013**, *8* (10), 772–781. https://doi.org/10.1038/nnano.2013.181.

(26) Sharma, V. K.; Filip, J.; Zboril, R.; Varma, R. S. Natural Inorganic Nanoparticles-Formation, Fate, and Toxicity in the Environment. *Chem. Soc. Rev.* **2015**, *44* (23), 8410–8423. https://doi.org/10.1039/c5cs00236b.

(27) Huber, R.; Stoll, S. Protein Affinity for TiO2 and CeO2 Manufactured Nanoparticles. From Ultra-Pure Water to Biological Media. *Colloids Surfaces A Physicochem. Eng. Asp.* **2018**, *553* (April), 425–431. https://doi.org/10.1016/j.colsurfa.2018.05.091.

(28) Quik, J.; Stuart, M.; Wouterse, M.; Peijnenburg, W.; Hendriks, J.; Van de meent, D. Natural Colloids Are the Dominant Factor in the Sedimentation of Nanoparticles. *Environ. Toxicol. Chem.* **2012**, *31*, 1019–1022. https://doi.org/10.1002/etc.1783.

(29) Sani-Kast, N.; Labille, J.; Ollivier, P.; Slomberg, D.; Hungerbühler, K.; Scheringer, M. A Network Perspective Reveals Decreasing Material Diversity in Studies on Nanoparticle Interactions with Dissolved Organic Matter. *Proc. Natl. Acad. Sci.* **2017**, *114* (10), E1756–E1765.

(30) Baker, T. J.; Tyler, C. R.; Galloway, T. S. Impacts of Metal and Metal Oxide Nanoparticles on Marine Organisms. *Environ. Pollut.* **2014**, *186*, 257–271. https://doi.org/https://doi.org/10.1016/j.envpol.2013.11.014.

(31) Lawrence, J. R.; Swerhone, G. D. W.; Dynes, J. J.; Hitchcock, A. P.; Korber, D. R. Complex Organic Corona Formation on Carbon Nanotubes Reduces Microbial Toxicity by Suppressing Reactive Oxygen Species Production. *Environ. Sci. Nano* **2016**, *3* (1), 181–189.

https://doi.org/10.1039/C5EN00229J.
(32) De Marchi, L.; Coppola, F.; Soares, A. M. V. M.; Pretti, C.; Monserrat, J. M.; Torre, C. della; Freitas, R. Engineered Nanomaterials: From Their Properties and Applications, to Their Toxicity towards Marine Bivalves in a Changing Environment. *Environ. Res.* **2019**, *178*, 108683. https://doi.org/https://doi.org/10.1016/j.envres.2019.108683.
(33) Ren, C.; Hu, X.; Zhou, Q. Influence of Environmental Factors on Nanotoxicity and Knowledge Gaps Thereof. *NanoImpact* **2016**, *2*, 82–92. https://doi.org/https://doi.org/10.1016/j.impact.2016.07.002.
(34) Wang, Z.; Zhang, L.; Zhao, J.; Xing, B. Environmental Processes and Toxicity of Metallic Nanoparticles in Aquatic Systems as Affected by Natural Organic Matter. *Environ. Sci. Nano* **2016**, *3* (2), 240–255. https://doi.org/10.1039/C5EN00230C.
(35) Baalousha, M. Effect of Nanomaterial and Media Physicochemical Properties on Nanomaterial Aggregation Kinetics. *NanoImpact* **2017**, *6*, 55–68. https://doi.org/https://doi.org/10.1016/j.impact.2016.10.005.
(36) Yu, S.; Liu, J.; Yin, Y.; Shen, M. Interactions between Engineered Nanoparticles and Dissolved Organic Matter: A Review on Mechanisms and Environmental Effects. *J. Environ. Sci.* **2018**, *63*, 198–217. https://doi.org/https://doi.org/10.1016/j.jes.2017.06.021.
(37) Ma, C.; White, J. C.; Dhankher, O. P.; Xing, B. Metal-Based Nanotoxicity and Detoxification Pathways in Higher Plants. *Environ. Sci. Technol.* **2015**, *49* (12), 7109–7122. https://doi.org/10.1021/acs.est.5b00685.
(38) Cui, D.; Zhang, P.; Ma, Y.; He, X.; Li, Y.; Zhang, J.; Zhao, Y.; Zhang, Z. Effect of Cerium Oxide Nanoparticles on Asparagus Lettuce Cultured in an Agar Medium. *Environ. Sci. Nano* **2014**, *1* (5), 459–465. https://doi.org/10.1039/C4EN00025K.
(39) Maria Magdalane, C.; Kaviyarasu, K.; Matinise, N.; Mayedwa, N.; Mongwaketsi, N.; Letsholathebe, D.; Mola, G. T.; AbdullahAl-Dhabi, N.; Arasu, M. V.; Henini, M.; Kennedy, J.; Maaza, M.; Jeyaraj, B. Evaluation on La2O3 Garlanded Ceria Heterostructured Binary Metal Oxide Nanoplates for UV/ Visible Light Induced Removal of Organic Dye from Urban Wastewater. *South African J. Chem. Eng.* **2018**, *26*, 49–60. https://doi.org/https://doi.org/10.1016/j.sajce.2018.09.003.
(40) Laga, S. M.; Townsend, T. M.; O'Connor, A. R.; Mayer, J. M. Cooperation of Cerium Oxide Nanoparticles and Soluble Molecular Catalysts for Alcohol Oxidation. *Inorg. Chem. Front.* **2020**, *7* (6), 1386–1393. https://doi.org/10.1039/C9QI01640F.
(41) Dvořák, F.; Szabová, L.; Johánek, V.; Farnesi Camellone, M.; Stetsovych, V.; Vorokhta, M.; Tovt, A.; Skála, T.; Matolínová, I.; Tateyama, Y.; Mysliveček, J.; Fabris, S.; Matolín, V. Bulk Hydroxylation and Effective Water Splitting by Highly Reduced Cerium Oxide: The Role of O Vacancy Coordination. *ACS Catal.* **2018**, *8* (5), 4354–4363. https://doi.org/10.1021/acscatal.7b04409.
(42) Fisher, T. J.; Zhou, Y.; Wu, T.-S.; Wang, M.; Soo, Y.-L.; Cheung, C. L. Structure–Activity Relationship of Nanostructured Ceria for the Catalytic Generation of Hydroxyl Radicals. *Nanoscale* **2019**, *11* (10), 4552–4561. https://doi.org/10.1039/C8NR09393H.
(43) Gottschalk, F.; Lassen, C.; Kjoelholt, J.; Christensen, F.; Nowack, B. Modeling Flows and Concentrations of Nine Engineered Nanomaterials in the Danish Environment. *Int. J. Environ. Res. Public Health* **2015**, *12* (5), 5581–5602.
(44) Johnson, A. C.; Park, B. Predicting Contamination by the Fuel Additive Cerium Oxide Engineered Nanoparticles within the United Kingdom and the Associated Risks. *Environ. Toxicol. Chem.* **2012**, *31* (11), 2582–2587.
(45) Sun, T. Y.; Gottschalk, F.; Hungerbühler, K.; Nowack, B. Comprehensive Probabilistic Modelling of Environmental Emissions of Engineered Nanomaterials. *Environ. Pollut.* **2014**, *185*, 69–76.
(46) O'Brien, N.; Cummins, E. Ranking Initial Environmental and Human Health Risk Resulting from Environmentally Relevant Nanomaterials. *J. Environ. Sci. Heal. Part A* **2010**, *45* (8), 992–1007.
(47) O'Brien, N. J.; Cummins, E. J. A Risk Assessment Framework for Assessing Metallic Nanomaterials of Environmental Concern: Aquatic Exposure and Behavior. *Risk Anal. An Int. J.* **2011**, *31* (5), 706–726.
(48) Keller, A. A.; Lazareva, A. Predicted Releases of Engineered Nanomaterials: From Global to Regional to Local. *Environ. Sci. Technol. Lett.* **2014**, *1* (1), 65–70.

https://doi.org/10.1021/ez400106t.
(49) Nanda, H. S. Preparation and Biocompatible Surface Modification of Redox Altered Cerium Oxide Nanoparticle Promising for Nanobiology and Medicine. *Bioeng. (Basel, Switzerland)* **2016**, *3* (4), 28. https://doi.org/10.3390/bioengineering3040028.
(50) Nethi, S. K.; Nanda, H. S.; Steele, T. W. J.; Patra, C. R. Functionalized Nanoceria Exhibit Improved Angiogenic Properties. *J. Mater. Chem. B* **2017**, *5* (47), 9371–9383. https://doi.org/10.1039/C7TB01957B.
(51) Chen, P.-L.; Chen, I.-W. Reactive Cerium(IV) Oxide Powders by the Homogeneous Precipitation Method. *J. Am. Ceram. Soc.* **1993**, *76* (6), 1577–1583. https://doi.org/https://doi.org/10.1111/j.1151-2916.1993.tb03942.x.
(52) Chen, H.-I.; Chang, H.-Y. Synthesis of Nanocrystalline Cerium Oxide Particles by the Precipitation Method. *Ceram. Int.* **2005**, *31* (6), 795–802. https://doi.org/https://doi.org/10.1016/j.ceramint.2004.09.006.
(53) Ramachandran, M.; Subadevi, R.; Sivakumar, M. Role of PH on Synthesis and Characterization of Cerium Oxide (CeO2) Nano Particles by Modified Co-Precipitation Method. *Vacuum* **2019**, *161*, 220–224. https://doi.org/https://doi.org/10.1016/j.vacuum.2018.12.002.
(54) Corsi, F.; Caputo, F.; Traversa, E.; Ghibelli, L. Not Only Redox: The Multifaceted Activity of Cerium Oxide Nanoparticles in Cancer Prevention and Therapy . *Frontiers in Oncology* . 2018, p 309.
(55) Mandoli, C.; Pagliari, F.; Pagliari, S.; Forte, G.; Di Nardo, P.; Licoccia, S.; Traversa, E. Stem Cell Aligned Growth Induced by CeO2 Nanoparticles in PLGA Scaffolds with Improved Bioactivity for Regenerative Medicine. *Adv. Funct. Mater.* **2010**, *20* (10), 1617–1624. https://doi.org/https://doi.org/10.1002/adfm.200902363.
(56) Trenque, I.; Magnano, G. C.; Bolzinger, M. A.; Roiban, L.; Chaput, F.; Pitault, I.; Briançon, S.; Devers, T.; Masenelli-Varlot, K.; Bugnet, M.; Amans, D. Shape-Selective Synthesis of Nanoceria for Degradation of Paraoxon as a Chemical Warfare Simulant. *Phys. Chem. Chem. Phys.* **2019**, *21* (10), 5455–5465. https://doi.org/10.1039/C9CP00179D.
(57) Zhang, Y.; Wu, X.; Hou, C.; Shang, K.; Yang, K.; Tian, Z.; Pei, Z.; Qu, Y.; Pei, Y. Dual-Responsive Dithio-Polydopamine Coated Porous CeO(2) Nanorods for Targeted and Synergistic Drug Delivery. *Int. J. Nanomedicine* **2018**, *13*, 2161–2173. https://doi.org/10.2147/IJN.S152002.
(58) Singh, S.; Ly, A.; Das, S.; Sakthivel, T. S.; Barkam, S.; Seal, S. Cerium Oxide Nanoparticles at the Nano-Bio Interface: Size-Dependent Cellular Uptake. *Artif. Cells, Nanomedicine, Biotechnol.* **2018**, *46* (sup3), S956–S963. https://doi.org/10.1080/21691401.2018.1521818.
(59) Mai, H.-X.; Sun, L.-D.; Zhang, Y.-W.; Si, R.; Feng, W.; Zhang, H.-P.; Liu, H.-C.; Yan, C.-H. Shape-Selective Synthesis and Oxygen Storage Behavior of Ceria Nanopolyhedra, Nanorods, and Nanocubes. *J. Phys. Chem. B* **2005**, *109* (51), 24380–24385. https://doi.org/10.1021/jp055584b.
(60) Dhall, A.; Self, W. Cerium Oxide Nanoparticles: A Brief Review of Their Synthesis Methods and Biomedical Applications. *Antioxidants* . 2018. https://doi.org/10.3390/antiox7080097.
(61) Kannan, S. K.; Sundrarajan, M. A Green Approach for the Synthesis of a Cerium Oxide Nanoparticle: Characterization and Antibacterial Activity. *Int. J. Nanosci.* **2014**, *13* (03), 1450018. https://doi.org/10.1142/S0219581X14500185.
(62) Cao, C.-Y.; Cui, Z.-M.; Chen, C.-Q.; Song, W.-G.; Cai, W. Ceria Hollow Nanospheres Produced by a Template-Free Microwave-Assisted Hydrothermal Method for Heavy Metal Ion Removal and Catalysis. *J. Phys. Chem. C* **2010**, *114* (21), 9865–9870. https://doi.org/10.1021/jp101553x.
(63) Kumar, A.; Kuang, Y.; Liang, Z.; Sun, X. Microwave Chemistry, Recent Advancements, and Eco-Friendly Microwave-Assisted Synthesis of Nanoarchitectures and Their Applications: A Review. *Mater. Today Nano* **2020**, *11*, 100076. https://doi.org/https://doi.org/10.1016/j.mtnano.2020.100076.
(64) Wang, H.; Zhu, J.-J.; Zhu, J.-M.; Liao, X.-H.; Xu, S.; Ding, T.; Chen, H.-Y. Preparation of Nanocrystalline Ceria Particles by Sonochemical and Microwave Assisted Heating Methods. *Phys. Chem. Chem. Phys.* **2002**, *4* (15), 3794–3799. https://doi.org/10.1039/B201394K.
(65) Gao, F.; Lu, Q.; Komarneni, S. Fast Synthesis of Cerium Oxide Nanoparticles and Nanorods. *J. Nanosci. Nanotechnol.* **2006**, *6* (12), 3812–3819. https://doi.org/10.1166/jnn.2006.609.
(66) Tao, Y.; Gong, F. H.; Wang, H.; Wu, H. P.; Tao, G. L. Microwave-Assisted Preparation of Cerium

Dioxide Nanocubes. *Mater. Chem. Phys.* **2008**, *112* (3), 973–976. https://doi.org/https://doi.org/10.1016/j.matchemphys.2008.07.018.
(67) Shirke, B. S.; Patil, A. A.; Hankare, P. P.; Garadkar, K. M. Synthesis of Cerium Oxide Nanoparticles by Microwave Technique Using Propylene Glycol as a Stabilizing Agent. *J. Mater. Sci. Mater. Electron.* **2011**, *22* (2), 200–203. https://doi.org/10.1007/s10854-010-0114-y.
(68) Singh, R. N.; Awasthi, R. *New and Future Developments in Catalysis: Chapter 16. Alcohol Fuel Cells*; Elsevier Inc. Chapters, 2013.
(69) Malik, M. A.; Wani, M. Y.; Hashim, M. A. Microemulsion Method: A Novel Route to Synthesize Organic and Inorganic Nanomaterials: 1st Nano Update. *Arab. J. Chem.* **2012**, *5* (4), 397–417. https://doi.org/https://doi.org/10.1016/j.arabjc.2010.09.027.
(70) El Shaer, S. S.; Salaheldin, T. A.; Saied, N. M.; Abdelazim, S. M. In Vivo Ameliorative Effect of Cerium Oxide Nanoparticles in Isoproterenol-Induced Cardiac Toxicity. *Exp. Toxicol. Pathol.* **2017**, *69* (7), 435–441. https://doi.org/https://doi.org/10.1016/j.etp.2017.03.001.
(71) Patil, S.; Kuiry, S. C.; Seal, S.; Vanfleet, R. Synthesis of Nanocrystalline Ceria Particles for High Temperature Oxidation Resistant Coating. *J. Nanoparticle Res.* **2002**, *4* (5), 433–438. https://doi.org/10.1023/A:1021696107498.
(72) Das, M.; Patil, S.; Bhargava, N.; Kang, J.-F.; Riedel, L. M.; Seal, S.; Hickman, J. J. Auto-Catalytic Ceria Nanoparticles Offer Neuroprotection to Adult Rat Spinal Cord Neurons. *Biomaterials* **2007**, *28* (10), 1918–1925. https://doi.org/https://doi.org/10.1016/j.biomaterials.2006.11.036.
(73) Lee, J.-S.; Choi, S.-C. Crystallization Behavior of Nano-Ceria Powders by Hydrothermal Synthesis Using a Mixture of H2O2 and NH4OH. *Mater. Lett.* **2004**, *58* (3), 390–393. https://doi.org/https://doi.org/10.1016/S0167-577X(03)00508-1.
(74) Karakoti, A. S.; Kuchibhatla, S. V. N. T.; Babu, K. S.; Seal, S. Direct Synthesis of Nanoceria in Aqueous Polyhydroxyl Solutions. *J. Phys. Chem. C* **2007**, *111* (46), 17232–17240. https://doi.org/10.1021/jp076164k.
(75) Kamruddin, M.; Ajikumar, P. K.; Nithya, R.; Tyagi, A. K.; Raj, B. Synthesis of Nanocrystalline Ceria by Thermal Decomposition and Soft-Chemistry Methods. *Scr. Mater.* **2004**, *50* (4), 417–422. https://doi.org/https://doi.org/10.1016/j.scriptamat.2003.11.010.
(76) Perez, J. M.; Asati, A.; Nath, S.; Kaittanis, C. Synthesis of Biocompatible Dextran-Coated Nanoceria with PH-Dependent Antioxidant Properties. *Small* **2008**, *4* (5), 552–556. https://doi.org/https://doi.org/10.1002/smll.200700824.
(77) Yin, L.; Wang, Y.; Pang, G.; Koltypin, Y.; Gedanken, A. Sonochemical Synthesis of Cerium Oxide Nanoparticles—Effect of Additives and Quantum Size Effect. *J. Colloid Interface Sci.* **2002**, *246* (1), 78–84. https://doi.org/https://doi.org/10.1006/jcis.2001.8047.
(78) Dutta, D. P.; Manoj, N.; Tyagi, A. K. White Light Emission from Sonochemically Synthesized Rare Earth Doped Ceria Nanophosphors. *J. Lumin.* **2011**, *131* (8), 1807–1812. https://doi.org/https://doi.org/10.1016/j.jlumin.2011.04.017.
(79) Agawane, S. M.; Nagarkar, J. M. Nano Ceria Catalyzed Synthesis of α-Aminophosphonates under Ultrasonication. *Tetrahedron Lett.* **2011**, *52* (27), 3499–3504. https://doi.org/https://doi.org/10.1016/j.tetlet.2011.04.112.
(80) Yadav, T. P.; Srivastava, O. N. Synthesis of Nanocrystalline Cerium Oxide by High Energy Ball Milling. *Ceram. Int.* **2012**, *38* (7), 5783–5789. https://doi.org/https://doi.org/10.1016/j.ceramint.2012.04.025.
(81) Vassie, J. A.; Whitelock, J. M.; Lord, M. S. Targeted Delivery and Redox Activity of Folic Acid-Functionalized Nanoceria in Tumor Cells. *Mol. Pharm.* **2018**, *15* (3), 994–1004. https://doi.org/10.1021/acs.molpharmaceut.7b00920.
(82) Davoodbasha, M.; Park, B.-R.; Rhee, W.-J.; Lee, S.-Y.; Kim, J.-W. Antioxidant Potentials of Nanoceria Synthesized by Solution Plasma Process and Its Biocompatibility Study. *Arch. Biochem. Biophys.* **2018**, *645*, 42–49. https://doi.org/https://doi.org/10.1016/j.abb.2018.02.003.
(83) Sendra, M.; Volland, M.; Balbi, T.; Fabbri, R.; Yeste, M. P.; Gatica, J. M.; Canesi, L.; Blasco, J. Cytotoxicity of CeO2 Nanoparticles Using in Vitro Assay with Mytilus Galloprovincialis Hemocytes: Relevance of Zeta Potential, Shape and Biocorona Formation. *Aquat. Toxicol.* **2018**, *200*, 13–20. https://doi.org/https://doi.org/10.1016/j.aquatox.2018.04.011.

(84) Zhang, H.; He, X.; Zhang, Z.; Zhang, P.; Li, Y.; Ma, Y.; Kuang, Y.; Zhao, Y.; Chai, Z. Nano-CeO2 Exhibits Adverse Effects at Environmental Relevant Concentrations. *Environ. Sci. Technol.* **2011**, *45* (8), 3725–3730. https://doi.org/10.1021/es103309n.

(85) Rodea-Palomares, I.; Boltes, K.; Fernández-Pinas, F.; Leganés, F.; García-Calvo, E.; Santiago, J.; Rosal, R. Physicochemical Characterization and Ecotoxicological Assessment of CeO2 Nanoparticles Using Two Aquatic Microorganisms. *Toxicol. Sci.* **2011**, *119* (1), 135–145.

(86) Fairbairn, E. A.; Keller, A. A.; Mädler, L.; Zhou, D.; Pokhrel, S.; Cherr, G. N. Metal Oxide Nanomaterials in Seawater: Linking Physicochemical Characteristics with Biological Response in Sea Urchin Development. *J. Hazard. Mater.* **2011**, *192* (3), 1565–1571.

(87) Collin, B.; Auffan, M.; Johnson, A. C.; Kaur, I.; Keller, A. A.; Lazareva, A.; Lead, J. R.; Ma, X.; Merrifield, R. C.; Svendsen, C. Environmental Release, Fate and Ecotoxicological Effects of Manufactured Ceria Nanomaterials. *Environ. Sci. Nano* **2014**, *1* (6), 533–548.

(88) Bour, A.; Mouchet, F.; Verneuil, L.; Evariste, L.; Silvestre, J.; Pinelli, E.; Gauthier, L. Toxicity of CeO2 Nanoparticles at Different Trophic Levels – Effects on Diatoms, Chironomids and Amphibians. *Chemosphere* **2015**, *120*, 230–236. https://doi.org/https://doi.org/10.1016/j.chemosphere.2014.07.012.

(89) Callaghan, N. I.; MacCormack, T. J. Ecophysiological Perspectives on Engineered Nanomaterial Toxicity in Fish and Crustaceans. *Comp. Biochem. Physiol. Part C Toxicol. Pharmacol.* **2017**, *193*, 30–41. https://doi.org/https://doi.org/10.1016/j.cbpc.2016.12.007.

(90) Canesi, L.; Frenzilli, G.; Balbi, T.; Bernardeschi, M.; Ciacci, C.; Corsolini, S.; Della Torre, C.; Fabbri, R.; Faleri, C.; Focardi, S.; Guidi, P.; Kočan, A.; Marcomini, A.; Mariottini, M.; Nigro, M.; Pozo-Gallardo, K.; Rocco, L.; Scarcelli, V.; Smerilli, A.; Corsi, I. Interactive Effects of N-TiO2 and 2,3,7,8-TCDD on the Marine Bivalve Mytilus Galloprovincialis. *Aquat. Toxicol.* **2014**, *153*, 53–65. https://doi.org/https://doi.org/10.1016/j.aquatox.2013.11.002.

(91) García, A.; Delgado, L.; Torà, J. A.; Casals, E.; González, E.; Puntes, V.; Font, X.; Carrera, J.; Sánchez, A. Effect of Cerium Dioxide, Titanium Dioxide, Silver, and Gold Nanoparticles on the Activity of Microbial Communities Intended in Wastewater Treatment. *J. Hazard. Mater.* **2012**, *199–200*, 64–72. https://doi.org/https://doi.org/10.1016/j.jhazmat.2011.10.057.

(92) Koehle-Divo, V.; Cossu-Leguille, C.; Pain-Devin, S.; Simonin, C.; Bertrand, C.; Sohm, B.; Mouneyrac, C.; Devin, S.; Giambérini, L. Genotoxicity and Physiological Effects of CeO2 NPs on a Freshwater Bivalve (Corbicula Fluminea). *Aquat. Toxicol.* **2018**, *198*, 141–148.

(93) Garaud, M.; Trapp, J.; Devin, S.; Cossu-Leguille, C.; Pain-Devin, S.; Felten, V.; Giamberini, L. Multibiomarker Assessment of Cerium Dioxide Nanoparticle (NCeO2) Sublethal Effects on Two Freshwater Invertebrates, Dreissena Polymorpha and Gammarus Roeseli. *Aquat. Toxicol.* **2015**, *158*, 63–74. https://doi.org/https://doi.org/10.1016/j.aquatox.2014.11.004.

(94) Ciacci, C.; Canonico, B.; Bilaniĉovă, D.; Fabbri, R.; Cortese, K.; Gallo, G.; Marcomini, A.; Pojana, G.; Canesi, L. Immunomodulation by Different Types of N-Oxides in the Hemocytes of the Marine Bivalve Mytilus Galloprovincialis. *PLoS One* **2012**, *7* (5), e36937.

(95) Auguste, M.; Balbi, T.; Montagna, M.; Fabbri, R.; Sendra, M.; Blasco, J.; Canesi, L. In Vivo Immunomodulatory and Antioxidant Properties of Nanoceria (NCeO2) in the Marine Mussel Mytilus Galloprovincialis. *Comp. Biochem. Physiol. Part C Toxicol. Pharmacol.* **2019**, *219*, 95–102.

(96) Falugi, C.; Aluigi, M. G.; Chiantore, M. C.; Privitera, D.; Ramoino, P.; Gatti, M. A.; Fabrizi, A.; Pinsino, A.; Matranga, V. Toxicity of Metal Oxide Nanoparticles in Immune Cells of the Sea Urchin. *Mar. Environ. Res.* **2012**, *76*, 114–121.

(97) Artells, E.; Issartel, J.; Auffan, M.; Borschneck, D.; Thill, A.; Tella, M.; Brousset, L.; Rose, J.; Bottero, J.-Y.; Thiery, A. Exposure to Cerium Dioxide Nanoparticles Differently Affect Swimming Performance and Survival in Two Daphnid Species. *PLoS One* **2013**, *8* (8), e71260.

(98) Hoecke, K. Van; Quik, J. T. K.; Mankiewicz-Boczek, J.; Schamphelaere, K. A. C. De; Elsaesser, A.; Meeren, P. Van der; Barnes, C.; McKerr, G.; Howard, C. V.; Meent, D. Van De. Fate and Effects of CeO2 Nanoparticles in Aquatic Ecotoxicity Tests. *Environ. Sci. Technol.* **2009**, *43* (12), 4537–4546.

(99) Manier, N.; Bado-Nilles, A.; Delalain, P.; Aguerre-Chariol, O.; Pandard, P. Ecotoxicity of Non-Aged and Aged CeO2 Nanomaterials towards Freshwater Microalgae. *Environ. Pollut.* **2013**, *180*, 63–70.

(100) Conway, J. R.; Hanna, S. K.; Lenihan, H. S.; Keller, A. A. Effects and Implications of Trophic Transfer

and Accumulation of CeO2 Nanoparticles in a Marine Mussel. *Environ. Sci. Technol.* **2014**, *48* (3), 1517–1524.
(101) Korsvik, C.; Patil, S.; Seal, S.; Self, W. T. Superoxide Dismutase Mimetic Properties Exhibited by Vacancy Engineered Ceria Nanoparticles. *Chem. Commun.* **2007**, No. 10, 1056–1058.
(102) Ciofani, G.; Genchi, G. G.; Mazzolai, B.; Mattoli, V. Transcriptional Profile of Genes Involved in Oxidative Stress and Antioxidant Defense in PC12 Cells Following Treatment with Cerium Oxide Nanoparticles. *Biochim. Biophys. Acta (BBA)-General Subj.* **2014**, *1840* (1), 495–506.
(103) Sun, C.; Li, H.; Chen, L. Nanostructured Ceria-Based Materials: Synthesis, Properties, and Applications. *Energy Environ. Sci.* **2012**, *5* (9), 8475–8505.
(104) Pulido-Reyes, G.; Rodea-Palomares, I.; Das, S.; Sakthivel, T. S.; Leganes, F.; Rosal, R.; Seal, S.; Fernández-Piñas, F. Untangling the Biological Effects of Cerium Oxide Nanoparticles: The Role of Surface Valence States. *Sci. Rep.* **2015**, *5* (1), 1–14.
(105) Yokel, R. A.; Hussain, S.; Garantziotis, S.; Demokritou, P.; Castranova, V.; Cassee, F. R. The Yin: An Adverse Health Perspective of Nanoceria: Uptake, Distribution, Accumulation, and Mechanisms of Its Toxicity. *Environ. Sci. Nano* **2014**, *1* (5), 406–428.
(106) Quik, J. T. K.; Lynch, I.; Van Hoecke, K.; Miermans, C. J. H.; De Schamphelaere, K. A. C.; Janssen, C. R.; Dawson, K. A.; Stuart, M. A. C.; Van De Meent, D. Effect of Natural Organic Matter on Cerium Dioxide Nanoparticles Settling in Model Fresh Water. *Chemosphere* **2010**, *81* (6), 711–715.
(107) Auffan, M.; Tella, M.; Santaella, C.; Brousset, L.; Paillès, C.; Barakat, M.; Espinasse, B.; Artells, E.; Issartel, J.; Masion, A. An Adaptable Mesocosm Platform for Performing Integrated Assessments of Nanomaterial Risk in Complex Environmental Systems. *Sci. Rep.* **2014**, *4* (1), 1–7.
(108) Garaud, M.; Auffan, M.; Devin, S.; Felten, V.; Pagnout, C.; Pain-Devin, S.; Proux, O.; Rodius, F.; Sohm, B.; Giambérini, L. Integrated Assessment of Ceria Nanoparticle Impacts on the Freshwater Bivalve Dreissena Polymorpha. *Nanotoxicology* **2016**, *10* (7), 935–944.
(109) Booth, A.; Størseth, T.; Altin, D.; Fornara, A.; Ahniyaz, A.; Jungnickel, H.; Laux, P.; Luch, A.; Sørensen, L. Freshwater Dispersion Stability of PAA-Stabilised Cerium Oxide Nanoparticles and Toxicity towards Pseudokirchneriella Subcapitata. *Sci. Total Environ.* **2015**, *505*, 596–605.
(110) Tella, M.; Auffan, M.; Brousset, L.; Morel, E.; Proux, O.; Chanéac, C.; Angeletti, B.; Pailles, C.; Artells, E.; Santaella, C. Chronic Dosing of a Simulated Pond Ecosystem in Indoor Aquatic Mesocosms: Fate and Transport of CeO 2 Nanoparticles. *Environ. Sci. Nano* **2015**, *2* (6), 653–663.
(111) Oriekhova, O.; Stoll, S. Heteroaggregation of Nanoplastic Particles in the Presence of Inorganic Colloids and Natural Organic Matter. *Environ. Sci. Nano* **2018**, *5* (3), 792–799.
(112) Van Hoecke, K.; De Schamphelaere, K. A. C.; Van der Meeren, P.; Smagghe, G.; Janssen, C. R. Aggregation and Ecotoxicity of CeO2 Nanoparticles in Synthetic and Natural Waters with Variable PH, Organic Matter Concentration and Ionic Strength. *Environ. Pollut.* **2011**, *159* (4), 970–976.
(113) Buffle, J.; Wilkinson, K. J.; Stoll, S.; Filella, M.; Zhang, J. A Generalized Description of Aquatic Colloidal Interactions: The Three-Colloidal Component Approach. *Environ. Sci. Technol.* **1998**, *32* (19), 2887–2899.
(114) Ostermeyer, A.-K.; Kostigen Mumuper, C.; Semprini, L.; Radniecki, T. Influence of Bovine Serum Albumin and Alginate on Silver Nanoparticle Dissolution and Toxicity to Nitrosomonas Europaea. *Environ. Sci. Technol.* **2013**, *47* (24), 14403–14410.
(115) Elieh-Ali-Komi, D.; Hamblin, M. R. Chitin and Chitosan: Production and Application of Versatile Biomedical Nanomaterials. *Int. J. Adv. Res.* **2016**, *4* (3), 411.
(116) Duncan, E.; Owens, G. Metal Oxide Nanomaterials Used to Remediate Heavy Metal Contaminated Soils Have Strong Effects on Nutrient and Trace Element Phytoavailability. *Sci. Total Environ.* **2019**, *678*, 430–437.
(117) Olivera, S.; Chaitra, K.; Venkatesh, K.; Muralidhara, H. B.; Asiri, A. M.; Ahamed, M. I. Cerium Dioxide and Composites for the Removal of Toxic Metal Ions. *Environ. Chem. Lett.* **2018**, *16* (4), 1233–1246.
(118) ATSDR, E. P. A. The ATSDR 2019 Substance Priority List. Agency for Toxic Substances and Disease Registry 2019.
(119) Jiang, G.-B.; Shi, J.-B.; Feng, X.-B. Mercury Pollution in China. *Environ. Sci. Technol.* **2006**, *40* (12), 3672–3678.

(120) Nunes, M.; Coelho, J. P.; Cardoso, P. G.; Pereira, M. E.; Duarte, A. C.; Pardal, M. A. The Macrobenthic Community along a Mercury Contamination in a Temperate Estuarine System (Ria de Aveiro, Portugal). *Sci. Total Environ.* **2008**, *405* (1–3), 186–194.
(121) Tunsu, C.; Ekberg, C.; Foreman, M.; Retegan, T. Targeting Fluorescent Lamp Waste for the Recovery of Cerium, Lanthanum, Europium, Gadolinium, Terbium and Yttrium. *Miner. Process. Extr. Metall.* **2016**, *125* (4), 199–203.
(122) Gworek, B.; Bemowska-Kałabun, O.; Kijeńska, M.; Wrzosek-Jakubowska, J. Mercury in Marine and Oceanic Waters—a Review. *Water, Air, Soil Pollut.* **2016**, *227* (10), 1–19.
(123) Faganeli, J.; Hines, M. E.; Covelli, S.; Emili, A.; Giani, M. Mercury in Lagoons: An Overview of the Importance of the Link between Geochemistry and Biology. *Estuar. Coast. Shelf Sci.* **2012**, *113*, 126–132.
(124) Coppola, F.; Henriques, B.; Soares, A. M. V. M.; Figueira, E.; Pereira, E.; Freitas, R. Influence of Temperature Rise on the Recovery Capacity of Mytilus Galloprovincialis Exposed to Mercury Pollution. *Ecol. Indic.* **2018**, *93*, 1060–1069.
(125) Velez, C.; Freitas, R.; Antunes, S. C.; Soares, A. M. V. M.; Figueira, E. Clams Sensitivity towards As and Hg: A Comprehensive Assessment of Native and Exotic Species. *Ecotoxicol. Environ. Saf.* **2016**, *125*, 43–54.
(126) Sokolova, I. M.; Lannig, G. Interactive Effects of Metal Pollution and Temperature on Metabolism in Aquatic Ectotherms: Implications of Global Climate Change. *Clim. Res.* **2008**, *37* (2–3), 181–201.
(127) Coppola, F.; Almeida, Â.; Henriques, B.; Soares, A. M. V. M.; Figueira, E.; Pereira, E.; Freitas, R. Biochemical Impacts of Hg in Mytilus Galloprovincialis under Present and Predicted Warming Scenarios. *Sci. Total Environ.* **2017**, *601*, 1129–1138.
(128) Nardi, A.; Mincarelli, L. F.; Benedetti, M.; Fattorini, D.; d'Errico, G.; Regoli, F. Indirect Effects of Climate Changes on Cadmium Bioavailability and Biological Effects in the Mediterranean Mussel Mytilus Galloprovincialis. *Chemosphere* **2017**, *169*, 493–502.
(129) Andrade, M.; De Marchi, L.; Pretti, C.; Chiellini, F.; Morelli, A.; Figueira, E.; Rocha, R. J. M.; Soares, A. M. V. M.; Freitas, R. The Impacts of Warming on the Toxicity of Carbon Nanotubes in Mussels. *Mar. Environ. Res.* **2019**, *145*, 11–21.
(130) Freitas, R.; Coppola, F.; De Marchi, L.; Codella, V.; Pretti, C.; Chiellini, F.; Morelli, A.; Polese, G.; Soares, A. M. V. M.; Figueira, E. The Influence of Arsenic on the Toxicity of Carbon Nanoparticles in Bivalves. *J. Hazard. Mater.* **2018**, *358*, 484–493.
(131) Pachauri, R. K.; Allen, M. R.; Barros, V. R.; Broome, J.; Cramer, W.; Christ, R.; Church, J. A.; Clarke, L.; Dahe, Q.; Dasgupta, P. *Climate Change 2014: Synthesis Report. Contribution of Working Groups I, II and III to the Fifth Assessment Report of the Intergovernmental Panel on Climate Change*; Ipcc, 2014.
(132) Coppola, F.; Almeida, Â.; Henriques, B.; Soares, A. M. V. M.; Figueira, E.; Pereira, E.; Freitas, R. Biochemical Responses and Accumulation Patterns of Mytilus Galloprovincialis Exposed to Thermal Stress and Arsenic Contamination. *Ecotoxicol. Environ. Saf.* **2018**, *147*, 954–962.
(133) Freitas, R.; Leite, C.; Pinto, J.; Costa, M.; Monteiro, R.; Henriques, B.; Di Martino, F.; Coppola, F.; Soares, A. M. V. M.; Solé, M. The Influence of Temperature and Salinity on the Impacts of Lead in Mytilus Galloprovincialis. *Chemosphere* **2019**, *235*, 403–412.
(134) Pinto, J.; Costa, M.; Leite, C.; Borges, C.; Coppola, F.; Henriques, B.; Monteiro, R.; Russo, T.; Di Cosmo, A.; Soares, A. M. V. M. Ecotoxicological Effects of Lanthanum in Mytilus Galloprovincialis: Biochemical and Histopathological Impacts. *Aquat. Toxicol.* **2019**, *211*, 181–192.
(135) Plakhova, T. V; Romanchuk, A. Y.; Yakunin, S. N.; Dumas, T.; Demir, S.; Wang, S.; Minasian, S. G.; Shuh, D. K.; Tyliszczak, T.; Shiryaev, A. A.; Egorov, A. V; Ivanov, V. K.; Kalmykov, S. N. Solubility of Nanocrystalline Cerium Dioxide: Experimental Data and Thermodynamic Modeling. *J. Phys. Chem. C* **2016**, *120* (39), 22615–22626. https://doi.org/10.1021/acs.jpcc.6b05650.
(136) Quik, J. T. K.; Velzeboer, I.; Wouterse, M.; Koelmans, A. A.; Van de Meent, D. Heteroaggregation and Sedimentation Rates for Nanomaterials in Natural Waters. *Water Res.* **2014**, *48*, 269–279.
(137) Keller, A. A.; Wang, H.; Zhou, D.; Lenihan, H. S.; Cherr, G.; Cardinale, B. J.; Miller, R.; Ji, Z. Stability and Aggregation of Metal Oxide Nanoparticles in Natural Aqueous Matrices. *Environ. Sci. Technol.* **2010**, *44* (6), 1962–1967.

(138) Thill, A.; Zeyons, O.; Spalla, O.; Chauvat, F.; Rose, J.; Auffan, M.; Flank, A. M. Cytotoxicity of CeO2 Nanoparticles for Escherichia Coli. Physico-Chemical Insight of the Cytotoxicity Mechanism. *Environ. Sci. Technol.* **2006**, *40* (19), 6151–6156.

(139) Dados, A.; Paparizou, E.; Eleftheriou, P.; Papastephanou, C.; Stalikas, C. D. Nanometer-Sized Ceria-Coated Silica–Iron Oxide for the Reagentless Microextraction/Preconcentration of Heavy Metals in Environmental and Biological Samples Followed by Slurry Introduction to ICP-OES. *Talanta* **2014**, *121*, 127–135.

(140) Li, Z.; Shen, Y.; Li, X.; Zhu, S.; Hu, M. Synergetic Catalytic Removal of Hg0 and NO over CeO2(ZrO2)/TiO2. *Catal. Commun.* **2016**, *82*, 55–60. https://doi.org/https://doi.org/10.1016/j.catcom.2016.04.019.

(141) Lurman, G. J.; Walter, J.; Hoppeler, H. H. The Effect of Seasonal Temperature Variation on Behaviour and Metabolism in the Freshwater Mussel (Unio Tumidus). *J. Therm. Biol.* **2014**, *43*, 13–23. https://doi.org/https://doi.org/10.1016/j.jtherbio.2014.04.005.

(142) Anestis, A.; Lazou, A.; Pörtner, H. O.; Michaelidis, B. Behavioral, Metabolic, and Molecular Stress Responses of Marine Bivalve Mytilus Galloprovincialis during Long-Term Acclimation at Increasing Ambient Temperature. *Am. J. Physiol. Integr. Comp. Physiol.* **2007**, *293* (2), R911–R921. https://doi.org/10.1152/ajpregu.00124.2007.

(143) Senthilkumar, R. P.; Bhuvaneshwari, V.; Ranjithkumar, R.; Sathiyavimal, S.; Malayaman, V.; Chandarshekar, B. Synthesis, Characterization and Antibacterial Activity of Hybrid Chitosan-Cerium Oxide Nanoparticles: As a Bionanomaterials. *Int J Biol Macromol* **2017**, *104* (Pt B), 1746–1752. https://doi.org/10.1016/j.ijbiomac.2017.03.139.

(144) Huang, X.; Li, L.-D.; Lyu, G.-M.; Shen, B.-Y.; Han, Y.-F.; Shi, J.-L.; Teng, J.-L.; Feng, L.; Si, S.-Y.; Wu, J.-H.; Liu, Y.-J.; Sun, L.-D.; Yan, C.-H. Chitosan-Coated Cerium Oxide Nanocubes Accelerate Cutaneous Wound Healing by Curtailing Persistent Inflammation. *Inorg. Chem. Front.* **2018**, *5* (2), 386–393. https://doi.org/10.1039/C7QI00707H.

(145) Villa, S.; Maggioni, D.; Hamza, H.; Di Nica, V.; Magni, S.; Morosetti, B.; Parenti, C. C.; Finizio, A.; Binelli, A.; Della Torre, C. Natural Molecule Coatings Modify the Fate of Cerium Dioxide Nanoparticles in Water and Their Ecotoxicity to Daphnia Magna. *Environ. Pollut.* **2020**, *257*, 113597. https://doi.org/https://doi.org/10.1016/j.envpol.2019.113597.

(146) Morosetti, B.; Freitas, R.; Pereira, E.; Hamza, H.; Andrade, M.; Coppola, F.; Maggioni, D.; Della Torre, C. Will Temperature Rise Change the Biochemical Alterations Induced in Mytilus Galloprovincialis by Cerium Oxide Nanoparticles and Mercury? *Environ. Res.* **2020**, *188*, 109778. https://doi.org/https://doi.org/10.1016/j.envres.2020.109778.

(147) Della Torre, C.; Maggioni, D.; Nigro, L.; Farè, F.; Hamza, H.; Protano, G.; Magni, S.; Fontana, M.; Riccardi, N.; Chiara, M.; Caruso, D.; Binelli, A. Alginate Coating Modifies the Biological Effects of Cerium Oxide Nanoparticles to the Freshwater Bivalve Dreissena Polymorpha. *Sci. Total Environ.* **2021**, *773*, 145612. https://doi.org/https://doi.org/10.1016/j.scitotenv.2021.145612.

Annex A

List of Publications and Communications

Publications

- Hamza, H.; Ferretti, A. M.; Innocenti, C.; Fidecka, K.; Licandro, E.; Sangregorio, C.; Maggioni, D. An Approach for Magnetic Halloysite Nanocomposite with Selective Loading of Superparamagnetic Magnetite Nanoparticles in the Lumen. Inorg. Chem. 2020. https://doi.org/10.1021/acs.inorgchem.0c01039.

- Villa, S.; Maggioni, D.; Hamza, H.; Di Nica, V.; Magni, S.; Morosetti, B.; Parenti, C. C.; Finizio, A.; Binelli, A.; Della Torre, C. Natural Molecule Coatings Modify the Fate of Cerium Dioxide Nanoparticles in Water and Their Ecotoxicity to Daphnia Magna. Environ. Pollut. 2020, 257, 113597. https://doi.org/https://doi.org/10.1016/j.envpol.2019.113597.

- Morosetti, B.; Freitas, R.; Pereira, E.; Hamza, H.; Andrade, M.; Coppola, F.; Maggioni, D.; Della Torre, C. Will Temperature Rise Change the Biochemical Alterations Induced in Mytilus Galloprovincialis by Cerium Oxide Nanoparticles and Mercury? Environ. Res. 2020, 188, 109778. https://doi.org/https://doi.org/10.1016/j.envres.2020.109778

- Della Torre, C.; Maggioni, D.; Nigro, L.; Farè, F.; Hamza, H.; Protano, G.; Magni, S.; Fontana, M.; Riccardi, N.; Chiara, M.; Caruso, D.; Binelli, A. Alginate Coating Modifies the Biological Effects of Cerium Oxide Nanoparticles to the Freshwater Bivalve Dreissena Polymorpha. Sci. Total Environ. 2021, 773, 145612. https://doi.org/https://doi.org/10.1016/j.scitotenv.2021.145612.

Poster communications:

- "**New synthetic strategy for Halloysite-SPION nanocomposites"**
  4th Italian School of Magnitism, Torino, 21-25 May 2018
  Hady Hamza, Daniela Maggioni
- **"Different approaches to load SPION inside lumen of halloysite nanotubes"**
  M&Ns-19, Paris, 17-19 July 2019
  Hady Hamza, Anna M. Ferretti, Daniela Maggioni

School attended:

- **4th Italian school of Magnetism** "Advanced Magnetic Materials and Devices for Biomedical Applications" Torino, 21-25 May 2018
- **School of Nanomedicine** 2019, Trieste, 11th – 13th December 2019.
- **International school of chemistry** 2020, Camerino,1st-6th September 2020